

Structural studies of low X-ray-scattering-contrast sites in light-element-doped inorganic energy materials

Christopher Foo

Linacre College

University of Oxford

Supervised by Prof. Edman Tsang, Prof. Chiu Tang, and Dr. Sarah Day

A thesis submitted for the degree of

Doctorate in Philosophy in Inorganic Chemistry

Declaration

I confirm that this thesis is a result of my original work except where specific reference is made. All the material from other sources has been properly and fully acknowledged.

Christopher Foo

April 2022

Dedication

To my parents, Charles and Pauline, who have loved me through everything.

Acknowledgements

Firstly, I would like to express my heartfelt gratitude to my supervisor Professor Edman Tsang for his support and guidance throughout the course of my DPhil study. I have learnt so much over the past years, through both the investment and trust shown to me. Your insights and advice have always been extraordinary, and have been the basis for my work, publications, thesis, and scientific perspectives as I move on from this period of study.

I also give many thanks to Prof. Chiu Tang, who is now happily enjoying (semi-)retirement. Thank you for providing me with the technical knowledge and practical experience of powder diffraction and refinement, which I have so learnt to love. You were an exemplary mentor, and I will never forget your integrity, leadership, and dedication to precision in all areas. Thanks also go to Dr. Sarah Day for taking over my supervision from Chiu. You have also been a great example of a scientist. Your combination of kindness and professional conduct has encouraged and inspired me since the first interview, which now feels like such a long time ago. On a more practical note, thank you both for your prolonged support on commissioning time, and allowing me more of it than I rightly deserved!

The three technical chapters of this thesis are indebted to certain collaborators. With respect to the TiO_2 work, Dr. Yiyang (Bruce) Li has been so informative and gracious in our collaboration. Together it was possible to combine structure and electronics in such a satisfying way, and yield some great research. With respect to the Pd-Li work, Dr. Tianyi Chen shared her expertise, which were kindly shared with me. With respect to the zeolite work, I give many thanks to Prof. Benedict Lo, who trusted my analyses and allowed me complete ownership of the RSXPD study. The trust and guidance from I10 staff Dr. Raymond

Fan and Prof. Paul Steadman were also fundamental. The contribution of Dr. Guangchao Li (University of Oxford and Hong Kong Polytechnic) to this work in the form of SSNMR is also significant, and all of the credit for these analyses are reserved for him. My deepest gratitude is given to these primary collaborators. Additionally, many thanks go to Josh Fellowes, with whom work was published on the Haber-Bosch, which is not presented here.

Practical assistance with various characterisation techniques has also been invaluable. Thanks go to the following people for their advice, practical help, and data analysis, as well as their kindness and patience through everything: Ping Luen (Baron) Ho and Tianyi Chen (TEM), Constantin Lebedev (DFT), Shogo Kawaguchi (SXPD at BL02b2), and Fanny Nascimento Costa (PDF at I15-1).

The post-docs I have had the privilege to work around have guided me as both academic and personal role-models. Many thanks go to Pu Zhao, Tugce Ayvali, Jianwei Zheng, Ian McPherson, and Karin Kleiner. More personally, special thanks go to all of the Tsang group members, in particular, Guangchao, Baron, and Leo for keeping me company when I occasionally turned up to my desk.

My DPhil study was jointly-funded by the EPSRC and the DLS. Here, I acknowledge them for their long-term financial and academic support, in particular, the funding extension granted due to the limitations of recent Covid times. I also acknowledge Linacre College for providing the less academic aspects of DPhil life in Oxford, and importantly introducing me to many friends and providing experiences that I will keep and cherish forever. Without my friends in Oxford, I would not have made it here; in particular, shout-out to the Hurst Street crew, the revolving cast of housemates at Tyler Row, and all the moving parts of my home-from-home Oxford Mutual Aid.

Lastly, the greatest thanks are given to my family: my Mum and Dad, sister Rachael, brother-in-law Chen, and baby niece Evangeline. In particular, my parents have made my path up to here possible. From the very beginning, you have loved me through everything, and over my years of study have supported me at every turn. I have no doubt that in my next chapter of life you will continue to be there for me, in a way that I could never deserve or be able to repay. Without you, I would never have made it anywhere. I am forever grateful, and will love you forever. I cannot thank you enough, but I will try. Thank you for being you, for making me me, and for everything else in between.

Abstract

The agile ammonia synthesis is a collection of energy generation and storage infrastructure, which allows sustainable, local, and independent energy provision by converting renewable energy to hydrogen and ammonia, as well as in battery energy storage systems such as lithium-ion batteries. Many of these systems utilise archetypal inorganic materials, in particular due to enhanced performance from the incorporation of light-element dopants. Here, three components of the agile ammonia synthesis pathway are investigated in order to better understand the complex structure-activity relationship, in particular by using complex in-situ, in-operando, and inelastic synchrotron X-ray powder diffraction.

The nitrogen doping of titania is shown to impart increased structural and electronic defects that can be exploited by photo-absorption of visible light to split water using nothing else but solar irradiance. The generation of oxygen vacancies was observed by anisotropic thermal expansion, and supported by DFT calculations and photocatalytic performance. The use of palladium nanoparticles as an electrochemical energy store by lithium intercalation has been evaluated, and in-depth phase transitions characterised. Though the intercalation process reduces the order of the host framework, the cycling capacity remains constant, indicating amorphisation does not equate to performance degradation. The location of preferential substitutional aluminium sites in zeolite ZSM-5 has been yielded by observing probe molecule adsorption, but also directly by exploiting high-contrast anomalous scattering. The results of various techniques are in broad agreement of the siting, which will have impact the understanding of zeolite synthesis and performance mechanisms.

Table of Contents

Chapter 1: Introduction 1

1.1 Project overview 1

1.2 The new energy landscape 3

1.3 Light-element doping 10

1.4 Thesis outline 14

1.5 References 16

Chapter 2: Fundamental concepts of characterisation 17

2.1 The crystalline solid-state 17

2.2 Characterisation of the solid-state 18

2.3 Fundamental concepts of XRD 20

2.4 Practical aspects of XRD 28

2.5 Synchrotron Radiation 31

2.6 Other synchrotron scattering techniques 33

2.7 Other analytical techniques 36

2.8 References 39

Chapter 3: Experimental procedures 41

3.1 General diffraction characterisation 41

3.2 Photocatalytic water-splitting of N-TiO_2 45

3.3 Electrochemical lithiation of palladium nanoparticles 49

3.4 Aluminium siting in zeolites 54

3.5 References 64

Chapter 4: Hydrogen evolution by photocatalytic water-splitting over nitrogen-doped TiO_2: oxygen vacancies and the structure-activity relationship 65

4.1 Abstract 65

4.2 Introduction 66

4.2.1 Agile ammonia synthesis and analytical context 66

4.2.2 Photocatalysis 67

4.2.3 TiO_2 as photocatalyst 68

4.2.4 Nitrogen-doped TiO_2 73

4.2.5 Nitrogenation to titanium nitride 75

4.2.6 Agile ammonia synthesis 76

4.2.7 Evaluation of characterisation techniques 76

4.2.8 Aims of investigation 77
4.3 Results and discussion 79
4.3.1 Nitrogen doping 79
4.3.2 Photocatalytic water-splitting at elevated temperature 83
4.3.3 Active-site defects by EPR 87
4.3.4 Anisotropic thermal expansion of anatase 90
4.3.5 Local structure distortions of oxygen vacancies by DFT 98
4.3.6 A new titanium oxynitride structure from high nitrogen-doping 105
4.3.7 Relationship to temperature-dependence of catalytic activity 111
4.4 Conclusions 113
4.5 References 116
Chapter 5: Electrochemical lithium storage in palladium nanoparticles: phase behaviour and stability 121
5.1 Abstract 121
5.2 Introduction 122
5.2.1 Agile ammonia synthesis and analytical context 122
5.2.2 Palladium nanoparticles 122
5.2.3 Light-element doping in transition metal lattices 123
5.2.4 Lithium-ion batteries (LIB) 126
5.2.5 Integration into grid-scale storage and AAS 127
5.2.6 Current structural characterisation and problems 128
5.2.7 Aims of investigation 129
5.3 Results and discussion 130
5.3.1 Optimising particle size for SXPD 130
5.3.2 Palladium nanoparticle synthesis: inadvertent $Pd^{int}C$ formation 130
5.3.3 Stability of thermally lithiated $Pd^{int}Li$ 133
5.3.4 Use as lithium storage material in lithium-ion batteries 144
5.3.5 Ex-situ identification of lithiated palladium phases 147
5.3.6 In-operando SXPD 151
5.3.7 Non-crystalline local order by PDF 174
5.4 Conclusions 177
5.5 References 181
Chapter 6: Locating framework aluminium in ZSM-5 for ammonia synthesis promotion and storage: assessment of indirect and direct characterisation methods 185
6.1 Abstract 185

6.2 Introduction 186
6.2.1 Context 186
6.2.2 Zeolites 188
6.2.3 Types of siting 190
6.2.4 Low scattering contrast 194
6.2.5 Aims of investigation 195
6.3 Results and Discussion 198
6.3.1 Indirect siting by STEM imaging of Ag adsorption 198
6.3.2 Indirect siting using TMPO as a probe molecule 202
6.3.3 Direct crystallographic siting by RSXPD 209
6.3.4 Comparative discussion of characterisation results 222
6.3.5 Chemical origins and implications 225
6.4 Conclusions 228
6.5 References 233
Chapter 7: Ending remarks 239
7.1 Agile ammonia synthesis and light-element doping 239
7.2 Archetypal inorganic frameworks and light-element doping 240
7.3 X-ray scattering techniques and light-element doping 241
7.4 Final remarks 245
Appendices
Chapter 3: Experimental procedures i
Chapter 4: TiO_2 iii
Chapter 5: Palladium ix
Chapter 6: Zeolites xx

List of Publications

- Chen, T.; Foo, C.; Tsang, S. C. E. Interstitial and Substitutional Light Elements in Transition Metals for Heterogeneous Catalysis. Chem. Sci. 2021, 12 (2), 517–532
- Foo, C.; Li, Y.; Lebedev, K.; Chen, T.; Day, S.; Tang, C.; Tsang, S. C. E. Characterisation of Oxygen Defects and Nitrogen Impurities in TiO_2 Photocatalysts Using Variable-Temperature X-Ray Powder Diffraction. Nat. Commun. 2021, 12 (1), 661
- Li, G.; Foo, C.; Yi, X.; Chen, W.; Zhao, P.; Gao, P.; Yoskamtorn, T.; Xiao, Y.; Day, S.; Tang, C. C.; Hou, G.; Zheng, A.; Tsang, S. C. E. Induced Active Sites by Adsorbate in Zeotype Materials. J. Am. Chem. Soc. 2021, 143 (23), 8761–8771
- Chen, T.; Foo, C.; Zheng, J. J. W.; Fang, H.; Nellist, P.; Tsang, S. C. E. Direct Visualization of Substitutional Li Doping in Supported Pt Nanoparticles and Their Ultra-Selective Catalytic Hydrogenation Performance. Chem. – Eur. J. 2021, 27 (47), 12041–12046
- Foo, C.; Fellowes, J.; Fang, H.; Large, A.; Wu, S.; Held, G.; Raine, E.; Ho, P.-L.; Tang, C.; Tsang, S. C. E. Importance of Hydrogen Migration in Catalytic Ammonia Synthesis over Yttrium-Doped Barium Zirconate-Supported Ruthenium Nanoparticles: Visualization of Proton Trap Sites. J. Phys. Chem. C 2021, 125 (42), 23058–23070
- Li, Y.; Wang, Z.; Wang, Y.; Kovács, A.; Foo, C.; E. Dunin-Borkowski, R.; Lu, Y.; A. Taylor, R.; Wu, C.; Edman Tsang, S. C. Local Magnetic Spin Mismatch Promoting Photocatalytic Overall Water Splitting with Exceptional Solar-to-Hydrogen Efficiency. Energy Environ. Sci. 2022, 15 (1), 265–277

List of Abbreviations

AAS	Agile ammonia synthesis
ASF	Anomalous scattering factors
BAS	Brønsted acid site
BESS	Battery energy storage system
CB	Conduction band
DAFS	Diffraction anomalous fine structure
DANES	Diffraction anomalous near-edge structure
DFT	Density functional theory
DLS	Diamond Light Source
EDX	Energy dispersive X-ray spectroscopy
EELS	Electron energy loss spectroscopy
EPR	Electron paramagnetic resonance
FWHM	Full-width half maximum
GoF	Goodness of fit
ICP-MS	Inductively-coupled plasma mass spectroscopy
KK	Kramers-Kronig
NPD	Neutron powder diffraction
PDF	Pair distribution function
RSXPD	Resonance soft X-ray powder diffraction
SSNMR	Solid-state nuclear magnetic resonance
STEM	Scanning transmission electron microscopy
SXPD	Synchrotron X-ray powder diffraction
TMPO	Trimethyl phosphine oxide
VB	Valence band
VT	Variable temperature
XPS	X-ray photoelectron spectroscopy
XRD	X-ray diffraction

List of Figures

Figure 1-1. (a) Negative energy prices from reference [2]. (b) Example of load-levelling using BESSs; reproduced from reference [3]. (c) Various energy technologies by discharge time at rated power; reproduced from reference [4]. (d) Prediction of most cost-efficient (lowest levelised cost) technology for all durations and frequency of discharge: LIB in red, hydrogen in black, pumped hydro in blue, compressed air in green; reproduced from reference [5]..... 5

Figure 1-2. Schematic of self-contained agile ammonia synthesis pathway, featuring many of the systems presented in this document. Renewable inputs shown in green, energy-vector-producing reactions in red, and storage solutions in orange..... 9

Figure 2-1. Schematic of the fulfilment of Bragg's law in real and reciprocal space. 22

Figure 2-2. Example of diffraction patterns viewed towards the propagating beam of (a) single-crystal (b) and powder showing Debye-Sherrer cones. 29

Figure 3-1. Diffractometer at I11, DLS..... 42

Figure 3-2. RASOR end-station on I10, DLS. Inset shows bespoke sample holder for powder samples on I10. 61

Figure 4-1. Schematics of photocatalysis in the context of water-splitting. Reproduced from reference [4]. 67

Figure 4-2. (a,b) Displayed unit-cells of rutile and anatase. Difference in electronic configuration of anatase and rutile.[24] (c) Band bending, and (d) variable vectorial charge-carrier separation by mid-gap defect trap sites. 70

Figure 4-3. (a) Schematic of n- and p-type semiconductors.[38] (b) Localised defect sites below the CB from oxygen vacancies and below the VB from hydrogen disorder.[5]..... 71

Figure 4-4. Effect of nitrogen doping on the electronic structure of (a) anatase and rutile,[23] (b) substitutional N^{2-} and interstitial N in anatase,[40] and (c) sub-gap transition from reduced Ti^{3+} electron trap to N_b•, forming diamagnetic N_b^-.[34] 74

Figure 4-5. TEM micrographs showing typical morphology of (a) A3, and (b) P3. (c, d) HAADF-STEM micrographs of P3..... 79

Figure 4-6. XPS spectra of N-P25 materials treated with ammonia at different temperatures. 80

Figure 4-7. (a) Nitrogen composition of P25 samples by XPS and ICP-MS. (b) Relative composition of substitutional nitrogen and interstitial nitrogen. 81

Figure 4-8. (a) UV-vis absorption spectra, (b) corresponding Tauc plots and average band-gaps. .. 82

Figure 4-9. Photocatalytic water-splitting activity over (a) pristine, and (b) nitrogen-doped TiO_2 materials under UV-visible light from a xenon lamp. 84

Figure 4-10. Control tests for photocatalytic activity under only visible light at 270°C. a) Demonstration of stoichiometric water-splitting by GC-MS over 50 h. b) Over 5-cycle test of P3. 85

Figure 4-11. Photocatalytic water-splitting activity N-TiO_2 samples at 270°C under visible-light irradiation only. 86

Figure 4-12. EPR spectra for (a) rutile and (b) anatase materials. (c) Hydrogen evolution of anatase catalysts under visible light against EPR-derived oxygen vacancy concentration. Error bars indicate the standard deviation..... 88

Figure 4-13. Absolute lattice parameters of pristine P0 (red) and highly-doped P3 (green) from room temperature to 500°C, separated by lattice parameter. 90

Figure 4-14. First derivative of lattice parameter against temperature, dx/dT, of pristine P0 (red) and highly-doped P3 (green) from room temperature to 500°C. 91

Figure 4-15. Linear thermal expansion coefficient α for the a- and c-axes of the anatase phase in P0 and P3. 93

Figure 4-16. Schematic of proposed mechanism for anisotropic thermal expansion. 95

Figure 4-17. Pristine anatase (101) supercell showing assigned depth environments and inequivalent (relative to surface, not vacancy) oxygen (red) and titanium (blue) sites at each depth. Volume of vacuum not shown. Note, there is no O_{s4} due to surface termination. 99

Figure 4-18. Oxygen vacancy structure V_{Oss3}: oxygen (red), titanium (blue), O_{b4} (pink), five-coordinate titanium (green). (b) Under-coordinated titanium sites shown isolated: recontextualise in $I4_1/amd$ axes by rotation. (c) Crystal field theory prediction of electronic configuration of titanium. 103

Figure 4-19. SXPD patterns of A0-A4. (a) Cubic reflections (111), (200), (220, and (311) denoted by *. (b) enlarged view of the (200) reflection of anatase and $TiNO_x$. Intensities normalised due to different data-collections causing different total intensities. 105

Figure 4-20. Phase identification of $TiNO_x$ by Rietveld refinement. Electron density maps of the $TiNO_x$ unit-cell: 2D cross-sections of electron density derived from the Fourier transform of (a) F_{obs} at one unit-cell length a from the origin along (011); (b) F_{diff} ($=F_{obs}–F_{calc}$) at 0.25a along (001). (c) iso-surface of electron density at 0.1 (red); grey: titanium, blue: nitrogen. 107

Figure 4-21. Fitting of Rietveld refinement of A4 at room temperature consisting of an anatase phase and a titanium oxynitride phase; blue: titanium, red: nitrogen, white: oxygen. 108

Figure 4-22. (a) VT-SXPD of A4; (b-d) enlarged regions showing the decomposition of $TiNO_x$ and increase in anatase intensity; (e) intensity of anatase (101) and TiN (200) plotted against temperature (negligible standard deviation not plotted). 109

Figure 4-23. Structural parameters of $TiNO_x$ from the Rietveld refinement of A4 during thermal oxidation; phase composition (red), lattice parameter (black), occupancy of interstitial oxygen site (blue). 110

Figure 4-24. Photocatalytic water-splitting activities over highly-doped N-TiO_2 samples P3, A3, and R3 photocatalysts at different temperatures under visible-light illumination. 111

Figure 5-1. Biphasic product of thermal lithiation. Laboratory-configuration XRD patterns of one-step palladium nanoparticle synthesis from $Pd(OAc)_2$ at different temperatures: (a) patterns; sample notation as (temperature [°C]/ramp-rate [°C min^{-1}]/hold-time [h]), and (b) lattice parameters and relative crystalline composition. (c) Varying hold-time showing kinetic limitation of carbon deintercalation. 131

Figure 5-2. (a) STEM image and (b) EDX spectrum of 50%Pd/SiO_2. (c and d) Lattice parameters and integrated intensities, respectively, as derived by Rietveld refinement of VT-SXPD of the 50%Pd/C. 132

Figure 5-3. TEM imaging and particle-size histogram of 50%Pd lithiated at 250°C for 12 hours. 133

Figure 5-4. Effect of temperature and lithium doping on palladium nanoparticles by laboratory-configuration XRD: (a) post-synthesis lithiated at different temperatures, (b) following post-synthesis washing with water and ethanol. 134

Figure 5-5. In-situ lithiated 50%Pd^{int}Li/C: (a) room temperature SXPD, and (b-d) VT-SXPD heatmaps of (111) and (200) for 0.2eq, 0.5eq, and 1.5eq, respectively, showing the stability of the lithiated phase up to very high temperature. 137

Figure 5-6. Rietveld refinement of VT-SXPD for pristine and in-situ lithiated palladium nanoparticles: Pd as dotted lines, Pd^{int}Li as solid lines. (a) Relative crystalline composition, (b) integrated intensity of the Bragg phases, (c) lattice parameters , and (d) thermal expansion from room temperature expressed as a percentage; control sample of monophasic pristine Pd shown in black. 139

Figure 5-7. Inhomogeneous phase partitioning at high temperature. (a) SXPD patterns of 0.2eq in-situ lithiated 50%Pd, showing the splitting of the expanded Pd^{int}Li at 440-515°C. (b) Lattice parameters of emergent contracted phases. 143

Figure 5-8. Assessing the electrochemical lithium capacity and behaviour of graphite anode material. (a) Cycling stability averaged over at least three cells; only discharge capacities shown for clarity. (b) Potential profiles of the first 5 cycles for graphite (red) and 20Pd/gr (spectrum); discharge as solid lines, charge as dotted lines. (c and d) dQ/dV plot of graphite and 20Pd/gr, respectively. 146

Figure 5-9. (a) Refinement of 50%Pd/gr showing significant $PdLi_2$. (b) Displayed structure of $PdLi_2$; palladium in grey (radius: 1.37 Å), lithium in green (radius: 1.57 Å). 148

Figure 5-10. (a) Ex-situ phase identification of discharged electrodes 50%Pd/cb and 50%Pd/gr (graphite composition not included). (b) Space-fill display of unit-cells and packing of relevant intermetallic compounds; palladium in grey (radius: 1.37 Å), lithium in green (radius: 1.57 Å)... 150

Figure 5-11. Electrochemical cycling of 50%Pd/gr during in-operando SXPD. (b) SXPD patterns of 50%Pd/gr plotted with arbitrary spacing, foregoing time (proportional to capacity) or potential dependence. 152

Figure 5-12. Schematic of initial observations of palladium phase-evolution by in-operando SXPD. 153

Figure 5-13. Derivative of intensity with respect to angle of 50%Pd/cb, and 50%Pd/gr. Peaks indicated by displaying extreme values of <-2000 in black, and >2000 in white; intermediate negative values shown in green, through to positive in red. Unmodelled short-lived reflections shown by blue circles. 154

Figure 5-14. Comparison of phase evolution of *cF* Pd by Rietveld refinement: (a) relative crystalline composition and absolute integrated Bragg area over the full cycling; (b) plotting against capacity or potential over the first discharge. 157

Figure 5-15. Identifying correlation in phase changes. Intensity plotted (a) against cumulative capacity, and (b) against cumulative potential. c) Four discharge and charge transitions. 158

Figure 5-16. Intensity over potential separated by cycle. Reversing the discharge *x*-axis allows the use of non-cumulative potentials, and allows the centring of the plot around low potentials. Note that the *x*-scales are different for discharge and charge. 159

Figure 5-17. Phase evolution of *cF* Pd over 1D over potential; labels show capacity in mA h g^{-1}. 161

Figure 5-18. Correlation of (a) *cF* Pd and (b) *hP* $PdLi_2$ at low potential over 1D. Potential points coloured by capacity values with key potentials labelled with capacity [mA h g^{-1}]; intensity axes both 700 arb. units, and *x*($PdLi_2$) axes both 0.01 Å. 162

Figure 5-19. Highly negatively-correlated intensities of *cF* Pd and *hP* $PdLi_2$: dI/dV against potential. Smoothed by calculating change over four data points. 164

Figure 5-20. Change in intensity with capacity, d*I*/d*Q* against cumulative capacity. Smoothed by calculating change over four data points. (a) The entire cycled range, and (b) omitting 1D in order to show minor changes. 166

Figure 5-21. Triphasic cycling of 1C. (a) d*I*/d*V* against potential, and (b) d*I*/d*Q* against capacity. Both intensity-derivative plots smoothed by calculating change over four data points. (c) Raw intensity values; labels show local maximum intensity of *cF* Pd (red) and $PdLi_2$ (yellow), and the appearance of *cP* PdLi (blue). (d) $PdLi_2$ lattice parameters against potential; capacity labels in [mA h g^{-1}] 168

Figure 5-22. Degradation of intensity and potential: comparing the energy and magnitude of transitions over cycling. 170

Figure 5-23. Lattice parameter changes for *hP* $PdLi_2$ over three full cycles..... 171

Figure 5-24. Representing the magnitude of the phase transitions by change in intensity. For discharge Δ*I*(final) and for charge Δ*I*(initial) are used. (a) Relative change. (b) Average absolute change; anomalous 1D(0→→2) (large magnitude) and 3C(2→→0) ($PdLi_2$ increases) removed from average. 173

Figure 5-25. Normalised intensity values showing increasing relative composition of *hP* $PdLi_2$ from *cP* PdLi. 174

Figure 5-26. PDF of post-mortem 50%Pd/cb Dotted lines show characteristic *hP* $PdLi_2$, solid lines show characteristic *cP* PdLi. 175

Figure 5-27. Schematic of potential ranges of phase transitions. (Pd↔↔$PdLi_2$) in green, (Pd↔ PdLi) in red, (PdLi↔$PdLi_2$) in blue. Unexpected direction (Pd$\underleftrightarrow{}$PdLi) transitions marked with * and darkened colour. 180

Figure 6-1. The promotion of ammonia yield by various zeolites derived by computational methods. Reproduced from reference [5]. 187

Figure 6-2. Displayed polyhedral structure of ZSM-5 showing the 12 chemically and crystallographically distinct T-sites, viewed along the (a) *a*-axis (sinusoidal channel), (b) *b*-axis (straight channel), and (c) *c*-axis (non-porous). 189

Figure 6-3. (a) Far-from-edge atomic form factors for Al^{3+} and Si^{4+}, which are dependent on scattering angle and independent of energy. (b) ASF for elemental Al^0 and Si^0, which are dependent on energy and independent of scattering angle. 195

Figure 6-4. STEM imaging of H-ZSM-5 orientated along the <010> zone axis. 196

Figure 6-5. Output of intensity-contrast software used to locate high contrast within channels that are attributed to adsorbed Ag atoms. 199

Figure 6-6. (a) Distribution of Ag adsorption and aluminium assignment in the straight channel of ZSM-5 as observed by TEM. (b) Radial representation of raw adsorption observations, and (c) Radial representation of aluminium assignment with the structural representation overlaid. Aluminium sites as derived by RXSPD show in yellow. 201

Figure 6-7. ^{1}H-^{31}P heteronuclear-correlation (HECTOR) spectra of TMPO/ZSM-5..... 204

Figure 6-8. (a) SXPD pattern and Rietveld refinement fitting of TMPO/H-ZSM-5. (b) NPD diffraction pattern and Rietveld refinement data of TMPO/H-ZSM-5. (c) Crystallographic model of the three distinct asymmetric TMPO locations as derived by Rietveld refinement of NPD as viewed down the *b*-axis. 207

Figure 6-9. Theoretical (shifted from Al^0 edge) and experimentally-derived ASF over the Al^{3+} K-edge of ZSM-5. Experimental real-part of the ASF *f'* yielded by KK transform. Experimentally sampled energies shown by drop-lines. 212

Figure 6-10. Simulated integrated intensities of the first 15 observed reflections at various energies for the T6 structure: (a) raw intensity, and (b) change in intensity from the previous energy pattern. 214

Figure 6-11. Average of the magnitude of change from the T0 structure (a) with respect to energy (markers show the experimentally sampled energies), and (b) with respect to T-site. 215

Figure 6-12. (a) The magnitude of the change in intensity from T0 of the first five reflections, averaged over the energy. (b) Simulated patterns at 1562 eV for all structures, and the experimental pattern, showing six consecutive reflections. 216

Figure 6-13. Magnified regions of RSXPD patterns against *d*-spacing that demonstrate the non-systematic changes in integrated intensity. 218

Figure 6-14. Integrated intensities of experimentally observed of ZSM-5 by RSXPD on I10 (whole range plotted in Figure S6-9): (a) absolute intensity, and (b) change in intensity relative to lowest energy 1540 eV. 220

Figure 6-15. Rietveld refinement against experimental RSXPD. (a) Example fitting at 1569 eV. (b) Refined aluminium occupancy. 222

Figure 6-16. Summary of aluminium siting across several characterisation techniques. For STEM, occupancy at the T6/T12 site attributed to both, denoted by *. 224

Figure 7-1. Repeated figure from Chapter 1: Introduction. Schematic of self-contained agile ammonia synthesis pathway, featuring many of the systems presented in this document. Renewable inputs shown in green, energy-vector-producing reactions in red, and energy vectors/storage solutions in orange. 239

List of Tables

Table 1-1. Difference in e^- as a result of light-element doping in various inorganic frameworks for energy applications. * Electron configuration of species is not well-established. 11

Table 2-1. The seven crystal systems of the crystalline solid-state. Reproduced from Advanced Certificate in Powder Diffraction on the Web, Birkbeck College.[2] 18

Table 3-1. Temperature calibration for VT-SXPD on I11, DLS. Fits to a linear function: $m = 0.8979260$, $c = 0.8694716$; $R = 0.9999$. 47

Table 4-1. Tabulated compositional and electronic characterisation. 81

Table 4-2. Oxygen-vacancy concentrations derived from EPR spectra of rutile and anatase materials. 89

Table 4-3. DFT results showing the absolute energy, relative energy to minimum structure V_{Oss3}, changes in *P1* lattice parameters of the (101) slab, and strain relative to the pristine slab. 100

Table 5-1. ICSD entries of bimetallic palladium-lithium structures. 125

Table 5-2. ICP-MS for thermally lithiated palladium nanoparticles. 135

Table 5-3. Temperature range of thermal instability of Pd and $Pd^{int}Li$ at various lithium doping levels by VT-SXPD. 142

Table 5-4. Structural information on palladium lithium phases, and interatomic distances. * Lithium atom density assumes the full occupancy of lithium sites. $^{\#}$ Not refined throughout. 149

Table 5-5. dQ/dV of several potential ranges during 1D, showing the majority of capacity is intercalated from 136-17 mV. 161

Table 5-6. Phase evolution of *cF* Pd and *hP* $PdLi_2$ during 1D. 165

Table 6-1. Ratio of integrated area of peaks based on the 1D ^{31}P SSNMR spectrum. 205

Table 6-2.TMPO adsorption sites in ZSM-5 by SXPD and NPD. 206

List of Equations

Equation 2-1. Bragg's Law, where n is the order of difraction, λ is the wavelength, d is the spacing, and θ is the angle of diffraction. 22

Equation 2-2. Relation between the magnitude of the scattering vector and the d-spacing. 23

Equation 2-3. Magnitude of the scattering vector 23

Equation 2-4. Experimental measurement of the structure factor, where I is intensity, and F is the structure factor. 25

Equation 2-5. The structure factor equation, where f is the atomic scattering factor, and x, y, and z are the site coordinates. 25

Equation 2-6. The complex structure factor, φ is the phase. 25

Equation 2-7. The electron-density equation, where ρ is the electron density, and V is the uni-cell volume. 26

Equation 2-8. Least-squares calculation, where y is the intensity. 26

Equation 2-9. Various residual calculatinos, where Δ is the fitting difference, w_i is the weighting, and y_i is the observed or calculated intensity. (a) Difference in calculated pattern from observed pattern; (b) overall percentage difference in calculated pattern from observed pattern, R_{wp}; (c) expected difference value R_{exp}, where N is the number of data points, P is the number of parameters, and C is the number of constraints on the model; (d) goodness of fit, where χ is the fractional calculated difference from the expected. 28

Equation 2-10. Brilliance of a photon beam, where Φ is photons per second per area, θ is the beam divergence (horizontal or vertical) in mrad, and 0.1%BW is the percentage of photons that deviate 0.1% from the central energy. 32

Equation 2-11. Modification of the atomic scattering factor by the complex ASF, where f_0 is the atomic scattering factor, f' is the real anomalous scattering factor, and f'' is the imaginary part. 33

Equation 2-12. Fluorescence is proportionate to absorption, and thus fluorescence, where K is a constant, and μ is the atomic absorption coefficient. 33

Equation 2-13. Kramers-Kronig relation. 34

Equation 2-14. The PDF from total scattering S(Q), where r is the interatomic distance, and Q is the Q-space = $(4\pi \sin(\theta))/\lambda$ 35

Equation 2-15. PDF generation from real-space model, where b is the atomic scattering factors, $\langle b \rangle$ is the stoichiometric weighting, δ is the interatomic distance, and ρ_0 is the average density 35

Equation 2-16. Binding energy by XPS, where E_{bind} is the binding energy, and E_{KE} is the photoelectron kinetic energy. 36

Equation 2-17. Derivation of band-gap by UV diffuse reflectance, where K and S are the absorption and back-scattering coefficients, respectively, C is a constant, and E_g is the band-gap. 36

Equation 2-18. Derivation of band-gap by UV diffuse reflectance by Tauc plot, where B is a constant, and γ is 2 in the context of indirect transitions, as will be used in this work. 37

Equation 2-19. Probing electronic environment by NMR, where γ is the gyromagnetic ratio, $\hbar$ is the reduced Planck constant, and B_0 is the magnetic field at the nucleus. 37

Equation 2-20. Energy transition of electron spin-flipping in EPR, where μ_B is the Bohr magneton. 38

Equation 4-1. General charge carrier formation in TiO_2. 67

Equation 4-2: Fujushima and Honda's water-splitting.[2] 68

Equation 4-3. General photocatalytic water-splitting. 68

Equation 4-4. Oxygen vacancy formation in TiO_2 and substitutional N-TiO_2.[40] 73

Equation 4-5. Oxygen vacancy formation in Kroger-Vink notation. 87

Equation 4-6. Linear thermal expansion coefficient α, where x is the lattice parameter and T is the temperature (Equation 4-6). 92

Equation 5-1. Vegard's law applied to $Pd^{int}Li$ at any given temperature by using experimentally observed thermal expansion of end-phases. xv

Chapter 1: Introduction

This chapter will provide a brief introduction to this document, including the overall context, structure, aims, and evaluation of the work.

1.1 Project overview

1.1.1 Origins and focus

The doctoral studentship was jointly funded by the EPSRC and the Diamond Light Source (DLS). The student was co-supervised by Prof. Edman Tsang (Chemistry, University of Oxford) and Prof. Chiu Tang (Principal Beamline Scientist for the High Resolution Powder Diffraction beamline (I11), DLS). Following Prof. Tang's retirement in 2020, Dr. Sarah Day took on the co-supervision. The project is primarily focussed on the novel characterisation of a variety of inorganic-based energy materials used in catalytic applications: in particular, structural identification and quantification of light elements such as hydrogen, lithium, nitrogen, and aluminium in crystalline structures using advanced in-situ and in-operando diffraction techniques.

1.1.2 Aims

It was aimed to use SXPD to uncover the structure-behaviour relationship of certain light-element dopants in heavy frameworks. As part of a structural study, the primary area of investigation is the nature of the doping and the effect on the host framework. Secondarily, the effects on system performance will be discussed. And when appropriate, there will also be evaluations of synthetic control and intelligent design by light-element doping. These are

all inextricably linked, with the unanswered questions of structure almost always linked to implications on performance/activity Although it is the aim to use structural characterisation to predict and explain enhanced performance, emergent phenomena are also useful in targeting experimentation and providing correlation. Thus, it has been paramount to understand this structure-activity context in order to ask relevant questions, and provide meaningful observations, which can be attributed to chemical processes. This work aims to contribute coherently to the existing literature, albeit from a predominantly structural perspective.

1.1.3 Energy applications

Additional to the themes of light-element doping and structural characterisation, much of this work is also unified by the applications of the materials in the energy sector. In particular, they can all be placed along the agile ammonia synthesis (AAS) process.

1) Sustainable hydrogen production from photocatalytic water splitting over N-doped TiO_2
2) Increasing ammonia synthesis rates in the Haber-Bosch reaction over ruthenium nanoparticles supported on barium yttrium zirconate perovskite
3) Promoted Haber-Bosch synthesis by ammonia confinement and storage in zeolite ZSM-5
4) Electrochemical energy storage in LIB by insertion into palladium nanoparticles as a battery energy storage system

In the interest of focus, the study on the hydrogen spill-over of perovskite supports will not be presented here, but the reader is directed towards the published work by Foo et al., entitled ‘Importance of Hydrogen Migration in Catalytic Ammonia Synthesis over Yttrium-Doped Barium Zirconate-Supported Ruthenium Nanoparticles: Visualization of Proton Trap Sites’.[1]

1.2 The new energy landscape

1.2.1 Societal context

The burning of fossil fuels by human-kind has resulted in the significant warming of the atmosphere, which is drastically changing the established climates in every region of the planet. Beginning during the Industrial Revolution, the temperatures of the land, sea, and air are increasing at an ever-increasing rate, which we will soon be powerless to remedy due to positive-feedback effects. The consequences of a hotter environment are now being observed in rising sea-levels, ocean acidification, loss of permafrost and icecaps, and the increased frequency and severity of extreme storms, flooding, droughts, and forest fires. This threatens to irreversibly remove plants, animals, and ecosystems from existence, and alter natural formations, cycles, and mechanisms from their current equilibrium. The effects of man-made heating of the atmosphere on the biosphere and global physical phenomena need to be widely and collectively accepted, considered, overcome, and countered.

The current and escalating desolation of arable land, destruction of settlements, and direct danger to human life is pushing us towards a global crisis relating not only to our methods and ability to produce energy and food, but also to the unchecked and insatiable demand for increased money, comfort, stability, and affluence. These most often come at the expense of others, both those we share the planet with in the present-day, and those belonging to future generations who will have to bear the consequences.

Furthermore, the effects of climate change do not affect all of us equally. The dangers of a warming planet are disproportionately impressed upon the Global South, who have historically contributed relatively little to the green-house gases that threaten their livelihoods

and lives themselves. There is little doubt that the sum of the truly massive populations that will be forced to leave uninhabitable regions will constitute a humanitarian crisis, the momentum of which is gaining pace.

This thesis will present chemical research on several key parts of the new low-emission energy landscape that will aid the global transition from a dirty, extractivist market to becoming a more sustainable and clean society.

1.2.2 Renewable energy and energy storage

Over the last few decades, the field of sustainable power generation has received much attention due to the pressing climate crisis. The efforts to convert solar, wind, and nuclear energy to electrical energy has been highly successful, with efficiencies and generation capacities still increasing at significant pace. However, producing large amounts of electrical power when it is not required is problematic for grid systems, risking blackouts and invoking negative energy prices (Figure 1-1a). It has been becoming increasingly clear that the utilisation of energy storage must also be incorporated into the energy landscape in order to level peak load.

Bulk power management by energy storage is already widely used in pumped hydro (Figure 1-1b). Load shifting is beginning to be utilised more in the form of hydrogen, ammonia, and redox flow batteries.[1–4] Meanwhile, high-frequency response in the form of battery energy storage systems (BESSs) and supercapacitors are also in the early stages of grid-scale integration. It is predicted that the cheapest solution to the majority of grid-level

storage problems will soon be almost entirely composed of hydrogen and lithium-ion batteries (LIB) (Figure 1-1d).[5]

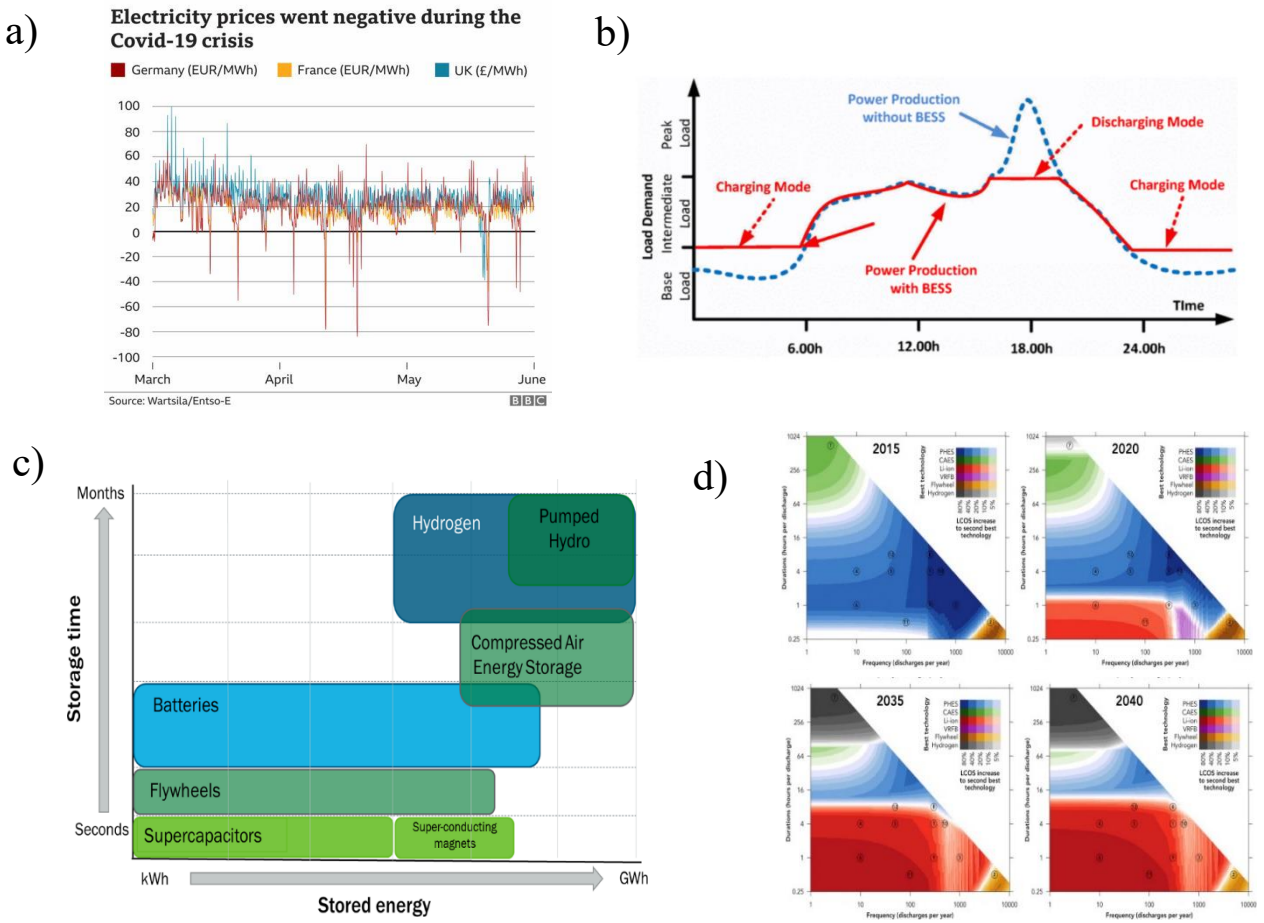


Figure 1-1. (a) Negative energy prices from reference [2]. (b) Example of load-levelling using BESSs; reproduced from reference [3]. (c) Various energy technologies by discharge time at rated power; reproduced from reference [4]. (d) Prediction of most cost-efficient (lowest levelised cost) technology for all durations and frequency of discharge: LIB in red, hydrogen in black, pumped hydro in blue, compressed air in green; reproduced from reference [5].

1.2.3 The chemical bond as an energy store

Intermittent renewable energy can be used to form chemicals as a physical fuel that can be transported, stored, and converted back to electrical energy by combustion or by fuel cells. Importantly, the energy degradation over time for chemical storage is theoretically as

low as zero, provided no side-reactions or leaks occur. Hydrogen and ammonia have emerged as good candidates due to their high energy density. Importantly, these fuels are carbon-free, emitting no greenhouse gases when used. However, the energy currently used to produce them is predominantly from fossil fuels.

Hydrogen is in a more mature stage of development than ammonia, with hydrogen fuel cells, electrolysers, and transport infrastructure becoming established.[1] Hydrogen is generally liquified for transport, exhibiting a specific energy of 33.3 kW h kg^{-1}.[6] However, this process is very energy intensive, currently requiring approximately one-third of the energy of the stored hydrogen.[6] Furthermore, the disadvantages associated with flammability, regulations, capital investment requirements, and relative energy cost to fossil fuels have left hydrogen's integration into the energy landscape with only minor promise.

Ammonia exhibits higher energy density (by volume) than hydrogen (as a liquid: 3.2 kW h L^{-1} or 11.5 MJ L^{-1} vs 2.4 kW h L^{-1} or 8.5 MJ L^{-1}).[7] Other advantages over hydrogen include its lower flammability and reactivity (though it is toxic), associated easier transport, relative ease of liquification, lower infrastructure costs, and greater applicability as maritime fuel. Of these, its relative safety is a significant benefit. It is easily detected by humans, lighter than air, easily dissolved in water, and able to be stored chemically as a solid.[7,8] Ammonia is also a good hydrogen store, making it simply a safer way of transporting hydrogen. Ammonia production will be a key part of a more sustainable and more integrated energy landscape, which is required to reduce and reverse our impact on the environment.

1.2.4 Ammonia and the Haber Bosch

In addition to ammonia as an energy vector, it is also a crucial commodity, with 88% of global production (2020: >146 million tons) used in the production of agricultural

fertiliser.[9] The dominant production method for ammonia is still the Haber–Bosch (HB) process, discovered in 1913.[10] It remains a challenging reaction to achieve because it is highly energetically unfavourable to overcome the high dissociation energy of N≡N (945 kJ mol^{-1})[11], requiring harsh reaction conditions (400–500°C, 150–300 bar)[12]. In addition, it is also highly energy-intensive due to the associated energy consumption of hydrogen synthesis from syngas.[18]

All of the requirements of the Haber-Bosch require energy input in some way. The reaction conditions themselves require large amounts of energy in both the required temperature and pressure; nitrogen is plentiful in the atmosphere (78.1%mol)[11], but requires energy to distil; and hydrogen is able to be produced by water splitting, but requires external electrical input. Thus, sustainable ammonia production is greatly desired in order to minimise the effect of power generation on the environment, whilst maintaining high supply of ammonia as both a commodity and energy vector. Increasing the efficiency of production has most often be directed towards decreasing the harsh synthetic conditions of the Haber-Bosch by the use of catalysts.[13–15] However, here the focus is turned to the inefficiency of intermittent renewable-energy sources, and the requirement of locally-produced reactants, in particular the hydrogen gas.

1.2.5 Agile ammonia synthesis (AAS)

It is undisputable that there are large profits available from the extraction of fossil fuels. The locations of these sources are fixed by geography, with the accessibility and generated wealth controlled by a select few. In recent decades, the increasing efficiency and decreasing price of renewable-energy sources has widened the accessibility of independent and sustainable energy to many more regions and countries. However, this renewable

infrastructure still typically requires connection to large-scale grid systems, which are inaccessible to small, rural communities, in particular those that are economically disadvantaged and culturally independent. The agile ammonia synthesis (AAS) process is aimed to provide these communities with local, secure, sustainable energy.

1.2.5.1 Improved access and infrastructure

The AAS process is characterised using local and renewable sources to form ammonia which can be stored or transported as a facile energy vector. Provided with local and facile hydrogen supply and nitrogen distillation, intermittent and excess renewable energy sources can be used to synthesise ammonia by a thermal Haber-Bosch process, which can be stored until demand requires it to be combusted to provide power during high load, or intermittent periods of low wind or solar irradiance. Very fast discharge of power for energy arbitrage or consumer/domestic use can be achieved by charging LIB or other BESS, diversifying the technology, rated power, and frequency response of the self-contained energy infrastructure. This entire process does not require a grid connection. Additionally, if a grid connection is present, energy storage and release can be as used as a load-shifting device for the external grid system with financial incentive. The whole process is characterised by the ease of starting and stopping power generation, its independence, and low emissions.

1.2.5.2 Sustainable electrical power and reactants

Nitrogen can be distilled from air using the local renewable electrical energy. In order for hydrogen to be produced locally, it must be obtained from water, which is relatively ubiquitous, as opposed to industrial exhausts such as syngas. In this thesis, the photocatalytic water-splitting reaction over nitrogen-doped TiO_2 will be explored.[16] In an adjacent report, we have shown that this is possible with no input of electrical energy, achieving photo-

excitation, high temperature, and high pressure using just illumination.[17] Regarding ammonia synthesis, here the example of the Haber-Bosch is used because it is most established. The ammonia can then be stored within porous structures or liquified as a safe and energy dense alternative to hydrogen. This is an example of a fully self-contained system from renewable wind or solar power for immediate consumption or charging of BESS, clean hydrogen production from water, ammonia production using renewable energy, and stable and safe storage for peak shaving and load shifting, using no external reagents apart from water and air. This process will constitute an important aspect of the transition from fossil-fuel dependence to sustainable energy generation.

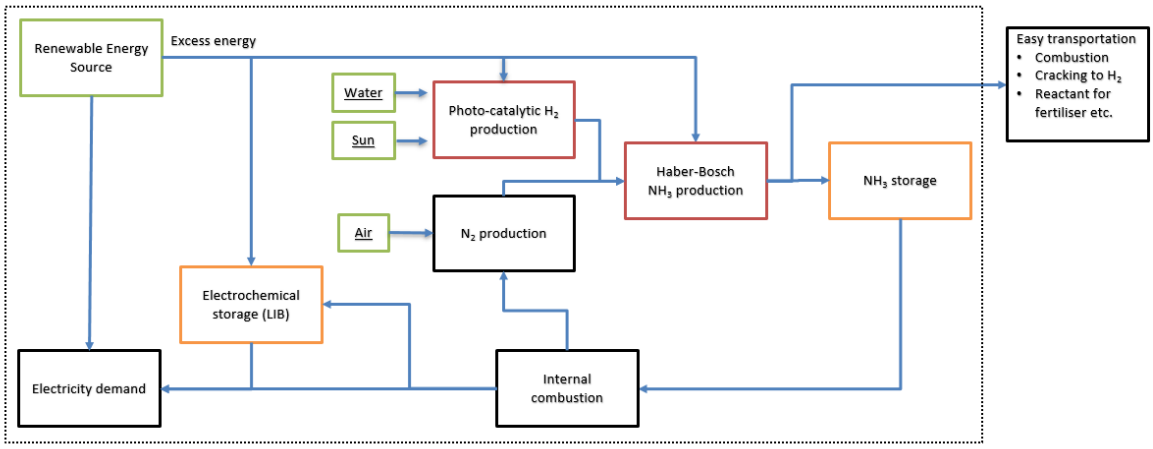


Figure 1-2. Schematic of self-contained agile ammonia synthesis pathway, featuring many of the systems presented in this document. Renewable inputs shown in green, energy-vector-producing reactions in red, and storage solutions in orange.

It is not within the scope of this thesis to discuss the combined energy efficiency or economic feasibility of the AAS, the practical aspects of investment, plant size, maintenance, expertise, or the future of electrical vs. thermal ammonia synthesis. The reader is directed to related literature.[18,19,20]

1.3 Light-element doping

The addition of foreign elements to the inorganic components of energy systems is of great industrial and scientific interest. For example, doping is an important step in catalyst synthesis for hydrogen production and ammonia synthesis,[16] as well as in intercalation processes in LIB. Terminology for the addition of foreign atoms is not well-defined. The process is referred to as doping, insertion, intercalation, alloying, which all have different connotations about the concentration, siting, phase behaviour, and the material application. The foreign atoms themselves can be described as dopants, defects, promotors, additives, guests, or even solute. Meanwhile the bulk material can also be called the framework, crystal lattice, host, or parent material.

1.3.1 Location

Paramount to understanding the emergent properties and altering of solid-state performance is the accurate identification of dopant siting and the effect on the local environment, whether crystalline or not. The current knowledge and methodology of identification of low-contrast sites inhibits the understanding of many systems and their structure-performance relationships. The gaps in the established knowledge of structural and electronic properties is limited by certain aspects of standard characterisation techniques, such as unnegotiable limitations of natural phenomena, precision and accuracy governed by instrumentation, restricted accessibility to computational power or centralised facilities, or simply lack of research interest.

1.3.1.1 Low scattering-contrast: the general analytical difficulty

Above all, the most difficult task for elastic scattering techniques is the distinguishing of sets of atoms with very similar scattering profiles (atomic form factor *f*; much more discussion to follow). For X-ray scattering, this is primarily pairs of elements that are adjacent in the periodic table; though, when ions are considered, extremely low contrast can result from isoelectronic, or simply similar electron configurations. Even worse, entire groups of similar scatterers can often be present in inorganic frameworks, e.g. $Ni^{2+/3+/4+}$, $Co^{3+/4+}$, and $Mn^{3+/4+}$ in the mixed-metal oxide $LiNi_xCo_yMn_zO_2$ ($x + y + z = 1$) (NCM) which is commonly used as a cathode material in lithium-ion batteries.[21]

For the studies presented herein, the expected changes in electron occupancy of a site are given in Table 1-1. For example, substitutional doping of Si^{4+} by Al^{3+} yields very low contrast of 0, which follows from the strict steric and electronic conditions required for doping.

Application	Initial occupancy	Final occupancy	Δe^-	Doping type
N-TiO_2 photocatalysis	O^{-2} (10)	N^{-2} (9) *	-1	substitutional
	vacant (0)	N (7) *	+7	interstitial
	O^{-2} (10)	vacancy (0)	-10	vacancy
Pd for LIB	vacant (0)	Li^+ (2)	+2	interstitial
Al siting in zeolites	Si^{4+} (10)	Al^{3+} (10)	0	substitutional

Table 1-1. Difference in e^- as a result of light-element doping in various inorganic frameworks for energy applications. * Electron configuration of species is not well-established.

1.3.1.2 Additional dependence of characterisation on dopant properties

There are other properties of doped systems that should be considered and ideally defined. These are often much more difficult to characterise than the enhanced bulk

physicochemical properties and performance. These properties will be discussed with emphasis on their elucidation by Bragg diffraction, and are not presented in any particular order.

Very generally, it is important to have a high relative concentration of dopant within a sample. This should ideally be present at a defined crystallographic site, rather than amorphously doped or on the particle surface. In this way, the ordering of the doping is important, e.g. if in zeolites, aluminium is substituted into silicon sites with low site selectivity, the doping will be much harder to characterise than highly ordered substitution.

Related to ordering, the number of sites/environments that the dopant can/does occupy will affect the contrast. A dopant may be present in large quantities and at sufficient periodicity, but if the sites are too numerous and too equally occupied, the total change in scattering may be small, e.g. in a zeolite, if aluminium occupies just one T-site, the contrast will be much higher than if it occupies multiple T-sites for a given total concentration.

Related to the total concentration, in order for a dopant or its effect to be observed by Bragg diffraction, the dopant must be reasonably concentrated across a powder or crystal. If the distribution is too wide, the periodicity cannot be observed, despite any site selectivity. Hence, if the same amount of dopant is used, inhomogeneous doping across a powder will be observed by diffraction better than homogeneous doping. This effect is seen in Chapter 5 on the palladium-lithium system in which a phase becomes partitioned, indicating inhomogeneous doping, rather than a homogeneous shift in the reflections. Evidently, at a unit-cell length-scale, the doping must be homogeneous.

Related to the homogeneity, the distribution of dopant may be influenced by the dopant already in the sample, either as a stabilising or destabilising effect. If a dopant

stabilises further doping, a positive-feedback loop will result in inhomogeneous nucleation. As a dopant this can be understood as sintering/aggregation, but is also seen for defects known as defect condensation. Of course, the opposite of stabilisation may also be true. The presence of a dopant atom may destabilise the local coordination and increase the energy of the configuration, eliminating the chemical preference for doping at nearby sites and precluding further doping. For example, it is generally accepted by Löwenstein's rule that the occupancy of a given tetrahedral site by aluminium precludes the adjacent tetrahedra from also being occupied by aluminium. Hence, any form of dopant condensation and appearance of a discrete aluminium oxide phase are impossible. This doping is inherently local and non-crystalline, and can be described as a crystallographic defect. This discussion of defects is raised due to the relevance of oxygen vacancies in Chapter 4 on TiO_2.

The effect of a dopant atom on the surrounding high-scattering framework atoms with respect to lattice parameter, space group changes, or electronic properties are easily characterised on both microscopic and macroscopic length-scales. In contrast, if there is no structural effect on the host framework, characterisation of the dopant is made much more difficult. However, the effect can be detrimental too. For example, the substitutional doping of aluminium at silicon sites in zeolites is fundamentally strenuous, which results in decreasing crystallinity with doping.

Finally, a very general point, the crystallinity of both the framework and the dopant should be maximised for data quality. The doping may be high in concentration across the powder, at a specific site with no other environment present, in a single domain, and distort the framework significantly, yet still not be easily observed if the doping is not strictly crystalline.

Generally, it is important to have good scattering-contrast in order to resolve dopant species directly. However, the remaining properties are also very important. In each chapter, the characterisation problem will constitute a different convolution of these issues, and will be discussed when appropriate.

1.3.2 Effect on performance

Once the structural and electronic effect of doping have been characterised, the effect on the performance of the material must be interrogated. In many cases, the location of dopant atoms and even the enhanced physicochemical properties of the ensemble may not be directly correlated to the enhanced performance. For example, irreversibly-intercalated interstitial lithium in palladium, inactive nitrogen species in N-TiO_2, or weak/inaccessible BAS sites in zeolites. This topic of causation and correlation will be discussed frequently throughout the thesis. Correctly identifying the location and mechanistic relevance of certain dopant species will lead to questions of synthetic control and selectivity. However, this issue of design is generally beyond the scope of this thesis.

1.4 Thesis outline

Following this introduction chapter, there will be a general presentation of the fundamental concepts of powder diffraction and the other supporting characterisation techniques. Following this, all of the experimental procedures will be presented. Then, this thesis will report three research studies in three separate chapters. Each will investigate crystalline structure and atomic arrangement of low-contrast sites within highly-scattering inorganic frameworks that are crucial to the AAS pathway. The three research chapters should be considered linked as a collective improvement in renewable energy provision as part of

the integrated self-contained AAS process, as well as linked by the themes of structural characterisation.

Though it is typical to introduce the background at the start of a doctoral thesis, it is thought to be more helpful to introduce the context of each chapter prior to the presentation of the work. There will be discussion of the material, application, why previous methods have not been inadequate to achieve full structural characterisation, by what methods we aimed to further the understanding of each system, and then primarily our findings on dopant properties, guest-host interaction, and effect on application performance. The studies have been summarised by the following titles which are used throughout.

- Hydrogen evolution by photocatalytic water splitting over nitrogen-doped TiO_2: oxygen vacancies and the structure-activity relationship
- Electrochemical lithium storage in palladium nanoparticles: phase behaviour and stability
- Locating framework aluminium in ZSM-5 for ammonia synthesis promotion and storage: assessment of indirect and direct characterisation methods

Firstly, nitrogen doping of TiO_2 as an enhanced activity photocatalyst for water splitting will be investigated, with the focus on both the nitrogen-doping and oxygen vacancies. This work is predominantly based on a published report by the author.[16] Secondly, lithium intercalation into palladium metal nanoparticles was investigated as a possible store for electrochemical energy in lithium-ion batteries as a high-frequency response and consumer-friendly energy vector. Thirdly, light-element doping into a much more complex framework was considered, namely substitutional aluminium doping in silicates in order to identify the origin of acidity, adsorption, and activity in zeolites. Lastly, there will be a short chapter of Ending Remarks.

1.5 References

(1) Foo, C.; Fellowes, J.; Fang, H.; Large, A.; Wu, S.; Held, G.; Raine, E.; Ho, P.-L.; Tang, C.; Tsang, S. C. E. Importance of Hydrogen Migration in Catalytic Ammonia Synthesis over Yttrium-Doped Barium Zirconate-Supported Ruthenium Nanoparticles: Visualization of Proton Trap Sites. J. Phys. Chem. C 2021, 125 (42), 23058–23070. https://doi.org/10.1021/acs.jpcc.1c04002.

(2) Five Key Questions about Energy after Covid-19. BBC News. June 9, 2020.

(3) Mehr, T. H.; Masoum, M. A. S.; Jabalameli, N. Grid-Connected Lithium-Ion Battery Energy Storage System for Load Leveling and Peak Shaving. In 2013 Australasian Universities Power Engineering Conference (AUPEC); 2013; pp 1–6. https://doi.org/10.1109/AUPEC.2013.6725376.

(4) Wieliczko, M.; Stetson, N. Hydrogen Technologies for Energy Storage: A Perspective. MRS Energy Sustain. 2020, 7. https://doi.org/10.1557/mre.2020.43.

(5) Schmidt, O.; Melchior, S.; Hawkes, A.; Staffell, I. Projecting the Future Levelized Cost of Electricity Storage Technologies. Joule 2019, 3 (1), 81–100. https://doi.org/10.1016/j.joule.2018.12.008.

(6) Sartbaeva, A.; Kuznetsov, V. L.; Wells, S. A.; Edwards, P. P. Hydrogen Nexus in a Sustainable Energy Future. Energy Environ. Sci. 2008, 1 (1), 79–85. https://doi.org/10.1039/B810104N.

(7) Lan, R.; Tao, S. Ammonia as a Suitable Fuel for Fuel Cells. Front. Energy Res. 2014, 2.

(8) Huang, Z.; Gallucci, J.; Chen, X.; Yisgedu, T.; Lingam, H. K.; Shore, S. G.; Zhao, J.-C. $Li_2B_{12}H_{12}{\cdot}7NH_3$: A New Ammine Complex for Ammonia Storage or Indirect Hydrogen Storage. J. Mater. Chem. 2010, 20 (14), 2743–2745. https://doi.org/10.1039/B923829H.

(9) Apodaca, L. Nitrogen Statistics and Information: NITROGEN (FIXED)—AMMONIA; Nitrogen Statistics and Information; United States Geological Survey, 2020; pp 116–117.

(10) Haber, F.; Le Rossignol, R. Über Die Technische Darstellung von Ammoniak Aus Den Elementen. Z. Für Elektrochem. Angew. Phys. Chem. 1913, 19 (2), 53–72. https://doi.org/10.1002/bbpc.19130190201.

(11) Ye, T.-N.; Park, S.-W.; Lu, Y.; Li, J.; Wu, J.; Sasase, M.; Kitano, M.; Hosono, H. Dissociative and Associative Concerted Mechanism for Ammonia Synthesis over Co-Based Catalyst. J. Am. Chem. Soc. 2021, 143 (32), 12857–12866. https://doi.org/10.1021/jacs.1c06657.

(12) Erisman, J. W.; Sutton, M. A.; Galloway, J.; Klimont, Z.; Winiwarter, W. How a Century of Ammonia Synthesis Changed the World. Nat. Geosci. 2008, 1 (10), 636–639. https://doi.org/10.1038/ngeo325.

(13) Foster, S. L.; Bakovic, S. I. P.; Duda, R. D.; Maheshwari, S.; Milton, R. D.; Minteer, S. D.; Janik, M. J.; Renner, J. N.; Greenlee, L. F. Catalysts for Nitrogen Reduction to Ammonia. Nat. Catal. 2018, 1 (7), 490–500. https://doi.org/10.1038/s41929-018-0092-7.

(14) Saadatjou, N.; Jafari, A.; Sahebdelfar, S. Ruthenium Nanocatalysts for Ammonia Synthesis: A Review. Chem. Eng. Commun. 2015, 202 (4), 420–448. https://doi.org/10.1080/00986445.2014.923995.

(15) Shetty, S.; Jansen, A. P. J.; van Santen, R. A. Active Sites for N_2 Dissociation on Ruthenium. J. Phys. Chem. C 2008, 112 (46), 17768–17771. https://doi.org/10.1021/jp8085478.

(16) Foo, C.; Li, Y.; Lebedev, K.; Chen, T.; Day, S.; Tang, C.; Tsang, S. C. E. Characterisation of Oxygen Defects and Nitrogen Impurities in TiO_2 Photocatalysts Using Variable-Temperature X-Ray Powder Diffraction. Nat. Commun. 2021, 12 (1), 661. https://doi.org/10.1038/s41467-021-20977-z.

(17) Li, Y.; Peng, Y.-K.; Hu, L.; Zheng, J.; Prabhakaran, D.; Wu, S.; Puchtler, T. J.; Li, M.; Wong, K.-Y.; Taylor, R. A.; Tsang, S. C. E. Photocatalytic Water Splitting by N-TiO 2 on MgO (111) with Exceptional Quantum Efficiencies at Elevated Temperatures. Nat. Commun. 2019, 10 (1), 4421. https://doi.org/10.1038/s41467-019-12385-1.

(18) Smith, C.; K. Hill, A.; Torrente-Murciano, L. Current and Future Role of Haber–Bosch Ammonia in a Carbon-Free Energy Landscape. Energy Environ. Sci. 2020, 13 (2), 331–344. https://doi.org/10.1039/C9EE02873K.

(19) Dincer, I.; Acar, C. Review and Evaluation of Hydrogen Production Methods for Better Sustainability. Int. J. Hydrog. Energy 2015, 40 (34), 11094–11111. https://doi.org/10.1016/j.ijhydene.2014.12.035.

(20) Siporin, S. E.; Davis, R. J. Use of Kinetic Models to Explore the Role of Base Promoters on Ru/MgO Ammonia Synthesis Catalysts. J. Catal. 2004, 225 (2), 359–368. https://doi.org/10.1016/j.jcat.2004.03.046.

(21) Erickson, E. M.; Schipper, F.; Penki, T. R.; Shin, J.-Y.; Erk, C.; Chesneau, F.-F.; Markovsky, B.; Aurbach, D. Review—Recent Advances and Remaining Challenges for Lithium Ion Battery Cathodes. J. Electrochem. Soc. 2017, 164 (1), A6341–A6348. https://doi.org/10.1149/2.0461701jes.

Chapter 2: Fundamental concepts of characterisation

2.1 The crystalline solid-state

The discrete solid-state emerges from the formation of strong chemical bonds between a large number of atoms in two- or three-dimensional space. One-dimensional non-molecular materials do not exhibit emergent phenomena as a result of bulk condensation, such as volume, density, surfaces, defects, or phase transitions. The crystalline solid-state is characterised by translational periodicity, which occurs due to the propensity of atoms within a solid to pack efficiently, as opposed to an amorphous, disordered arrangement. A material is said to be crystalline when the translational repetition of an arrangement of atoms can reproduce the whole crystal. Amorphous materials do not possess this degree of translational symmetry. Their arrangements are not necessarily random, but, pertinent to this thesis, they lack the periodicity to diffract constructively.

The translational symmetry of a three-dimensional volume is the basis for the unit-cell. This volume is a parallelepiped which has an equivalent lattice point at each vertex. It can be described using three lattice parameters a, b, and c, and three interfacial angles α, β, and γ. Depending on the rotational symmetry of the crystal, a number of these six parameters are correlated and/or constrained. It is not possible for a translationally-repeating lattice to possess k-fold rotation, for $k > 6$, or $k = 5$, due to the crystallographic restriction theorem.[1] As a result, there are a finite number of characteristic rotational symmetries which are observed as seven crystal systems that possess specific numbers and orders of rotational symmetry (Table 2-1).

Crystal system	Characteristic symmetry	Unit-cell parameters	Independent parameters
Triclinic	1× 1-fold	$a \neq b \neq c$; $\alpha \neq \beta \neq \gamma$	6
Monoclinic	1× 2-fold	$a \neq b \neq c$; $\alpha = \gamma = 90°$; $\beta \neq 90°$	4
Orthorhombic	3× 2-fold	$a \neq b \neq c$; $\alpha = \beta = \gamma = 90°$	3
Tetragonal	1× 4-fold	$a = b \neq c$; $\alpha = \beta = \gamma = 90°$	2
Trigonal	1× 3-fold	$a = b \neq c$; $\alpha = \beta = 90°$; $\gamma = 120°$	2
Hexagonal	1× 6-fold	$a = b \neq c$; $\alpha = \beta = 90°$; $\gamma = 120°$	2
Cubic	4× 3-fold	$a = b = c$; $\alpha = \beta = \gamma = 90°$	1

Table 2-1. The seven crystal systems of the crystalline solid-state. Reproduced from Advanced Certificate in Powder Diffraction on the Web, Birkbeck College.[2]

The seven crystal systems yield 14 Bravais lattices as a result of centring: primitive (P), face-centred (F), body-centred (I), and *a*-face-centred (A). There are a finite number of ways symmetry elements can be applied to the 14 Bravais lattices, which yields 230 space groups. These sets of symmetry operations can describe the arrangement of atoms in any crystal. In the Tables for Crystallography,[3] they are listed in increasing symmetry: first by crystal system, then Laue class, then lattice centring.

2.2 Characterisation of the solid-state

2.2.1 Structural vs. electronic characterisation

The distinction between structural and electronic properties and characterisation is not generally necessary; however, it will be helpful in the reading of this document. The work that comprises this thesis was primarily concerned with providing additional information and understanding of the crystalline atomic structure. Electronic characterisation is often presented as a supporting technique, and as an intermediate emergent property in the definition of the structure-electronic-activity relationship.

2.2.2 Direct vs. indirect characterisation

A distinction between indirect and direct characterisation will also be helpful. Some experiments directly observe the presence or properties of a light-element dopant (either in structure or electronics), while others observe the effects of the dopant on other atoms (either in structure or electronics). Evidently, directness is desired, but often comes with shortcomings and disadvantages, which will be discussed, particularly in Chapter 6 on zeolite characterisation.

The directness of a characterisation is not solely inherent on the technique, but also the design of experiment. For example, in Chapter 6, STEM (or microscopy/imaging in general) is considered a direct method of characterisation in the case of distinguishing silicon and aluminium from each other using atomic-resolution EELS. However, it is also used indirectly to observe the adsorption of probe atoms at BAS. Evidently the former is more desired, but turns out to be less applicable due to the difficulty in obtaining measurements.

Another example is for XRD, which is the predominant technique used in this work. It is generally unable to resolve occupancy of light-elements at low-contrast sites, relying on indirect characterisation through observation of the highly scattering framework. In Chapter 4 on TiO_2 materials, the effect of nitrogen doping is observed through the effect on bulk thermal expansion and the emergence of a new nitride phase; and in Chapter 5 on the palladium-lithium system, crystalline phase changes are almost entirely characterised by the change in the highly-scattering framework. In Chapter 6 on zeolite characterisation, XRD is shown to be a direct technique when using inelastic scattering, which increases the scattering contrast by dispersive element-specific effects.

This distinction between direct and indirect experiments is not universally applied throughout the literature of solid-state characterisation, but in this study it is deemed important when considering the weight and significance of certain analyses and their conclusions.

2.3 Fundamental concepts of XRD

2.3.1 History

The interaction of high energy X-rays with matter has long been well-understood. Max von Laue received the Nobel Prize in Physics in 1914 for reporting the diffraction of X-rays by crystals using both wave and particle models. Further research by father and son William and Lawrence Bragg focused on structural characterisation, which won them the Nobel Prize in 1915. The advent of XRD analysis coincided with and aided the early understanding of atomic structure, chemical bonding, electromagnetism, and quantum mechanics. The versatile and non-destructive nature of XRD analysis led to the technique becoming instrumental in the characterisation of crystalline materials over the following century.

2.3.2 Physical theory

Much of this section is based on the references [2,4].

2.3.2.1 Electromagnetic radiation and electrons

In the elastic regime, the degree to which a photon is scattered by an atom is defined by a characteristic atomic scattering factor f for each element. As this is dependent on the electron density of an element, it is also dependent on electronic configuration and hence ion specific. It is essentially the diffraction pattern for a single unbound atom; this scattering behaviour is reasonable to apply to bound and multi-atom systems. Though seemingly in

units of electrons, the scattering factor is actually a ratio of the scattering intensity against that of a single unbound electron. The tabulated values for elements in their ground state have been long-known and are commonly found.[5] Atomic scattering factors are not energy-dispersive: they do not vary with incident energy. On the other hand, they are highly dependent on the scattering angle, with scattering becoming increasingly weak at high angles.

The exact nature of the interaction between electromagnetic radiation and an electron is beyond the scope of this thesis. It is sufficient to say that the interaction is not as simple or classical as a change in momentum, but depends greatly on the oscillation of the electron. This is more relevant in the context of inelastic scattering, and will be discussed further elsewhere. In a standard XRD experiment the interaction is ideally completely elastic.

2.3.2.2 Diffraction

There will be some interaction between a wave of wavelength λ and a physical feature of dimension d when $\lambda \sim d$. This leads to limitations in the use of visible light in the observation of small objects, i.e. objects smaller than ~400 nm require lower wavelength waves. For this reason, electron microscopes were developed, in which the wavelength can be low enough to yield atomic-resolution imaging. Crucial to the interaction of X-rays with crystals, and matter generally, is that the wavelength of X-rays (0.01-100 Å) spans the typical interatomic distances in solids: generally, on the Ångström (0.1 nm) length-scale.

2.3.2.3 Bragg diffraction

When a crystal is exposed to a concentrated X-ray beam, the diffracted photons from a set of periodic planes interfere with one another as individual wave-functions, which form areas of high and low flux known as a diffraction pattern. Bragg's Law states that the angle

at which high flux is detected (Bragg diffraction) is dependent on the wavelength of the incident radiation and the *d*-spacing of the periodicity within the crystal. In order to result in constructive interference, the path difference between two diffracted waves must be an integer number *n* of wavelengths λ (Figure 2-1). By inspecting the geometry of the system, it is found that this is only fulfilled for a given *d*-spacing when the incident radiation is at angle θ from the diffracting plane (Equation 2-1).

$$n\,\lambda = 2\,d\,\sin(\theta)$$

Equation 2-1. Bragg's Law, where *n* is the order of difraction, λ is the wavelength, *d* is the spacing, and θ is the angle of diffraction.

The periodicity of a crystal can be described as conceptual planes of various spacings *d*, and angles with respect to the three spatial axes *a*, *b*, and *c*. These planes are known as Miller planes and are defined by three integers *hkl*.

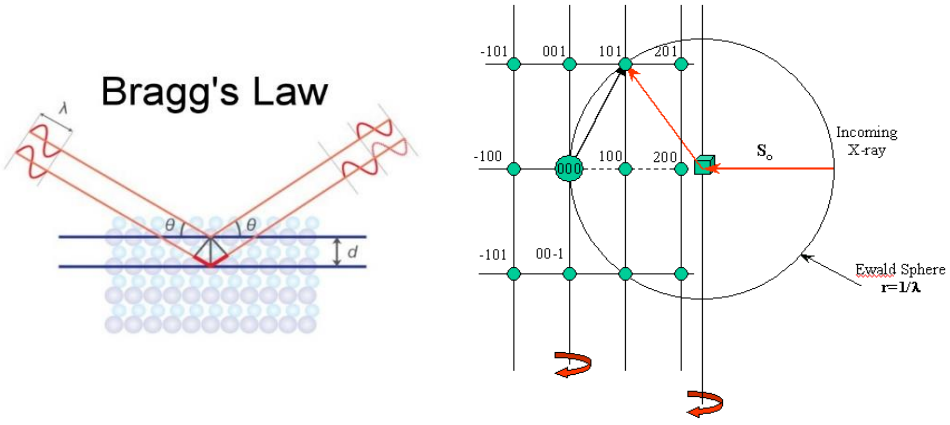


Figure 2-1. Schematic of the fulfilment of Bragg's law in real and reciprocal space.

2.3.2.4 Reciprocal space and the Ewald sphere

In real space, the periodicity of a crystal can be easily visualised by the repeating arrangement of atoms in a lattice. In reciprocal space, the arrangement of atoms in real-space can be expressed as a set of points corresponding to the Miller planes of the crystal. This reciprocal lattice extends in dimensions of h, k, and l, with the distance of any reflection from the through-vector origin point (000) being equal to the inverse of the real-space d-spacing of the given Miller plane, $1/d$ or d^* (Equation 2.2).

$$|S| = \frac{1}{d}$$

Equation 2-2. Relation between the magnitude of the scattering vector and the d-spacing.

In order to determine which reflections will be observed for a given wavelength, it is helpful to consider a reciprocal space construction, the Ewald sphere (Figure 2-1). The magnitude of the vector of the incident X-ray beam in reciprocal space $|S_0|$ is equal to $1/\lambda$. The beam is then scattered at the origin by the sample crystal, for which the magnitude is also $1/\lambda$ for elastic scattering. The vectors of all possible elastically scattered X-rays form a sphere in reciprocal space called the Ewald sphere. Considering this, an isosceles triangle is formed, for which the scattering vector S can be found by trigonometry using the scattering angle 2θ. Through the explicit consideration of reciprocal space vectors, the importance of assuming elastic interactions is shown. Clearly, the vectors of many and variably inelastic scattering events would not form a sphere.

$$|S| = \frac{2\sin(\theta)}{\lambda}$$

Equation 2-3. Magnitude of the scattering vector

Combining Equation 2-2 and Equation 2-3, the Bragg equation is once again formed. Thus, only points of the reciprocal lattice that intersect the Ewald sphere are theoretically observable by Bragg diffraction. (This possibility of observation says nothing about space-group forbidden reflections or the intensity of the Bragg diffraction.) In order to achieve the intersection of as many reflections, the reciprocal lattice is rotated around the origin by rotating the crystal.

For powder samples, many orientations are already being sampled; hence any given reflection will appear at many different points at reciprocal length d_{hkl}* from the reciprocal origin, i.e. form another sphere in reciprocal space. It follows that all reflections of equal *d*-spacing will become merged into a single peak with multiplicity greater than 1. In this way, coincident reciprocal-space spheres of Friedel pairs, such as (100) and (-100), appear as a coincident peak against *d*-spacing, such as in powder diffraction. A similar phenomenon is the coincidence of reflections of approximately equal *d*-spacing, even when not necessarily symmetry-related. The intersection of this sphere and the Ewald sphere yields a circle that is formed by the vectors **s** of any scattered X-ray with scattering angle 2θ. These vectors form a cone in both real and reciprocal space, known as the Debye-Sherrer cone, which will be discussed further in context of particle averaging and image detectors.

This reciprocal-space perspective is helpful in many ways. The Ewald sphere construction is able to intuitively explain the Bragg conditions using vectors. It becomes very intuitive that increasing the beam energy will increase the size of the sphere in reciprocal space, and allow higher order, low *d*-spacing reflections to be observed. It is also intuitive that the scattering angle of a given *d*-spacing reflection will decrease as the wavelength is decreased.

2.3.2.5 Reflection intensity and structure factors

The intensity of a given observable reflection (*hkl*) is dependent on the contents of the unit-cell, namely the structure factor F_{hkl}.

$$I_{hkl} \propto |F_{hkl}|^2$$

Equation 2-4. Experimental measurement of the structure factor, where *I* is intensity, and *F* is the structure factor.

It is calculated by summing the contribution to the scattering of a certain set of conceptual planes of periodicity over all atoms in a unit-cell (Equation 2-5). The square of the magnitude of F_{hkl} is then proportional to the intensity of the reflection (Equation 2-4). From these relationships, it is simple to see how the atomic arrangement and hence the space group, govern the intensity of reflections, and importantly the phase.

$$F_{(hkl)} = \sum_{j=1}^{atoms} f_j \, e^{[i\, 2\pi(hx_j+ky_j+lz_j)]}$$

Equation 2-5. The structure factor equation, where *f* is the atomic scattering factor, and *x*, *y*, and *z* are the site coordinates.

However, the structure factor is a complex number that contains both real and imaginary parts, i.e. magnitude and phase.

$$\mathbf{F}_{(hkl)} = F_{(hkl)} \, . \, e^{[i\, \phi(hkl)]}$$

Equation 2-6. The complex structure factor, φ is the phase.

It is simple to see that if the atomic structure and phases are known, then the structure factors can be calculated. However, the aim in diffraction experiments is most frequently the elucidation of atomic arrangement from structure factors. The array of structure factors and their values are a reflection of reciprocal space. In order to transform into real space, the

Fourier transform is applied, yielding electron density. For every point (*x,y,z*) in the unit-cell, the contribution of each structure factor (that is, each set of planes) is calculated by the following equation. Crucially, this is highly dependent on the phase of the structure factor which is unable to be directly experimentally measured.

$$\rho_{(x,y,z)} = \frac{1}{V}\sum_{-\infty}^{+\infty}\sum_{-\infty}^{+\infty}\sum_{-\infty}^{+\infty}\left|F_{(hkl)}\right| \cdot e^{[-i2\pi\,(hx+ky+lz-\phi(hkl)]}$$

Equation 2-7. The electron-density equation, where ρ is the electron density, and V is the uni-cell volume.

There are many methods that can be used to yield the phases, e.g. no negative electron density and atomicity (direct methods)[6], deconvoluting Patterson maps,[7] and multi-wavelength anomalous dispersion (MAD)[8].

2.3.3 XRD refinement

Much of this section is based on reference [9]. The iterative fitting of a calculated pattern to observed data is known as refinement. This fitting uses the leas-square method, in which the sum of the square of the differential is minimised.

$$\sum_i \{y_i(obs) - y_i(calc)\}^2$$

Equation 2-8. Least-squares calculation, where *y* is the intensity.

2.3.3.1 Pawley refinement

In a Pawley refinement, the observed diffraction pattern is fitted using the number of reflections defined by the unit-cell symmetry, dependent on the space group, the three lattice parameters, and the three interfacial angles. Other than these parameters, there is no real-space model with regard to electron density. There are no calculated structure factors and no

basis to predict reflection intensity. Though intensities are refined parameters, they are independent parameters with no common structural model that links them;[10] though the physical basis of background and peak shape are shared. Despite this, Pawley refinements are very good at phase composition analysis, space group confirmation, establishing lattice parameters, and the inspection of sample texture, artefacts of crystal shape, or preferred orientation. A major disadvantages of this method occurs for highly overlapping peaks, as they are highly negatively correlated. The intensities of these reflections are unable to be extracted without linking the values to a structural model.

2.3.3.2 Rietveld refinement

Like Pawley refinements, the Rietlveld method also refines parameters that define the shape of the unit-cell. However, Rietveld also uses a real-space structural model in order to establish a correlation between the intensity of reflections, and therefore aid the resolution of overlapping reflections.[10] A real-space unit-cell can be transformed into a calculated diffraction pattern using phases based on assumptions and constraints, or may well be random. The calculated pattern is then compared to the observed pattern by the least-squares method. Differences are due to an incorrect model and phase, which are altered and the iterative process continued until convergence. The elucidation of the phase component of the array of structure factors is an integral part of obtaining a structure solution from experimental diffraction data.

2.3.3.3 Refinement residuals

The measurement of coincidence with the observed pattern is crucial in the least-squares method, which aims to minimise such a value (Equation 2-9a). This discrepancy is often expressed as a percentage, called the R_{wp} (Equation 2-9b).[11] Often, this residual can be

unexpectedly low or high due to aspects of the observed data, rather than the structural model. For example, SXPD data has many datapoints; the overall pattern is thus much more difficult to fit than a low resolution pattern. This is also the reason that high-resolution SXPD data are able to yield much more accurate and valid structural models. Hence an expected residual is calculated, which acts as a minimum value for the R_{wp} (Equation 2-9c), which is used to calculate a relative goodness-of-fit (GoF) (Equation 2-9d), which tends to unity.

$$\text{(a) } \Delta = \sum_i w_i \{y_i(obs) - y_i(calc)\}^2$$

$$\text{(b) } R_{wp} = \sqrt{\frac{\sum_i w_i \{y_i(obs) - y_i(calc)\}^2}{\sum_i w_i \, y_i(obs)^2}} \times 100\%$$

$$\text{(c) } R_{exp} = \sqrt{\frac{N - P + C}{\sum_i w_i \, y_i(obs)^2}} \times 100\%$$

$$\text{(d) } GoF = \chi^2 = \left(\frac{R_{wp}}{R_{exp}}\right)^2$$

Equation 2-9. Various residual calculatinos, where Δ is the fitting difference, w_i is the weighting, and y_i is the observed or calculated intensity. (a) Difference in calculated pattern from observed pattern; (b) overall percentage difference in calculated pattern from observed pattern, R_{wp}; (c) expected difference value R_{exp}, where N is the number of data points, P is the number of parameters, and C is the number of constraints on the model; (d) goodness of fit, where χ is the fractional calculated difference from the expected.

2.4 Practical aspects of XRD

2.4.1 Sample preparation: single crystal vs. powder

For single crystal experiments, the reflections have unique positions in space proportionate to the *hkl* of the corresponding Miller plane. However, for powder samples, the orientations of the various crystals are not aligned with each other (nor generally to the beam), hence yielding many overlying rotated diffraction patterns. When many crystal orientations are sampled, these sum to a cone of diffracted X-rays known as Debye-Sherrer cones (Figure

2-2b). This overlap of symmetry-related reflections leads to multiplicity and the significant reduction in distinct reflections. Powder data are collected only with respect to *d*-spacing, disregarding any *h*, *k*, and *l*, inequivalences in reciprocal space. A single integrated intensity representative of many lattice planes leads to a loss of information, especially relating to texture, such as orientation and crystal shape. On the other hand, powder diffraction has many benefits. It foregoes the need to find specific reflections by rotation since all orientations are already being sampled in a polycrystalline powder. Thus, all reflections should be observed in any radial slice of the Debye-Sherrer cone, though many will be overlapping and indistinct. Additionally, nanosized particles suffer from poor crystallinity due to lower number of diffraction events, and the increased proportion of volume at the disordered surface as opposed to the bulk.

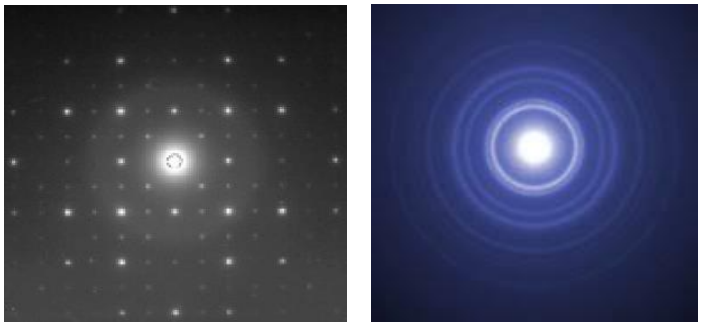


Figure 2-2. Example of diffraction patterns viewed towards the propagating beam of (a) single-crystal (b) and powder showing Debye-Sherrer cones.

Despite these disadvantages, powder diffraction is still far more implementable and applicable. Most pertinent to this thesis is the similarity of polycrystalline samples to real-world applications. The applications of many inorganic frameworks in adsorption and catalysis require high surface to volume ratios due to the dependence of activity on the solid-state surface, to either a liquid, a gas, or another solid. Small particles achieve high

performance, and may often operate and degrade very differently to a large single crystal. Hence, even though single crystal may yield more data, it is not necessarily relevant to the application setting and the chemistry of the nanoparticle system.

To give an example relevant to this thesis, though a single-crystal of N-TiO_2 may yield greater resolution of reflections and more accurate intensity, the proven high performance photocatalysis is only known to occur using nanoparticles which themselves have been subject to nitrogenation by ammonia. The particle-size effects of both the nitrogenating and catalysis are significant. This thesis will aim to characterise various materials in an environment and condition that is as close to their native in-operando performance as possible. Additionally, the crystallisation of large single crystals is often very challenging, so powder diffraction is often the chosen experiment in order to ease sample preparation.

2.4.2 Evaluation of XRD

Much of the power of XRD lies in the chemical understanding of the system. This is pertinent in the design of the data collection with respect to the sample (composition, particle/crystallite size, crystallinity, etc.) and the instrumentation (synchrotron-source, beam energy, detector, geometry, etc.). Chemical knowledge is also crucial in the quantitative analysis and refinement, the results of which are highly dependent on the chemical assumptions and restraints applied to the real-space structural model. These are required to have good physical basis to maintain validity.

Post-refinement, it is often the case that XRD data can yield so much information that the characterisation problem can become over-populated with unrelated observations, regardless of the validity. It is the aim of this work to not fall into this trap, but to provide as

much additional and relevant structural information on a system, and importantly correlate this back to the synthetic conditions, catalytic mechanisms, and electrochemical transitions.

There are many limitations of laboratory configuration XRD, many of which are inter-related, including geometry, low flux, invariable energy, low/no monochromation, low collimation, and fixed sample environments. All of these properties are improved at synchrotron-source XRD beamlines. Many of the observation and analyses presented in this work are only possible by the superior data quality conferred by the synchrotron beam, detectors, and specialised environments.

2.5 Synchrotron Radiation

2.5.1 Physical theory

Electrons are charged particles, and can be deflected (change in momentum) by using magnets, which results in the emission of electromagnetic radiation tangential to the curvature of the electron path. This can then be manipulated with respect to physical size, collimation, energy, and coherency. At DLS, the ring current is 300 mA, made up of ~900 bunches of pulse length 20 ns, with interval 72 ns, yielding a total energy of 3 GeV.[12]

2.5.2 Advantages of synchrotron experiments

The collection of XRD data at synchrotrons offers many advantages to standard laboratory configurations. Though this is primarily due to the brilliance of the beam, other factors are significant, including high precision instrumentation, sample environments, and field-leading expertise. This results in the relatively simple collection of high-quality data for interesting and difficult experiments, which should not be taken for granted.

2.5.2.1 *Beam properties*

Much of the advantageous properties of synchrotron-source radiation are expressed in the brilliance of the beam (Equation 2-10). The brilliance at the sample on I11 is ~10^{17} ph s^{-1} mm^{-2} $mrad^{-2}$ 0.1%BW^{-1} (10 keV).

$$Brilliance = \frac{\phi_{ph}}{\theta_h . \theta_v \times 0.1\%BW}$$

Equation 2-10. Brilliance of a photon beam, where Φ is photons per second per area, θ is the beam divergence (horizontal or vertical) in mrad, and 0.1%BW is the percentage of photons that deviate 0.1% from the central energy.

The high photon flux imparts good signal-to-noise ratio allowing the detection of weak/diffuse scattering and sufficient diffraction events in highly-scattering in-situ environments. The low energy bandwidth is required for conversion of angle-dependence to *d*-spacing. The large energy range of synchrotrons also enables greater *Q*-space to be accessed, as well as varied and accurate spectroscopy. The small and controlled beam size at the sample is achieved by various slits and mirrors in the optics hutches, which allows the analysis of micron/nanometre-scale through the high precision targeting and rastering across a sample to give morphological and architectural information. This small beam size is also related to the high collimation, where diffracted beam reaches the detectors with very low angular divergence, and hence high angular resolution.

2.6 Other synchrotron scattering techniques

2.6.1 Resonance diffraction

2.6.1.1 History and physical basis

In 1925, Kramers and Heisenberg published their landmark report on the quantum mechanics of X-ray scattering by an atomic electron, including understanding of inelastic scattering, excitations, and the conservation of energy.[13] They discovered that in the resonant regime the scattering factor, *f*, must be corrected by two anomalous scattering factors (ASF), *f*' and *f*'' (Equation 2-11). Unlike the atomic scattering factor, the anomalous factors vary as a function of the incident energy and do not vary as a function of scattering angle. Evidently changes to the scattering factors impact the structure factors and the corresponding Fourier transform that yields electron density (Equation 2-5 and Equation 2-7).

$$f = f_0(2\theta) + f'(\lambda) + i\,f''(\lambda)$$

Equation 2-11. Modification of the atomic scattering factor by the complex ASF, where f_0 is the atomic scattering factor, *f*' is the real anomalous scattering factor, and *f*'' is the imaginary part.

The real and imaginary parts of the ASF are 180° and 90° out-of-phase with the normally scattered X-rays, leading to a decrease in intensity of the beam. The complex ASF is the physical origin of electronic transitions at characteristic edges by X-ray absorption. Hence *f*'' is proportional to the fluorescence over the edge, and can be measured as such (Equation 2-12).

$$f''(E) = K\,\mu(E)$$

Equation 2-12. Fluorescence is proportionate to absorption, and thus fluorescence, where *K* is a constant, and μ is the atomic absorption coefficient.

The real and imaginary ASF are not independent. They can be calculated from each other by the Kramers-Kronig relation (Equation 2-13)[14]. Hence, experimentally derived fluorescence measurements can yield the full ASF, as will be shown in Chapter 7 on zeolites.

$$f'(E) = \frac{2}{\pi}\int_{-\infty}^{\infty} \frac{x\, f''(x)}{x^2 - E^2}\, dx$$

Equation 2-13. Kramers-Kronig relation.

2.6.1.2 Use in structural characterisation

Using these fundamental discoveries, Mark and Szilard showed that diffraction from RbBr was dependent on the incident energy, in which the isoelectronic scattering equivalence is broken to yield reduced symmetry, and additional supercell reflections.[15] After other early work,[16–18] it has become more standard to use resonance to distinguish between adjacent *Z* pairs, e.g. Sm/Eu in $EuSm_2O_4$,[19] Fe/Co in $Co_2Fe(PO_4)_2$,[20] and Ga/Ge in clathrates.[21]

As well as the distribution of electron density, resonance diffraction can also elucidate charge and orbital ordering, magnetic properties, pleochroic effects,[22] quadrupole scattering,[23] and phase changes.[24] It is even possible to crystallographically distinguish between valence states of a given element within a crystal by using the sensitivity of the ASF to absorption energy, e.g. $Mn^{2+/3+}$ in pumpellyite silicates,[25] and $Mn^{3+/4+}$ in perovskites[26].

2.6.1.3 Analysis and refinement

By using the theoretical or experimentally derived ASF, the occupancy or location of absorbing atoms can be refined. Difference in the fitting can be minimised by varying the occupancy of the anomalous scatterer, yielding the previously inaccessible resolution of low *Z*-contrast sites. This theoretically can be achieved using only one diffraction pattern,

provided enough is known about the structure and the contrast of the anomalous scattering is high enough, though in this work many will be used to ensure validity.

2.6.2 Pair distribution function

In much of XRD refinement and analysis, the background of a pattern is modelled using a polynomial that is defined by least-squares iteration with no constrains, restraints, or chemical assumptions; the fitting is purely mathematical, and rarely a quantitative metric. This diffuse scattering under and around Bragg peaks contains information on the local order rather than the bulk, such as surface reconstruction, point defects, nanoscale particle shape and size, and short-range distortion.[27]

The Fourier transform of the total scattering yields the pair distribution function (PDF), which is a radial distribution function for interatomic distances. This pattern can then be fit using the refinement methods discussed above. The calculated pattern of an atomistic model is yielded by Equation 2-15.[28]

$$G(r) = \frac{2}{\pi}\int_{Q_{min}}^{Q_{max}} Q[S(Q) - 1]\sin(Qr)\,dQ$$

Equation 2-14. The PDF from total scattering S(Q), where r is the interatomic distance, and Q is the Q-space = $(4\pi \sin(\theta))/\lambda$.

$$G(r) = \sum_{ij}\left[\frac{b_i b_j}{< b >}\delta\left(r - r_{ij}\right)\right] - 4\pi\rho_0$$

Equation 2-15. PDF generation from real-space model, where b is the atomic scattering factors, $<b>$ is the stoichiometric weighting, δ is the interatomic distance, and ρ_0 is the average density.

2.7 Other analytical techniques

2.7.1 X-ray photoelectron spectroscopy

Irradiating a material with X-rays that exceed the electron binding energy results in excitation and the emission of photoelectrons. Measuring the kinetic energy of these electrons can characterise the electronic transitions, states, and structure, yielding elemental composition, oxidation state, and chemical environment.

$$E_{bind} = hv - E_{KE}$$

Equation 2-16. Binding energy by XPS, where E_{bind} is the binding energy, and E_{KE} is the photoelectron kinetic energy.

However, the photoelectrons are highly attenuated within the sample. Thus, despite the high X-ray penetration depth, only photoelectrons emitted from the surface (nanometres) are detected. Knowing this, the technique can be used to show surface-bulk contrast in a range of properties.

2.7.2 UV-vis diffuse reflectance spectroscopy

Diffuse reflectance spectroscopy allows the characterisation of optical properties without suspension in liquid media. Unlike liquids, solids scatter much more light by specular reflection and diffuse back-scattering, which can be detected separately, in order to yield the band-gap.[29,30] Tauc plots are used to extract this value.

$$F(R_\infty) = \left[\frac{K}{S}\, hv\right]^2 = C\ (hv - E_g)$$

Equation 2-17. Derivation of band-gap by UV diffuse reflectance, where K and S are the absorption and back-scattering coefficients, respectively, C is a constant, and E_g is the band-gap.

$$(F(R_\infty)h\nu)^{\frac{1}{\gamma}} = B(h\nu - E_g)$$

Equation 2-18. Derivation of band-gap by UV diffuse reflectance by Tauc plot, where *B* is a constant, and γ is 2 in the context of indirect transitions, as will be used in this work.

2.7.3 Solid-state nuclear resonance spectroscopy

The energy degeneracy of nuclear-spin states is broken in a magnetic field, the extent of which is dependent on the nuclear-specific gyromagnetic ratio and the field at the nucleus, which varies with chemical environment, called shielding. The nuclei are excited by irradiation with radiowaves and allowed to decay. The standard presentation of data is plotted against chemical shift in parts per million (ppm), which is the difference of the resonance frequency of the signal from a standard of trimethyl silane on that spectrometer.[31] The solid-state experiment suffers from angle-dependent broadening and shifting, which can be reduced by spinning the sample at a specific angle of ~54.74° with respect to the magnetic field.

$$\Delta E = h\nu = \gamma \hbar B_0$$

Equation 2-19. Probing electronic environment by NMR, where γ is the gyromagnetic ratio, $\hbar$ is the reduced Planck constant, and B_0 is the magnetic field at the nucleus.

2.7.4 Electron paramagnetic resonance spectroscopy

Analogous to NMR, the degeneracy of the spin of an unpaired electron can be broken in a magnetic field. The change in energy (m_s = ½ ↔ -½) is dependent on the magnetic moment of the electron (*g*-factor), and can be determined by varying the field under constant irradiation by microwaves, which needs to be much higher frequency than NMR.[32] The *g*-factor is characteristic of chemical environment, with the signal strength yielding information

on concentration. It is particularly useful for the speciation of electronic defects, shown later in the context of oxygen vacancies in TiO_2.

$$\Delta E = h\nu = g\,\mu_B\,B_0$$

Equation 2-20. Energy transition of electron spin-flipping in EPR, where μ_B is the Bohr magneton.

2.7.5 TEM

Visible light is too low energy to visualise nanometre and atomic structure. Electrons through a sample can be used to produce images based on simple transmission. STEM employs rastering to improve spatial resolution, while high-angle annular dark-field imaging improves the counting statistics and lowers the background from the through-beam. The resolution of ~1 Å is easily attainable using STEM.

2.7.6 Electron spectroscopy

Electron spectroscopy allows compositional mapping during imaging. Energy-dispersive X-ray spectroscopy (EDX) functions by detecting emitted characteristic X-rays from electronic relaxation transitions. The position of the peaks in the spectrum identifies the element, whereas the intensity of the signal corresponds to the concentration of the element.

Electron energy loss spectroscopy (EELS) relies on measuring inelastically scattered (5-100 mrad) electrons themselves. The loss in the energy of the beam is characteristic of certain electronic transitions, and yields information on composition and electronic state. Analogous phenomena to XANES and XAFS can also be observed, called electron loss near-edge structure (ELNES) and extended energy-loss fine structure EXELFS.[33]

2.8 References

(1) Yue, Z. A Rigorous Proof on the Crystallographic Restriction Theorem to Establish Human Being. Bp. Int. Res. Crit. Inst. BIRCI-J. Humanit. Soc. Sci. 2018, 1 (4), 25–28. https://doi.org/10.33258/birci.v1i4.86.

(2) Cockcroft, J.; Barnes, P. Advanced Certificate in Powder Diffraction on the Web. Birkbeck College.

(3) Paufler, P. Complete Online Set of International Tables for Crystallography, Vols. A–G. Edited by H. Fuess, Th. Hahn, H. Wondratschek, U. Müller, U. Shmueli, E. Prince, A. Authier, V. Kopský, D. B. Litvin, M. G. Rossmann, E. Arnold, S. Hall and B. McMahon. Springer, Jointly Published with the IUCr, 2007. Price for Online Access USD 2080.00. EISBN: 978-1-4020-5259-0, Doi: 10.1107/97809553602060000001, Http://It.Iucr.Org. Acta Crystallogr. A 2007, 63 (6), 483–483. https://doi.org/10.1107/S0108767307041207.

(4) Structure Determination from Powder Diffraction Data; David, W. I. F., Shankland, K., McCusker, L. B., Bärlocher, C., Eds.; International Union of Crystallography Monographs on Crystallography; Oxford University Press: Oxford, 2006. https://doi.org/10.1093/acprof:oso/9780199205530.001.0001.

(5) Henke, B. L.; Gullikson, E. M.; Davis, J. C. X-Ray Interactions: Photoabsorption, Scattering, Transmission, and Reflection at E = 50-30,000 EV, Z = 1-92. At. Data Nucl. Data Tables 1993, 54 (2), 181–342. https://doi.org/10.1006/adnd.1993.1013.

(6) Hauptman, H. The Direct Methods of X-Ray Crystallography. Science 1986, 233 (4760), 178–183. https://doi.org/10.1126/science.233.4760.178.

(7) Feng, J. Deconvolution of the Interatomic Vector Set Using a Convolution Table. Acta Crystallogr. A 2009, 65 (Pt 1), 48–50. https://doi.org/10.1107/S010876730802936X.

(8) Hendrickson, W. A. Anomalous Diffraction in Crystallographic Phase Evaluation. Q. Rev. Biophys. 2014, 47 (1), 49–93. https://doi.org/10.1017/S0033583514000018.

(9) Bail, A. L. Whole Powder Pattern Decomposition Methods and Applications: A Retrospection. Powder Diffr. 2005, 20 (4), 316–326. https://doi.org/10.1154/1.2135315.

(10) Pawley, G. S. Unit-Cell Refinement from Powder Diffraction Scans. J. Appl. Crystallogr. 1981, 14 (6), 357–361. https://doi.org/10.1107/S0021889881009618.

(11) Toby, B. H. R Factors in Rietveld Analysis: How Good Is Good Enough? Powder Diffr. 2006, 21 (1), 67–70. https://doi.org/10.1154/1.2179804.

(12) Martin, I. https://www.diamond.ac.uk/Science/Machine.html (accessed 2022 -04 -07).

(13) Kramers, H. A.; Heisenberg, W. Über die Streuung von Strahlung durch Atome. Z. Für Phys. 1925, 31 (1), 681–708. https://doi.org/10.1007/BF02980624.

(14) Kronig, R. de L. On the Theory of Dispersion of X-Rays. JOSA 1926, 12 (6), 547–557. https://doi.org/10.1364/JOSA.12.000547.

(15) Mark, H.; Szilard, L. Ein einfacher Versuch zur Auffindung eines selektiven Effektes bei der Zerstreuung von Röntgenstrahlen. Z. Für Phys. 1925, 33 (1), 688–691. https://doi.org/10.1007/BF01328354.

(16) Coster, D.; Knol, K. S.; Prins, J. A. Unterschiede in der Intensität der Röntgenstrahlen-reflexion an den beiden 111-Flächen der Zinkblende. Z. Für Phys. 1930, 63 (5), 345–369. https://doi.org/10.1007/BF01339610.

(17) Bradley, A. J.; Rodgers, J. W.; Bragg, W. L. The Crystal Structure of the Heusler Alloys. Proc. R. Soc. Lond. Ser. Contain. Pap. Math. Phys. Character 1934, 144 (852), 340–359. https://doi.org/10.1098/rspa.1934.0053.

(18) Ramachandran, G. N.; Raman, S. A New Method For The Structure Analysis Of Non-Centrosymmetric Crystals. Curr. Sci. 1956, 25 (11), 348–351.

(19) Attfield, J. P. Determination of Valence and Cation Distributions by Resonant Powder X-Ray Diffraction. Nature 1990, 343 (6253), 46–49. https://doi.org/10.1038/343046a0.

(20) Warner, J. K.; Wilkinson, A. P.; Cheetham, A. K.; Cox, D. E. Comparative Study of Elemental Contrast by Resonant X-Ray and Neutron Powder Diffraction. J. Phys. Chem. Solids 1991, 52 (10), 1251–1256. https://doi.org/10.1016/0022-3697(91)90200-J.

(21) Zhang, Y.; Lee, P. L.; Nolas, George. S.; Wilkinson, A. P. Gallium Distribution in the Clathrates $Sr_8Ga_{16}Ge_{30}$ and $Sr_4Eu_4Ga_{16}Ge_{30}$ by Resonant Diffraction. Appl. Phys. Lett. 2002, 80 (16), 2931–2933. https://doi.org/10.1063/1.1473236.

(22) Templeton, D. H.; Templeton, L. K. X-Ray Dichroism and Polarized Anomalous Scattering of the Uranyl Ion. Acta Crystallogr. Sect. A 1982, 38 (1), 62–67. https://doi.org/10.1107/S0567739482000114.
(23) Finkelstein, K. D.; Shen, Q.; Shastri, S. Resonant X-Ray Diffraction near the Iron K Edge in Hematite Fe2O3. Phys. Rev. Lett. 1992, 69 (10), 1612–1615. https://doi.org/10.1103/PhysRevLett.69.1612.
(24) Mukhamedzhanov, E. Kh.; Kovalchuk, M. V.; Borisov, M. M.; Ovchinnikova, E. N.; Troshkov, E. V.; Dmitrienko, V. E. Resonant Diffraction of Synchrotron Radiation in Rubidium Dihydrophosphate Crystals. Crystallogr. Rep. 2010, 55 (2), 174–181. https://doi.org/10.1134/S1063774510020021.
(25) Artioli, G.; Pavese, A.; Bellotto, M.; Collins, S. P.; Lucchetti, G. Mn Crystal Chemistry in Pumpellyite; a Resonant Scattering Powder Diffraction Rietveld Study Using Synchrotron Radiation. Am. Mineral. 1996, 81 (5–6), 603–610. https://doi.org/10.2138/am-1996-5-607.
(26) Grenier, S.; Hill, J. P.; Gibbs, D.; Thomas, K. J.; Zimmermann, M. v.; Nelson, C. S.; Kiryukhin, V.; Tokura, Y.; Tomioka, Y.; Casa, D.; Gog, T.; Venkataraman, C. Resonant X-Ray Diffraction of the Magnetoresistant Perovskite $Pr_{0.6}Ca_{0.4}MnO_3$. Phys. Rev. B 2004, 69 (13), 134419. https://doi.org/10.1103/PhysRevB.69.134419.
(27) Billinge, S. J. L. The Rise of the X-Ray Atomic Pair Distribution Function Method: A Series of Fortunate Events. Philos. Trans. R. Soc. Math. Phys. Eng. Sci. 2019, 377 (2147), 20180413. https://doi.org/10.1098/rsta.2018.0413.
(28) Terban, M. W.; Billinge, S. J. L. Structural Analysis of Molecular Materials Using the Pair Distribution Function. Chem. Rev. 2022, 122 (1), 1208–1272. https://doi.org/10.1021/acs.chemrev.1c00237.
(29) Escobedo Morales, A.; Sánchez Mora, E.; Pal, U. Use of Diffuse Reflectance Spectroscopy for Optical Characterization of Un-Supported Nanostructures. Rev. Mex. Fis. Suppl. 2007, 53, 18–22.
(30) Makuła, P.; Pacia, M.; Macyk, W. How To Correctly Determine the Band-gap Energy of Modified Semiconductor Photocatalysts Based on UV–Vis Spectra. J. Phys. Chem. Lett. 2018, 9 (23), 6814–6817. https://doi.org/10.1021/acs.jpclett.8b02892.
(31) Hoffman, R. E. Standardization of Chemical Shifts of TMS and Solvent Signals in NMR Solvents. Magn. Reson. Chem. MRC 2006, 44 (6), 606–616. https://doi.org/10.1002/mrc.1801.
(32) Di Valentin, C.; Pacchioni, G.; Selloni, A.; Livraghi, S.; Giamello, E. Characterization of Paramagnetic Species in N-Doped TiO2 Powders by EPR Spectroscopy and DFT Calculations. J. Phys. Chem. B 2005, 109 (23), 11414–11419. https://doi.org/10.1021/jp051756t.
(33) Hofer, F.; Schmidt, F. P.; Grogger, W.; Kothleitner, G. Fundamentals of Electron Energy-Loss Spectroscopy. IOP Conf. Ser. Mater. Sci. Eng. 2016, 109, 012007. https://doi.org/10.1088/1757-899X/109/1/012007.

Chapter 3: Experimental procedures

3.1 General diffraction characterisation

3.1.1 Laboratory-configuration XRD

Powder X-ray diffraction was performed on a Bruker D8 ADVANCE ECO using Cu $K\alpha_1$ radiation (λ = 1.5406 Å) generated operating at 40 kV and 40 mA. Patterns were typically measured with 0.1 s exposure at 0.01° interval to the angle above the last reflection of interest.

3.1.2 SXPD on I11

Data collection on the High Resolution Powder Diffraction beamline I11,[1] DLS, UK was assisted by Prof. Chiu Tang, Prof. Stephen Thompson, and Dr. Sarah Day. On I11, the multi-analyser crystal detectors (MAC) are used for high-resolution experiments. The primary radius (source to sample) is 48,000 mm, and the secondary radius (sample to MAC detector) is 430 mm. This large primary distance ensures high collimation of the beam at the sample. Each of the five MAC arms contains nine Si(111) analysing crystals, yielding 45 channels. These crystals are exposed to sample-diffracted beam, leading to a second diffraction event by Si(111) which is detected by a photomultiplier device. This double-diffraction method benefits from narrow rocking curves with an effective slit width of 0.015 mm, and low energy bandpass (energy acceptance: $\Delta E/E \sim 10^{-4}$)[1], which improves angular resolution and signal-to-noise ratio relative to standard slits. This angle rejection leads to significant reduction in flux at the detector, causing this method to be only feasible at

synchrotron sources. The five units cover a 2θ angular range of 0-150°, and simultaneously collect data while rotating in 2θ. The angular resolution of the MAC detector is ~0.001°.

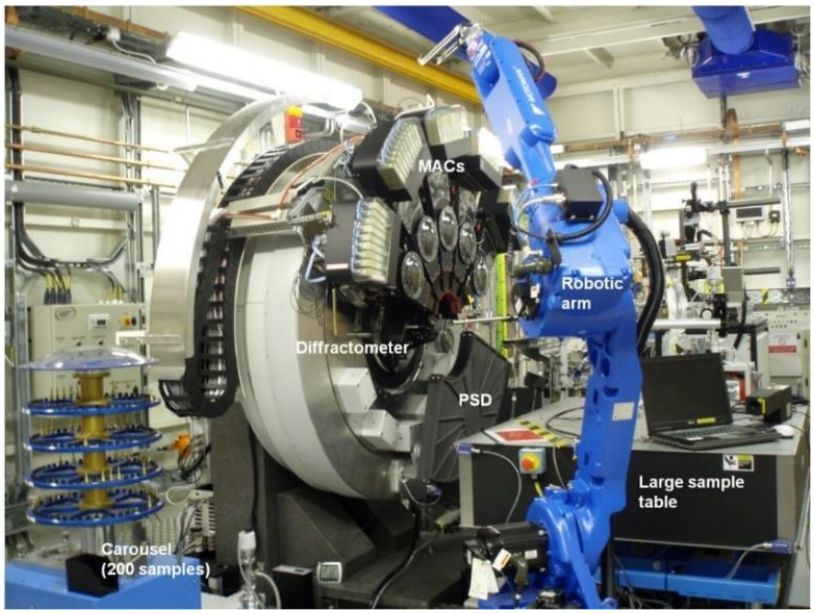


Figure 3-1. Diffractometer at I11, DLS.

3.1.2.1 Ex-situ capillary samples

Powder samples are ground until homogeneous, and loaded into borosilicate capillaries of internal diameter 0.5 mm. The diffraction data are collected in Debye-Sherrer geometry using a multi-analyser crystal (MAC) diffractometer (R_s = 430 mm) over an angular range of 2-150° in 2θ over a 30-minute exposure period. Capillaries are spun in the ω-axis. Typically, the beam-energy was specified to be 15 keV. The beam at the sample is 0.8 mm (v) × 2.5 mm (h), yielding an approximate irradiated volume of 1 mm^3. Patterns were collected at room temperature under atmospheric conditions unless otherwise specified.

3.1.2.2 Angular calibration

Instrumental deviation in the beam energy and zero-error were defined by a Pawley refinement against a silicon standard (NIST SRM640c) pattern collected using MAC detectors from 0°-150° in 2θ for an exposure time of 1800 s, against the well-defined ten significant-figure lattice parameter of 5.431020511 Å.[2] Silicon is highly crystalline and exhibits large crystal sizes, capable of producing extremely narrow peaks (typical FWHM ~0.01°). The ten-significant-figure value was fixed, and the wavelength and angular zero-error allowed to refine. The wavelength is typically refined to at least six significant figures when expressed in Ångströms, and the zero-error to at least three significant figures.

3.1.3 SXPD on BL02b2, Japan

Data collection on BL02b2,[3] Spring-8, Japan was assisted by Dr. Shogo Kawaguchi. Samples were packed into borosilicate capillaries as above. Detection used a MYTHEN PSD. Samples were typically scanned over an exposure time of 2×100 s. Wavelength and zero-error were refined against a NIST 674b CeO_2 standard.

3.1.4 XRD refinement

All structural refinements were carried out in TOPAS.[4] VESTA was used for electron-density visualisation.[5] Unless otherwise stated, background was initially fitted by Chebyshev polynomial, then fixed, refined, then fixed; peak shape was described by the modified Thompson-Cox-Hastings pseudo-Voigt using six parameters; axial divergence was initially set to 7 then refined; Lorentzian factor set to 90 for SXPD, and 0 for laboratory-source XRD. Refinements were judged by visual inspection of the fitting, R_{wp}, and GoF values.

3.1.4.1 Sequential batch refinement

It is not feasible to judge the effect of certain assumptions and models on the fitting for datasets of dozens of patterns. Performing the refinement for all patterns separately before tweaking parameterisation is infeasible. Hence, for large sets of data that are sequential by either temperature or electrochemistry, it is more sensible to carry out batch refinements. This is a procedure run through the command line that queues a large number of refinements to be executed automatically. These can be run unsupervised leading to enormous increase in the time-efficiency and scope of analysis. Historically, they have been able to be run simultaneously alongside other batch refinements, though frustratingly this functionality was recently removed in TOPAS 6.

The disadvantage of batch refinements is the lack of fit-visualisation during convergence. Calculated patterns are only accessible after the refinement has moved to the next pattern. Due to this, refinements were run to an excess of iterations as trialled by individual refinements (usually 100s).

3.1.5 Other techniques

3.1.5.1 ICP-MS

The composition of an inorganic sample is often analysed by dissolution, and ionisation in order to be separated by z/m ratio. Samples were sent to Research Centre of Atatürk University, Turkey for compositional analysis on an Agilent 7800 ICP-MS. Approximately 20 mg of sample was digested in 2 mL of concentrated HNO_3, then diluted with DI water to 100 mL. A 0.3 mL aliquot of this solution was diluted to 15 mL using 2% HNO_3.

3.2 Photocatalytic water-splitting of N-TiO_2

3.2.1 Materials

Pure ST01 anatase was obtained from Ishihara Sangyo, Japan, and pure rutile powder from Signma-Aldrich. Mixed phase P25 (75% anatase, 25%rutile) was obtained from Degussa. TMPO was obtained from Sigma-Aldrich, and used as received.

3.2.2 Synthesis of N-doped TiO_2

Various TiO_2 powders were nitrogen-doped using an ammonia treatment by annealing under pure ammonia flow at various temperatures (5°C min^{-1}) for 8 hours. The samples were allowed to cool and used without further treatment. The degree of nitrogen doping was controlled by the temperature of the reaction which was set at 550°C, 600°C, 620°C, and 750°C yielding samples denoted as A1, A2, A3, and A4 respectively. Likewise, the ammonia treatment at different temperatures was also performed on rutile TiO_2 (R0) and P25 TiO_2 (P0) powder samples. R0 was treated with ammonia flow at 650°C, 700°C and 750°C, which are denoted as R1, R2 and R3, while P0 at 550°C, 600°C and 620°C, denoted as P1, P2 and P3.

3.2.3 Electronic characterisation

3.2.3.1 XPS

Measurements were carried out on a Thermo Fisher Scientific NEXSA spectrometer at the Research Complex at Harwell. Survey scans were obtained at a pass energy of 200 eV, 5 scans with step size 1 eV, whereas for those detailed spectra 50 eV pass energy, 10 scans with 0.1 eV step size were used. Fitting was carried out by Dr. Jianwei Zheng.

3.2.3.2 UV-vis diffuse reflectance spectroscopy

Measurements were carried out on a Perkin Elmer Lambda 750S spectrometer within the Chemistry Department, University of Oxford. 50 mg of sample was pressed on a holder and scanned between 200-1500 nm.

3.2.3.3 EPR

Measurements were carried out on a Bruker EMX EPR spectrometer within the Chemistry Department, University of Oxford. 50 mg of sample was packed into EPR tubes (internal diameter: 0.6 mm, external diameter: 0.84 mm). The incident energy was fixed to an X-band frequency of 9.4 GHz and the magnetic field varied over 2800-4000 Gauss.

3.2.4 Structural characterisation

3.2.4.1 VT-SXPD of N-anatase, P25 and N-P25

Data were collected at I11, DLS, UK. Wavelength and zero-error were refined to 0.824875(1) Å and +0.00467(5)°, respectively. Samples of P25 and N-P25 were scanned at room temperature and 50°C intervals between 100°C and 500°C. Heating was conducted using a hot-air blower at 10°C min^{-1}, with an equilibration time of 2 minutes allowed before each scan.

It was known that the input temperature of the hot-air blower is not the actual temperature at the sample. This is due to instrumental error, as well as the temperature differential between the air and the sample. The calibration of the input value to the sample-temperature was conducted at the start of the beamtime by measuring the thermal expansion of platinum metal powder at room temperature, which is well-defined.[6] The change in lattice parameter can then be ascribed to an absolute temperature.

Patterns were collected at 100°C, 200°C, 300°C, 400°C, and 500°C. The lattice parameters were determined by Pawley refinement (average R_{wp} = 12.53%). These values had a standard deviation in the order of 1×10^{-5} Å. The experimental lattice parameters were compared to the theoretical values yielded by a seven-term polynomial to yield the actual sample-temperature.[6] Propagating errors throughout the calculation, the sample-temperature is known with a standard deviation of <2.0°C (Table 3-1). The relationship between the input and actual temperature was fitted well by a linear function, with the calibrated temperatures found to be consistently around 10% below the input temperature.

Input temperature / °C	Measured a / Å	Δa / Å	$\Delta a/a_0$	Calibrated temperature / °C
22.5	3.92379(8)	0	0	22.5
100	3.92621(1)	0.00241(1)	0.000615(3)	88(2)
200	3.92958(1)	0.00578(1)	0.001473(3)	181(1)
300	3.9330(1)	0.00917(1)	0.002338(3)	272(1)
400	3.93641(1)	0.01261(1)	0.003213(3)	362(1)
500	3.93986(1)	0.01606(1)	0.004094(4)	451(1)

Table 3-1. Temperature calibration for VT-SXPD on I11, DLS. Fits to a linear function: m = 0.8979260, c = 0.8694716; R = 0.9999.

Not all temperatures used in the TiO_2 experiment were directly sampled during temperature calibration. The remaining temperatures (50°C, 150°C, 250°C, 350°C, and 450°C) were calculated by linear interpolation between the two closest sampled points (Table S3-1). These interpolated values exhibited slightly higher errors, but the greatest still being low (an input temperature of 150°C being calibrated to 134°C ± 2.2°C. These errors are carried through the subsequent calculations.

3.2.4.2 Phase analysis of high-temperature synthesis

SXPD data of pristine and nitrogen-doped anatase, rutile and P25 were also collected at beamline BL02B2 at SPring-8, Japan.[3] Wavelength and zero-error were refined to

0.689556 Å and -0.00015°, respectively. Samples were scanned over an angular range of 4-78° in 2θ over a 10-minute exposure period (sum of 2×5 min). Each sample was scanned at room temperature and at high temperature 500°C. For VT-SXPD an exposure time of 2×100 s was used at 20°C intervals between 60°C and 580°C.

3.2.5 Photocatalytic water-splitting activity tests

Photocatalytic water splitting experiments were carried out in a batch process by Dr. Yiyang Li. Typically, 5 mg of photocatalyst was added to 10 mL of deionised water under stirring in a 25 mL stainless-steel autoclave equipped with two quartz windows (diameter: 10 mm, thickness: 18 mm). The system was pressurised with 2 bar of Ar gas, and heated to various temperatures, after which a tungsten light (70 W, Glamox Professional 2000) was applied to provide visible-light irradiation. After 2 hours of reaction, the autoclave was cooled naturally to room temperature. The amounts of hydrogen and oxygen were measured by gas chromatography.

3.2.6 Vacancy structure optimisation

The structural optimisation presented in this work was performed by Dr. Qinging Deng (IFW Dresden) using the Vienna Ab-initio Simulation Package (VASP) program[7,8] within the projector-augmented wave (PAW)[9] to investigate the local atomic reconfiguration of oxygen vacancies introduced at the surface and sub-surface of (101) TiO_2 anatase. The pristine slab contained three TiO_2 layers, totalling 108 atoms: 36 Ti and 72 O atoms.

The exchange-correlation interactions were described with the generalised gradient approximation (GGA)[10] in the form of the Perdew, Burke and Ernzernhof (PBE) functional[11]. The kinetic energy cut-off for the plane-wave basis set was set as 450 eV, and the distance of

vacuum layer was set to be more than 15 Å, which is sufficiently large to avoid interlayer interactions. The Grimme van-der-Waals/dispersion-correction scheme DFT-D3[12] was applied to the anatase TiO_2 (101) surface. The electronic self-consistent field (SCF) tolerance was set to 10^{-5} eV. Fully relaxed geometries and lattice parameters were obtained by optimising all atomic positions until the Hellmann–Feynman forces were less than 0.02 eV $Å^{-1}$. The *k*-points samplings with a gamma-centred Monkhorst-Pack scheme[13] were 8×8×1 for structural optimisations.

3.3 Electrochemical lithiation of palladium nanoparticles

3.3.1 Materials

Carbon-black (Vulcan XC72R GP-3921, particle size: 50 nm) was purchased from CABOT. Palladium acetate ($Pd(OAc)_2$), ethanol and lithium acetate dihydrate ($Li(OAc)\cdot 2H_2O$) were purchased from Sigma-Aldrich, and used as received.

3.3.2 Synthesis

3.3.2.1 Palladium nanoparticles

The procedure established by Chen et al.[14] for supported palladium nanoparticles involved a single-step reduction under inert gas from a palladium acetate, $Pd(OAc)_2$, precursor. This was adapted to yield high palladium loading carbon black. Typically, a target palladium loading of 50%wt was used. Carbon black (200 mg) and $Pd(OAc)_2$ (169 mg) were ground until homogeneous, then decanted into an alumina crucible, and placed in a quartz-tube furnace. The system was purged with argon at 500 cm^3 min^{-1} for at least 15 minutes. Under continuous argon flow, the reaction was heated to 550°C at 10°C min^{-1}, held for 4 hours, before being allowed to cool to room temperature. The temperature, heating rate,

and hold duration were varied during investigation, and will be referred to by the notation: temperature/rate/hold-time; for example, the procedure above yields sample 550/10/4. Palladium supported on carbon black are referred to as Pd/cb, and palladium supported on graphite as Pd/gr.

3.3.2.2 Post-synthesis lithiation

Pre-formed palladium nanoparticles and $Li(OAc)\cdot 2H_2O$ were ground until homogeneous, in various stoichiometries. The powder was transferred into a round-bottom flask, and degassing with nitrogen over 15 minutes. Under continuous nitrogen flow, the reaction was heated to 250°C for 2 hours, before being allowed to cool to room temperature. The resultant powder was washed with 50 mL of water, then 50 mL ethanol.

3.3.2.3 In-situ lithiation

The procedure for palladium nanoparticles was repeated, but $Li(OAc).2H_2O$ was also ground with the powder.

3.3.3 TEM and electron spectroscopy

Imaging was carried out by Ping-Luen Ho in the Materials Department, University of Oxford. The samples were dispersed using 1 mg of sample in approximately 1 mL of dry ethanol. The mixture was sonicated for 30 minutes to form a uniform suspension. One drop of the suspension on a Holey carbon film 400 copper mesh grid forms a dispersed film less than 200 nm thick, and dried in the air prior to analysis. Finally, the copper sample grid was transferred to a JEOL ARM-200F for measurement. The following parameters were used: probe current of 80 pA, a semi-convergence angle of 23-25 mrad, accelerating voltage of 200 kV. The microscope was aligned before every experiment by using a gold standard sample

ensuring 0.08 nm resolution under normal conditions. EDX was carried out using a Centurion spectrometer. EELS was carried out on a Gatan GIF Quantum 965 ER with an energy resolution of 0.9 eV, a beam diameter of approximately 100 nm, and semi-collection angle of ~2.5 mrad. Data processing of EELs spectra included pre-edge background subtraction, removal of plural scattering by Fourier-ratio deconvolution and normalisation by integration of the post-edge intensity.

3.3.4 VT-SXPD

VT-SXPD was carried out at BL02b2. Wavelength and zero-error were refined to 0.689556 Å and -0.00015°, respectively. Non-doped and in-situ lithiated 0.2 eq, 0.5 eq, and 1.5 eq samples formed under 305/2/12 conditions were scanned from room temperature to 515°C at 15°C intervals.

3.3.5 LIB characterisation

Cell assembly and cycling were carried out using facilities at I11, DLS.

3.3.5.1 Electrodes and cell assembly

The Pd/gr material was ground with carbon black and PVDF binder to yield a 70:20:10 mixture, which was transferred to a small vial. N-methyl pyrrolidone (NMP) was added (1 ml per 100 mg of Pd/gr) and stirred at 500 rpm for 10 minutes. The slurry was coated onto copper foil (35 um) using a doctor blade, using 200 μm wet clearance. The wet layer was dried in a vacuum oven at 70°C overnight, resulting in a layer of average thickness ~50 μm. For Pd/cb materials, no additional carbon black was added; a Pd/cb to PVDF ratio of 90:10 was used. Twice the solvent was required to suspend the high surface-area carbon black (2 ml per 100 mg of Pd/cb).

Electrodes ($\varnothing$ = 15 mm) were punched from the layer, then calendared under 1 tonne for 30 seconds, weighed, and activated under vacuum at 70°C overnight in a Schlenk tube. The electrodes were transferred to an argon glovebox without exposure to air.

Electrodes were assembled into CR2032 coin cells using specially-drilled stainless steel components: the top and bottom outer casings, and the spacer have a 6 mm centred hole to allow maximum flux at the sample. The holes in the outer casings were filled with specially manufactured glass discs (thickness: 0.3 mm; diameter: 6 mm) and sealed from the inside and outside with sticky Kapton film. Lithium metal was cleaned, thinned, and pressed on to the spacers. Glass microfiber separators (20 mm) were saturated with 225 µl of electrolyte, 1 M $LiPF_6$ in 3:7 (v:v) ethyl carbonate: ethyl methyl carbonate; herein all reference to electrolyte is to this mixture. The cells were crimped, and their OCVs measured to ensure no short-circuiting.

3.3.5.2 Electrochemical cycling

Cycling was carried out on an MTI BST8-3. The standard cell cycling was conducted using constant current applied at 100 mA g^{-1}. Additional experiments include fast cycling, rate sweeps, varying potential window, and holding the cell at high voltage (not constant current) after every charge.

3.3.5.3 In-operando SXPD during LIB cycling

A bespoke cell-holder was fixed at the beam-pipe in EH2, I11-1, DLS, UK. The Pixium area detector on I11-1 was used in preference to the high-resolution MAC detectors on I11 in order to maximise counting statistics and avoid grainy data due to the lack of ω-spinning and known large particle size of 50%wt palladium nanoparticles. This detector

yields an angular resolution of 0.009° over a range of 0-36° 2θ . The incident beam energy was input as 25 keV. Wavelength and zero-error were refined to 0.4970866 Å and +0.00161°, respectively.

3.3.5.4 Post-mortem analysis

Pd-^{int}Li/C NPs was painted on a 0.1 mm borosilicate glass capillary at room temperature. The data were collected in beamline I11 equipped with a position sensitive detectors (PSD), in the 2θ 0-150° with 0.002° data binning.

After cycling, cells were disassembled in an argon glovebox using a bespoke jig adapted from industry-standard equipment and machined by Mr. Jonathan Potter (I11, DLS). The electrodes were naturally dried, scraped from the current collector, ground into a fine powder, and packed into capillaries. The capillaries were sealed with Cristoseal and vacuum grease, removed from the glovebox, and flame-sealed.

3.3.5.5 Ex-situ X-ray pair distribution function

Post-mortem material was packed into 1 mm internal-diameter borosilicate capillaries in an argon glovebox, and sealed using Cristaseal and a small amount of wax. Uncycled electrode material was also packed under ambient conditions and sealed in the same way, as well as a thermally lithiated Pd^{int}Li.

Post-mortem electrode materials were submitted to I15-1, DLS. The beam energy was 76.6 keV (Q_{max} up to 40 Å^{-1}), focussing to 700 μm × 150 μm at the sample. Data were collected using a Perkin Elmer XRD 1611 CP3 with an active area of 409.6 mm × 409.6 mm (100 μm pixel size) up to 63° 2θ at room temperature and pressure.

The capillaries used for XPDF data collection are 1 mm, which are much larger than those for Bragg scattering experiments. The maximisation of sample volume is much more important than minimising the length of sample in the axis of the beam. Similarly, self-absorption is not a significant problem on I15-1 due to very high beam energy. Much larger capillaries required a much larger volume of sample in order to fill enough of the length and also to achieve good packing stability. Hence, in order to submit enough sample for analysis, for each submission, at least three cells were assembled and cycled to the same specification and the most similar two cells with respect to capacity and dQ/dV behaviour were combined. The capillaries were spun at 5 Hz in the ω-axis.

3.4 Aluminium siting in zeolites

3.4.1 Materials

Zeolite H-ZSM-5 (Si/Al=25) was obtained in its proton form from SRIFT-Sinopec, China. TMPO and silver nitrate were obtained with 99% purity or above from Sigma-Aldrich, used as received.

3.4.2 Adsorption of probe molecules

3.4.2.1 TMPO adsorption

The parent H-ZSM-5 material was activated at 550°C for 6 hours, then further dehydrated under vacuum on a Schlenk line, in order to remove adsorbed water and other impurity gas molecules. The pressure was kept below 10^{-3} Pa. The temperature was gradually increased at a rate of 1°C min^{-1} and held at 300°C for 24 hours, after which the sample was allowed to cool naturally. Under static vacuum, 0.2 mL of degassed TMPO solution (0.1 M in dichloromethane, Cl_2H_2C) was injected into the flask. Then the sample was held at 175°C

overnight, in order for the TMPO to fully diffuse into the zeolite, before transfer to an argon glovebox.

3.4.2.2 Silver adsorption

Single atom silver was impregnated within ZSM-5 by the procedure reported by Lin et al.[15], which is presented as follows. The sample was calcined in air at 480°C for 2 hours with a ramp rate of 1°C min^{-1}. Silver nitrate (54 mmol) was dissolved in deionised water (30 mL). Throughout the process the solution was covered with foil to prevent light-induced agglomeration. Dilute aqueous sodium hydroxide was used to keep the pH ~7, in order to avoid metal precipitation. The solution was stirred for 24 hours, washed with deionised water, and vacuum dried at 70°C overnight. Finally, the powder was calcined in air at 550°C for 12 hours with a ramp rate of 5°C min^{-1}.

3.4.3 TMPO/ZSM-5

3.4.3.1 SSNMR of TMPO/ZSM-5

SSNMR experiments were carried out on a Bruker Advance III 400WB spectrometer at Hong Kong Polytechnic University in collaboration with Dr. Guangchao Li. The TMPO/ZSM-5 sample was transferred into a ZrO_2 rotor with a Kel-F endcap under nitrogen atmosphere in a glovebox. The chemical shifts of ^{1}H, ^{27}Al, ^{29}Si, and ^{31}P were calibrated using adamantane (1.74 ppm), aqueous $Al(NO_3)_3$ (1 M, 0 ppm), Kaolin (-91.5 ppm), and $(NH_4)_2HPO_4$ (1 ppm), respectively.

For ^{1}H, the sample was additionally dehydrated in vacuum at 400°C for 10 h before analysis at a resonance frequency of 399.33 MHz using a 4 mm probe with a spinning rate of 10 kHz, a $\pi/2$ pulse length of 3.8 μs, and a recycle delay of 5 s.

For 1D ^{31}P cross-polarisation (CP) and all the 2D experiments were performed at resonance frequency of 104.22 MHz. For ^{31}P CP and 2D ^{31}P-^{1}H hetero-nuclear correlation, a 4 mm probe was used with a sample spinning rate of 10 kHz, a contact time of 4 ms, a pulse length of 4.6 μs, and a recycle delay of 3 s. For 2D ^{31}P-^{31}P proton-driven spin diffusion, ^{1}H→^{31}P CP (contact time of 4 ms) was used to prepare the initial ^{31}P signal. The π/2 pulse width of ^{31}P is 4.6 μs and the mixing time was set to 100 ms. The experiments were acquired with 64 scans per experiment and 360 experiments in the State-TPPI scheme.

The ^{27}Al and ^{29}Si experiments were carried out with samples that were fully hydrated at ambient temperature overnight in a desiccator. ^{27}Al and ^{29}Si experiments were carried out on a Varian InfinityPlus-300 spectrometer with the Larmor frequencies of 78.16 MHz, 59.59 MHz, and 121.50 MHz, respectively. ^{27}Al MAS NMR spectra were recorded with a pulse length of 0.2 μs, a recycle delay of 1 s, and a spinning rate of 10 kHz. ^{29}Si MAS NMR spectra with high-power proton decoupling were recorded on a 7.5 mm probe with a spinning rate of 3.5 kHz, a pulse length of 5.2 μs, and a recycle delay of 80 s.

3.4.3.2 SXPD and NPD of TMPO/ZSM-5

The TMPO/ZSM-5 was loaded into a capillary in an argon glovebox. SXPD data were collected on the MAC with an exposure time of at least 30 mins. Wavelength and zero-error were refined to λ = 0.688160 Å, and -0.00028°, respectively.

NPD data were collected at the General Purpose Powder Diffractometer (GDDP), China Spallation Neutron Source (CSNS), Dongguan, China, using the time-of-flight diffractometer GPPD. The sample was loaded in a vanadium can of diameter 9.1 mm in an argon glove box. Wavelength and zero-error were refined to λ = 1.4940(1) Å, and -0.02269°, respectively, using a $Na_2Al_2Ca_3F_{14}$.

3.4.4 STEM imaging of Ag/ZSM-5

The high-angle annular dark-field scanning transmission electron microscopy (HAADF-STEM) images of pristine ZSM-5 was carried out using an aberration-corrected E02 JEOL ARM-300F. The microscope was operated at 300 kV in HAADF-STEM mode with HAADF detector collection semi-angle from 70 to 270 mrad, the probe array sizes of 1024×1024, a dwell time of 0.3 μs per pixel. The probe current was set at 15 pA. The unfiltered contrast of the raw HAADF-STEM images cannot be directly interpreted as chemical structure. This effect can be compensated by nonlinear filtering algorithm based on Gaussian low-pass filter adding Wiener filter.

3.4.5 DFT calculations of local vacancy geometry

The structural optimisation presented in this work was performed by Dr. Guangchao Li using VASP[7,8] within the projector-augmented wave (PAW).[9] The exchange-correlation interactions were described with the generalised gradient approximation (GGA)[10] in the form of the Perdew, Burke and Ernzernhof (PBE) functional.[11] The Grimme van-der-Waals/dispersion-correction scheme DFT-D3 was added to the GGA energy to account for the long range-interactions.[12] The kinetic energy cut-off for the plane-wave basis set was set to 500 eV. The *k*-points sampling of Brillouin zone used a gamma-centred Monkhorst-Pack scheme of (1×1×1).[13] The convergence criterion for the electronic self-consistency measured by the change in the total energy between successive iterations was set to 10^{-6} eV. Fully relaxed geometries and lattice parameters were obtained by optimizing all atomic positions within a conjugate-gradient algorithm until all the forces acting on the atoms were lower than 0.03 eV $Å^{-1}$.

3.4.6 Resonant Soft X-ray Powder Diffraction on I10

3.4.6.1 Calibration, corrections and procedure

Energy calibration on I10

On I10, it is said that the energy is known to ±1 eV. Energy scans were conducted by the detection of fluorescence emission. The fluorescence point-detector was placed orthogonal to the beam in order to maximise detector-flux. The beam energy is calibrated to the literature values of aluminium and gadolinium reference foils over the K- and M2-edges respectively. The scans were normalised and differentiated, with the energy at which $d^2(I)/d(E)^2 = 0$ taken to be the edge energy.

As is standard on I10, highly clean gadolinium foil was easily placed into the beam by an automated process within the vacuum of the beampipe. The M2-edge appears at 1688.8 eV, which agrees with the literature value of 1688.3 eV: ΔE = +0.5 eV (Figure S3-2). Aluminium foil was wrapped around the carbon-fibre sample holder and placed into the beam by manual alignment using the internal camera. The Al K-edge for the foil reference material is observed at 1558.3 eV, which is a higher discrepancy against the literature value of 1559.6 eV: (ΔE = -1.3 eV). This is attributed to the mixed oxidation state of the foil. The Al^0 edge is somewhat convoluted with the Al^{3+} edge that was also present. The calibration by gadolinium is used herein. All further references to beam energy on I10 have been linearly shifted by -0.5 eV, unless otherwise mentioned.

ASF derivation: transmittance or fluorescence

Theoretical ASF are taken from the database within the Hephaestus software for which the energy interval is 1 eV. Standard literature values for ASF are based on quantum

mechanical calculations for isolated atoms developed by Cromer and Libermann and described by a function of 13 coefficients. These theoretical values are used across the literature, but the assumption coordinated atoms will behave like isolated atoms is not particularly valid for two reasons. Firstly, the incident X-ray can excite core electrons into molecular orbitals which are system dependent with respect to local bonding. And secondly, the interaction of photoelectrons with the surrounding shells of atoms can result in backscattering that can affect the absorption coefficient of the original absorber.

ASF derivation from fluorescence

The fluorescence spectrum were collected from 1519.6 eV to 1640.0 eV. In order to convert the fluorescence to *f*', the scan was calibrated between the known Al *f*' values at a far-below-edge and far-above-edge energies of 1520 eV and 1640 eV, respectively (literature Al^0 ASF energy-shifted by +2.9 eV to experimental Al^{3+} edge) (Figure S3-3). The range of the experimental fluorescence collection was thought to be wide enough to derive the real part of the ASF by the KK transform. All KK transform here was carried out by the web-app provided by ReMagX.[16] Unfortunately, the KK transform of fluorescence *f*'' for this range yields *f*' values that are greatly affected by termination error. Based on the procedure by Evans and Pettifer,[17] the data were linearly extrapolated from the lower and upper limits yielding a *f*' spectrum which approaches and tends away from the edge in a much more expected way.

Geometry correction and 1D patterns

The detector on RASOR is a flat image detector that is processed through two-theta in order to find magnetic peaks. This method is acceptable for I10 because the peak can be centred at the centre of the detector, at which the peak overlaps the two-theta arc. However,

as we are collecting a whole diffraction pattern, we require the use of the entire detector, which introduces angular error.

Flat image detectors are commonly used for powder diffraction, but are usually orientated perpendicular to the propagating beam, and centred at the through-beam in order to sample the entire Debye-Scherrer cone. This is useful for counting statistics, observing texture, and angular calibration. However, when a small flat detector is processed along the 2θ arc, only one row of pixels with respect to the y-axis (beam axis) can be said to intersect the arc, with the remaining rows deviating from the arc as a tangent. The assumption that the length of the detector covers the equivalent length of the 2θ arc is incorrect and results in assignment of intensity at too high or low angle, proportionate with the distance from the y-centre of the detector by $\tan(\Delta 2\theta)$. This introduces non-negligible angular error but can be minimised and corrected.

Geometric artefacts from the flat detector can be minimised by placing the detector as close to the sample in the z/beam axis as possible, which minimises the geometric deviation from the two-theta arc, as well as consolidating reflections closer to the centre, and increasing the Q-space collected. Though placing the detector very close to the sample can increase accessible Q-space, the perpendicular configuration is physically limited to collecting photons scattered between and not including 0° and 90°. For this experiment, many of the reflections of interest are above 90° (lower d-spacing imparts greater structural accuracy, and higher angle imparts lower contribution from the non-dispersive atomic scattering factors); these angles are geometrically impossible to collect using a perpendicular flat detector.

Following geometry correction, the frames were concatenated. The 2D data were linearly collapsed by integration with respect to the azimuthal angle to yield 1D patterns. The curvature of the Debye-Sherrer cone can be seen in the *x*-axis (conventionally towards the centre of the synchrotron). As the through-beam, and hence the zero-point is not observed in every frame, the azimuthal angle was calibrated to the expected lattice parameters from the high-resolution data. Though the detection configuration is not optimised for the scattering geometry, corrections can be made. This correction noticeably improved peak shape and resolution.

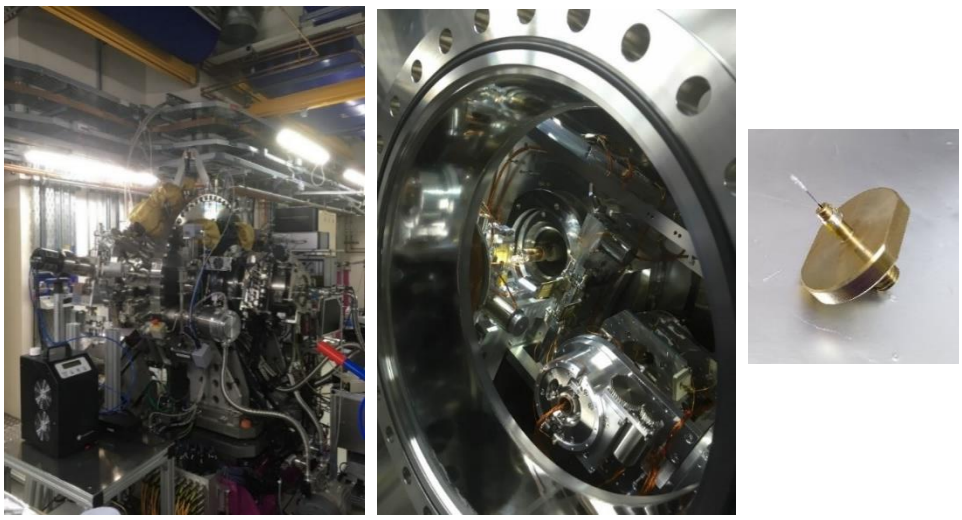


Figure 3-2. RASOR end-station on I10, DLS. Inset shows bespoke sample holder for powder samples on I10.

Procedure optimisation

Without previous experience of collecting full powder patterns on I10, several mistakes were made in the data collection. Firstly, in the initial beamtime, initial scans suffered from poor particle averaging due to unoptimised exposure time and sample spinning. Subsequently, the carbon-fibre rod was rotated through 90° in the ω-axis for each 10° frame.

The angular range of the detector at a distance of 138 mm is 10° 2θ. The detector was initially processed along the 2θ arc continuously, yielding averaged intensity with respect to angle. However, frequent failure of the detector motor resulted in many incomplete patterns, prompting a change of procedure on following visits.

Additionally, problems were encountered with the beam energy. It was found that the energy readback from the monochromator had a large discrepancy to the input values, occasionally reading 100s of eV from the intended value. However, reflections did appear in approximately their expected positions. Hence the error is in the monochromator readout rather than the beam energy. This was attributed to faults with the monochromator motor as I10 is not optimised for taking beam from the third harmonic (>1800 eV), and is not carried out frequently. Risks associated with switching harmonics were not considered when planning the experiment, and therefore not minimised; energies at Al and Si K-edges were even alternated occasionally. Subsequent data collections were planned to minimise monochromator movement.

3.4.6.2 Experimental

High-resolution data-collection on I11

Far-from-edge vacuum pattern were collected at I11, DLS. Wavelength and zero-error were refined to 0.8265219 Å and -0.00008°, respectively. A pristine ZSM-5 sample was scanned at room temperature at 10^{-6} bar using the MAC detector.

Sample mounting

The sample was required to be coated on a carbon-fibre rod using an adhesive on a bespoke brass sample-holder designed in collaboration with the mechanical workshop at

DLS (Figure 3-2). The adhesive was required to yield minimal residue in high vacuum, so several gels were trialled due to their minimal solids-content. The carbon-fibre rod was dipped in various gels, then the Z38 zeolite, left under dynamic vacuum for 1 hour, then mounted on I11. Kapton and stainless-steel rods were also used, but did not offer enough rigidity, or adhesion, respectively. Carex exhibited no impurities and the best background, hence was chosen as the gel adhesive. Additional to its good properties for diffraction, Carex also has the advantage of being silicon-free (cosmetic hand-creams such as E45 often contain silicone), which is crucial for reducing absorption over the silicon absorption edge. Carex is also higher in ethanol content and less viscous, which aided sample adhesion and vacuum pump-down times.

The holder was only handled with gloves to avoid contaminating with grease, which would slow/limit the vacuum. The chamber was evacuated to $<10^{-6}$ mbar over three hours. Within the chamber, the fibre was orientated in the horizontal plane of the beam. Alignment was carried out using an internal camera, then with respect to diffracted intensity. The beam dimensions are approximately 0.2 mm × 0.2 mm.

Data collection

The detector is small image detector (10×10 cm), which must be cryo-cooled before data collection, and warmed before exposing to atmospheric conditions. It was moved in 10° increments from 30°-150° with an angular resolution of 0.006°. Angular overlap of 1° between frames was collected in order to facilitate data concatenation. For each position, the sample was rocked in omega through 90° in 5° steps. For each step, data were collected for 5 s. Hence for a given detector position, the sample was exposed for 90 seconds. Each full-pattern scan requires approximately 2 h.

3.5 References

(1) Thompson, S. P.; Parker, J. E.; Potter, J.; Hill, T. P.; Birt, A.; Cobb, T. M.; Yuan, F.; Tang, C. C. Beamline I11 at Diamond: A New Instrument for High Resolution Powder Diffraction. Rev. Sci. Instrum. 2009, 80 (7), 075107. https://doi.org/10.1063/1.3167217.

(2) Tiesinga, E.; Mohr, P.; Newell, D.; Taylor, B. The 2018 CODATA Recommended Values of the Fundamental Physical Constants https://physics.nist.gov/cuu/Constants/index.html (accessed 2020 -10 -22).

(3) Kawaguchi, S.; Takemoto, M.; Osaka, K.; Nishibori, E.; Moriyoshi, C.; Kubota, Y.; Kuroiwa, Y.; Sugimoto, K. High-Throughput Powder Diffraction Measurement System Consisting of Multiple MYTHEN Detectors at Beamline BL02B2 of SPring-8. Rev. Sci. Instrum. 2017, 88 (8), 085111. https://doi.org/10.1063/1.4999454.

(4) Coelho, A. A. TOPAS and TOPAS-Academic: An Optimization Program Integrating Computer Algebra and Crystallographic Objects Written in C++. J. Appl. Crystallogr. 2018, 51 (1), 210–218. https://doi.org/10.1107/S1600576718000183.

(5) Momma, K.; Izumi, F. VESTA 3 for Three-Dimensional Visualization of Crystal, Volumetric and Morphology Data. J. Appl. Crystallogr. 2011, 44 (6), 1272–1276. https://doi.org/10.1107/S0021889811038970.

(6) Arblaster, J. W. Crystallographic Properties of Platinum. Platin. Met. Rev 1997, 41 (1), 12.

(7) Kresse, G.; Furthmüller, J. Efficient Iterative Schemes for Ab Initio Total-Energy Calculations Using a Plane-Wave Basis Set. Phys. Rev. B 1996, 54 (16), 11169–11186. https://doi.org/10.1103/PhysRevB.54.11169.

(8) Kresse, G.; Furthmüller, J. Efficiency of Ab-Initio Total Energy Calculations for Metals and Semiconductors Using a Plane-Wave Basis Set. Comput. Mater. Sci. 1996, 6 (1), 15–50. https://doi.org/10.1016/0927-0256(96)00008-0.

(9) Blöchl, P. E. Projector Augmented-Wave Method. Phys. Rev. B 1994, 50 (24), 17953–17979. https://doi.org/10.1103/PhysRevB.50.17953.

(10) Perdew, null; Burke, null; Ernzerhof, null. Generalized Gradient Approximation Made Simple. Phys. Rev. Lett. 1996, 77 (18), 3865–3868. https://doi.org/10.1103/PhysRevLett.77.3865.

(11) Perdew, J. P.; Ernzerhof, M.; Burke, K. Rationale for Mixing Exact Exchange with Density Functional Approximations. J. Chem. Phys. 1996, 105 (22), 9982–9985. https://doi.org/10.1063/1.472933.

(12) Grimme, S.; Antony, J.; Ehrlich, S.; Krieg, H. A Consistent and Accurate Ab Initio Parametrization of Density Functional Dispersion Correction (DFT-D) for the 94 Elements H-Pu. J. Chem. Phys. 2010, 132 (15), 154104. https://doi.org/10.1063/1.3382344.

(13) Monkhorst, H. J.; Pack, J. D. Special Points for Brillouin-Zone Integrations. Phys. Rev. B 1976, 13 (12), 5188–5192. https://doi.org/10.1103/PhysRevB.13.5188.

(14) Ellis, I. T.; Wolf, E. H.; Jones, G.; Lo, B.; Meng-Jung Li, M.; York, A. P. E.; Edman Tsang, S. C. Lithium and Boron as Interstitial Palladium Dopants for Catalytic Partial Hydrogenation of Acetylene. Chem. Commun. 2017, 53 (3), 601–604. https://doi.org/10.1039/C6CC08404D.

(15) Lin, W.-C.; Wu, S.; Li, G.; Ho, P.-L.; Ye, Y.; Zhao, P.; Day, S.; Tang, C.; Chen, W.; Zheng, A.; W. Lo, B. T.; Tsang, S. C. E. Cooperative Catalytically Active Sites for Methanol Activation by Single Metal Ion-Doped H-ZSM-5. Chem. Sci. 2021, 12 (1), 210–219. https://doi.org/10.1039/D0SC04058D.

(16) https://remagx.org/KK.html.

(17) Evans, G.; Pettifer, R. F. CHOOCH: A Program for Deriving Anomalous-Scattering Factors from X-Ray Fluorescence Spectra. J. Appl. Crystallogr. 2001, 34 (1), 82–86. https://doi.org/10.1107/S0021889800014655.

Chapter 4: Hydrogen evolution by photocatalytic water-splitting over nitrogen-doped TiO_2: oxygen vacancies and the structure-activity relationship

4.1 Abstract

Nitrogen-doped TiO_2 is well-known to be an excellent photocatalyst. As well as widening absorption to visible light, nitrogen dopants promote the formation of oxygen vacancies and therefore trapped electrons that can facilitate proton reduction. We have tested a range of TiO_2 materials (rutile, anatase and mixed phases commercial P25) with and without nitrogen-doping, for hydrogen evolution and shown that this activity only becomes significant at temperatures above 200°C. By VT-SXPD, an unusual anisotropic thermal expansion of anatase has revealed a structure-electronic-performance relationship between nitrogen doping, oxygen-vacancy formation, and photocatalytic activity. By DFT calculations, local reorganisation around oxygen vacancies are shown to agree with the bulk distortion and anisotropy. Vacancies are shown to migrate towards the sub-surface under dynamic equilibrium.

For highly doped anatase, a new cubic titanium oxynitride phase is identified as an inadvertent side-product. This additional component present in high activity catalyst powders provides important information for the fundamental understanding of the excellent photocatalysis using visible light.

4.2 Introduction

4.2.1 Agile ammonia synthesis and analytical context

The reactants for the Haber-Bosch process, and thus the AAS, are dinitrogen and dihydrogen. Hydrogen production at low cost is much more challenging than nitrogen, due to its reactivity and absence in natural environments. Here, we investigate hydrogen evolution by photocatalytic water-splitting over TiO_2 materials. These materials have been doped with the light-element nitrogen in order to change the electronic properties, with regard to bandgap alteration, charge-carrier separation and lifetime, and oxygen-vacancy formation energy, all of which are introduced below.

In this chapter, analytical problems of this system include the biphasic mixture containing *$I4_1/amd$* anatase and *$P4_2/mnm$* rutile, the presence of both interstitial and substitutional nitrogen-doping, the importance of host-guest electron transfer, and significant focus on defects and vacancies. In particular, the identification of oxygen vacancies are of great mechanistic importance for catalysis, as well as an analytical conundrum as low-scattering sites. Characterisation of the impact of defects on the framework is required, in particular the metal coordination and electronics, the effect on performance, and the level of control we can have over the abstraction and subsequent defect reorganisation.

This work was led by the author and can be found as a published article by Foo et al. entitled 'Characterisation of oxygen defects and nitrogen impurities in TiO_2 photocatalysts using variable-temperature X-ray powder diffraction'.[1] This chapter has largely been adapted from the published article.

4.2.2 Photocatalysis

The absorption of light by the promotion of an electron from the valence band (VB) into the conduction band (CB), leaves a hole in the VB (Equation 4-1). These charge-carrier species have associated potentials that are able to drive charge transfer and thus chemical reaction.[2] The hole can perform oxidation, while the electron can perform reduction (Figure 4-1).

$$h\nu \rightarrow e^- + h^+$$

Equation 4-1. General charge carrier formation in TiO_2.

Crucial to the performance of a photocatalyst is the ability to separate the holes and electrons from recombination; the reverse of Equation 4-1 results in the emission of energy as heat or radiation, which can be considered a loss. Often the separation is performed by a heterojunction such as a metal or metal oxide decoration. The vectorial charge transfer down thermodynamic gradients allows for the charge-carriers to be physically separated, thus inhibiting recombination, and promoting interfacial charge transfer at the surface for catalysis.[3]

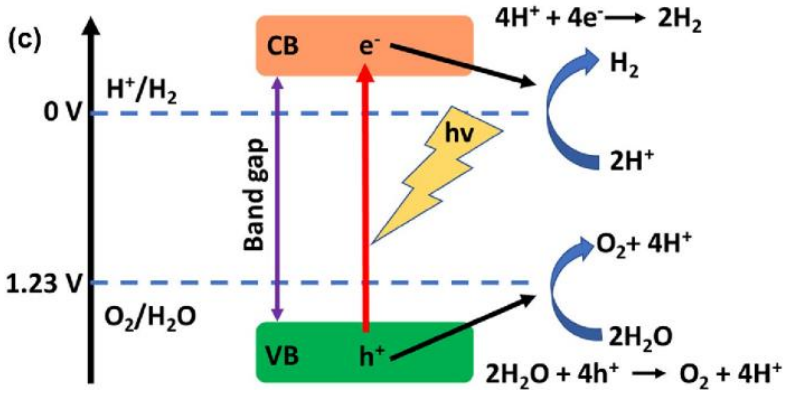


Figure 4-1. Schematics of photocatalysis in the context of water-splitting. Reproduced from reference [4].

4.2.3 TiO_2 as photocatalyst

TiO_2 materials have use in a wide range of photocatalytic applications including the hydrogen-evolution reaction,[5–8] disinfection,[9] pollutant degradation,[10,11] and dye-sensitised photocatalysis.[12,13] The CB of TiO_2 is lower in energy than the reduction potential of H^+/H_2, and its VB is more positive than O_2/H_2O.[4] The dominant photoexcitation in TiO_2 is between the O 2p and Ti 3d. It is widely studied due to its strong photo-responsivity, low cost, natural abundance, low toxicity, water insolubility, and high chemical and thermal stability.

TiO_2 was first applied as a photocatalyst in 1972 by Fujishima and Honda who demonstrated a photoelectrochemical (PEC) water-splitting system.[14] They showed that no external current was required to split water using rutile and platinum electrodes in aqueous electrolyte (Equation 4-2):

$$\text{Rutile anode: } H_2O + 2\ h^+ \rightarrow \tfrac{1}{2}\ O_2 + 2\ H^+$$

$$\text{Pt cathode: } 2\ H^+ + 2\ e^- \rightarrow H_2$$

Equation 4-2: Fujushima and Honda's water-splitting.[2]

By combining Equation 4-1 and Equation 4-2, the general water-splitting over TiO_2 is yielded.

$$H_2O + h\nu \rightarrow \tfrac{1}{2}\ O_2 + H_2$$

Equation 4-3. General photocatalytic water-splitting.

4.2.3.1 TiO_2 polymorphs

There are many polymorphs of TiO_2, including anatase (A), rutile (R) and brookite (Figure 4-2), which all exist naturally in minerals. There is also rich phase-variation across

temperature and pressure:[15] monoclinic *Pbmm* tungsten bronze (TiO_2(B))[16], monoclinic *P2₁/c* ZrO_2 baddeleyite (TiO_2(MI))[17], orthorhombic *Pbcn* columbite (TiO_2(OI))[18], orthorhombic *Pnma* cotunnite TiO_2(OII)[19], cubic $Fm\bar{3}m$ (TiO_2(C1))[20–22]. This wide range of polymorphs will be revisited during the phase identification of a new titanium oxynitride.

Anatase contains only one inequivalent titanium and one inequivalent oxygen site. However, the bonds between them are inequivalent, with each oxygen atom being bound equatorially to two titanium atoms (*ab*), and axially to another (*c*). This nomenclature, which is usually associated with discrete coordination chemistry, is used in an influential report by Di Valentin et al.[23], and will be used during this chapter. The wide varieties of syntheses and morphologies of TiO_2 are beyond the scope of this thesis.[6–8,24–28]

4.2.3.2 Polymorph dependence

Rutile, and anatase are semi-conductors (rutile: 3.0 eV, anatase: 3.2 eV).[2] Anatase exhibits greater photocatalytically activity due to a higher Fermi level and wider bandgap.[2] In anatase, charge-carriers have longer lifetime than in rutile, as well as deeper and steeper band-bending, which leads to increased concentration and spatial separation of charge-carriers: holes at the surface and electrons deeper in the lattice.[24,29] The electronic factors that contribute to the photocatalytic activity of TiO_2 have been researched for some years, but the underlying mechanisms are still not clear.

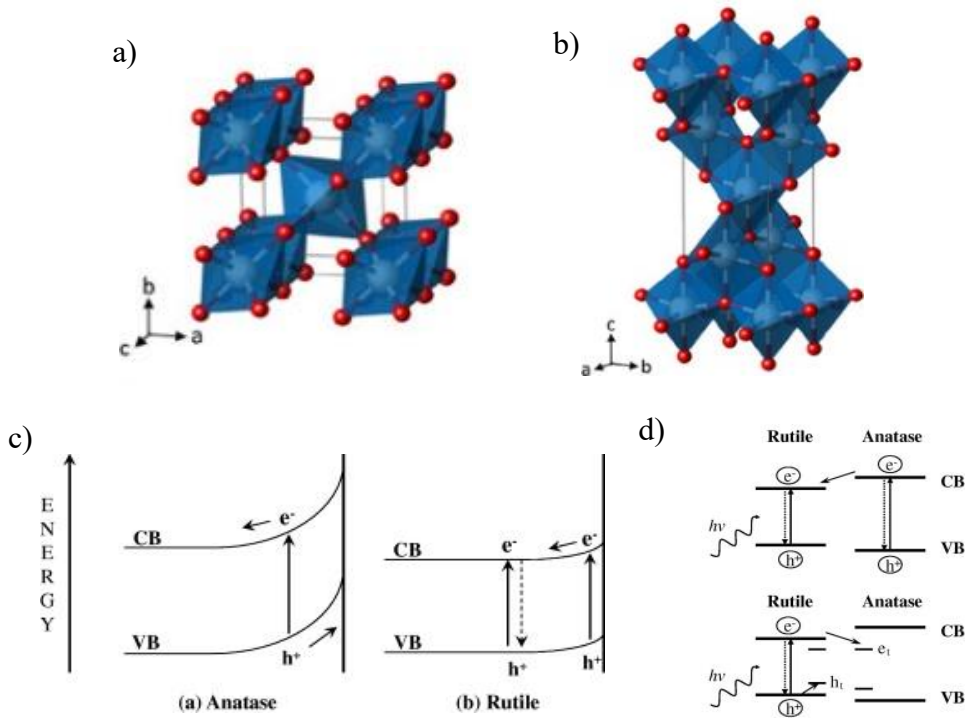


Figure 4-2. (a,b) Displayed unit-cells of rutile and anatase. Difference in electronic configuration of anatase and rutile.[24] (c) Band bending, and (d) variable vectorial charge-carrier separation by mid-gap defect trap sites.

Charge carrier separation is also enhanced in mixed-phase anatase and rutile TiO_2, as shown by the correlation between connectivity and activity.[30,31] The heterojunction results in band bending and vectorial charge transfer (Figure 4-2c,d). Synergistic relationship is commonly observed in the superior performance of commercially available Degussa P25 (herein referred to simply as P25), which is formed by flame hydrolysis of $TiCl_4$ in hydrogen and oxygen.[24] It has been shown to exclusively trap holes at the surface, while electrons are trapped within the lattice.[32] These defects at the solid-solid interface are commonly understood to be highly active, while ordered facets are entirely inactive.[33] In this work P25 is investigated along with pure phase anatase and rutile materials.

4.2.3.3 Oxygen vacancies: increasing number of charge carriers

Oxygen vacancies are crucial to the photoactivity of TiO_2 materials. The extraction of neutral oxygen atoms results in lattice reduction and electron transfer to the Ti band structure forming excited Ti^{3+} species.[34] The donor states lie below the CB as a localised trap for unpaired electrons that can undergo visible-light transitions, hence forming an n-type semiconductor which promotes water oxidation (Figure 4-3).[35,36] Despite increasing photo-efficiency and charge-carrier generation, these sites are also reported to be recombination centres.[37]

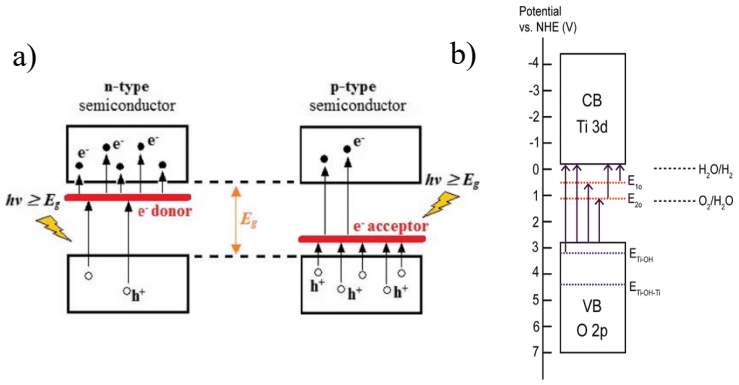


Figure 4-3. (a) Schematic of n- and p-type semiconductors.[38] (b) Localised defect sites below the CB from oxygen vacancies and below the VB from hydrogen disorder.[5]

It has been shown that the polymorph and exposed facets of TiO_2 materials significantly affect the concentration of total oxygen vacancies.[39] The formation of electronic defects, such as interstitial dopants and vacancies with unpaired electrons, can be observed by EPR measurements.[40,41] Proportionate to photocatalytic activity, the anatase (101) surface supports a very high bulk concentration, which indicates oxygen vacancies beyond the surface; meanwhile rutile (110) and anatase (001) have very low concentrations of total vacancies. This finding was further supported by interrogating the energies of various oxygen-vacancy sites by DFT calculations.[42] EPR also shows that surface oxygen vacancies

are prone to oxidisation in air,[27] by being filled by oxygen from O_2 and H_2O over time, causing the delocalisation of the electrons and a similar inert activity to visible light to pristine TiO_2. They also showed that re-calcining the N-TiO_2 in a N_2 atmosphere regenerated surface oxygen vacancies.[43] Treatment by reducing atmosphere such as hydrogen gas results in the significant increase in the concentration of oxygen vacancies.[5,35] These materials are often black or dark blue, due to such strong visible absorption. Moderately reduced TiO_2, so called grey TiO_2, is reported to be more catalytically active than highly reduced black TiO_2.[27]

4.2.3.4 Light-element doping: reducing the bandgap

The wide bandgap of TiO_2 anatase limits its absorption of solar irradiance to only the UV region, which comprises 3-5% of solar energy.[2,3] Introducing dopant atoms into the TiO_2 framework can reduce the band-gap and enhance the utilisation of visible light.[34,37,40,44] Cation- or anion-doping results in isolated electronic states in the mid-gap, which act as electron/hole traps. This can be achieved using metal ions, in which the redox of the dopant can form charge-carriers.[45] But these dopants often form deep lying localised d-states and act as recombination centres.[44] Herein only light-elements will be considered.

Substitutional carbon doping can also be achieved.[6] Choi et al. even showed that carbon incorporation can be achieved during the TiO_2 syntheses in a one-pot process using titanium butoxide.[46] They emphasise that the doping can occur unintentionally from the organic precursor. Similarly, nitrogen can be incorporated in-situ by a one-step process.[25,28] Nitrogen is often incorporated in a post-synthesis ammonia treatment, which is the method used in this work.[8,37,47,48] In-situ doping will also be discussed further in reference to the palladium-lithium system in Chapter 5. Additionally, the focus of Chapter 6 on zeolite

characterisation will involve arguments of the effect of synthesis dynamics and nucleation on aluminium siting.

4.2.4 Nitrogen-doped TiO_2

Nitrogen-doping TiO_2 enhances the presence of structural defects and reduces the band-gap for photo-excitation, enabling the absorption of the plentiful visible-light region of the solar-irradiance spectrum, thus resulting in enhanced photocatalytic performance. The activity originates from a sub-band-gap transition rather than a decrease in the band-gap.[48,49] Asahi et al. showed nitrogen dopants to form localised states below the CB that decrease the band-gap but are sufficiently reducing to perform hydrogen-evolution H^+/H_2O.[44] Wang et al. also showed that nitrogen-doping results in a shallow isolated N 2p state that can be used for visible-light transitions and reduction of O_2 or H^+ to superoxide radicals or hydrogen gas, respectively.[37] This transition composes a small proportion of UV transitions, which are dominated by excitation directly from the delocalised VB. The photo-generated holes in the N 2p are too localised to participate significantly to the photoactivity, but act as recombination centres, along with the localised Ti^{3+} mid-gap states.

4.2.4.1 Substitutional or interstitial

In pristine TiO_2 the oxygen-vacancy formation energy is 4.2 eV, but substitutional nitrogen at oxygen sites can localise and stabilise the excess electrons, decreasing the formation energy dramatically to 0.6 eV.[37,40,50]

$$TiO_2 \rightarrow TiO_{2-x} + xV_O + \tfrac{1}{2}\, xO_2 \qquad 4.2\ \text{eV}$$

$$TiO_{2-y}N_y \rightarrow TiO_{2-y-x}N_y + xV_O + \tfrac{1}{2}\, xO_2 \qquad 0.6\ \text{eV}$$

Equation 4-4. Oxygen vacancy formation in TiO_2 and substitutional N-TiO_2.[40]

Similarly, Asahi et al. showed by calculations that substitutional doping forms the most desirable electronic structure due to the mixing of dopant N 2p with the framework O 2p,[44] resulting in shallow localised states above the anatase VB (Figure 4-4). However, in rutile substitutional doping causes a lowering of the O 2p and an overall blueshift.[23] Elsewhere, Hoang et al. show substitutional nitrogen and Ti^{3+} to be wholly responsible for the increased activity of N-TiO_2.[8]

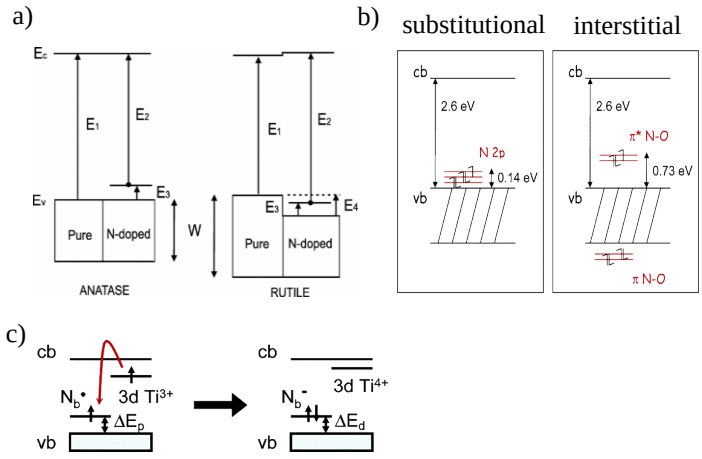


Figure 4-4. Effect of nitrogen doping on the electronic structure of (a) anatase and rutile,[23] (b) substitutional N^{2-} and interstitial N in anatase,[40] and (c) sub-gap transition from reduced Ti^{3+} electron trap to N_b•, forming diamagnetic N_b^-.[34]

Interstitial nitrogen also reportedly enhances catalysis. Diwald et al. used a post-synthesis ammonia treatment to decrease the bandgap to ~2.4 eV, which they attribute to interstitial nitrogen. They also identify a substitutional N^{2-} species at the oxygen site, which is catalytically inactive.[47] It has been reported that interstitial nitrogen increases the concentration of oxygen vacancies, while substitutional nitrogen decreases the concentration.[51]

Clearly there are conflicting reports of the electronic effects of nitrogen doping, yielding an overall ambiguous photocatalytic mechanism and structure-activity relationship of N-TiO_2 materials. Thus, there is no complete understanding of the structure-activity relationship. It is beyond the scope to discuss in any more depth aspects of charge-carrier lifetimes and recombination, particle morphology, surface interaction and mechanisms, and catalytic configuration.

4.2.5 Nitrogenation to titanium nitride

Treating anatase powder with ammonia at elevated temperature has been experimentally shown to yield full conversion to cubic titanium nitride $Ti^{+3}N^{-3}$, exhibiting the $Fm\bar{3}m$ rock-salt structure. The material is widely recognised as a material for bio-electrical components,[52] but has also been researched as a photocatalyst, particularly due to its broad absorption in the visible region.[53–55] Instead of total nitridation of TiO_2, there are several reports of the formation of titanium oxynitride for application in photocatalytic and photonic materials.[56] Though phase identification for complex multi-phasic TiO_2 powders yielded by ammonia treatment have been reported, the structures of titanium oxynitride remain largely inferred and uncharacterised.[57,58] Do et al. report the tuneable non-stoichiometric composition of titanium oxynitride, TiN_xO_y, between the end-phases of pure TiO_2 and TiN. The lattice parameter of the cubic phase is noted as being intermediate between the two end-composition $Fm\bar{3}m$ phases of titanium(II) oxide (4.185 Å) and titanium nitride (4.241 Å).[59,60] Some have used this observation to apply the linear Vegard's law and assume substitutional doping to yield values for composition.[59] Despite this, there are no complete structure solutions for the oxygen site within the nitride structure.

4.2.6 Agile ammonia synthesis

We have previously reported that oxygen vacancies formed during nitrogen-doping at elevated temperature greatly contribute to improved visible-light absorption and act as the surface active sites, leading to enhanced photocatalytic water-splitting activities and quantum efficiencies.[43] Though elevated temperatures may seem impractical and cost-inefficient, we reported a water-splitting system that is completely driven by visible-light, in which high temperature is achieved by an optical floating-zone light furnace. The provision of sustainable hydrogen using zero electrical power is an excellent candidate for the self-contained AAS pathway.[61]

4.2.7 Evaluation of characterisation techniques

As with all heterogeneous catalysis, photocatalytic water-splitting over TiO_2 is a surface phenomenon involving the direct interaction of water molecules with the surface. Bulk and sub-surface species may be involved in charge-carrier generation or trapping, but ultimately the pertinent species lie at the interface, where coordination is highly disordered. Thus, only surface charge-carriers are directly involved in the proton reduction and hydroxide oxidation. However, due to the reactivity and transience of such states, the direct identification and observation of the amorphous surface phenomena is difficult. STEM is a good method to observe surface defects.[62] Meanwhile total defects (irrespective of depth) can be characterised by resonant photoemission spectroscopy (RESPES) and X-ray absorption spectroscopy (XAS). The precise nature of the species and reorganisation that form active surface sites is desired. For example, it is known that Ti^{3+} weakens oxygen coordination.[26]

Though these reports all highlight the nature and importance of surface structural changes, they make no reference to the parent bulk structure. It is well-known that the

movement of charge-carriers involves the bulk, in particular oxygen vacancy diffusion from the surface to the sub-surface and bulk.[7] However, there is still a lack of detail with respect to the structure-activity relationship of this dynamic equilibrium. Early reports of TiO_2-based photocatalysts concede that the enhanced photocatalytic activity cannot be directly correlated to changes in bulk structure by crystallographic methods, as such small changes cannot be easily resolved.[44] But both surface and bulk characterisation are crucial for finally understanding N-TiO_2 photocatalysis. XRD is a well-known technique for monitoring changes in TiO_2, but often suffers from a lack of chemical hypothesis related to photocatalysis, and in particular interrogation of the effect of defects and impurities.[63,64]

4.2.8 Aims of investigation

It is aimed to nitrogen-dope various TiO_2 materials in order to achieve advantageous bang-gap narrowing and decrease in oxygen vacancy formation energy. We then aim to provide structural characterisation of the nitrogen dopant, oxygen-vacancy formation, and photocatalytic mechanism, which can inform further catalyst development and fundamental understanding: namely which phases and species are relevant to the photocatalysis and the fundamental underlying principles for the strong photocatalytic effect at different concentrations of impurities and at different temperatures.

Characterisation of the nitrogen-doping itself involves determining its location (interstitial or substitutional), total concentration, homogeneity, and distribution with respect to depth. Structural characterisation by SXPD was desired for nitrogen-doped TiO_2 (N-TiO_2), which had been previously shown by our group (6746 μmol g^{-1} h^{-1} at 270°C)[43,65] to be a highly efficient and effective photocatalyst in the hydrogen evolution reaction by water-splitting.

Initially, this investigation was intended to be directed towards an in-operando SXPD experiment on I11, in which the crystal structure of the material would be monitored during photocatalysis, i.e. in the presence of high temperature and pressure in the presence of water. Crystalline structural behaviour would then be easily correlated to catalytic performance. However, the creation of an appropriate sample environment proved difficult. Foregoing the in-operando experiment, a simple VT-SXPD was aimed to reveal high temperature behaviour that can still be correlated to oxygen vacancies by electronic and catalytic characterisation.

4.2.8.1 Outline

Electronic techniques were used in order to define the nature of the dopant, its concentration, and the effect on oxygen vacancies in variously rutile, anatase, and P25 (commercial mixed phase) materials. Investigation into the temperature dependence of photocatalytic activity are then presented (experiments and analysis was performed by Yiyang Lee). An in-depth structural study of VT-SXPD was carried out to correlate bulk structural behaviour to electronic properties and the enhanced catalytic performance.

4.3 Results and discussion

4.3.1 Nitrogen doping

An initial study was carried out on the commercially-available P25 TiO_2 powder, which is stated to consist of anatase and rutile in a 75:25 mass ratio. Materials were nitrogen-doped in NH_3 flow at 550°C, 600°C, and 620°C: labelled P1, P2, and P3. Analogous monophasic anatase and rutile materials were also nitrogen doped in this way, yielding A0-A3 and R0-R3. The analysis by TEM and HAADF-STEM micrographs indicates the successful formation of TiO_2-based nanoparticles by the characteristic (101) lattice spacing of anatase TiO_2 (0.35 ± 0.02 nm) (Figure 4-5).

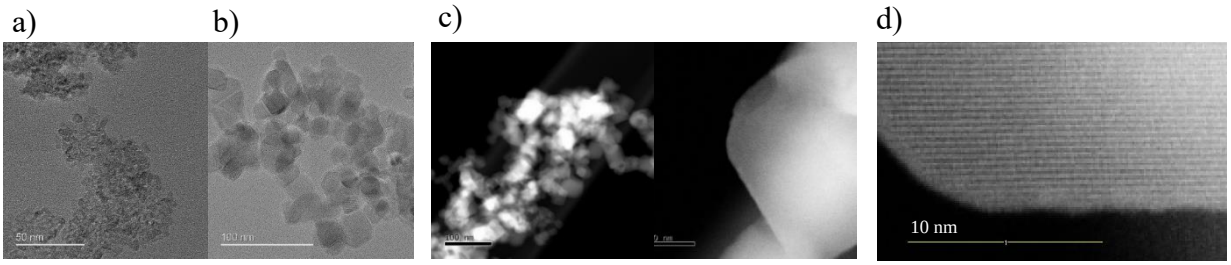


Figure 4-5. TEM micrographs showing typical morphology of (a) A3, and (b) P3. (c, d) HAADF-STEM micrographs of P3.

Laboratory-configuration XRD confirms the P25 powders to be biphasic anatase/rutile mixtures, though at a greater anatase composition than expected of ~85:15 (Figure S4-1a). This was also seen by Raman spectroscopy, in which the characteristic Raman-active vibrational modes of anatase at 144, 196, 396, 544, and 636 cm^{-1} were observed, but the characteristic rutile modes (448 or 612 cm^{-1}) were weak (Figure S4-1b).[66,67] However, the This does not change upon nitrogen-doping. The phase composition and crystallinity are also largely unchanged by XRD, showing that no major crystalline structural change is occurring. The patterns for the monophasic anatase samples show that the

crystallinity is improved, observed as increasing intensity and narrower peaks (Figure S4-1c). This is attributed to sintering at high temperature, also observed by Zhang et al.[68]

The presence of nitrogen was shown by XPS. The expected titanium signal was observed as two peaks corresponding to Ti $2p_{3/2}$ and Ti $2p_{1/2}$ at 458 eV and 464 eV, respectively (Figure 4-6), which is in agreement with Ti^{4+} in TiO_2.[51] For P3, there is a shift of the signals to higher energy, which is evidence of the formation of Ti^{3+}, which occurs at 457 eV. Likewise, the observed O 1s peak at 530 eV is characteristic of oxygen in the TiO_2 lattice and N-doped TiO_2.[40,41]

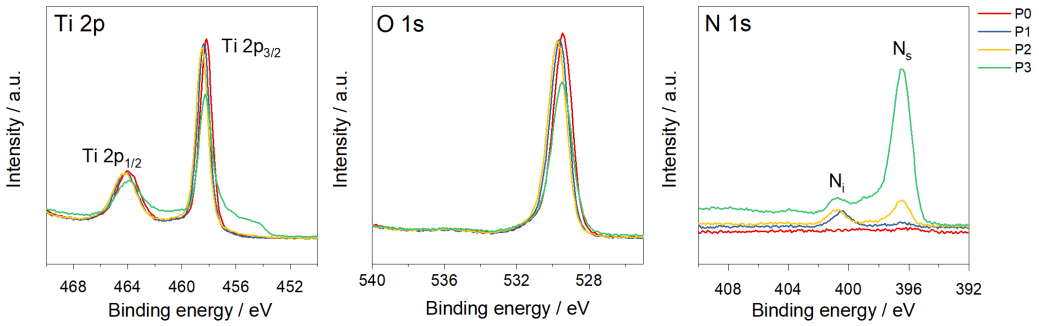


Figure 4-6. XPS spectra of N-P25 materials treated with ammonia at different temperatures.

The increasing N 1s signal also showed the concentration of nitrogen to be non-linearly proportionate to ammonia-treatment temperature (Figure 4-6). This compositional information is also shown by ICP-MS. However, these values are consistently higher than those derived from XPS. The small discrepancy (Figure 4-7a) is attributed to differences in the penetration depth of the techniques; XPS only probes the surface, whereas ICP-MS reflects total composition. Hence, the discrepancy indicates non-homogeneous elemental distribution with respect to depth, namely lower nitrogen composition at the surface.

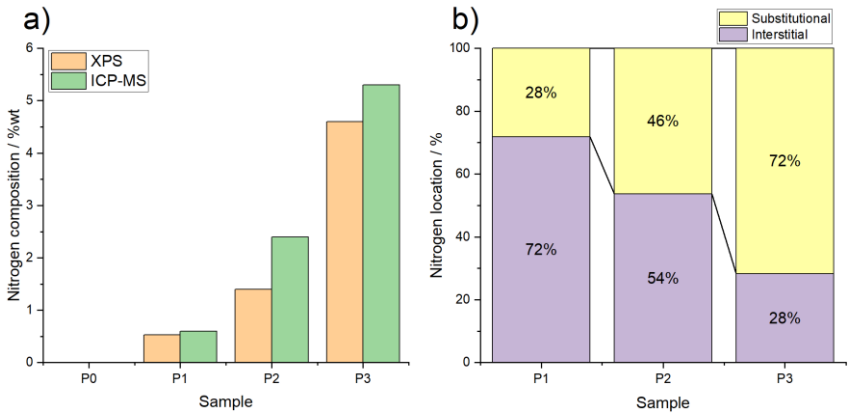


Figure 4-7. (a) Nitrogen composition of P25 samples by XPS and ICP-MS. (b) Relative composition of substitutional nitrogen and interstitial nitrogen.

The nature of the doping can be determined from XPS also. There are clearly two N 1s peaks at 396 eV and 401 eV (Figure 4-6), which can be assigned to nitrogen substitutionally doped at oxygen sites (N_s), and interstitially doped nitrogen atoms in the lattice (N_i), respectively.[40,41] It is known that synthesis precursors, conditions, and stoichiometry have significant impact on the resulting N_i:N_s ratio.[28,69]

Sample	NH_3 treatment temperature / °C	Nitrogen composition by XPS / %wt	N_i / %	N_s / %	N_i : N_s ratio	Nitrogen composition by ICP-MS / %wt	Band-gap by Tauc plot / eV
P0	N/A	0	N/A	N/A	N/A	0	3.18
P1	550	0.53	71.8	28.2	2.54	0.6	2.27
P2	600	1.4	53.7	46.3	1.16	2.4	1.75
P3	620	4.6	28.2	71.8	0.39	5.3	1.22

Table 4-1. Tabulated compositional and electronic characterisation.

From pristine P0 to P1, ammonia treatment at (550°C) is shown to result in 0.5%wt nitrogen-doping; this occurs primarily at the interstitial site (N_i:N_s = 2.54) (Figure 4-7b). For P2 (600°C), the signal for substitutionally-doped nitrogen increases whilst the interstitial signal remains approximately unchanged (N_i:N_s = 1.16). For P3 (620°C), there is a

significantly greater nitrogen composition of 4.6%wt, which significantly favours occupancy of substitutional sites (N_i:N_s = 0.39). This is in agreement with the literature, in that substitutional doping occurs at higher temperatures.[69] Thus, the nitrogen-doping is shown to be successful.

As has long been known, increasing the nitrogen content in anatase reduces the band-gap, resulting in more absorption of the visible spectrum. This has been shown here by UV-vis diffuse reflectance spectroscopy. The pristine P0 sample exhibits an absorption edge at 390 nm, but nitrogen-doping results in an additional broad edge at 500 nm, which is observed for samples P1, P2, and P3 (Figure 4-8a). Higher temperature ammonia treatment leads to significant broadening, shifting the additional absorption edge to the visible and infrared regions.

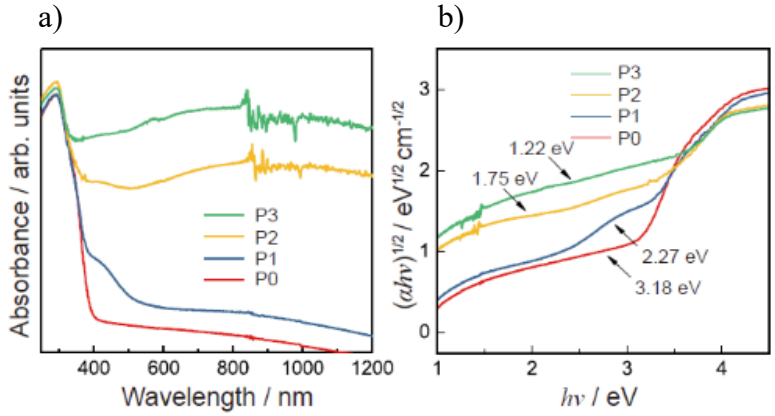


Figure 4-8. (a) UV-vis absorption spectra, (b) corresponding Tauc plots and average band-gaps.

Tauc plots can be used to yield a discrete value for the direct band-gap. From 3.18 eV in P0, nitrogen-doping reduces the band-gap to 1.22 eV in the highest nitrogen-content P3 sample (Figure 4-8b). The reduced band-gap makes it easier to form charge-carriers, and also leads to greater quantum efficiency by the broad absorption range over more of the solar

spectrum. This wavelength of the absorption lengthens from 390 nm to 1000 nm, resulting in near-complete absorption of the visible spectrum (380-740 nm); P2 and P3 even show quite strong absorption in the near-IR region (700-1000 nm). This was also seen by a colour change from white pristine samples to the darker, grey of the intermediate P1 and P2 samples, and black P3 samples. The increase in total absorption of the N-doped TiO_2 is directly attributed to the photo-excitation of colour centres and defects from localised mid-gap states to the CB, which should increase the photocatalytic activity.[34,37]

4.3.2 Photocatalytic water-splitting at elevated temperature

In order to obtain a clear understanding of the behaviours of different phases, the monophasic anatase and rutile samples were nitrogen-doped using the same procedure as for P25 materials. Catalytic testing was carried out by Dr. Yiyang Li. Initially all samples was tested at 270°C under only visible light. For the pristine samples, no activity was observed. On the other hand, the nitrogen-doped catalysts are highly active under visible light only (discussed later, Figure 4-11). When the irradiation spectrum was broadened to include visible and UV light, the pristine samples were shown to be photocatalytically active (Figure 4-9a). This is in agreement with the UV-vis spectroscopy of P25 materials above, which showed only a UV active bandgap for pristine P25 of 390 nm.

Firstly, the pristine samples, though active, exhibit an order of magnitude less activity than their highly doped equivalents. Even under combined UV/visible light, the activity of the non-doped samples was reasonably low (<600 μmol g^{-1} h^{-1}). Secondly, the rutile is much less active for both doping levels. The activity is fairly similar to anatase at low temperature, but at 270°C the activity of rutile is an order of magnitude lower. This is consistent with the well-known relative inactivity of pure rutile for photocatalytic hydrogen evolution; though

this is not to say that the phase is inactive in P25. Thirdly, it is noted that over a narrow temperature range, the activity increases significantly. The temperature dependences are approximately similar but the number of temperatures sampled is low. What phenomenon between 200°C and 270°C initiates this increased activity?

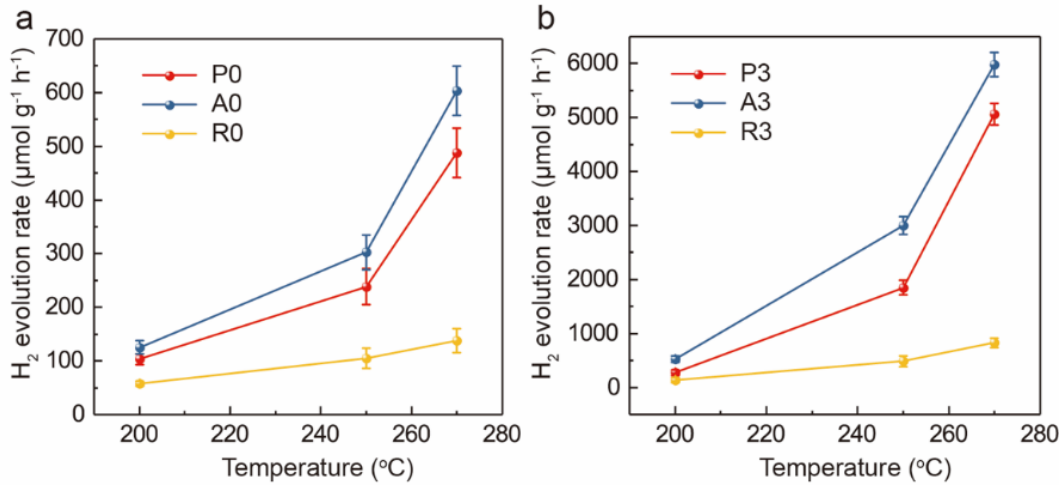


Figure 4-9. Photocatalytic water-splitting activity over (a) pristine, and (b) nitrogen-doped TiO_2 materials under UV-visible light from a xenon lamp.

In order to show that this reaction is photocatalytic in nature, control tests were carried out: (1) no catalyst, (2) no irradiation at all (P3 catalyst used), and (3) no catalyst and no irradiation. All of these control tests yielded zero hydrogen evolution, clearly showing that the activity is a result of the combination of both light and the N-TiO_2 catalyst. Furthermore, GC-MS was used to characterise the reaction exhaust of highly nitrogen-doped A3 and P3 catalysts under only visible light over 50 hours (Figure 4-10a). The reaction is shown to produce H_2 and O_2 in a 2:1 molar ratio which is indicative of the stoichiometric splitting of water.

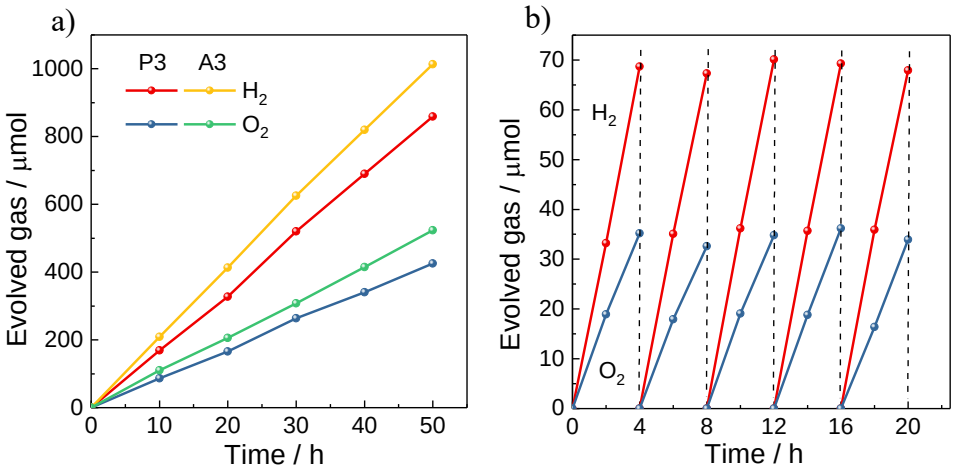


Figure 4-10. Control tests for photocatalytic activity under only visible light at 270°C. a) Demonstration of stoichiometric water-splitting by GC-MS over 50 h. b) Over 5-cycle test of P3.

A P3 catalyst was then monitored over five 4-hour batch reactions. Again, the molar ratio is consistent with water-splitting (Figure 4-10b). The stability of the activity shows the catalytic nature of the reaction, with no evidence of the stoichiometric consumption of the catalyst through decreasing yields. In both experiments, no nitrogen gas was observed. This shows that the nitrogen-dopant is not involved stoichiometrically in the reaction as a stoichiometric hole scavenger. It also indicates that no nitrogen abstraction from the framework is occurring, and the nitrogen doping is stable under operating conditions. This is reasonable as it is known that that the electro-oxidation of N^{3-} to N_2 requires significantly higher potentials than that of OH^- to occur, and the nitride oxidation is only favourable as a molten medium in the complete absence of water.[70] Hence, it is shown that the hydrogen evolution is the product of photocatalytic water-splitting, and that the N-TiO_2 is not consumed stoichiometrically with hydrogen yield.

Under UV-visible light, A3 exhibited the highest activity of 6000 μmol g^{-1} h^{-1}. From here, the testing omits the UV light in order to prove the extended range of absorption. At the highest temperature of 270°C, A3 is again shown to be the most active, exhibiting an activity of 4000 μmol g^{-1} h^{-1}. It is clear that the photocatalytic performance of anatase and P25 is strongly dependent on the nitrogen-doping levels; meanwhile all nitrogen-doped rutile exhibited similar activities.

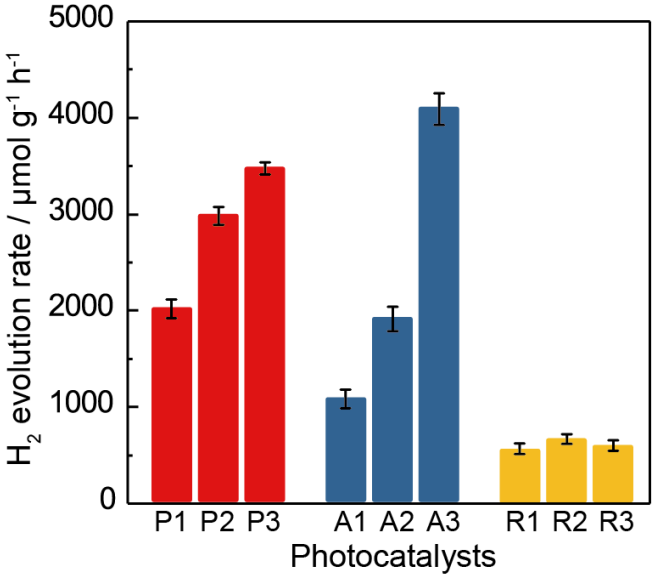


Figure 4-11. Photocatalytic water-splitting activity N-TiO_2 samples at 270°C under visible-light irradiation only.

The P25 exhibits an intermediate catalytic performance for P3; though interestingly, the activity of P1 and P2 are greater than A1 and A2, respectively. This improved performance is indicative of improved exciton separation by band-bending mechanisms which are often reported in rutile-anatase mixtures.[31,71] The higher work-function of anatase is likely to result in downward bending and accommodation of electrons, facilitating hydrogen reduction. Inversely, the rutile accepts holes, facilitating oxygen evolution.

4.3.3 Active-site defects by EPR

From P0 being an inactive catalyst under visible light, the addition of nitrogen in P1, P2 and P3 leads to increasing photocatalytic activity. We attribute this activity directly to increasing concentrations of oxygen vacancies. It is widely known that nitrogen-doping TiO_2 results in a decrease in the formation energy of oxygen vacancies, as well as the decrease in band-gap shown above. Hence nitrogen-doping is known to increase the number of charge carriers and provide a lower energy transition. It is predicted that there will be a correlation between the concentration of oxygen vacancies and photocatalytic hydrogen evolution. The characteristic redox-active unpaired electron in TiO_2 that results from oxygen vacancies (Equation 4-5) is observable by EPR at $g = 2.003$.[51,72,73]

$$O_O^X \rightarrow V_O^{\cdot\cdot} + 2\ e^{\prime} + \tfrac{1}{2}\ O_2\ (g)$$

Equation 4-5. Oxygen vacancy formation in Kroger-Vink notation.

In order to deconvolute the constituent phases of P25, the monophasic pristine and N-doped rutile and anatase samples were analysed (). The oxygen-vacancy signal is present in both rutile and anatase materials. The signal was observed for the undoped R0 catalyst, which is attributed to the ease of formation of surface oxygen defects during synthesis. According to DFT calculations by Cheng and Selloni, 3.68 eV is required to create surface oxygen vacancies on rutile (110), which is more favourable than 4.15 eV of anatase (101).[42] After initial nitrogen-doping, the signal increases considerably from an oxygen-vacancy concentration of 1.36×10^{14} g^{-1} in R0 to 2.18×10^{14} g^{-1} for R1. For higher nitrogen-composition rutile catalysts, the signal increases proportionately, but not significantly, with R3 not exceeding an oxygen-vacancy concentration of 2.58×10^{14} g^{-1} (Table 4-2). This indicates that the oxygen vacancies are mainly created on the local surface with no formation or migration

to deeper layers, causing a limiting concentration. This again matches with the prohibitively high V_O formation value of 5 eV in creating sub-surface oxygen vacancy in rutile.[42] As predicted, the low concentration of oxygen vacancies is correlated with the poor rate of hydrogen evolution for these catalysts (<1000 μmol g^{-1} h^{-1}).

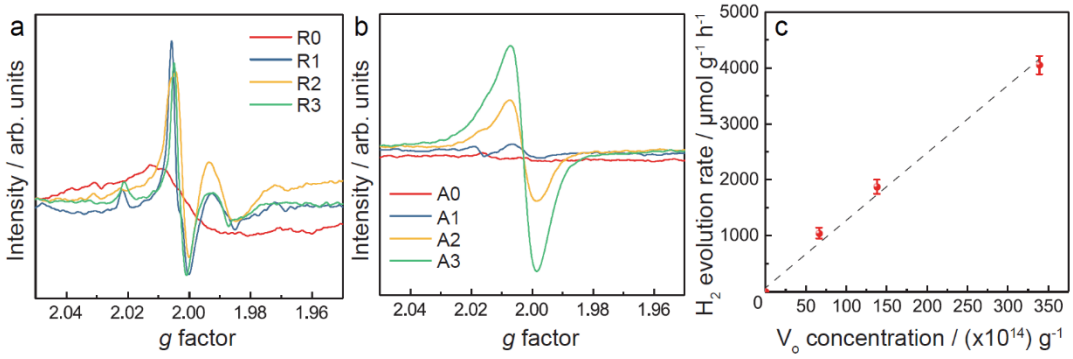


Figure 4-12. EPR spectra for (a) rutile and (b) anatase materials. (c) Hydrogen evolution of anatase catalysts under visible light against EPR-derived oxygen vacancy concentration. Error bars indicate the standard deviation.

In contrast, the strength of the signal for anatase has a much more significant dependence on the nitrogen content, indicating that the concentration of surface oxygen-vacancies is wholly attributed to the concentration of dopant atoms. It is significant that the signal for A3 is over 100-times that of R3, reaching a concentration of 339 × 10^{14} g^{-1}. At this concentration, the catalytic activity is far above any rutile catalyst, exhibiting the highest activity under only visible light reported in this work of 4000 μmol g^{-1} h^{-1}. In fact, for anatase it is shown that a highly linear correlation exists between oxygen-vacancy concentration and photocatalytic activity (c).

Sample	Oxygen vacancy concentration / (10^{14}) g^{-1}	Oxygen to vacancy molar ratio
R0	1.36	1.1×10^{8}
R1	2.18	6.9×10^{7}
R2	2.41	6.3×10^{7}
R3	2.58	5.8×10^{7}
A0	Not detected	-
A1	66.1	2.3×10^{6}
A2	138	1.1×10^{6}
A3	339	4.5×10^{5}

Table 4-2. Oxygen-vacancy concentrations derived from EPR spectra of rutile and anatase materials.

The photocatalysis in anatase is greatly facilitated by large quantities of oxygen vacancies and Ti^{3+} beyond the surface tri-layer, particularly in comparison to the inactive rutile polymorph. Hence, it is observed that oxygen-vacancy concentration increases with nitrogen-doping for both phases, with anatase exhibiting a much larger absolute concentration, which has a stronger non-limited dependence on nitrogen composition, and a highly linear correlation with photocatalytic activity. Converting the concentrations to a molar ratio shows that approximately one in 1,000,000 oxygens sites is vacant.

In summary, generally it has been shown that ammonia treatment at higher temperatures yields higher nitrogen composition, which results in lower formation energy and greater concentration of oxygen vacancies at a given temperature, increasing photocatalytic hydrogen evolution. The catalysts P3, A3, and R3 were also tested under combined UV-visible irradiation, with the absorption of visible light increasing the photocatalytic activity by approximately 50% (Figure 4-9).

4.3.4 Anisotropic thermal expansion of anatase

4.3.4.1 Thermal expansion of anatase and rutile within P25

It was found that SXPD could not yield the location of nitrogen either as an interstitial atom ($\Delta e^- = +7$) or as a substitutional atom ($\Delta e^- = -1$), either due to low-scattering contrast or low crystallinity. Despite the failure to detect bulk structural change by XRD, there are clearly indications that oxygen-vacancy formation is facilitated by nitrogen-doping at low nitrogen content. Instead the focus was turned to the emergent property of increased oxygen vacancies and their effect on the framework. In order to detect changes in the sub-surface and bulk, we studied the change in lattice parameters with respect to temperature by high-resolution VT-SXPD at I11, DLS. Pristine and highly-doped P25 samples, P0 and P3, were analysed under atmospheric conditions using the MAC detector. A Pawley refinement using a biphasic anatase-rutile model yielded a good fit (Figure S4-2): for P0, all residuals were R_{wp} <3.9% and GoF <1.2, and for P3, R_{wp} <4.1%, GoF <1.6 (Table S4-1).

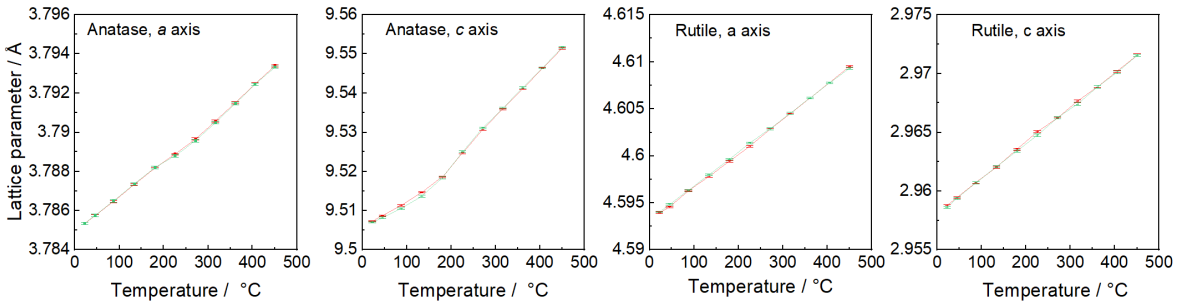


Figure 4-13. Absolute lattice parameters of pristine P0 (red) and highly-doped P3 (green) from room temperature to 500°C, separated by lattice parameter.

To a certain extent, the lattice parameters exhibit typical thermal expansions reported previously in the literature (Figure 4-13).[63,64] For both P0 and P3, both constituent phases exhibit the same lattice parameters to three decimal places. Over this temperature to 450°C, rutile expands in the *ab*-axis from 4.594 Å to 4.609 Å (Δa = +0.015 Å, 0.33%), and in the *c*-axis from 2.959 Å to 2.972 Å (Δc = +0.013 Å, 0.44%). The expansion is highly linear for both parameters. This is explicitly shown by a constant first derivative against temperature, d*x*/d*T*: d*a*/d*T* = 3.5×10^{-5} Å °C^{-1}, and d*c*/d*T* = 3.0×10^{-5} Å °C^{-1} (Figure 4-14). Thus, the second derivative for both *a* and *c* equals zero: $d^2(x)/d(T)^2 = 0$. Rutile will largely not be discussed further.

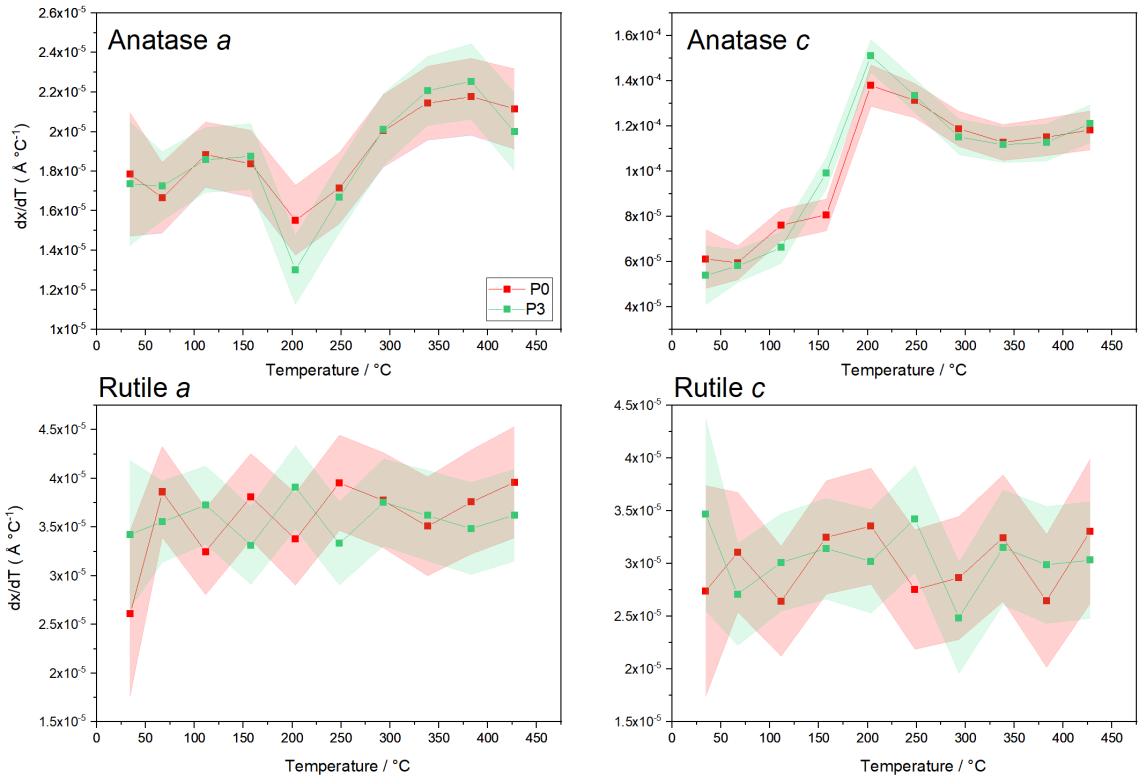


Figure 4-14. First derivative of lattice parameter against temperature, d*x*/d*T*, of pristine P0 (red) and highly-doped P3 (green) from room temperature to 500°C.

For anatase, the *ab*-axes expands from 3.785 Å to 3.793 Å (Δa =+ 0.008 A, +0.21%), and the *c*-axis from 9.507 Å to 9.552 Å (Δa = +0.045 Å, 0.47%). These changes as a percentage of the original value are greater for anatase than rutile, indicating greater reorganisation. In particular, the *c*-axis is shown to increase by a considerable amount relative to the other axes. This results in the unit-cell becoming increasing tetragonal (from c/a = 2.511 to 2.517, Figure S4-3), with implications on the titanium coordination and the electronic structure. Unlike rutile, the expansion of both axes in anatase is non-linear, as they increase faster with temperature, i.e. the first derivative is not constant. Not only this, the phase exhibits both increases and decreases in gradient. This is observed in the absolute lattice parameters as an inflection. The most interesting observation is that these inflections in the *a*- and *c*-axes are opposite and at the same temperature (Figure 4-13).

4.3.4.2 Anisotropic thermal expansion coefficients

In order to compare these gradients, the linear thermal expansion coefficients, α, were calculated (linear as opposed to the volume thermal-expansion coefficient) (Equation 4-6) (Table S4-2).

$$\alpha_x = \frac{1}{x}\left(\frac{\mathrm{d}x}{\mathrm{d}T}\right)$$

Equation 4-6. Linear thermal expansion coefficient α, where x is the lattice parameter and T is the temperature (Equation 4-6).

Both α_a and α_c generally increase with increasing temperature, showing that the rate of expansion is increasing with temperature (Figure 4-15). Though clearly not linear, the order of magnitude of the second derivative of length can be estimated by using the low temperature and high temperature regimes (excluding 150-300°C): for *a*, 10^{-8} Å $°C^{-2}$, and for

c, 10^{-7} Å $°C^{-2}$. Not only is *c* increasing at a greater rate than *a*, the rate of increase in expansion is also increasing at a much greater rate.

Unexpectedly, an unusual feature is centred around 200°C, which is negatively correlated between the equatorial and axial axes. At 150°C, α_a starts to exhibit a decrease; meanwhile at the same temperature, α_c increases. Both changes peak at 200°C, after which the trends gradually lessen until 350°C, where the linear second derivative is again observed. The similar onset and fading temperatures of the features indicate a common mechanism for both P0 and P3, but with the latter exhibiting greater deviations, which are confirmed to be valid by the distinct separation of the values including their error. We attribute this anisotropic linear thermal expansion to the structural reorganisation of anatase caused by oxygen-vacancy formation. (Initial work has been carried out on repeating and changing the atmosphere to inert argon, and has shown these observations to be repeatable.)

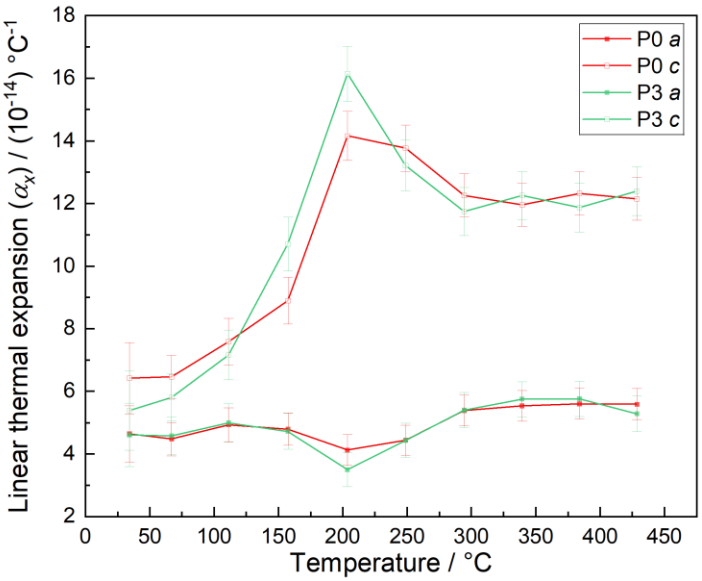


Figure 4-15. Linear thermal expansion coefficient α for the *a*- and *c*-axes of the anatase phase in P0 and P3.

Error analysis

Processing the lattice parameter values in this way has significant impacts on the error. The standard deviation for the lattice parameters are typically of the order 10^{-5} Å. This is equivalent to a relative error, $d(\sigma)/d(x)$, of the order 1×10^{-5} or 0.001%. The effect of rebinning the data had negligible effect. Though this relative uncertainty may seem insignificant, the calculation of thermal-expansion coefficients involves the change in lattice parameters. The difference between two lattice parameters at different temperatures ($\Delta x = x(T_f) - x(T_i)$) is much smaller than the absolute lattice parameters; hence the relative uncertainty is much higher. The resulting thermal-expansion coefficients typically have a relative uncertainty of ~10% (Figure 4-15). This is a particular problem at low temperature when the thermal expansion is low. As with most synchrotron experiments presented in this thesis, no methodological errors are identified.

4.3.4.3 Mechanism of anisotropic distortion

The simultaneous inverse behaviour of the *a*/*b*-axes and the *c*-axis is reminiscent of the Jahn-Teller distortion, commonly observed in octahedral complexes. In the anatase structure, titanium is coordinated by six oxygen atoms as an octahedron. Here, it is proposed that the anisotropic coordination distortion of octahedral titanium is observed as bulk anisotropic behaviour.

The inequivalent axes of the tetragonal space group $I4_1/amd$ is also manifested in the asymmetry that yields two distinct Ti-O bonds: four short equatorial bonds (*ab*-plane), and two slightly longer axial bond (*c*-axis).[42] This asymmetry is seen in the low temperature regime, <150°C, the axes expand anisotropically in that the *c*-axis expands at a much greater absolute and fractional rate. The ground-state exhibits an already lengthened axis that is more

susceptible to vibration, lengthening and eventual bond-breaking through thermal excitation. This causes a larger absolute value in α_c than α_a, and also a larger rate of increase in α_c.

At 150°C, the lengthening in the *c*-axis becomes too large causing geometric instability. Although in a formal oxidation state of +4, the d-electron density of Ti^{4+} is non-zero: $d^{>0}$. The material is not completely ionic; thus, a degree of electron sharing through the six Ti-O bonds will result in some d-occupancy. It is thought that the anisotropic change in coordination will induce a contractive force on the equatorial bonds in order to maintain the electron density of the titanium atom. This stabilisation is essentially a description of the Jahn-Teller distortion. As the orbitals with *z*-component are stabilised by the axial elongation, the *x*/*y*-component orbitals will increase in energy by a contraction towards the central atom. If this distortion occurs in high enough concentration across the crystal, the coordination distortion will be observed as bulk crystalline distortion. Factoring in the normal thermal expansion, the unit-cell will exhibit a constant absolute expansion. But it is thought that this mechanism can explain the decreasing rate of increase in the *ab*-plane and the increasing rate in the *c*-axis.

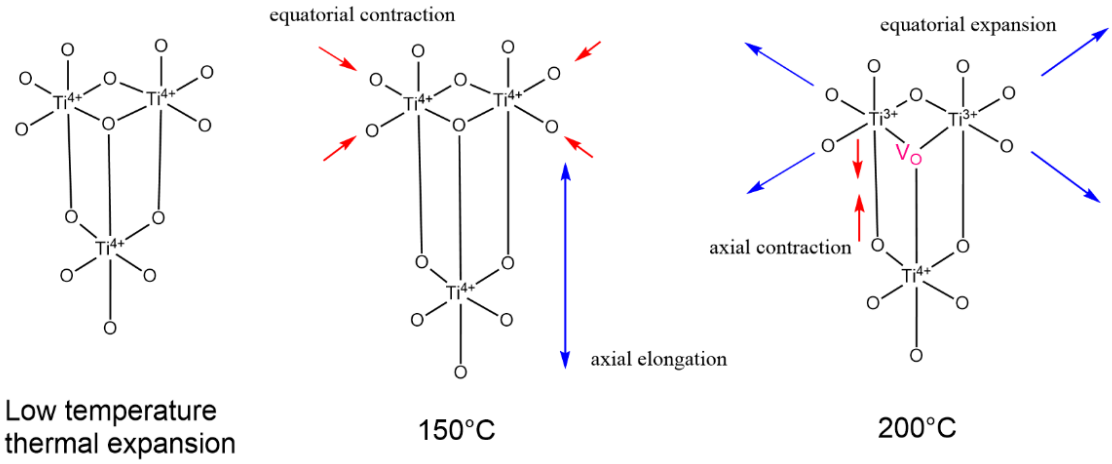


Figure 4-16. Schematic of proposed mechanism for anisotropic thermal expansion.

At 200°C, the inverse anisotropic behaviour is observed, which is attributed to the inverse distortion of equatorial elongation and axial contraction. We postulate that this is likely to be caused of the formation of oxygen vacancies in anatase, which are known to occur at 200°C, as previously shown by variable-temperature EPR (Figure S4-4)[43]. Specifically, we believe that these are ordered sub-surface oxygen vacancies in P25 that are able to be measured by VT-SXPD, which exist within the lattice under dynamic equilibrium with surface oxygen vacancies.

An oxygen vacancy forms three under-coordinated titanium sites, which are approximately coordinated as square pyramids. Two have the vacancy in the *ab* plane (*ab*-pyramid), $Ti_{V,eq}$, and one with the vacancy in the *c*-axis (*c*-pyramid), $Ti_{V,ax}$. Thus, the geometric equivalence of the titanium sites has been broken. The two electrons retained by the lattice following oxygen evolution ($O_O \rightarrow V_O^{2+} + ½\ O_2 + 2\ e^-$) are known to become localised on two separate Ti 3d orbitals, forming two reduced Ti^{3+} (d^1) species.[29] Thus, the electronic equivalence of the titanium site has been broken. It is not generally discussed in the literature whether the geometric and electronic inequivalences are correlated. Here, we suggest that the electrons are localised on the *ab*-pyramidal titanium sites, due to the shorter $(Ti\text{-}O)_{eq}$ bond relative to $(Ti\text{-}O)_{ax}$.

The *ab*-pyramidal Ti^{3+} undergoes standard energy-driven Jahn-Teller distortions due to the energy minimisation of the single electron by *z*-destabilisation. The *c*-axis contracts and the *ab*-plane elongates. This is the observed behaviour in α_c and α_a at 200°C. The *c*-pyramidal would behave inversely, but this titanium is not formally reduced to d^1; though it has been said that it will likely the *d*-count will likely be non-zero. This comparably low d-count will result in comparably less Jahn-Teller distortion. Thus, the *c*-pyramidal inverse

distortion are weak and overpowered by the two *ab*-pyramidal distortions. We suggest that these temperature-dependent distortions in the anatase structure affect the bulk structure significantly enough to be observed by SXPD.

By 300°C, the anisotropic features seem to cancel out and return to the standard constant second-derivative expansion observed below 150°C. This is thought to occur due to the two counter-distortions cancelling each other, becoming balanced above 350°C (Figure 4-13b).

4.3.4.4 Effect of nitrogen on anisotropic thermal behaviour

So far, the discussion presented has been true of both pristine P0 and nitrogen-doped P3, as they exhibit similar trends. This is reasonable since both exhibit the same octahedral asymmetry in the ground-state and are known to be vulnerable to oxygen-vacancy formation at elevated temperatures. However, N-TiO_2 is known to decrease oxygen-vacancy formation energy by the localisation of the electron charge-carrier in a mid-gap interstitial nitrogen orbital.[50] Based on this, for N-TiO_2 should exhibit anisotropy of greater magnitude at a lower temperature. Indeed, the magnitude of the oxygen-vacancy-induced distortion after 250°C is larger for P3 than P0. Hence, the difference between the curves yields the effect of extrinsic oxygen-vacancy formation from nitrogen doping. Thus, the increased magnitude of the electronically driven Jahn-Teller is attributed to the nitrogen-dopant. Furthermore, the magnitude of the inverse distortion observed at lower temperatures is much larger for P3 also. This is attributed to substitutionally-doped nitrogen because the Ti-N bond is longer than Ti-O,[50] which also occurs for B-TiO_2.[74] Thus, the susceptibility to excessive *c*-elongation and resulting *ab*-contraction is greater. This also occurs at a lower temperature for P3, starting at 100°C rather than 150°C for P0.

4.3.5 Local structure distortions of oxygen vacancies by DFT

4.3.5.1 Structure energy: surface to sub-surface migration

In order to rationalize the anisotropic thermal properties of anatase, the effect of oxygen vacancies on local structure was investigated by computation calculations. It is well-known that oxygen vacancies and irradiation cause significant reorganisation.[26] A small anatase supercell was modelled and optimised by ab-initio DFT simulations. The supercell of the *P1* space group contains no symmetry elements (other than the identity operation), and hence no equivalent sites. The supercell was orientated with the dominant (101) surface exposed to 15 Å of vacuum by terminating oxygen sites. The slab contained three layers of TiO_2 units labelled s (surface), ss (sub-surface), and b (bulk); the slab thickness was approximately 8.85Å. In each tri-layer stacked towards the surface of anatase (101), there are four oxygen environments and two titanium environments that are equivalent with respect to depth. Thus, these are labelled as either surface, sub-surface, or bulk: O_1, O_2, O_3, O_4, Ti_1, and Ti_2 (Figure 4-17).

The calculated lattice parameters of pristine anatase structure matched with the high-resolution SXPD at room temperature (a = 3.810 Å, +0.63%; c = 9.440 Å, -0.68%). Oxygen-vacancy structures were optimised by removing the following oxygen atoms: O_{s1}, O_{s2}, O_{s3}, and O_{ss3} (Figure 4-17); the vacancy structures will be referred to as V_{Os1}, V_{Os2}, V_{Os3}, and V_{Oss3}, respectively.

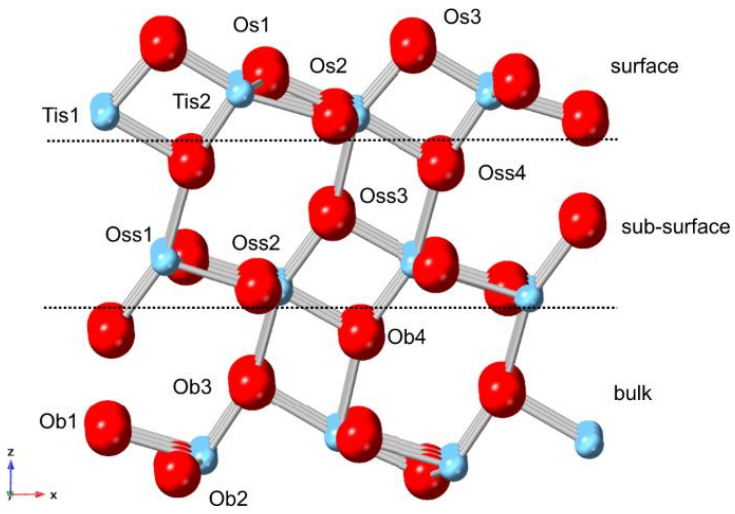


Figure 4-17. Pristine anatase (101) supercell showing assigned depth environments and inequivalent (relative to surface, not vacancy) oxygen (red) and titanium (blue) sites at each depth. Volume of vacuum not shown. Note, there is no O_{s4} due to surface termination.

It is interesting to note from the optimised energies that the lowest energy vacancy-structure is that of the ordered sub-surface vacancy (V_{Oss3}) rather than those with surface vacancies (V_{Os1}, V_{Os2}, V_{Os3}), which has been reported previously.[75] Anatase (101) has a relatively low surface energy compared to other facets, which requires more energy to create surface vacancies. Consequently, in contrast to other TiO_2 facets as well as other oxides, we and others have shown that sub-surface oxygen-vacancy formation is more energetically favourable.

Here, the difference in stability between the two lowest energy structures (V_{Os3} and V_{Oss3}) is 0.37 eV. This was also demonstrated by Cheng and Selloni[42] who reported a stability difference between these sites of 0.46 eV, corresponding to a relative probability of a surface vacancy of 4.0×10^{-9} and 1.6×10^{-3} at 300 K and 900 K, respectively. Their results support our simulations that the lowest energy vacancy-structure is yielded by removing the O_{ss3} sub-surface oxygen rather than surface oxygen. Additionally, they demonstrated that the next-

deeper site of O_{b3} is similarly stable to O_{ss3}, and in contrast that all sub-surface and bulk vacancies in rutile are highly disfavoured. It is the stable sub-surface/bulk oxygen vacancies that are believed to be crucial in the superior photoactivity of anatase (101), as it allows the mobility of vacancies away from the surface, delimiting the total concentration of vacancies. Additionally, this promotes charge separation as holes tend to travel to the surface. Indeed, according to the calculations by Fisicaro et al.,[76] oxygen vacancies can travel along the *P1 c*-axis from a higher energy O_{s1} vacancy to the global-minimum vacancy at O_{ss3} ($V_{Os1} \rightarrow V_{Oss3}$).

4.3.5.2 Local reorganisation: additional under-coordinated geometries

In order to understand the structure-activity relationship of these materials, the precise coordination and local environment of the vacancy site and adjacent titanium atoms should be defined. This geometry will have effect on the electronic configuration of the material, impacting photocatalytic activity.

Lattice parameters

When the vacancy is introduced, the distortions change the *P1* unit-cell lattice parameters. All unit-cell angles are still >89.5°, hence the unit-cell will be considered orthorhombic, with changes in lattice parameter comparable to each other (Table 4-3).

Vacancy	Energy / eV	Relative energy to lowest / eV	*a* / Å	*b* / Å	*c* / Å	Strain *a*	Strain *b*	Strain *c*
V_{Os1}	-937.38	1.04	10.448	11.399	23.651	0.002	0.008	-0.010
V_{Os2}	-937.64	0.78	10.438	11.369	23.736	0.001	0.005	-0.007
V_{Os3}	-938.05	0.37	10.439	11.332	23.810	0.002	0.002	-0.003
V_{Oss3}	-938.42	0.00	10.453	11.268	23.914	0.003	-0.004	0.001

Table 4-3. DFT results showing the absolute energy, relative energy to minimum structure V_{Oss3}, changes in *P1* lattice parameters of the (101) slab, and strain relative to the pristine slab.

While the change in the *a*-axis is reasonably constant, there is clearly a positive correlation between the *b*-axis strain and energy, and a negative correlation between *c*-strain and energy. Configurations that exhibit highly contracted *c*-axes are less stable. Inversely, configurations that exhibit expanded *b*-axes are less stable (Table 4-3). Seemingly, collapsing of the structure in the surface vector is unstable, and reorganisation by contracting the *b*-axis is preferred.

Coordination and environment

The lattice parameters for the *P1* supercell discussed in this section so far cannot be directly compared to the diffraction data presented earlier in this report, which used the $I4_1/amd$ axes of tetragonal anatase. The axes can be reassigned by rotation around the *b*-axis (into the page) by 68.8° (Figure S4-5). Here, the primary discussion will relate to the tetragonal axes for which the anisotropic thermal expansion was defined.

The pristine slab structure can be described as edge-sharing chains of 4M-rings extending in the *P1* supercell *b*-axis (equivalent to the $I4_1/amd$ *b*-axis) comprised of $Ti_{_1}$, $Ti_{_2}$, $O_{_1}$, and $O_{_2}$, and another chain extending approximately along the *c*-axis (equivalent to the $I4_1/amd$ *a*-axis) comprised of $Ti_{_1}$, $Ti_{_2}$, $O_{_3}$, and $O_{_4}$. These are usually equivalent in bulk anatase. The latter of these chain was shown by Fisicaro et al. to be a pathway for vacancy diffusion.[76] However, they did not discuss the geometry of the distortions or the possible effect on electronic configuration and photocatalysis.

For all vacancy structures, removing an oxygen from a 4M-ring results in the remaining oxygen atom moving towards the vacancy/surface, forming a more linear [Ti-O-Ti] moiety (

Table S4-3). The lowest energy vacancy (V_{Oss3}) exhibits the most linear moiety and the greatest change in angle by far, from a near right angle (98°) to nearly linear (170°): $\Delta\theta$ = +72°. Meanwhile, the reorganisation in the other structures exhibit changes in angle of only between +20° and +36°. This co-linear moiety in V_{Oss3} will have impact on the electronic configurations of the constituent titanium atoms, and thus the band-gap and photoexcitation properties.

The remaining oxygen atom that moves towards the surface is from the deeper-lying bulk layer, [Ti_{ss1}-O_{b4}-Ti_{ss2}]. The oxygen atom is effectively no longer associated with the deeper tri-layer (Ti_{b2}-O_{b4}: 2.134 Å to 3.684 Å), explicitly showing the migration of oxygen atoms towards the surface. This new oxygen site can be described as pseudo-interstitial site in between the two titanium atoms. Clearly, the presence of an interstitial oxygen atom in the sub-surface void is stabilising.

During the analysis of the VT-SXPD, there was discussion of the possible titanium coordinations after oxygen abstraction, namely three under-coordinated pyramidal titanium atoms. In the (101) nomenclature, a V_{Oss3} vacancy yields Ti_{s1} and Ti_{ss1} with equatorial vacancies (*$I4_1$/amd a*/*b* pyramidal) and Ti_{ss2} with an axial vacancy (*$I4_1$/amd c*-pyramidal). However, this prediction of titanium coordination assumed no structural reorganisation. Considering the interstitial oxygen observed here, an additional under-coordinated titanium site is shown to form in the bulk tri-layer, becoming *a*/*b* pyramidally coordinated (Figure 4-18). The two sub-surface sites however are now more equivalent, exhibiting an intermediate geometry. The surface site is still considered to be *a*/*b*-pyramidal.

Based on crystal field stabilisation theory, the interstitial is now out of plane and will lessen the stabilisation of the original vacancy. This will be a lower magnitude than the

vacancy and the electronic configuration is thought to remain approximately similar. The differing geometries of the four under-coordinated titanium atoms will evidently influence their orbital configurations and their electron-trapping capabilities. Here, a simplified view of the coordination has only considered the central metal atom. Simulations are required on the effect of geometry on the molecular orbitals in particular.

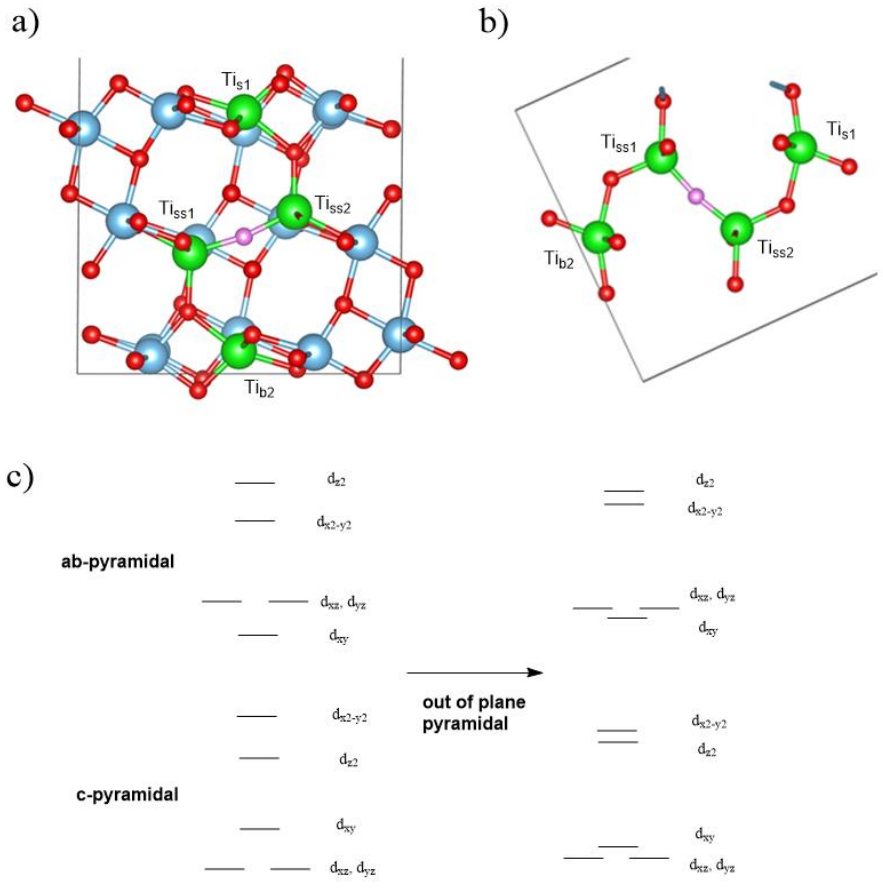


Figure 4-18. Oxygen vacancy structure V_{Oss3}: oxygen (red), titanium (blue), O_{b4} (pink), five-coordinate titanium (green). (b) Under-coordinated titanium sites shown isolated: recontextualise in *$I4_1/amd$* axes by rotation. (c) Crystal field theory prediction of electronic configuration of titanium.

Bond lengths

The bond lengths of the four under-coordinated titanium sites how that most of the bond-lengths are decreasing, indicating a collapse of structure (Table S4-4). Simulating the effect on the bulk, the bond lengths were averaged according to their axis of direction. The co-linear interstitial oxygen was considered to be of *c*-character for Ti_{ss1}, and of *a*-character for Ti_{ss2}, due to the slightly bent geometry (interchanging this assignment has insignificant effect on the averaged values). The *a*-character bonds exhibit an average positive strain of +0.102, while the *c*-character bonds exhibit a negative strain of -0.030. The *b*-character bonds do not exhibit appreciable strain (-0.001). This trend of an expanding *a*/*b* plane and a contracting *c*-axis is in agreement with the anisotropic behaviour observed by VT-SXPD.

These DFT calculations and the inspection of their structure have shown that the sub-surface oxygen vacancies are favoured over surface vacancies, and that migration towards the bulk is likely to occur. The local reorganisation of an adjacent oxygen atom results in the unexpected under-coordination of another titanium site, which is shown to result in anisotropic distortion at the bond-length scale. Crystallographic techniques are generally unable to detect disordered oxygen vacancies. However, the subtle structural changes caused by vacancy mobility and local reorganisation has been observed by VT-SXPD as anisotropic thermal expansion of the anatase phase in P25. Hence, the in-depth structural study of rutile, anatase and mixed phase P25, with and without nitrogen-doping, by VT-SXPD indicates that there exists a direct correlation between the nitrogen-doping, oxygen vacancies, local structural reorganisation, anisotropic thermal expansion, and enhanced photocatalytic activity.

4.3.6 A new titanium oxynitride structure from high nitrogen-doping

High-resolution SXPD of the monophasic anatase samples A0-A3 was carried out at BL02b2 at SPring-8, Japan (Figure 4-19). The materials exhibited additional peaks that are consistent with a cubic $Fm\bar{3}m$ rock-salt phase. These reflections grew in intensity as the doping temperature was increased for pure anatase and P25 materials, hence are correlated with nitrogen composition. The phase strongly resembled titanium nitride $Ti^{3+}N^{3-}$ which is formed by nitridation of anatase and accompanying oxygen evolution. As discussed earlier in this report, XPS shows that at increased temperatures, substitutional doping becomes dominant over interstitial doping and the emergence of a Ti^{3+} signal (Figure 4-6).

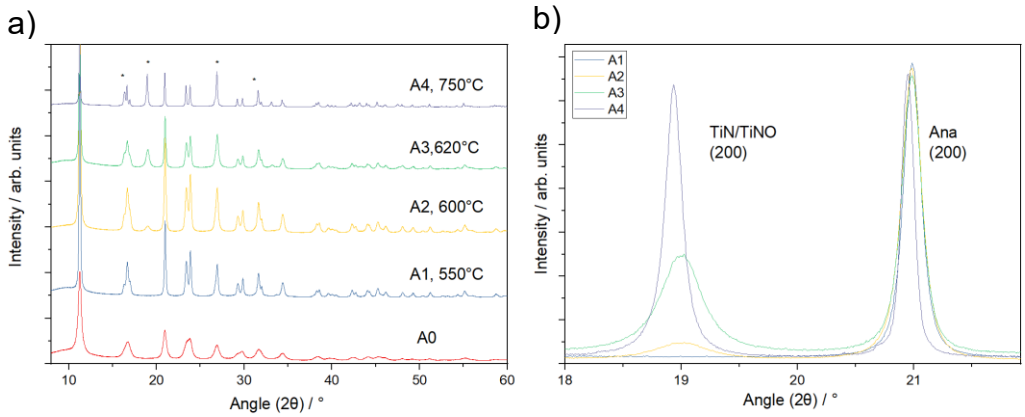


Figure 4-19. SXPD patterns of A0-A4. (a) Cubic reflections (111), (200), (220, and (311) denoted by *. (b) enlarged view of the (200) reflection of anatase and $TiNO_x$. Intensities normalised due to different data-collections causing different total intensities.

In order to observe this phase more strongly, an even higher nitrogen composition anatase was synthesised at 750°C, labelled A4. The emergent $Fm\bar{3}m$ phase became significantly more dominant relative to A3 with narrower peaks due to microcrystalline sintering (Figure 4-19). However, modelling the cubic phase as titanium nitride yielded an unsatisfactory fit, in particular for the reflections (111) (d = 2.415 Å) and (200) (d = 2.092 Å). Of additional note, the presence of rutile was not observed in the diffraction patterns, despite

the prolonged thermal treatment at 750°C being sufficient for the conversion of anatase into rutile which relative to anatase is the more thermodynamically stable polymorph, as previously seen in XRD studies.[57]

The model yielded chemically reasonable lattice parameters for anatase (a_{ana} = 3.7852 Å, c_{ana} = 9.5106 Å). The value for the cubic phase (a_{TiN} = 4.1843 Å) was much lower than the known lattice parameter of 4.235 Å.[77] The Ti-N bond length is 2.09216 Å, which is significantly shorter than the expected length of 2.12 Å. This lattice parameter is notably more similar to that of $Fm\bar{3}m$ titanium(II) oxide TiO (4.184 Å) which is formed at high temperatures from titanium(IV) oxide and titanium metal.[78] Overall the fitting was reasonable (R_{wp} = 3.38%, GoF = 1.98) (Table S4-5). However, though the Ti^{3+} occupancy refined to near unity (0.9998), the occupancy of the nitrogen atom refined to a chemically unreasonable value of 1.48.

The phase information derived from the Rietveld refinement was applied to the observed structure factors in order to synthesise electron density maps (Figure 4-20a). The rock-salt structure of highly electron dense titanium Ti^{3+} and lower-density nitrogen N^{3-} is expected. However, large unmodelled electron density was observed at the nitrogen site (0, 0, 0.5). This is due to nitrogen being in the N^{3-} anion in the structure rather than the neutral atom used (10 electrons rather than 7) since the fitting depends critically on both electron density of atom and site occupancy. As the atomic scattering factors for N^{3-} are unavailable in the refinement program, the isoelectronic O^{2-} was used instead (slightly differing electron

density). The occupancy of this atom then refined to a more chemically sensible value of 1.01 (R_{wp} = 3.39%, GoF = 1.99).

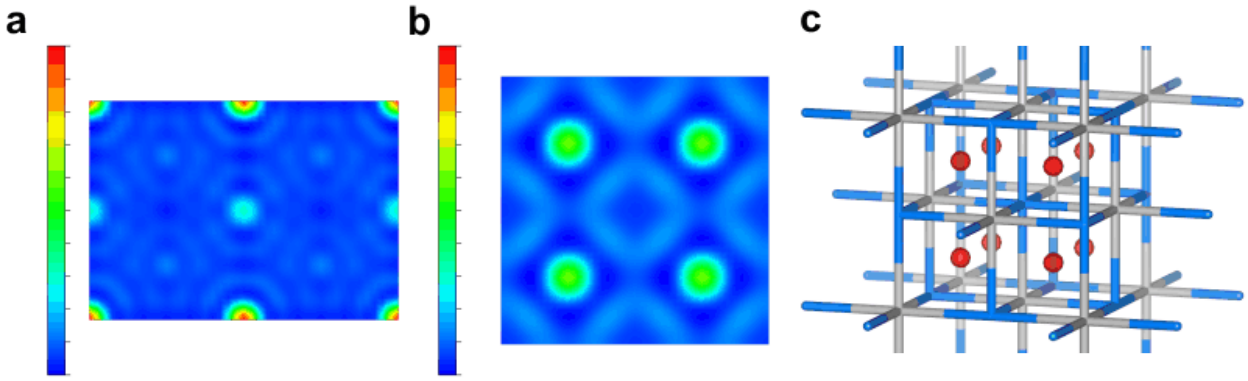


Figure 4-20. Phase identification of $TiNO_x$ by Rietveld refinement. Electron density maps of the $TiNO_x$ unit-cell: 2D cross-sections of electron density derived from the Fourier transform of (a) F_{obs} at one unit-cell length a from the origin along (011); (b) F_{diff} (=F_{obs}–F_{calc}) at 0.25a along (001). (c) iso-surface of electron density at 0.1 (red); grey: titanium, blue: nitrogen.

Additionally, unexpected electron density at the tetrahedral hole positions (0.25, 0.25, 0.25) was also observed. This is more clearly observed in the Fourier difference electron density map, shown in 2D and 3D (Figure 4-20b and c). Introducing a neutral oxygen atom into the tetrahedral hole further improves the fit (R_{wp}= 3.35%, GoF = 1.96) (Figure 4-21). Thus, the phase is modelled as $Ti^{3+}_{0.95}N^{3-}_{1.07}O_{0.03}$ rather than standard $Ti^{3+}N^{3-}$, which results in the Fourier difference map becoming more homogeneous (Figure S4-6). This can be thought of as an oxygen-doped titanium nitride, though the pathway of formation is not known.

The occupancy of the site is 0.03 ± 0.003 resulting in the formula $Ti^{3+}_{0.95}N^{3-}_{1.07}O_{0.03}$, which has a net charge of -0.38. It is therefore conceivable that significant N^{3-} inclusion in the previously discussed N-TiO_2 anatase phase generates significant concentrations of Ti^{3+} and V_O^{2+}, as a precursor to the nitride phase with residual framework oxygen to occupy the interstitial sites. Although for N-TiO_2, the dominant Bragg phase is anatase, both can thus be regarded as oxynitride structures.

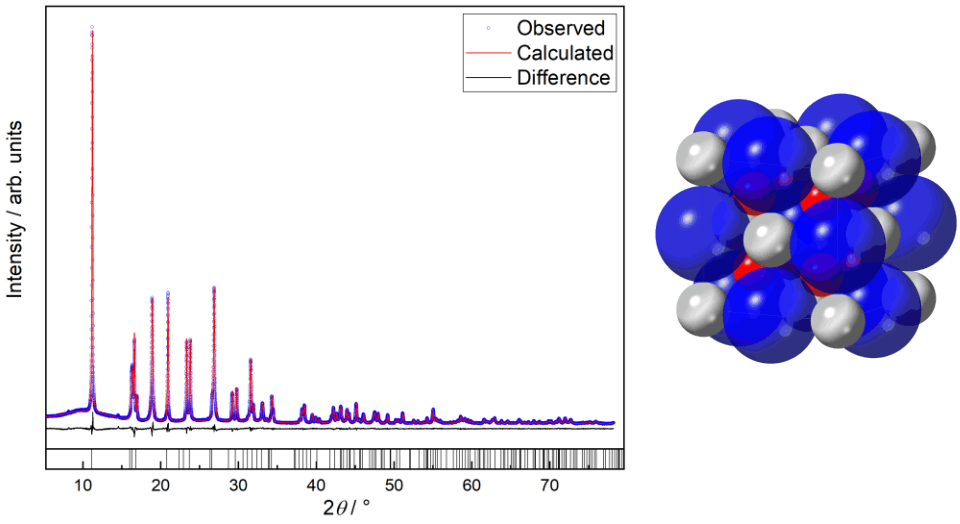


Figure 4-21. Fitting of Rietveld refinement of A4 at room temperature consisting of an anatase phase and a titanium oxynitride phase; blue: titanium, red: nitrogen, white: oxygen.

4.3.6.1 $TiNO_x$ stability by VT-SXPD

VT-SXPD data were also collected on beamline BL02b2, SPring-8 for the thermal oxidation of A4 in air from room temperature to 580°C, collecting data every 20°C yielding 29 patterns (Figure 4-22a). The fitting residual was R_{wp} < 3.5%, GoF < 2.0. Rietveld refinement was carried out; full tabulation in Table S4-6. At room temperature the sample was found to be composed of 67.8%wt anatase (N-TiO_2) and 32.2%wt $TiNO_x$ phase. The $TiNO_x$ is stable until 240°C, after which the peaks decrease in intensity, exhibiting a steeper

decrease at 340°C, then completely disappearance by 520°C (Table S4-6, Figure 4-23). This is a remarkably low thermal stability compared to non-oxygen-doped titanium nitride which only reaches full degradation at 1000°C.[79]

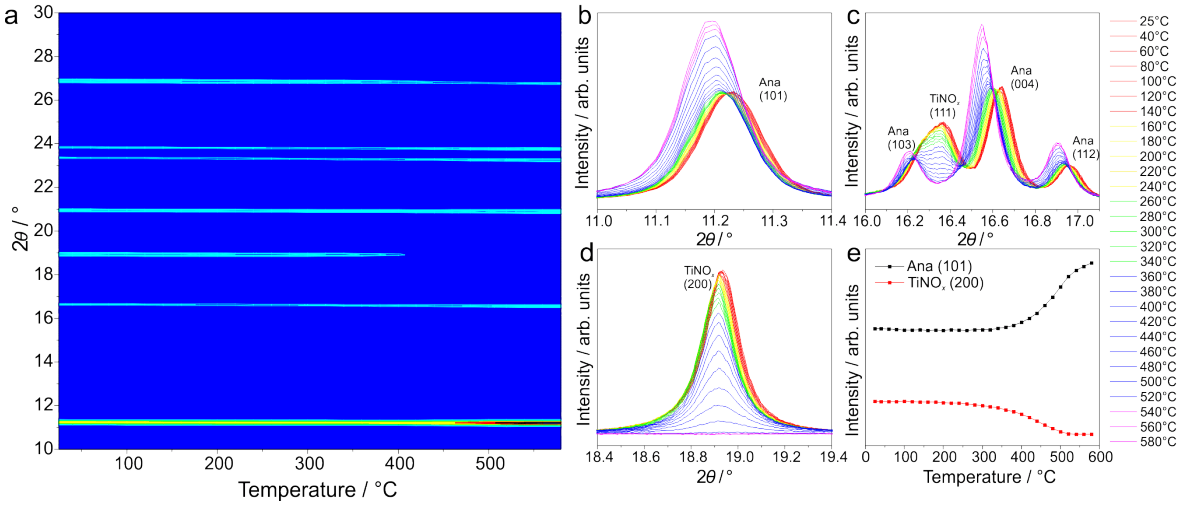


Figure 4-22. (a) VT-SXPD of A4; (b-d) enlarged regions showing the decomposition of $TiNO_x$ and increase in anatase intensity; (e) intensity of anatase (101) and TiN (200) plotted against temperature (negligible standard deviation not plotted).

Anatase is shown to be the dominant decomposition product of $TiNO_x$ phase in air, shown by the negatively-correlated integrated intensity of the anatase phase. This must occur through the loss of nitrogen and accommodation of oxygen, likely the reverse of the process that formed the phase from anatase. Indeed, the occupancy of interstitial oxygen gradually increases before the phase conversion (Figure 4-23). Thus, this clearly shows that the interchangeable phase between anatase and nitride is dependent on nitrogen and oxygen availability in the oxynitride structures at elevated temperature.

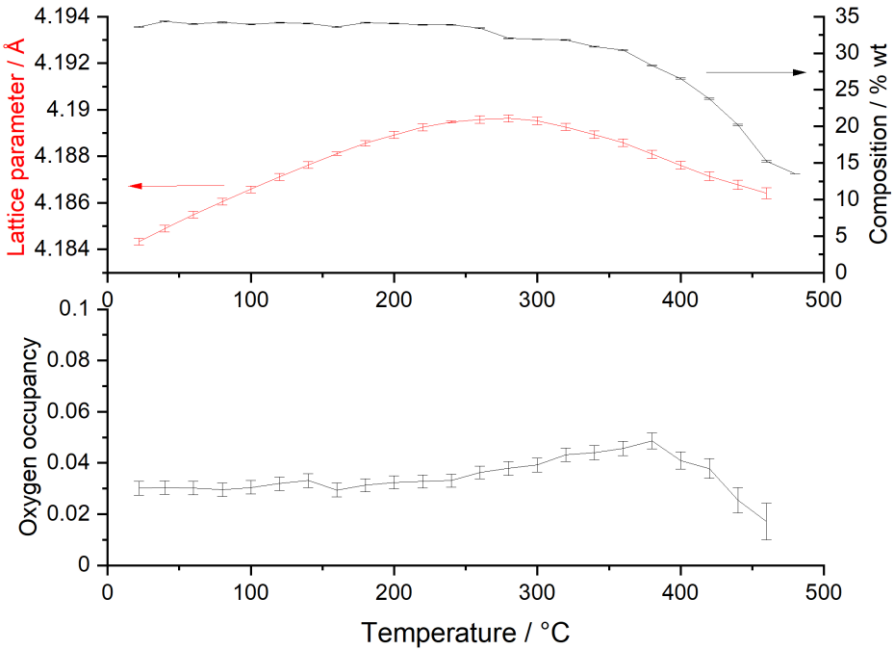


Figure 4-23. Structural parameters of $TiNO_x$ from the Rietveld refinement of A4 during thermal oxidation; phase composition (red), lattice parameter (black), occupancy of interstitial oxygen site (blue).

The modified oxynitride structure of TiN may also contribute to the high photocatalytic activity of highly nitrogen-doped composite TiO_2 materials under visible light. It is well-known that these exists a synergy between anatase and rutile phases in mixed-phase catalysts. The identification of another component in A4 by diffraction does not preclude the presence of this structure in a disordered, less crystalline form in lower doped samples. The question as to whether this phase is participating in the photocatalysis is very important in fully understanding the system.

4.3.7 Relationship to temperature-dependence of catalytic activity

The effect of temperature was first investigated over samples of highest nitrogen-doping, A3, R3 and P3. For A3 and P3 there is a clear onset of photocatalytic activity at 200°C, showing exponential increase (Figure 4-24).

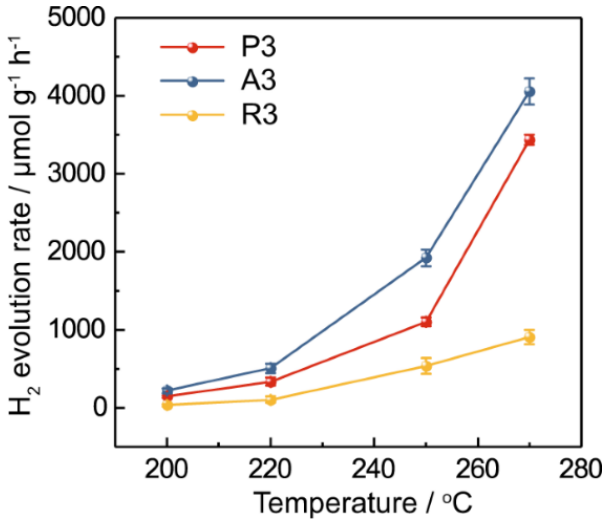


Figure 4-24. Photocatalytic water-splitting activities over highly-doped N-TiO_2 samples P3, A3, and R3 photocatalysts at different temperatures under visible-light illumination.

Meanwhile, the activities of R3, although slightly increased at elevated temperatures, remained at a low level. This onset in activity coincides with the counter Jahn-Teller mechanism (Figure 4-15) attributed to the onset of oxygen-vacancy formation in the asymmetric nitrogen-doped anatase phase at 200°C. Indeed, using these catalytic data, the activation barrier for hydrogen evolution has been calculated to be 60.6 kJ mol^{-1}, which is in good agreement with the activation barrier for oxygen-vacancy formation of 62.5 kJ mol^{-1}, which we derived from variable-temperature EPR (Figure S4-4). Additionally, this formation energy is in good agreement with the reported activation energy for oxygen-vacancy mobility in anatase of 67.5 kJ mol^{-1},[42,80] which indicates that the formation of oxygen vacancies in

anatase is limited by the diffusion of vacancies into the sub-surface. It is ambiguous whether the rate-limiting step may be the formation or mobility of oxygen vacancies.

At low nitrogen-doping, the nitrogen-dopant increases the concentration of V_O^{2+} and Ti^{3+}, and also reduces the band-gap to the visible light regime, as demonstrated here. Nevertheless, the formation of H_2 is attributed to H^+ reduction of water on the catalyst surface by photoexcited electrons trapped at surface Ti^{3+}, while O_2 formation is attributed to oxidation of hydroxyl ions (OH^-) from water over surface V_O^{2+}, which migrate towards the sub-surface in dynamic equilibrium. Similarly, at high nitrogen-doping, OH^- from water over unfilled interstitial sites in $TiNO_x$ phase can be oxidised to O_2 and provide electrons to regenerate Ti^{4+} to Ti^{3+}, after H_2 formation from H^+ reaction. This demonstrates the same pathway for photoexcitation by bandgap modification as in the N-TiO_2 structures.

We also postulate that the anatase-oxynitride mixture may benefit from band-bending effects, which result in stronger charge separation, greater exciton lifetime, and enhanced catalytic activity, as has been shown for other anatase systems.[31,71] Like rutile, the work function of titanium nitride is lower than anatase. This indicates that the titanium-nitride-like oxynitride phase will confer similar charge separation.

4.4 Conclusions

4.4.1 Summary

In summary, nitrogen was successfully doped into TiO_2 materials which increased absorption in the visible region as well as increasing the concentration of oxygen vacancies. This was correlated to superior photocatalytic hydrogen-evolution activity. We suggest that the large sub-surface oxygen-vacancy concentration and facile oxygen mobility indicates that the anatase phase is a superior photocatalyst for water-splitting, especially compared with rutile which only has limited and immobile surface vacancies.[42] Effects of this were seen in an unusual anisotropic thermal expansion of anatase. Furthermore, the same anisotropy was observed in DFT calculations of the local reorganisation of the sub-surface following oxygen vacancies. Additionally, at high level of nitrogen-doping of anatase, a titanium oxynitride phase with interstitial oxygen was observed. This work provides an additional component in the fundamental understanding of the bandgap modification in N-TiO_2 materials, and will inform wider hypotheses and perspectives on this system.

Consequently, we present important links between structure, sub-surface oxygen vacancies, nitrogen-doping, and photocatalytic activity of anatase catalysts at various temperatures. Ultimately, we report the influence of structural modification on electronic phenomena for a highly active photocatalytic hydrogen-evolution catalyst.

4.4.2 Evaluation and future work

4.4.2.1 Structure-activity relationship

The pure TiO_2 and N-TiO_2 show similar temperature dependences in the VT-SXPD experiment. It is expected that the favourable formation of oxygen vacancies and their

migration to the sub-surface and bulk would increase the anisotropic thermal expansion feature (supported by the DFT calculations). It is desired to conduct additional experiments. The VT-SXPD of P0 and P3 have been repeated under inert argon atmosphere on I11, but these data are too recent to be analysed here. It is somewhat surprising perhaps that ~5%wt of nitrogen dopant can have such an impact on the bulk diffraction. Hence this dependence should be investigated by analysing the intermediately doped samples. Correlating these properties with the type and proportion of nitrogen doping would be interesting. It has been reported that interstitial nitrogen increases the concentration of oxygen vacancies, while substitutional nitrogen decreases the concentration.[51]

The initial aim of in-operando SXPD is still desired. A stable sample environment was not able to created, but is easily within technical possibility. We acknowledge that the presence of water could affect the adsorptive properties of surface oxygen vacancies in the samples, as well as the relative stability of the sub-surface vacancies.[81,82] Hence, the ex-operando SXPD may not be representative of the experimental conditions. This experiment should be carried out at high pressure and under illumination too.

4.4.2.2 Bulk framework distortion, local reorganisation, and activity

Defining locally distorted titanium coordination by experimental observation is crucial in order to fully uncover the structure-activity relationship, which could be possible by PDF analysis of the total scattering. The highly distorted titanium coordination and the movement of 'interstitial' oxygen towards the surface shown by DFT calculations needs further investigation. In particular, the electronic configurations of the metal centres is desired. It is a deficiency that the calculated vacancy structures involved no nitrogen-dopant.

4.4.2.3 Nitrogen dopant

The lack of focus on the type of nitrogen doping is regretful. The scope of this work did not focus on the location or nature of the dopant as much as was envisaged, mainly due to the focus shifting to the novel thermal expansion and emergent oxynitride phase. The failure to directly observe dopant atoms and vacancies is predominantly attributed to the crystallinity of the sites, rather than the low scattering-contrast. A more complete structure-activity relationship is desired including more focus on nitrogen structurally.

The control of the ratio of interstitial and substitutional doping is beyond the scope of this study, but fine control is reported.[28,69] The synthesis method and conditions will affect the total concentration, type of doping, and spatial distribution. Discussion on the impact of these properties on the framework reorganisation, electronics, and activity were not considered under the scope of the work. For future work, it is desired in particular to understand much more about the formation of the new oxynitride phase: primarily whether synthetic parameters can yield control over the phase composition of the sample, as well as the stoichiometry of the compound itself.

4.5 References

(1) Foo, C.; Li, Y.; Lebedev, K.; Chen, T.; Day, S.; Tang, C.; Tsang, S. C. E. Characterisation of Oxygen Defects and Nitrogen Impurities in TiO_2 Photocatalysts Using Variable-Temperature X-Ray Powder Diffraction. Nat. Commun. 2021, 12 (1), 661. https://doi.org/10.1038/s41467-021-20977-z.

(2) Lan, Y.; Lu, Y.; Ren, Z. Mini Review on Photocatalysis of Titanium Dioxide Nanoparticles and Their Solar Applications. Nano Energy 2013, 2 (5), 1031–1045. https://doi.org/10.1016/j.nanoen.2013.04.002.

(3) Kumar, S. G.; Devi, L. G. Review on Modified TiO_2 Photocatalysis under UV/Visible Light: Selected Results and Related Mechanisms on Interfacial Charge Carrier Transfer Dynamics. J. Phys. Chem. A 2011, 115 (46), 13211–13241. https://doi.org/10.1021/jp204364a.

(4) Kalanur, S. S.; Duy, L. T.; Seo, H. Recent Progress in Photoelectrochemical Water Splitting Activity of WO_3 Photoanodes. Top. Catal. 2018, 61 (9), 1043–1076. https://doi.org/10.1007/s11244-018-0950-1.

(5) Wang, G.; Wang, H.; Ling, Y.; Tang, Y.; Yang, X.; Fitzmorris, R. C.; Wang, C.; Zhang, J. Z.; Li, Y. Hydrogen-Treated TiO_2 Nanowire Arrays for Photoelectrochemical Water Splitting. Nano Lett. 2011, 11 (7), 3026–3033. https://doi.org/10.1021/nl201766h.

(6) Khan, S. U. M.; Al-Shahry, M.; William B. Ingler, J. Efficient Photochemical Water Splitting by a Chemically Modified N-TiO_2. Science 2002. https://doi.org/10.1126/science.1075035.

(7) Matsuoka, M.; Kitano, M.; Takeuchi, M.; Anpo, M.; Thomas, J. M. Photocatalytic Water Splitting on Visible Light-Responsive TiO_2 Thin Films Prepared by a RF Magnetron Sputtering Deposition Method. Top. Catal. 2005, 35 (3), 305–310. https://doi.org/10.1007/s11244-005-3838-9.

(8) Hoang, S.; Berglund, S. P.; Hahn, N. T.; Bard, A. J.; Mullins, C. B. Enhancing Visible Light Photo-Oxidation of Water with TiO_2 Nanowire Arrays via Cotreatment with H_2 and NH_3: Synergistic Effects between Ti^{3+} and N. J. Am. Chem. Soc. 2012, 134 (8), 3659–3662. https://doi.org/10.1021/ja211369s.

(9) Blake, D. M.; Maness, P.-C.; Huang, Z.; Wolfrum, E. J.; Huang, J.; Jacoby, W. A. Application of the Photocatalytic Chemistry of Titanium Dioxide to Disinfection and the Killing of Cancer Cells. Sep. Purif. Methods 1999, 28 (1), 1–50. https://doi.org/10.1080/03602549909351643.

(10) Ani, I. J.; Akpan, U. G.; Olutoye, M. A.; Hameed, B. H. Photocatalytic Degradation of Pollutants in Petroleum Refinery Wastewater by TiO_2- and ZnO-Based Photocatalysts: Recent Development. J. Clean. Prod. 2018, 205, 930–954. https://doi.org/10.1016/j.jclepro.2018.08.189.

(11) Verbruggen, S. W. TiO_2 Photocatalysis for the Degradation of Pollutants in Gas Phase: From Morphological Design to Plasmonic Enhancement. J. Photochem. Photobiol. C Photochem. Rev. 2015, 24, 64–82. https://doi.org/10.1016/j.jphotochemrev.2015.07.001.

(12) Wang, Z.; Lang, X. Visible Light Photocatalysis of Dye-Sensitized TiO_2: The Selective Aerobic Oxidation of Amines to Imines. Appl. Catal. B Environ. 2018, 224, 404–409. https://doi.org/10.1016/j.apcatb.2017.10.002.

(13) Grätzel, M. Solar Energy Conversion by Dye-Sensitized Photovoltaic Cells. Inorg. Chem. 2005, 44 (20), 6841–6851. https://doi.org/10.1021/ic0508371.

(14) Fujishima, A.; Honda, K. Electrochemical Photolysis of Water at a Semiconductor Electrode. Nature 1972, 238 (5358), 37–38. https://doi.org/10.1038/238037a0.

(15) Zhu, T.; Gao, S.-P. The Stability, Electronic Structure, and Optical Property of TiO_2 Polymorphs. J. Phys. Chem. C 2014, 118 (21), 11385–11396. https://doi.org/10.1021/jp412462m.

(16) Liu, Z.; Andreev, Y. G.; Robert Armstrong, A.; Brutti, S.; Ren, Y.; Bruce, P. G. Nanostructured TiO_2(B): The Effect of Size and Shape on Anode Properties for Li-Ion Batteries. Prog. Nat. Sci. Mater. Int. 2013, 23 (3), 235–244. https://doi.org/10.1016/j.pnsc.2013.05.001.

(17) Sato, H.; Endo, S.; Sugiyama, M.; Kikegawa, T.; Shimomura, O. Baddeleyite-Type High-Pressure Phase of TiO_2. Science 1991, 251, 786–788. https://doi.org/10.1126/science.251.4995.786.

(18) Dubrovinskaia, N. A.; Dubrovinsky, L. S.; Ahuja, R.; Prokopenko, V. B.; Dmitriev, V.; Weber, H.-P.; Osorio-Guillen, J. M.; Johansson, B. Experimental and Theoretical Identification of a New High-Pressure TiO_2 Polymorph. Phys. Rev. Lett. 2001, 87 (27), 275501. https://doi.org/10.1103/PhysRevLett.87.275501.

(19) Dubrovinsky, L. S.; Dubrovinskaia, N. A.; Swamy, V.; Muscat, J.; Harrison, N. M.; Ahuja, R.; Holm, B.; Johansson, B. The Hardest Known Oxide. Nature 2001, 410 (6829), 653–654. https://doi.org/10.1038/35070650.

(20) Mattesini, M.; de Almeida, J.; Dubrovinsky, L.; Dubrovinskaia, N.; Johansson, B.; Ahuja, R. Cubic TiO_2 as a Potential Light Absorber in Solar-Energy Conversion. Phys. Rev. B 2004, 70 (11).

(21) Mattesini, M.; de Almeida, J. S.; Dubrovinsky, L.; Dubrovinskaia, N.; Johansson, B.; Ahuja, R. High-Pressure and High-Temperature Synthesis of the Cubic TiO_2 Polymorph. Phys. Rev. B 2004, 70 (21), 212101. https://doi.org/10.1103/PhysRevB.70.212101.

(22) Niu, M.; Cheng, D.; Cao, D. Fluorite TiO_2(111) Surface Phase for Enhanced Visible-Light Solar Energy Conversion. J. Phys. Chem. C 2014, 118 (35), 20107–20111. https://doi.org/10.1021/jp504818j.

(23) Di Valentin, C.; Pacchioni, G.; Selloni, A. Origin of the Different Photoactivity of N-Doped Anatase and Rutile TiO_2. Phys. Rev. B 2004, 70 (8), 085116. https://doi.org/10.1103/PhysRevB.70.085116.

(24) Li, G.; Gray, K. A. The Solid–Solid Interface: Explaining the High and Unique Photocatalytic Reactivity of TiO_2-Based Nanocomposite Materials. Chem. Phys. 2007, 339 (1), 173–187. https://doi.org/10.1016/j.chemphys.2007.05.023.

(25) Yin, S.; Aita, Y.; Komatsu, M.; Sato, T. Visible-Light-Induced Photocatalytic Activity of $TiO_{2-x}N_y$ Prepared by Solvothermal Process in Urea–Alcohol System. J. Eur. Ceram. Soc. 2006, 26 (13), 2735–2742. https://doi.org/10.1016/j.jeurceramsoc.2005.05.012.

(26) Nakata, K.; Fujishima, A. TiO_2 Photocatalysis: Design and Applications. J. Photochem. Photobiol. C Photochem. Rev. 2012, 13 (3), 169–189. https://doi.org/10.1016/j.jphotochemrev.2012.06.001.

(27) Zhou, X.; Liu, N.; Schmuki, P. Photocatalysis with TiO_2 Nanotubes: "Colorful" Reactivity and Designing Site-Specific Photocatalytic Centers into TiO_2 Nanotubes. ACS Catal. 2017, 7 (5), 3210–3235. https://doi.org/10.1021/acscatal.6b03709.

(28) Lynch, J.; Giannini, C.; Cooper, J. K.; Loiudice, A.; Sharp, I. D.; Buonsanti, R. Substitutional or Interstitial Site-Selective Nitrogen Doping in TiO_2 Nanostructures. J. Phys. Chem. C 2015, 119 (13), 7443–7452. https://doi.org/10.1021/jp512775s.

(29) Schneider, J.; Matsuoka, M.; Takeuchi, M.; Zhang, J.; Horiuchi, Y.; Anpo, M.; Bahnemann, D. W. Understanding TiO_2 Photocatalysis: Mechanisms and Materials. Chem. Rev. 2014, 114 (19), 9919–9986. https://doi.org/10.1021/cr5001892.

(30) Wu, C.; Yue, Y.; Deng, X.; Hua, W.; Gao, Z. Investigation on the Synergetic Effect between Anatase and Rutile Nanoparticles in Gas-Phase Photocatalytic Oxidations. Catal. Today 2004, 93–95, 863–869. https://doi.org/10.1016/j.cattod.2004.06.087.

(31) Ohno, T.; Tokieda, K.; Higashida, S.; Matsumura, M. Synergism between Rutile and Anatase TiO_2 Particles in Photocatalytic Oxidation of Naphthalene. Appl. Catal. Gen. 2003, 244 (2), 383–391. https://doi.org/10.1016/S0926-860X(02)00610-5.

(32) Hurum, D. C.; Gray, K. A.; Rajh, T.; Thurnauer, M. C. Recombination Pathways in the Degussa P25 Formulation of TiO_2: Surface versus Lattice Mechanisms. J. Phys. Chem. B 2005, 109 (2), 977–980. https://doi.org/10.1021/jp045395d.

(33) Somorjai, G. A.; Bratlie, K. M.; Montano, M. O.; Park, J. Y. Dynamics of Surface Catalyzed Reactions; the Roles of Surface Defects, Surface Diffusion, and Hot Electrons. J. Phys. Chem. B 2006, 110 (40), 20014–20022. https://doi.org/10.1021/jp062569d.

(34) Livraghi, S.; Paganini, M. C.; Giamello, E.; Selloni, A.; Di Valentin, C.; Pacchioni, G. Origin of Photoactivity of Nitrogen-Doped Titanium Dioxide under Visible Light. J. Am. Chem. Soc. 2006, 128 (49), 15666–15671. https://doi.org/10.1021/ja064164c.

(35) Chen, X.; Liu, L.; Yu, P. Y.; Mao, S. S. Increasing Solar Absorption for Photocatalysis with Black Hydrogenated Titanium Dioxide Nanocrystals. Science 2011, 331 (6018), 746–750. https://doi.org/10.1126/science.1200448.

(36) Ganduglia-Pirovano, M.; Hofmann, A.; Sauer, J. Oxygen Vacancies in Transition Metal and Rare Earth Oxides: Current State of Understanding and Remaining Challenges. Surf. Sci. Rep. 2007, 62 (6), 219–270. https://doi.org/10.1016/j.surfrep.2007.03.002.

(37) Wang, J.; Tafen, D. N.; Lewis, J. P.; Hong, Z.; Manivannan, A.; Zhi, M.; Li, M.; Wu, N. Origin of Photocatalytic Activity of Nitrogen-Doped TiO_2 Nanobelts. J. Am. Chem. Soc. 2009, 131 (34), 12290–12297. https://doi.org/10.1021/ja903781h.

(38) Monfort, O.; Plesch, G. Bismuth Vanadate-Based Semiconductor Photocatalysts: A Short Critical Review on the Efficiency and the Mechanism of Photodegradation of Organic Pollutants. Environ. Sci. Pollut. Res. 2018, 25 (20), 19362–19379. https://doi.org/10.1007/s11356-018-2437-9.

(39) Thomas, A. G.; Flavell, W. R.; Mallick, A. K.; Kumarasinghe, A. R.; Tsoutsou, D.; Khan, N.; Chatwin, C.; Rayner, S.; Smith, G. C.; Stockbauer, R. L.; Warren, S.; Johal, T. K.; Patel, S.; Holland, D.; Taleb,

A.; Wiame, F. Comparison of the Electronic Structure of Anatase and Rutile TiO_2 Single-Crystal Surfaces Using Resonant Photoemission and x-Ray Absorption Spectroscopy. Phys. Rev. B 2007, 75 (3), 035105. https://doi.org/10.1103/PhysRevB.75.035105.

(40) Di Valentin, C.; Pacchioni, G.; Selloni, A.; Livraghi, S.; Giamello, E. Characterization of Paramagnetic Species in N-Doped TiO_2 Powders by EPR Spectroscopy and DFT Calculations. J. Phys. Chem. B 2005, 109 (23), 11414–11419. https://doi.org/10.1021/jp051756t.

(41) Jiang, J.; Xing, Z.; Li, M.; Li, Z.; Wu, X.; Hu, M.; Wan, J.; Wang, N.; Besov, A. S.; Zhou, W. In Situ Ti3+/N-Codoped Three-Dimensional (3D) Urchinlike Black TiO_2 Architectures as Efficient Visible-Light-Driven Photocatalysts. Ind. Eng. Chem. Res. 2017, 56 (28), 7948–7956. https://doi.org/10.1021/acs.iecr.7b01693.

(42) Cheng, H.; Selloni, A. Surface and Subsurface Oxygen Vacancies in Anatase TiO_2 and Differences with Rutile. Phys. Rev. B 2009, 79 (9), 092101. https://doi.org/10.1103/PhysRevB.79.092101.

(43) Li, Y.; Peng, Y.-K.; Hu, L.; Zheng, J.; Prabhakaran, D.; Wu, S.; Puchtler, T. J.; Li, M.; Wong, K.-Y.; Taylor, R. A.; Tsang, S. C. E. Photocatalytic Water Splitting by N-TiO_2 on MgO (111) with Exceptional Quantum Efficiencies at Elevated Temperatures. Nat. Commun. 2019, 10 (1), 4421. https://doi.org/10.1038/s41467-019-12385-1.

(44) Asahi, R.; Morikawa, T.; Ohwaki, T.; Aoki, K.; Taga, Y. Visible-Light Photocatalysis in Nitrogen-Doped Titanium Oxides. Science 2001, 293 (5528), 269–271. https://doi.org/10.1126/science.1061051.

(45) Jiang, D.; Otitoju, T. A.; Ouyang, Y.; Shoparwe, N. F.; Wang, S.; Zhang, A.; Li, S. A Review on Metal Ions Modified TiO_2 for Photocatalytic Degradation of Organic Pollutants. Catalysts 2021, 11 (9), 1039. https://doi.org/10.3390/catal11091039.

(46) Park, Y.; Kim, W.; Park, H.; Tachikawa, T.; Majima, T.; Choi, W. Carbon-Doped TiO2 Photocatalyst Synthesized without Using an External Carbon Precursor and the Visible Light Activity. Appl. Catal. B Environ. 2009, 91 (1), 355–361. https://doi.org/10.1016/j.apcatb.2009.06.001.

(47) Diwald, O.; Thompson, T. L.; Zubkov, T.; Walck, S. D.; Yates, J. T. Photochemical Activity of Nitrogen-Doped Rutile TiO_2(110) in Visible Light. J. Phys. Chem. B 2004, 108 (19), 6004–6008. https://doi.org/10.1021/jp031267y.

(48) Irie, H.; Watanabe, Y.; Hashimoto, K. Nitrogen-Concentration Dependence on Photocatalytic Activity of $TiO_{2-X}N_x$ Powders. J. Phys. Chem. B 2003, 107 (23), 5483–5486. https://doi.org/10.1021/jp030133h.

(49) Lindgren, T.; Mwabora, J. M.; Avendaño, E.; Jonsson, J.; Hoel, A.; Granqvist, C.-G.; Lindquist, S.-E. Photoelectrochemical and Optical Properties of Nitrogen Doped Titanium Dioxide Films Prepared by Reactive DC Magnetron Sputtering. J. Phys. Chem. B 2003, 107 (24), 5709–5716. https://doi.org/10.1021/jp027345j.

(50) Di Valentin, C.; Finazzi, E.; Pacchioni, G.; Selloni, A.; Livraghi, S.; Paganini, M. C.; Giamello, E. N-Doped TiO_2: Theory and Experiment. Chem. Phys. 2007, 339 (1), 44–56. https://doi.org/10.1016/j.chemphys.2007.07.020.

(51) Tryba, B.; Wozniak, M.; Zolnierkiewicz, G.; Guskos, N.; Morawski, A.; Colbeau-Justin, C.; Wrobel, R.; Nitta, A.; Ohtani, B. Influence of an Electronic Structure of N-TiO_2 on Its Photocatalytic Activity towards Decomposition of Acetaldehyde under UV and Fluorescent Lamps Irradiation. Catalysts 2018, 8 (2), 85. https://doi.org/10.3390/catal8020085.

(52) Sait, R.; Govindarajan, S.; Cross, R. Nitridation of Optimised TiO2 Nanorods through PECVD towards Neural Electrode Application. Materialia 2018, 4, 127–138. https://doi.org/10.1016/j.mtla.2018.09.015.

(53) Clatworthy, E. B.; Yick, S.; Murdock, A. T.; Allison, M. C.; Bendavid, A.; Masters, A. F.; Maschmeyer, T. Enhanced Photocatalytic Hydrogen Evolution with TiO_2–TiN Nanoparticle Composites. J. Phys. Chem. C 2019, 123 (6), 3740–3749. https://doi.org/10.1021/acs.jpcc.8b09221.

(54) Ishii, S.; Shinde, S. L.; Jevasuwan, W.; Fukata, N.; Nagao, T. Hot Electron Excitation from Titanium Nitride Using Visible Light. ACS Photonics 2016, 3 (9), 1552–1557. https://doi.org/10.1021/acsphotonics.6b00360.

(55) Barragan, A. A.; Hanukovich, S.; Bozhilov, K.; Yamijala, S. S. R. K. C.; Wong, B. M.; Christopher, P.; Mangolini, L. Photochemistry of Plasmonic Titanium Nitride Nanocrystals. J. Phys. Chem. C 2019, 123 (35), 21796–21804. https://doi.org/10.1021/acs.jpcc.9b06257.

(56) Kharitonov, A.; Kharintsev, S.; Kharintsev, S. Tunable Optical Materials for Multi-Resonant Plasmonics: From TiN to TiON [Invited]. Opt. Mater. Express 2020, 10 (2), 513–531. https://doi.org/10.1364/OME.382160.

(57) Zhang, Z.; Goodall, J. B. M.; Morgan, D. J.; Brown, S.; Clark, R. J. H.; Knowles, J. C.; Mordan, N. J.; Evans, J. R. G.; Carley, A. F.; Bowker, M.; Darr, J. A. Photocatalytic Activities of N-Doped Nano-Titanias and Titanium Nitride. J. Eur. Ceram. Soc. 2009, 29 (11), 2343–2353. https://doi.org/10.1016/j.jeurceramsoc.2009.02.008.

(58) Yoo, J. B.; Yoo, H. J.; Jung, H. J.; Kim, H. S.; Bang, S.; Choi, J.; Suh, H.; Lee, J.-H.; Kim, J.-G.; Hur, N. H. Titanium Oxynitride Microspheres with the Rock-Salt Structure for Use as Visible-Light Photocatalysts. J. Mater. Chem. A 2016, 4 (3), 869–876. https://doi.org/10.1039/C5TA06758H.

(59) Yang, X.; Li, C.; Yang, B.; Wang, W.; Qian, Y. Optical Properties of Titanium Oxynitride Nanocrystals Synthesized via a Thermal Liquid–Solid Metathesis Reaction. Chem. Phys. Lett. 2004, 383 (5), 502–506. https://doi.org/10.1016/j.cplett.2003.11.037.

(60) Do, H.; Wu, Y.-H.; Dai, V.-T.; Peng, C.-Y.; Yen, T.-C.; Chang, L. Structure and Property of Epitaxial Titanium Oxynitride Grown on MgO(001) Substrate by Pulsed Laser Deposition. Surf. Coat. Technol. 2013, 214, 91–96. https://doi.org/10.1016/j.surfcoat.2012.11.008.

(61) Li, J.; Liu, Y.; Zhu, Z.; Zhang, G.; Zou, T.; Zou, Z.; Zhang, S.; Zeng, D.; Xie, C. A Full-Sunlight-Driven Photocatalyst with Super Long-Persistent Energy Storage Ability. Sci. Rep. 2013, 3 (1), 2409. https://doi.org/10.1038/srep02409.

(62) Diebold, U. The Surface Science of Titanium Dioxide. Surf. Sci. Rep. 2003, 48 (5), 53–229. https://doi.org/10.1016/S0167-5729(02)00100-0.

(63) Hummer, D. R.; Heaney, P. J.; Post, J. E. Thermal Expansion of Anatase and Rutile between 300 and 575 K Using Synchrotron Powder X-Ray Diffraction. Powder Diffr. 2007, 22 (4), 352–357. https://doi.org/10.1154/1.2790965.

(64) Ling, W.; Wang, H.-J.; Li, T. In Situ High Temperature X-Ray Diffraction Study of Anatase and Rutile. Acta Phys Sin 2013, 62 (14), 146402. https://doi.org/10.7498/aps.62.146402.

(65) Li, Y.; Tsang, S. C. E. Recent Progress and Strategies for Enhancing Photocatalytic Water Splitting. Mater. Today Sustain. 2020, 9, 100032. https://doi.org/10.1016/j.mtsust.2020.100032.

(66) Savio, A. K. P. D.; Fletcher, J.; Smith, K.; Iyer, R.; Bao, J. M.; Robles Hernández, F. C. Environmentally Effective Photocatalyst CoO–TiO_2 Synthesized by Thermal Precipitation of Co in Amorphous TiO_2. Appl. Catal. B Environ. 2016, 182, 449–455. https://doi.org/10.1016/j.apcatb.2015.09.047.

(67) Ren, Z.; Chen, C.; Fu, X.; Wang, J.; Fan, C.; Qian, G.; Wang, Z. TiO_2/C Composites Nanorods Synthesized by Internal-Reflux Method for Lithium-Ion Battery Anode Materials. Mater. Lett. 2014, 117, 124–127. https://doi.org/10.1016/j.matlet.2013.11.058.

(68) Zhang, K.; Zhou, W.; Zhang, X.; Sun, B.; Wang, L.; Pan, K.; Jiang, B.; Tian, G.; Fu, H. Self-Floating Amphiphilic Black TiO_2 Foams with 3D Macro-Mesoporous Architectures as Efficient Solar-Driven Photocatalysts. Appl. Catal. B Environ. 2017, 206, 336–343. https://doi.org/10.1016/j.apcatb.2017.01.059.

(69) Zhang, Z.; Wang, X.; Long, J.; Gu, Q.; Ding, Z.; Fu, X. Nitrogen-Doped Titanium Dioxide Visible Light Photocatalyst: Spectroscopic Identification of Photoactive Centers. J. Catal. 2010, 276 (2), 201–214. https://doi.org/10.1016/j.jcat.2010.07.033.

(70) Ito, Y.; Goto, T. Electrochemistry of Nitrogen and Nitrides in Molten Salts. J. Nucl. Mater. 2005, 344 (1), 128–135. https://doi.org/10.1016/j.jnucmat.2005.04.030.

(71) Nagaraj, B.; Devi, L. G. Silver Metalized Mixed Phase Manganese-Doped Titania: Variation of Electric Field and Band Bending within the Space Charge Region with Respect to the Silver Content. J. Mol. Catal. Chem. 2014, 390, 142–151. https://doi.org/10.1016/j.molcata.2014.03.019.

(72) Yang, G.; Jiang, Z.; Shi, H.; Xiao, T.; Yan, Z. Preparation of Highly Visible-Light Active N-Doped TiO_2 Photocatalyst. J. Mater. Chem. 2010, 20 (25), 5301–5309. https://doi.org/10.1039/C0JM00376J.

(73) Misra, S. K.; Andronenko, S. I.; Tipikin, D.; Freed, J. H.; Somani, V.; Prakash, O. Study of Paramagnetic Defect Centers in As-Grown and Annealed TiO_2 Anatase and Rutile Nanoparticles by a Variable-Temperature X-Band and High-Frequency (236 GHz) EPR. J. Magn. Magn. Mater. 2016, 401, 495–505. https://doi.org/10.1016/j.jmmm.2015.10.072.

(74) Liu, G.; Yin, L.-C.; Wang, J.; Niu, P.; Zhen, C.; Xie, Y.; Cheng, H.-M. A Red Anatase TiO_2 Photocatalyst for Solar Energy Conversion. Energy Environ. Sci. 2012, 5 (11), 9603–9610. https://doi.org/10.1039/C2EE22930G.

(75) Li, H.; Guo, Y.; Robertson, J. Calculation of TiO_2 Surface and Subsurface Oxygen Vacancy by the Screened Exchange Functional. J. Phys. Chem. C 2015, 119 (32), 18160–18166. https://doi.org/10.1021/acs.jpcc.5b02430.

(76) Fisicaro, G.; Filice, S.; Scalese, S.; Compagnini, G.; Reitano, R.; Genovese, L.; Goedecker, S.; Deretzis, I.; La Magna, A. Wet Environment Effects for Ethanol and Water Adsorption on Anatase TiO_2 (101) Surfaces. J. Phys. Chem. C 2020, 124 (4), 2406–2419. https://doi.org/10.1021/acs.jpcc.9b05400.

(77) Hasegawa, M.; Yagi, T. Systematic Study of Formation and Crystal Structure of 3d-Transition Metal Nitrides Synthesized in a Supercritical Nitrogen Fluid under 10 GPa and 1800K Using Diamond Anvil Cell and YAG Laser Heating. J. Alloys Compd. 2005, 403 (1), 131–142. https://doi.org/10.1016/j.jallcom.2005.04.197.

(78) Banus, M. D.; Reed, T. B.; Strauss, A. J. Electrical and Magnetic Properties of TiO and VO. Phys. Rev. B 1972, 5 (8), 2775–2784. https://doi.org/10.1103/PhysRevB.5.2775.

(79) Hou, X.-M.; Hu, X.-J.; Chou, K.-C. Kinetics of Thermal Oxidation of Titanium Nitride Powder at Different Oxidizing Atmospheres. J. Am. Ceram. Soc. 2011, 94 (2), 570–575. https://doi.org/10.1111/j.1551-2916.2010.04084.x.

(80) Scheiber, P.; Fidler, M.; Dulub, O.; Schmid, M.; Diebold, U.; Hou, W.; Aschauer, U.; Selloni, A. (Sub)Surface Mobility of Oxygen Vacancies at the TiO_2 Anatase (101) Surface. Phys. Rev. Lett. 2012, 109 (13), 136103. https://doi.org/10.1103/PhysRevLett.109.136103.

(81) Hussain, H.; Tocci, G.; Woolcot, T.; Torrelles, X.; Pang, C. L.; Humphrey, D. S.; Yim, C. M.; Grinter, D. C.; Cabailh, G.; Bikondoa, O.; Lindsay, R.; Zegenhagen, J.; Michaelides, A.; Thornton, G. Structure of a Model TiO_2 Photocatalytic Interface. Nat. Mater. 2017, 16 (4), 461–466. https://doi.org/10.1038/nmat4793.

(82) Zhao, W.-N.; Liu, Z.-P. Mechanism and Active Site of Photocatalytic Water Splitting on Titania in Aqueous Surroundings. Chem. Sci. 2014, 5 (6), 2256–2264. https://doi.org/10.1039/C3SC53385A.

Chapter 5: Electrochemical lithium storage in palladium nanoparticles: phase behaviour and stability

5.1 Abstract

A thermal lithiation of palladium nanoparticles that was developed by the Tsang group yields interstitial lithium-doping at the octahedral holes.[1–3] The synthesis conditions were further studied to show inhomogeneous de/lithiation, and optimised to yield monophasic samples. An in-situ lithiation process was used for the first time, and shown by VT-SXPD to increase the thermal stability by more than 300°C. Complex doping-dependent phase behaviour was observed at high temperature- and reciprocal-space resolution, involving the inter-transfer of lithium atoms between different phases in the powder ensemble referred to as occupancy equilibration.

The thermal lithiation was directly compared with electrochemical lithiation as an LIB anode material. The pristine nanoparticles exhibited stable and good capacity as a cyclable lithium store by electrochemical lithiation. In-operando SPXD data correlated the electrochemical stability to unexpected but discrete phase transitions. Much more significant rearrangement and lithiation was observed than the thermal method, with indication of significant volume changes of the palladium and increased disorder on de/lithiation. Despite this, the discharge or charge process is very stable at a molar capacity of ~1 electrons per Pd, with ex-situ PDF showing local order is retained.

5.2 Introduction

5.2.1 Agile ammonia synthesis and analytical context

Hydrogen produced from renewable sources is a requirement of the agile ammonia synthesis, as part of the self-contained energy generation/storage framework. However, the daily and seasonal intermittency of wind and solar cannot provide a stable supply of hydrogen or electrical power for the ammonia synthesis. It is not desirable to maintain large-scale hydrogen storage, which can be costly and dangerous. Here, we present an investigation on the use of palladium nanoparticles as an anode material for lithium ion batteries (LIB), as part of the integration of battery energy storage systems (BESS) into grid-management, particularly for high frequency-response.

The previous chapter investigated the structural characterisation of nitrogen dopants and oxygen vacancies. Regarding the analytical context of this work, the host framework is much simpler than TiO_2: only one host element, which has relatively fixed formal oxidation state (lithium ion also retaining a fixed formal oxidation state), in principle only interstitial doping is known, in principle only one polymorph present, increased unit-cell symmetry with full equivalence of all sites, and less focus on defects and vacancies.

5.2.2 Palladium nanoparticles

Zero-valent transition-metal nanoparticles are an archetypal system in the chemical sciences which have received much research, as both monometallic (e.g. Au,[4] Pt,[5] Pd[1,6]) and bimetallic nanoparticles.[7–10] Palladium is an important component in many catalysts, in both homogeneous[11] and heterogeneous systems,[2,12–15] as well as encapsulation inside porous frameworks as clusters.[16–18] These systems are generally well-characterised in terms of

strain,[15,19] facet-dependence,[20] size-dependence,[21,22] and nucleation[23,24] but their versatility remains under-explored., in particular with respect to light-element doping and alloys.

5.2.3 Light-element doping in transition metal lattices

5.2.3.1 Packing and geometry

Whether or not a dopant is incorporated into a metal lattice is highly dependent on the matching of size and electronic properties, much like archetypal guest-host interactions in biological systems.[25] In the solid-state, there are some general rules about the packing of atoms, which are loosely upheld and respected. The limiting-ratio range between the radii of the framework and dopant atom of tetrahedral sites is 0.225-0.414 and for octahedral sites 0.414-0.732. The most common structure of palladium (163 pm) is the $Fm\bar{3}m$ cubic close-packed arrangement. The size range for the tetrahedral site is from 37 pm to 67 pm, and 68 pm to 119 pm for the octahedral site. Hence, hydrogen, lithium, boron, and carbon are able to be doped interstitially, while oxygen is too large. The main dopant discussed in this work is lithium. Elemental lithium is precluded from insertion as a ground-state atom due to its large radius 167 pm (radius ratio = 1.0). However, lithium ions (76 pm) are able to occupy the octahedral-hole sites. Indeed, adjacent unpublished research from the Tsang group has shown the Bader charge of interstitial lithium in palladium to be near +1.[3]

5.2.3.2 Variety of dopants

Palladium hydride is a well-researched compound with application in hydrogen storage, purification, and sensing.[23,26,27] The phase transformation from the pristine metal has been monitored by in-situ coherent X-ray imaging showing tensile surface stress and internal microstrain during doping.[19] Vogel et al. followed the phase transition by in-situ XRD,

showing repeated low impact on defects and structure, referred to by them as hydrogen breathing.[28] In-situ characterisation during electro-sorption has also been shown.[29] Interstitial boron has been shown to enhance catalysis in formic acid oxidation,[30] oxygen reduction,[31] and partial hydrogenation of acetylene.[2] Interstitial carbon doping has been shown to enhance ultra-selective hydrogenation, with characterisation by TEM and EDX, in-operando XAS and XANES, and SXPD.[14,27,32,33]

Interstitial dopants in palladium are metastable structures at room temperature, which are unstable and vulnerable to deintercalation. Thermal and oxidative stability must be considered. Boron is the most stable interstitial dopant (250°C), followed by lithium (150-200°C), and then carbon (150°C).[2]

5.2.3.3 Palladium-lithium

Previous publications from the Tsang group have primarily investigated thermal lithiation doping, which yields the topotactic $Fm\bar{3}m$ $Pd^{int}Li$ which exhibits improved catalysis in the selective hydrogenation of acetylene.[2] The studies showed occupancy at the interstitial octahedral hole and strain at both an atomic and nanoparticle length-scale. Sakamoto et al. found the solubility of lithium in palladium to be ~4%mol at room temperature, increasing to 10.3%mol.[34] The maximum lithium intercalation was calculated in theoretical works to be dependent on the charge transfer to the palladium framework of 0.1 electron per Pd, i.e. 10% lithium occupancy.[35] By NPD, Ziemecki et al. refined a structural model to show this experimentally with an occupancy of ~15%,[36] which is in agreement with other reports.[37] The Tsang group have more recently used XPDF to show an occupancy of 13.7%.[38] It is usual in the literature to use Vegard's law to estimate lithium occupancy based on the known maximum lithium occupancy and maximum lattice parameter.

Occurrences of discrete palladium-lithium phases in literature

In 1966, a discrete *Pm*$\bar{3}$*m* PdLi phase was reported by Ferro.[39] This is analogous to the previously reported gold-lithium intermetallic compound, *Pm*$\bar{3}$*m* ($Au_{0.9}Li_{0.1}$)Li, which is approximately equimolar.[40] In a following paper,[41] they reported *P6/mmm* $PdLi_2$, which is structurally analogous to the previously reported $PtLi_2$. However, they failed to determine the structures of several phases. These were solved by Van Vucht et al.[42] and shown to exhibit analogous structures to the gold- and platinum-lithium systems (Table 5-1). The previously unidentified phases were a low lithium *Fm*$\bar{3}$*m* Pd_7Li, an equimolar *P*$\bar{6}$*m2* PdLi, and high-lithium *Fm*$\bar{3}$*m* $PdLi_3$ and *I*$\bar{4}$*3d* Pd_4Li_{15}. All of these palladium-lithium phases were synthesised by heating the pure lithium and palladium powders under reduced pressure of argon at high temperatures (800°C), followed by prolonged annealing (600°C for up to 3 days). Loebich et. al reported two fractional phases $Pd_{0.94}Li_{0.06}$ and $Pd_{5.26}Li_{2.74}$.[43,44]

Reference	Space group	Pd	Li	Lithium ratio	Volume / A^{-3}	Analogous structure
Hull (1921)[45]	*Fm*$\bar{3}$*m*	1	0	N/A	61.6	-
Ferro (1966)[39]	*Pm*$\bar{3}$*m*	1	1	1.00	26.6	AuLi
Ferro (1968)[41]	*P6/mmm*	2	1	0.50	42.3	Pt_2Li
van Vucht et al. (1976)[42]	*Fm*$\bar{3}$*m*	7	1	0.14	449.5	Pt_7Li
‘’	*P*$\bar{6}$*m2*	1	1	1.00	27.4	PtLi
‘’	*Fm*$\bar{3}$*m*	1	3	3.00	236.8	$AuLi_3$
‘’	*I*$\bar{4}$*3d*	4	15	3.75	1216.8	Au_4Li1_5
Loebich et al. (1977)[43]	*Fm*$\bar{3}$*m*	0.94	0.06	0.06	58.3	-
Loebich et al. (1979)[44]	P_12/m	5.26	2.74	0.52	112.1	-

Table 5-1. ICSD entries of bimetallic palladium-lithium structures.

These phases are considered to be discrete intermetallic phases. Here, a note of notation has to be made. In this thesis, the topotactic expanded *Fm*$\bar{3}$*m* lithiated phase that experiences solid-solution behaviour is referred to as $Pd^{int}Li$. This notation is meant to

distinguish the material from the equimolar primitive phase $Pm\bar{3}m$ PdLi which requires a discrete phase transition.

5.2.4 Lithium-ion batteries (LIB)

5.2.4.1 Fundamental theory

In a typical lithium-ion cell, two electrodes are separated by an electronically insulating separator and electrolyte. Electrical energy can be used to drive electron transfer between two electrodes to yield a thermodynamically disfavoured product. Current is allowed to flow around the external circuit, while lithium ions move through the electrolyte in order to retain charge balancing at the electrodes. The high chemical energy can be stored by removing the external circuit, and then can be released when desired. In secondary cells (rechargeable), both electrodes carry out cathodic and anodic processes in an alternating cycle. The convention is to refer to electrodes with respect to their redox participation under equilibrating conditions (discharge), i.e. the high reduction potential electrode, ~3-4 V vs. Li^+/Li, that is reduced under discharge is the cathode, and the low reduction potential electrode, ~0-3 V vs. Li^+/Li , that is oxidised is the anode.

5.2.4.2 Electrode materials

Lithium insertion mechanisms

Cathode materials are dominated by conversion-type electrode materials. Many of the lithium metal oxide systems undergo formal redox and exhibit discrete and significant phase changes upon cycling.[46] A typical cathode material is lithium nickel manganese cobalt oxide (NMC) which has a theoretical capacity of ~275 mA h g^{-1} (though not currently attainable due to high instability under deep delithiation)[46]. Meanwhile, the archetypal anode material

is graphite, which is also the archetypal example of intercalation-type lithium insertion (372 mA h g^{-1}). The change in the structure of this type of material is topotactic, observed by continuous or discrete changes in lattice parameter, or as slight atomic rearrangement to a structure highly symmetry-related to the original. Alloy-type materials generally belong to groups III, IV, and V, and can accept lithium ions in host-to-guest ratios of much greater than 1 as an intermetallic alloy.[47] Much is said about silicon as the next significant increase in anode capacity due to the extremely high theoretical capacity of 3572 mA h g^{-1}, calculated based on the fully lithiated alloy $Li_{15}Si_4$.[48,49] However, materials that operate alloying mechanisms currently suffer from large volumetric expansion, which causes loss of contact with the current collector, uncontrolled SEI formation, and electrode pulverisation.[47] This is often prevented by encapsulation that prohibits expansion, or by hierarchical morphologies that allow expansion.[50,51]

Coulombic capacity

5.2.5 Integration into grid-scale storage and AAS

Levelling peak load by using battery energy-storage systems (BESS) is an inevitable part of the new energy landscape, and will be a significant energy vector within the AAS. LIB are the most mature technology, being calculated to become the primary energy-storage mechanism by 2030.[52] As opposed to chemical energy, which can offer bulk power, LIB fulfil a wider range of grid power-management due to their flexibility. The majority of grid-scale LIB integration is for energy arbitrage, which is the buying and selling of energy at fluctuating prices for economic gain. Through market forces, there is an incentive to load-levelling and peak shaving. Importantly, this does not require large facilities or investment, but is equally effective as the sum of many small BESS. The rise of better and cheaper LIB

will introduce the bifunctional energy consumer/supplier, who is more independent, and a utility in themselves for traditional energy suppliers to buy from.[53] Additionally, LIB in particular can operate at a range of power ratings and can be deployed very quickly at low cost. By inputting or removing energy, the frequency of the grid can be maintained, known as frequency response.

5.2.6 Current structural characterisation and problems

Despite the archetypal simple structure of Pd-Li, the poorly-scattering lithium dopant makes characterisation difficult especially at low concentration, with most elastic and spectroscopic methods interrogating the palladium framework.[27] Analysis using NPD is also hindered by the very high neutron absorption cross-section of lithium, causing opposite problems in data collection and analysis. In this work, crystalline changes in the palladium framework will be the primary method in discerning the nature of the doping.

It is emphasised that there have been no new entries for bimetallic palladium-lithium materials in the ICSD, even of the known compounds, since 1979. Furthermore, only the report by van Vucht is written in English. Many subsequent reports focus on the eutectic system, which assesses the solubility of palladium into lithium, and frequently involves the distinct Pd_7Li phase.[54–56] Closer to our application, palladium foil has been electrochemically lithiated using lithium electrolytes, with characterisation predominantly focussing on the depth of lithium penetration.[57] However, palladium is not lithiated against lithium metal and never with intention to demonstrate cyclability or energy storage. Hence, it is believed that the palladium-lithium system remains highly under-researched.

5.2.7 Aims of investigation

Here, we aim to investigate the palladium-lithium system as a possible lithium-storage material in LIB, with an eventual aim to observe the phase evolution by an in-operando SXPD experiment. Palladium is a good candidate due to the ability to accommodate lithium ions, high number of interstitial sites, rigid framework, and high conductivity. It was thought that the framework will allow the insertion of many lithium ions at a reasonable gravimetric capacity and volume expansion. Similarly, it has been reported that the repeated electro-sorption of hydrogen results in negligible defects and degradation.[28] Hence, it was envisaged that the material may be a low expansion-high capacity anode material LIB anode material. It was aimed to provide comprehensive structural and mechanistic characterisation of the electrochemical lithiation at high temporal and reciprocal-space resolution. The focus of the research will be on the mechanism of lithium storage and subsequent phase degradation. However, in-depth analysis of the LIB system, such as ink formulation, electrolyte optimisation, and investigative cycling experiments were quickly side-lined.

5.2.7.1 Outline

Firstly, investigation of the thermal lithiation was carried out, which aimed to further understand the $Pd^{int}Li$ phase, in particular, monitoring the effect of synthesis on Bragg diffraction properties and the subsequent delithiation monitored by VT-SXPD. This work builds on previous work on the palladium-lithium system by the Tsang group, which showed that chemical lithiation of palladium metal results in interstitial doping at the octahedral hole.[3,38,58] Secondly, the general suitability of the material as an electrochemical lithium store was evaluated, involving an in-operando SXPD experiment. A comparison between the two lithiation methods is presented.

5.3 Results and discussion

5.3.1 Optimising particle size for SXPD

The eventual aims of this investigation involved the use of palladium nanoparticles as an anode material in LIBs and the collection of in-operando diffraction data, for which particle size and distribution is a crucial parameter. On I11, an in-operando coin-cell is unable to be spun in the ω-axis, which is important for good counting statistics in Debye-Sherer transmission geometry. Additionally, the electrode is very thin (0.1 mm^3 irradiated volume compared to ~1 mm^3 for capillaries). In order to maximise the total palladium on the electrode (for sample in the beam), increase the crystallinity (for flux at the detector), and increase the particle size (for peak shape) the palladium loading of the supported nanoparticles was chosen to be high at 50%wt. Large crystallites do not solve the problem of particle averaging, but a large number of crystallites using the high loading should be beneficial. Additionally, the effect of poor sample averaging was minimised by using the image detector on I11-1.

5.3.2 Palladium nanoparticle synthesis: inadvertent $Pd^{int}C$ formation

Though the report by Ellis et al.[2] states that the solid-state lithiation using lithium acetate can yield high palladium loading, there has been difficulty yielding pure products. Similar to literature, we observe only Pd at 450°C and 550°C (a = 3.89 Å) (Figure 5-1). However, we also show that at lower temperatures of 350°C and 250°C, there is a co-existence of two $Fm\bar{3}m$ phases: Pd (a = 3.89 Å) and a broader expanded phase Pd_{exp} (a = 3.99 Å) (Δa = 0.1 Å). The larger unit cell is indicative of uniform tensile strain caused by interstitial occupancy.[2,13,59] Rietveld refinement shows that at 250°C these phases exist in a 76:24 mass ratio (expanded to pristine). Increasing the temperature to 350°C (350/2/1)

decreases the relative crystalline composition of the expanded phase to 70:30. At 450°C (450/2/1), the Pd_{exp} is completely absent, with only the pristine Pd observed, as is the case for 550/2/1. This behaviour is congruent with TGA results by Chan et al.[14] Clearly, at 350°C some kinetic barrier is partially overcome, and fully overcome above 450°C. Indeed, heating at 350°C for extending duration does eventually yield the pristine monophasic product (Figure 5-1c).

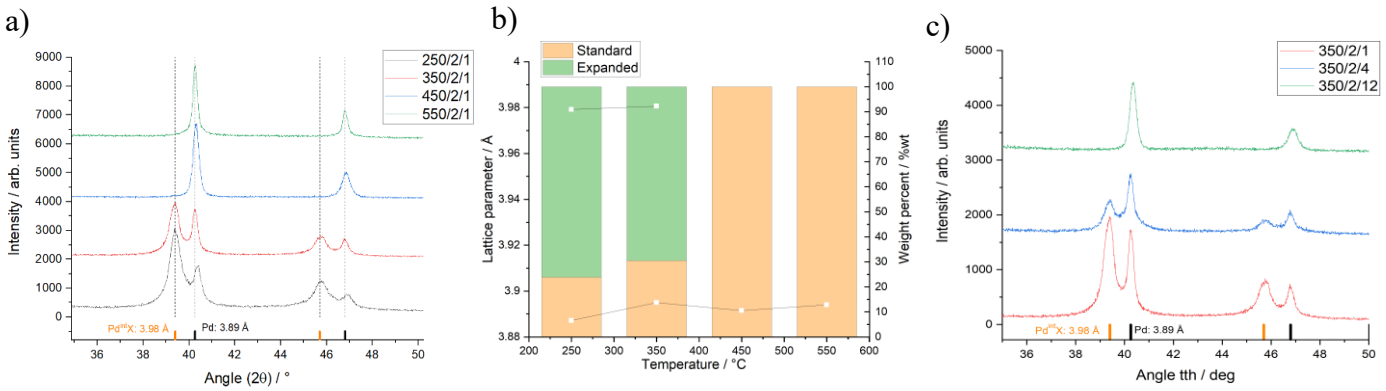


Figure 5-1. Biphasic product of thermal lithiation. Laboratory-configuration XRD patterns of one-step palladium nanoparticle synthesis from $Pd(OAc)_2$ at different temperatures: (a) patterns; sample notation as (temperature [°C]/ramp-rate [°C min^{-1}]/hold-time [h]), and (b) lattice parameters and relative crystalline composition. (c) Varying hold-time showing kinetic limitation of carbon deintercalation.

This expanded lattice was eventually found to be due to interstitial carbon shown by EDX of silica-supported nanoparticles (2.4 ± 1.9%wt). This $Pd^{int}C$ is known and discussed above in the Introduction. The expanded phase is only metastable relative to Pd, stable up to 152°C in air. The thermal decomposition was assessed by VT-SXPD (Figure 5-2), showing conversion to Pd by the negatively correlated integrated intensity of the Pd after the transition (Figure 5-2d). This is in good agreement with Ziemecki et al.[36] who reported that the pristine

lattice is restored after subsequent heating at 600°C in an inert atmosphere, or 150°C in atmosphere containing oxygen.

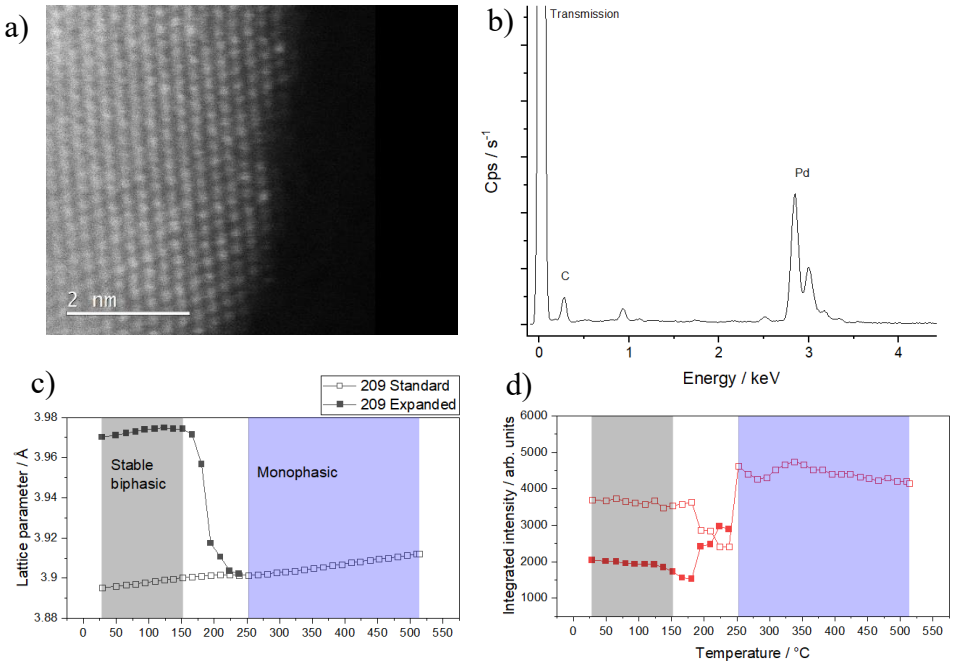


Figure 5-2. (a) STEM image and (b) EDX spectrum of 50%Pd/SiO_2. (c and d) Lattice parameters and integrated intensities, respectively, as derived by Rietveld refinement of VT-SXPD of the 50%Pd/C.

Additional to the temperature onset and phase product of the de-intercalation, an important insight into the transition's effect on the framework order is the peak broadening. Here the effect of elevated temperature results in the broadening of the reflections, indicating that the de-intercalation transition increases the disorder. The disorder of $Pd^{int}C$ has been reported in the increased Debye-Waller factors of the framework.[60] This is counter to usual arguments of increased domain size due to thermal reorganisation, either through intra-particle sintering over grain boundaries or inter-particle agglomeration. This theme of disorder on de/lithiation will be revisited during the discussion of electrochemical lithiation.

All of these results are consistent with the formation of $Pd^{int}C$, which is known to be doped at the octahedral hole,[32,36,60] increasing the lattice parameter by 2.6% to ~2.99 Å.[60] In the literature, this has been achieved by ethylene hydrogenation,[26,33] glucose encapsulation,[13,14] and CO disproportionation[37]. As far as we can determine, carbon-doping by an acetate precursor has not been reported. This can be described as in-situ carbon-doping, which will later inspire an in-situ lithiation procedure. Interestingly, a report of in-situ one-step carbon doping has already been cited in this thesis but in the context of a carbon-doped TiO_2 photocatalyst.[61]

5.3.3 Stability of thermally lithiated $Pd^{int}Li$

Previous reports from the Tsang group have shown that chemically lithiated palladium can be formed by post-synthesis heating with lithium acetate dihydrate to between 200°C and 350°C, after which interstitial lithium is no longer stable.[2] A sample of 50%Pd/C was lithiated by heating at 250°C for 12 hours using 0.35 eq of lithium acetate precursor, yielding a distribution of small and large nanoparticles of ~6 nm and~16 nm (Figure 5-3; EDX: Figure S5-1). Direct imaging of the lithium was not possible.

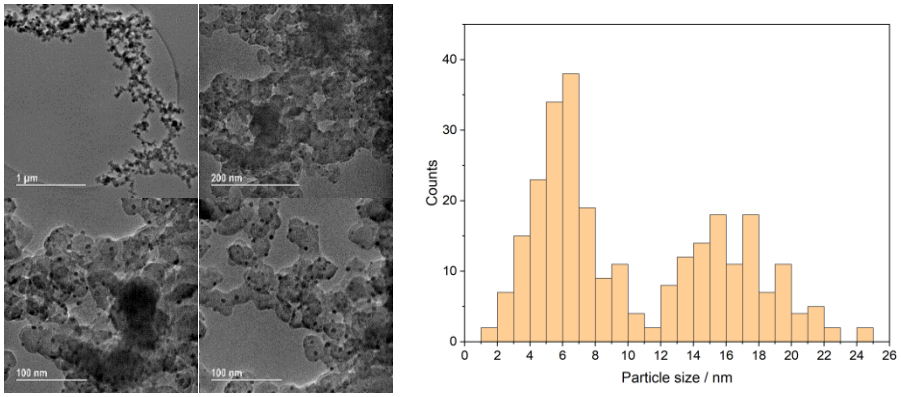


Figure 5-3. TEM imaging and particle-size histogram of 50%Pd lithiated at 250°C for 12 hours.

The successful retention of the crystalline structure was shown by laboratory-configuration XRD (Figure 5-4). Analogous to $Pd^{int}C$, all reflections are shifted to lower angle due to expansion in the framework. Chemically, this is understood as a dominant expanded $Pd^{int}Li$ phase (98%wt) and a minor unexpanded Pd (2%wt) that has not been lithiated. Using an excess of lithium (3.5 eq), there is complete conversion to $Pd^{int}Li$, with no significant change in lattice parameter (Figure 5-4). There is no evidence of any of the palladium-lithium intermetallic compounds presented in the introduction.

When the temperature is increased to 350°C, using an excess of lithium again yielded a monophasic expanded $Pd^{int}Li$ phase. However, using low amounts of lithium (0.35 eq) at elevated temperature results in the regeneration of the pristine Pd phase. It is thought that at 350°C, the intercalation is unstable, but the excess of lithium allows the retention of interstitial dopant and the expanded phase. The interclaation also shows greater stability against washing when 3.5 eq is used (Figure 5-4b). Thus, a large excess is shown to stabilise the expanded lattice against thermal decomposition and dissolution.

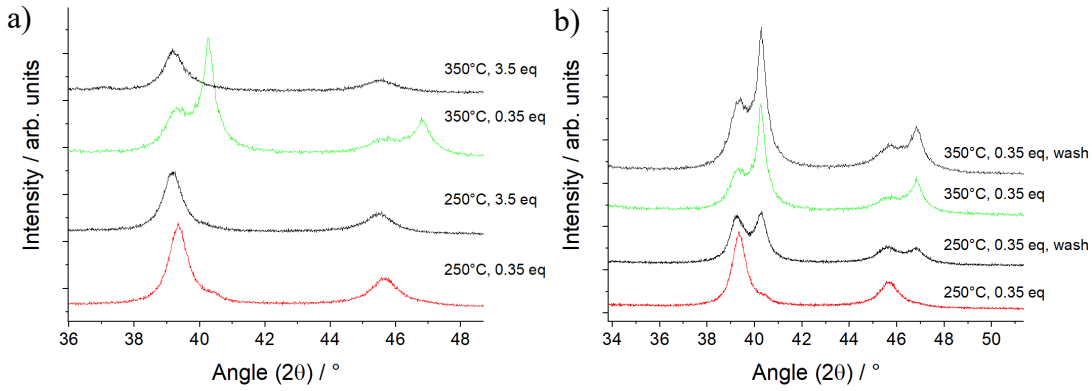


Figure 5-4. Effect of temperature and lithium doping on palladium nanoparticles by laboratory-configuration XRD: (a) post-synthesis lithiated at different temperatures, (b) following post-synthesis washing with water and ethanol.

5.3.3.1 ICP-MS: the framework-dopant relationship

So far, it has not been determined how much lithium is actually doped into the framework. ICP-MS was carried out on the highly lithiated 250°C and 350°C sample, both before and after washing. The non-washed samples exhibit a Li:Pd molar ratio of 0.372 and 0.355, respectively, showing that the large excess of lithium precursor is not retained by the sample. The most surprising observation is that both washed samples exhibit almost no lithium content, exhibiting a 10-fold decrease in lithium content. The washed samples retain the expanded unit-cell despite not containing appreciable lithium, indicating that the presence of the expanded phase may not always be directly correlated to the presence of lithium. This has implications on the assumed effect of lithiation and assumed use of $Pd^{int}Li$ in relation to improved catalytic performance.

Sample	Pd / ppb	Li / ppb	Li:Pd	Remaining Li relative to initial / %
250°C, 3.5eq	1.67×10^{8}	6.20×10^{7}	0.372	
250°C, 3.5eq, washed	4.72×10^{8}	3.90×10^{5}	0.001	0.22
350°C, 3.5eq	2.02×10^{8}	7.19×10^{7}	0.355	
350°C, 3.5eq, washed	3.72×10^{8}	9.03×10^{6}	0.024	6.84

Table 5-2. ICP-MS for thermally lithiated palladium nanoparticles.

5.3.3.2 In-situ lithiation

The inadvertent intercalation of interstitial carbon ($Pd^{int}C$) by the palladium precursor can be regarded as an in-situ doping process. Using this as inspiration, an in-situ lithiation was carried out by including lithium acetate in the palladium-reduction reaction. The only similar procedure in literature is the pre-lithiation of a support before nanoparticle growth, which is shown to result in different catalytic selectivity.[62] It is postulated that lithium can be

intercalated into the framework during the formation of the nanoparticle by a one-step in-situ process, resulting in increased penetration depth, concentration, homogeneity, and stability.

The reduction conditions were at 350°C for 12 hours in order to ensure full decarbonisation, whilst retaining lithium. From these conditions, if any expanded phase is observed for this, it is reasonably attributed to $Pd^{int}Li$. (A temperature of 250°C was also used which showed greater stability to washing (Figure S5-2)). Three levels of in-situ doping were synthesised using 0.2 eq, 0.5 eq, and 1.5 eq, as well as a standard non-doped sample, Pd. For the lithiated samples, the dominant phase is the expanded $Pd^{int}Li$. The mass composition of the weak Pd phase was similar for all samples at 4%wt (Figure 5-5a). It is hypothesised that the similar proportion of unlithiated Pd is due to entropic reasons. The lattice parameter of the lithiated phase $a(Pd^{int}Li)$ = 4.00 Å was the same for all samples to three significant figures. Thus, all lithiated samples are thought to be maximally lithiated. Indeed, the expected occupancy of Li in $Pd^{int}Li$ is ~15%mol,[36–38] indicating that the lithium composition is maximised even for 0.2eq. However, with greater lithium doping, the intensity decreases, showing a loss of crystallinity on lithiation.[60] This point will be explored much further in the context of LIB cyclability.

5.3.3.3 Thermal stability by VT-SXPD

The thermal stability of the in-situ lithiated samples was analysed by VT-SXPD (BL02b2, SPring-8) up to 513°C under air at an interval of 15°C (full heat-maps shown in Figure S5-3). The temperature is known to 0.1°C, as calibrated by Dr. Shogo Kawaguchi; however, it is not within 0.1°C of the input temperature. Hence, over the three samples the sampled temperatures are not coincident but highly accurate. Temperatures will be rounded

to the nearest 5°C in order to establish an equivalence between the datasets, which given the temperature interval, is deemed acceptable.

It has been previously shown that $Pd^{int}Li$ is restored to pristine Pd by heating above 150°C in air.[2] It should be noted that the rather large temperature intervals of that experiment (50°C) show a discrete transition from $Pd^{int}Li$ to Pd. Here, the much smaller interval was hoped to show more information on the lithiation dynamics. It was expected that the $Pd^{int}Li$ will disappear above ~150°C, restoring the Pd phase, analogous to the deintercalation of carbon (Figure 5-2).

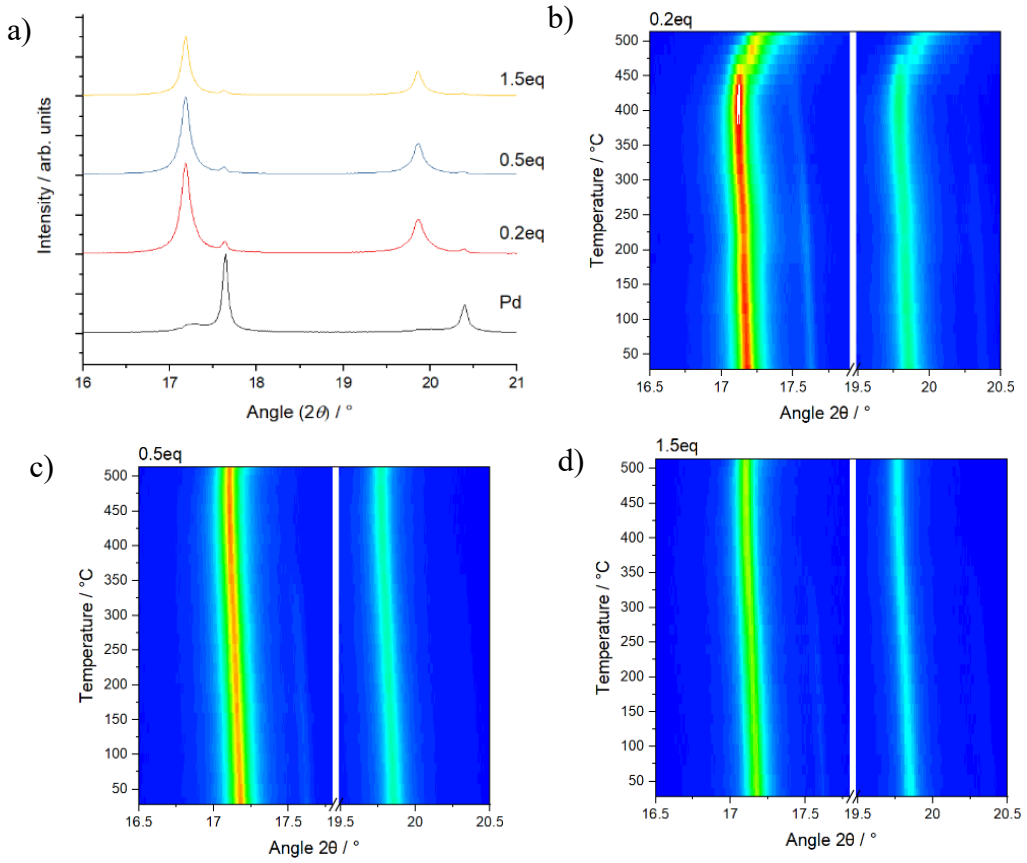


Figure 5-5. In-situ lithiated 50%$Pd^{int}Li$/C: (a) room temperature SXPD, and (b-d) VT-SXPD heatmaps of (111) and (200) for 0.2eq, 0.5eq, and 1.5eq, respectively, showing the stability of the lithiated phase up to very high temperature.

However, instead of observing deintercalation ($Pd^{int}Li \rightarrow Pd$) at 150°C, the expanded $Pd^{int}Li$ is stable and is present at the highest temperature of 510°C for all samples. There is no significant disappearance of $Pd^{int}Li$ at any point, and consequently no formation of Pd. Furthermore, we observed the instability of the pristine Pd phase, which is considered to be the stable ground-state. This behaviour indicates an intercalation reaction ($Pd \rightarrow Pd^{int}Li$). This extended stability of $Pd^{int}Li$ and the absence of a clear delithiation transition is counter to all expectations based on the current understanding of the system.

As an aside, a low-angle impurity phase is observed which decomposes at a similar temperature for all samples (Figure S5-4). Also, at high-temperature, an impurity phase emerges at similar temperatures for all samples (Figure S5-5). These phases have not been indexed successfully due to their relatively weak intensity, especially above 15°. Some discussion can be found in the Appendix.

Stable regime up to 150°C

Rietveld refinement was carried out for each dataset individually. For the 0.2eq, 0.5, and 1.5eq datasets, the average R_{wp} = 8.74%, 8.26%, and 8.98%, respectively, and the average GoF = 1.36, 1.22, and 1.13, respectively (Table S5-1). Both the prolonged thermal stability and the unexpected intercalation are shown to be dependent on lithium doping. For the higher lithiation 0.5eq/1.5eq, $Pd^{int}Li$ remains above 93%wt over the full temperature range up to 510°C. Meanwhile for 0.2eq, the $Pd^{int}Li$ remains high (above 90%wt) until above 400°C, at which the phase splits into two phases, and the relative crystalline composition value is partitioned, causing peak overlap and poor peak resolution. The temperature-dependent behaviour of this phase will reveal much about the system.

The relative crystalline composition of all samples remains constant up to 150°C (Figure 5-6a), which is also seen in the absolute integrated intensities (Figure 5-6b). Throughout this period of phase stability, the lattice parameter increases approximately linearly, as is expected for thermal expansion (Figure 5-6c). All phases are shown to be coincident with the thermal expansion of a control pristine palladium sample (Figure 5-6d).

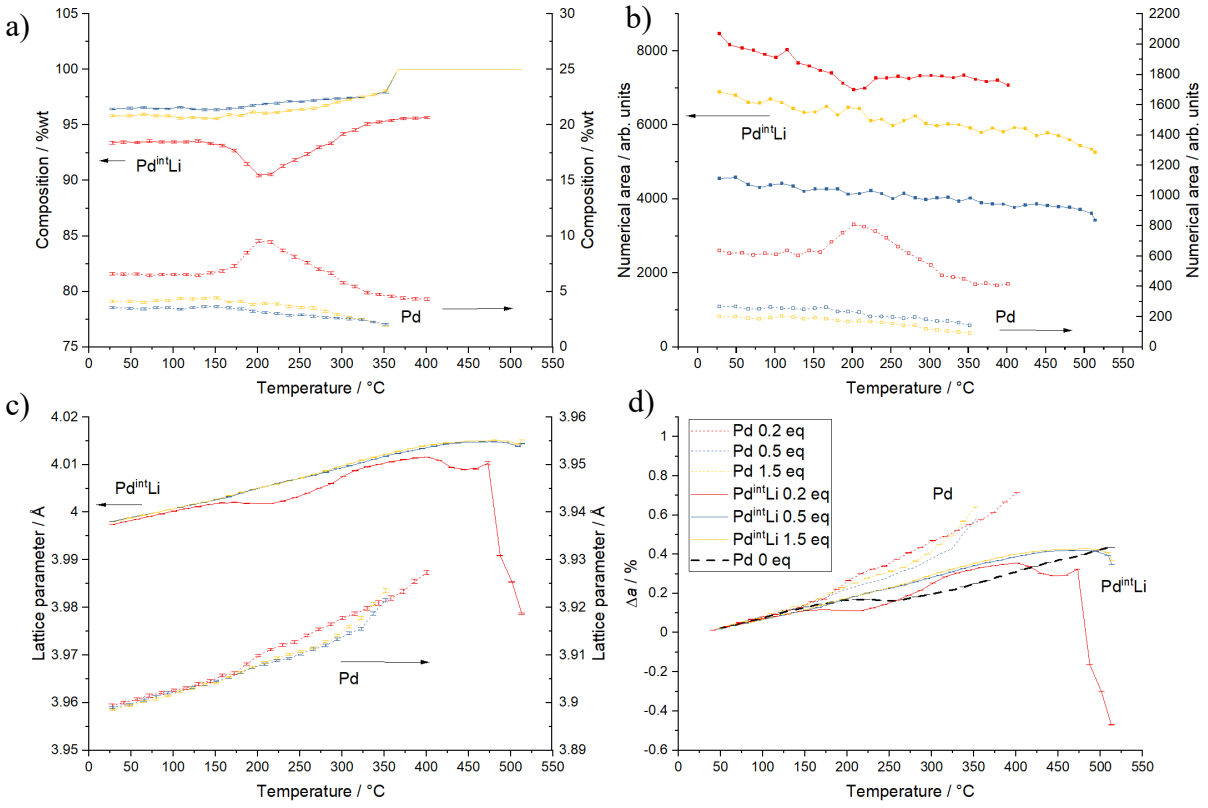


Figure 5-6. Rietveld refinement of VT-SXPD for pristine and in-situ lithiated palladium nanoparticles: Pd as dotted lines, $Pd^{int}Li$ as solid lines. (a) Relative crystalline composition, (b) integrated intensity of the Bragg phases, (c) lattice parameters , and (d) thermal expansion from room temperature expressed as a percentage; control sample of monophasic pristine Pd shown in black.

Occupancy equilibration at 150°C: only for low doping

For 0.2eq, at 150°C, composition of pristine Pd steeply increases, peaking at 10%wt at 200°C, which is mirrored by a decrease in the expanded $Pd^{int}Li$ phase, as is the case for the intensity (Figure 5-6b). This is the deintercalation transition of $Pd^{int}Li \rightarrow Pd$, which is occurring at an expected temperature in air; this is supported by similar trends in lattice parameter. The lattice parameters moving towards each other is a phenomenon that has not been observed before in this work. It is interpreted as deintercalation from the expanded phase, and migration to the pristine phase, yielding a partially lithiated Pd phase and a partially delithiated $Pd^{int}Li$. This retention of the dopant atom within the crystalline system is more akin to reorganisation than abstraction, herein referred to as occupancy equilibration. This equilibration can be estimated by Vegard's law, which is made more complex by the different thermal-expansion dependencies (see Appendix Chapter 5: Vegard's Law). Essentially, these values attempt to deconvolute the expansion in lattice parameter from thermal expansion and chemical effects of dopant-framework interaction. A maximally doped $Pd^{int}Li$ is assumed to be 0.15 occupied. For 0.2eq, the occupancy equilibration is shown to result in a $Pd^{int}Li$ Vegard occupancy of 0.14 while increasing the Vegard occupancy of Pd to a plateau at 0.03 at 400°C. The chemical expansion of Pd is greater than the contraction of $Pd^{int}Li$, resulting in a total Vegard occupancy that exceeds 0.15, which assuming an inviolate Vegard's law, implies a source of additional lithiation.

Meanwhile, occupancy equilibration is not observed for 0.5eq/1.5eq by composition or lattice parameter values. It is hypothesised that the palladium nanoparticles are encapsulated by a physical barrier that prevents dopant loss to atmosphere. Overcoming the kinetic barrier to deintercalation then results in the reabsorption of lithium to the low-

occupancy phase as a closed system. Meanwhile, the highly doped materials may have such a physical barrier that they are not exposed to the oxidising atmosphere.

Reverse occupancy equilibration at 200°C: only for low doping

The occupancy equilibration trends for 0.2eq in intensity are reversed at 200°C, as well as the recovery of $a(Pd^{int}Li)$, which indicates a reverse occupancy equilibration towards $Pd^{int}Li$. However, a(Pd) remains at a consistently expanded value. This is another example of an increasing Vegard occupancy for the ensemble, indicating increasing total lithium occupancy. Again, it is emphasised that none of the occupancy equilibration trends are observed for 0.5eq/1.5eq.

Thermal decomposition of Pd

For 0.5eq/1.5eq, after 150°C the pristine Pd phase begins to decrease, which also coincides with the lattice parameter increasing by more than the thermal expansion (Figure 5-6d). The increase in lattice parameter with temperature is approximately linear until 300°C, when a steeper increase eventually results in the phase disappearing at 380°C and 365°C, for 0.5eq and 1.5eq respectively (Figure 5-6). This is taken to be some intercalation, though the $Pd^{int}Li$ phase here is unaffected in intensity and lattice parameter. There is no increase in the intensity of $Pd^{int}Li$ throughout the temperature range, with no evidence of occupancy equilibration. The Pd may also be being lithiated amorphously. Such amorphous lithiation event at high temperature further indicates a volume-restricted encapsulated system with an internal lithium reservoir.

For 0.2eq, the pristine Pd is still stable at 400°C, but is very weak. It is unclear when it disappears below the background because the $Pd^{int}Li$ phase begins to shift to higher angle

causing peak overlap. This deintercalation of $Pd^{int}Li$ is observed as a split into two distinct phases from ~460°C. Regardless of the exact decomposition temperature, the Pd is shown to disappear from ~345°C to 460°C, while the slowing thermal expansion of $Pd^{int}Li$ indicates delithiation at 415°C. Meanwhile for 0.5eq/1.5eq, there is a small decrease in $I(Pd^{int}Li)$ from 480°C. For this reason, the start of the thermal instabilities of $Pd^{int}Li$ are said to be 415°C, 480°C, and 480°C. The 0.2eq exhibits greater Pd stability but lower $Pd^{int}Li$ stability (Table 5-3).

Lithium precursor / eq	Pd / °C	$Pd^{int}Li$ / °C
0.2	~345 - ~460	415 - >515
0.5	~150 - 380	480 - >515
1.5	~150 - 365	480 - >515

Table 5-3. Temperature range of thermal instability of Pd and $Pd^{int}Li$ at various lithium doping levels by VT-SXPD.

$Pd^{int}Li$ instability and phase partitioning

The splitting of the expanded $Pd^{int}Li$ in 0.2eq is due to two populations of particles being delithiated at different rates (Figure 5-7). These inhomogeneous contractions can be expressed as Vegard occupancies, showing that by 515°C the expected stoichiometries are appreciably delithiated: $PdLi_{0.010}$ and $PdLi_{0.078}$. This behaviour has not been observed for this system before. Modelling these phases is difficult due to the unknown variation in lattice parameters, peak shapes, and relative crystalline composition. For 0.5eq/1.5eq, delithiation is observed in the last pattern at 515°C, but as an emergent contracted phase while the original phase remains at the expected lattice parameter (Figure S5-7).

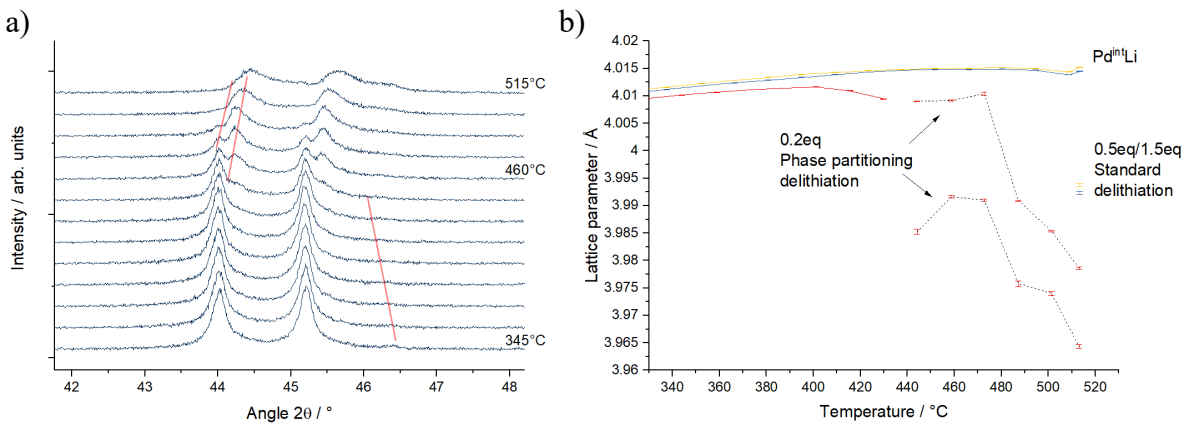


Figure 5-7. Inhomogeneous phase partitioning at high temperature. (a) SXPD patterns of 0.2eq in-situ lithiated 50%Pd, showing the splitting of the expanded $Pd^{int}Li$ at 440-515°C. (b) Lattice parameters of emergent contracted phases.

Discussion of unexpected thermal stability

By room-temperature Bragg diffraction methods, these three materials appeared very similar. However, it was shown by VT-SXPD that the thermal properties are very different, yielding bountiful information of these chemically different ensembles. The stability of $Pd^{int}Li$ at high temperature for all doping levels is explained by the hypothesis of a kinetic barrier due to nanoparticle encapsulation. The deintercalation at 150°C of 0.2eq indicates exposure to air, while the occupancy equilibration (and subsequent reverse equilibration) indicates a closed system. The disappearance of pristine Pd phase for all samples also indicates a close system, and with an internal reservoir of lithium precursor. This reservoir is shown to be large for higher doped samples because Pd disappears at lower temperatures.

Lithium acetate is no longer present as a precursor having been combusted during the synthesis process. It may seem feasible that carbon from the support is being doped into the palladium, but this has never been observed, and we have in this thesis shown that carbon is

unstable in the palladium lattice in air 150-250°C. Instead, it its postulated that the local lithium reservoir is lithium oxide or lithium nitride.

Without arguments of a physical shell around the palladium nanoparticle, it is difficult to explain the stability of the expanded phase. However, the observations are believed to be valid and interrelated. In-situ encapsulation of palladium nanoparticles is known;[14,63] thus the hypothesis presented is deemed to be reasonable. The possibility of retaining the lithium dopant and associated chemical enhancements for catalysis, while increasing thermal stability is an exciting prospect. Examples are known of designed encapsulation in order to decrease deactivation and sintering, and increase size selectivity, conductivity, and yield.[50,63,64] In many cases, these encapsulated materials are used in LIB as enhanced-performance electrode materials.[50,51]

5.3.4 Use as lithium storage material in lithium-ion batteries

The lithiation and delithiation process is clearly not well-understood, and the post-synthesis VT-SXPD is perhaps not the ideal technique to monitor it. The use of a thermal solid-state lithiation procedure does not produce a reliable homogeneous system with respect to temperature or the accessibility of lithium precursor. The electrochemical lithiation process may be more homogeneous, discrete, controlled, and quantitative than thermal methods. To further probe the lithiation-delithiation process in this environment, attention was turned to applying the palladium nanoparticles as LIB anode material. Though the initial aims of the investigation involved the assessment of palladium nanoparticles as anode materials, it is additionally contextualised as a further investigation into the dynamic de/lithiation transitions, which were difficult to monitor by thermal methods. Properties such as electrochemical capacity, reversibility, stability, and voltage plateaus will be considered. However,

investigation and discussion of electrolyte interactions, energy efficiency, overpotentials, capacitance, and degradation are not given much attention.

5.3.4.1 Electrochemical cycling

Effect of support

Graphite is the incumbent anode material in LIB. It offers good stability, and reasonable capacity, while being cheap and naturally abundant. An electrode of only graphite active material was cycled over 30 cycles at a constant gravimetric current of 100 mA g^{-1} (with respect to the total mass) between 0.01-3.00 V vs. Li^+/Li. The performance is shown to be stable at ~380 mA h g^{-1} (averaged over seven cells), which is in reasonable agreement with the theoretical value of 372 mA h g^{-1}. Supported palladium nanoparticles were synthesised by the methods described earlier to yield 20%wt Pd/gr, which exhibited only slightly lower stable capacity than graphite (350 mA h g^{-1}). Correcting for the 80%wt of graphite (also presuming PVDF binder is inactive), the contributing capacity from Pd was calculated to be 240 mA h g_{Pd}^{-1}, which equates to a molar capacity of 0.96 electrons per Pd atom (Figure 5-8a). This stoichiometry indicates a $PdLi_x$ phase, where $x = 0$ to 1. This level of lithium doping is much higher than the thermally lithiated palladium materials (ICP-MS: Li:Pd = 0.4), attributed to the highly reducing potentials near the lithium-plating potential. However, this capacity is for the entire electrode, and may not reflect the stoichiometry of either a discrete Bragg phase or even any formal association with the palladium.

The potential profiles of graphite and 20Pd/gr are highly distinct (Figure 5-8). Both exhibited discharge plateaus at ~80 mV and ~50 mV, and charging plateaus at ~120 mV and 150 mV, which are easily observed in the dQ/dV plots (Figure 5-8c). This difference of ~70 mV is the origin of the non-Coulombic energy inefficiency of LIB. The greater area

bounded by the reduction curve than the oxidation curve is indicative of the formation of the solid-electrolyte interface and the associated irreversible capacity loss. After the first two cycles, the redox occurs at consistent potentials to at least cycle 10.

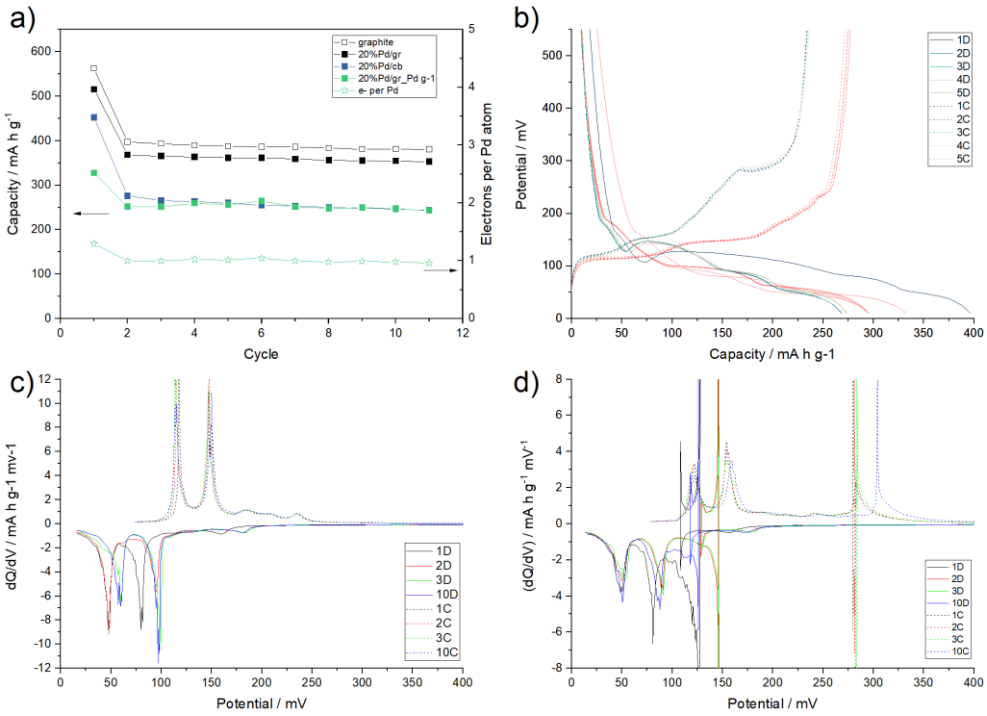


Figure 5-8. Assessing the electrochemical lithium capacity and behaviour of graphite anode material. (a) Cycling stability averaged over at least three cells; only discharge capacities shown for clarity. (b) Potential profiles of the first 5 cycles for graphite (red) and 20Pd/gr (spectrum); discharge as solid lines, charge as dotted lines. (c and d) d*Q*/d*V* plot of graphite and 20Pd/gr, respectively.

The Pd material exhibited additional non-discrete solid-solution activity, and another plateau under discharge at ~150 mV and under charge at ~280 mV. Both of these additional features are accompanied by non-monotonic potential, which will be correlated to certain phase transitions by in-operando SXPD shortly. However, this yields confusing d*Q*/d*V* plots. It is sufficient to note that (1) the additional redox occurs at lower energy than lithium intercalation into graphite, (2) the initial overpotential is greater at ~130 mV, and (3) by cycle

10 the overpotential has increased to ~170 m due to changes in both discharge and charge potentials (130 mV and 300 mV, respectively).

5.3.5 Ex-situ identification of lithiated palladium phases

It was acknowledged that it is difficult to deconvolute the electrochemical properties of graphite and palladium. Phase-specific characterisation would render this much simpler. The lithium intercalation process was desired to be observed by SXPD in order to elucidate effects on reversibility, crystallinity, lattice-parameter changes, particle size, and microstrain. As well as the expected $Fm\bar{3}m$ palladium phase, many additional reflections were also observed. Indexing the unknown phases was non-trivial, but eventually found to be $Pm\bar{3}m$ PdLi (CsCl-type) and *P6/mmm* $PdLi_2$ ($CaHg_2$-type) (Figure 5-9). These phases are reported very seldom in literature,[65] and in no cases in relation to electrochemical cycling. The pristine $Fm\bar{3}m$ Pd, $Fm\bar{3}m$ $Pd^{int}Li$, $Pm\bar{3}m$ PdLi, and *P6/mmm* $PdLi_2$ phases will be referred to by their Bravais lattice and reported composition in order to aid clarity: *cF* Pd, *cF* $Pd^{int}Li$, *cP* PdLi, *hP* $PdLi_2$.

5.3.5.1 $PdLi_2$: anisotropic volume expansion

Post-mortem electrodes were extracted and analysed by both laboratory-configuration and synchrotron XRD in inert gas environments. A discharged electrode of 50%wt Pd on graphite and carbon-black were both analysed by SXPD. The lower resolution of the PSD on I11 (9 mdeg vs. 1 mdeg using MAC) was deemed sufficient to carry out phase identification. Both samples exhibited the expected *cF* Pd phase, but the unexpectedly the dominant phase was *hP* $PdLi_2$.

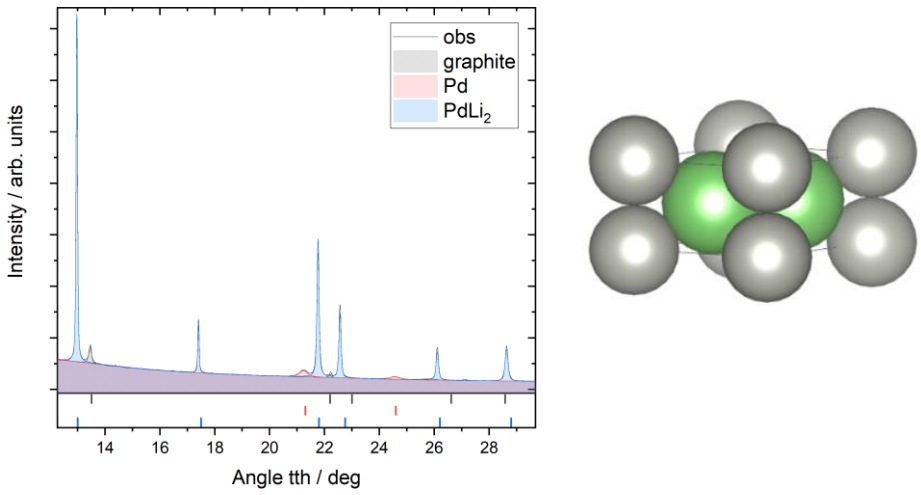


Figure 5-9. (a) Refinement of 50%Pd/gr showing significant $PdLi_2$. (b) Displayed structure of $PdLi_2$; palladium in grey (radius: 1.37 Å), lithium in green (radius: 1.57 Å).

The $PdLi_2$ assumes the AlB_2-type structure (Figure 5-9). In relation to the $Fm\bar{3}m$ palladium parent-structure, *hP* $PdLi_2$ can be described as an expanded framework in which two Li sites occupy a single octahedral hole. The lithium atoms are colinearly aligned with the (110) plane, which pushes the eight coordinating palladium atoms outwards. Inducing anisotropy to the octahedral hole results in a hexagonal unit-cell (*P6/mmm*, a = 4.24 Å, c = 2.75 Å) of [A-B] repeated layers, i.e. the hexagonally close-packed structure.

The emergence of unexpected phases affects the aims of the investigation in finding a low volume-expansion anode material. Changes in lattice parameters and unit-cell volumes can be misleading. Instead, it is more representative of the atomic arrangement to report first- and second-shell Pd-Pd interatomic distances. In *cF* Pd, any given Pd has a first Pd shell that is 6-coordinate (2.76 Å). For *hP* $PdLi_2$, this shell is split into two: an axial two-coordinate first shell (2.75 Å) (*c*-axis), and an equatorial (*ab*-plane) four-coordinate second shell (4.24 Å). It is interesting to note that in the *c*-axis, the palladium framework contracts by 0.02 Å (-0.8%), while the *ab*-axes lengthen by 1.48 Å (+54.5%). The overall density

decreases markedly, which is expected for such a high-lithium phase. Overall gravimetric densities are not considered due to the uncertainty over lithium occupancy, which will be discussed below. The palladium atom-density decreases from 0.07 Pd A^{-3} to 0.02 Pd A^{-3} (Table 5-4). This anisotropic behaviour at the atomic level is analogous to the reorganisation of titanium atoms during the formation of oxygen vacancies discussed earlier in Chapter 4 on TiO_2 photocatalysts.

Phase	Space group	Lattice parameter / Å	1st shell Pd-Pd / Å	1st shell Li-Li / Å	Pd $Å^{-3}$	Li $Å^{-3}$ *
Pd	$Fm\bar{3}m$	3.891	2.762	N/A	0.068	0
$Pd^{int}Li$	$Fm\bar{3}m$	~4.0	2.828	2.828	0.063	0.063
PdLi	$Pm\bar{3}m$	2.987 #	2.987	2.987	0.038	0.038
$PdLi_2$	*P6/mmm*	*a*: 4.242, *c*: 2.742	2.742	2.452	0.023	0.047

Table 5-4. Structural information on palladium lithium phases, and interatomic distances. * Lithium atom density assumes the full occupancy of lithium sites. # Not refined throughout.

It is noted that we do not expect (nor have observed) preferred orientation of the powder on the electrode. Hence, the significant anisotropic expansion in the *xy* plane may simply average over the powder ensemble as an isotropic expansion. It needs to be considered what impacts this anisotropic volume change at the atomic length-scale has on particle morphology, SEI formation, irreversible capacity loss, and electrode pulverisation.[47]

5.3.5.2 Phase composition and PdLi

The crystalline mass ratios of the *cP* Pd and *hP* PdLi were different for 50%Pd/cb and 50%Pd/gr: 21:79 and 8:92, respectively (Figure 5-10). The graphite-supported nanoparticles exhibited a higher composition of *hP* $PdLi_2$, which indicates the enhanced accessibility or kinetics of graphite over carbon-black-supported nanoparticles. This is contrary to expectations based on the surface area of the materials: carbon black: 15-64 m^2 g^{-}

[1] vs. graphite: 0.6 m^2 g^{-1}. Greater dispersion is evidently not significant. The pertinent property is thought to be the electrical conductivity. The small spherical particles of carbon black offer much reduced electrical conductivity, exhibiting resistivity of ~10^{-1}-10^{-2} Ω cm compared to graphite at ~10^{-4} Ω cm. This increased conductivity increases the total conversion to *hP* $PdLi_2$ at this current density.

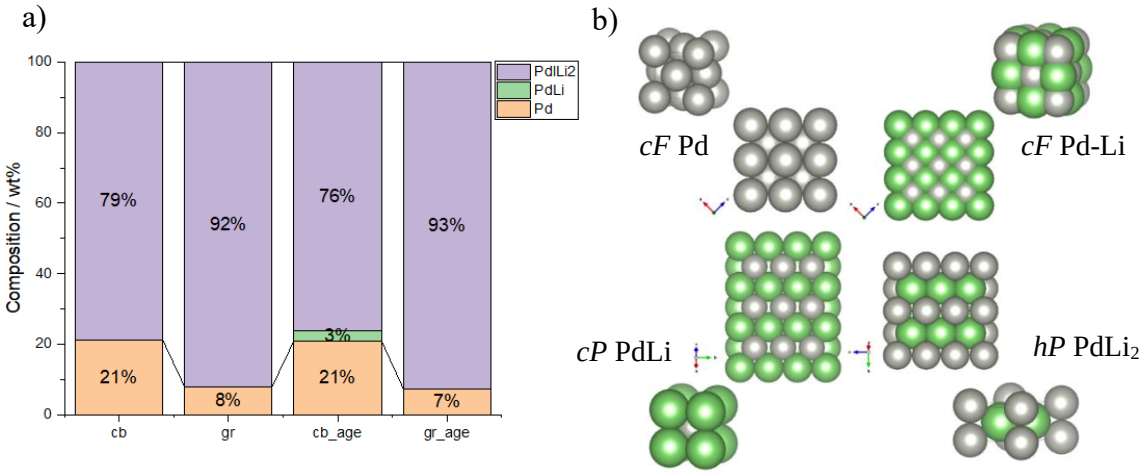


Figure 5-10. (a) Ex-situ phase identification of discharged electrodes 50%Pd/cb and 50%Pd/gr (graphite composition not included). (b) Space-fill display of unit-cells and packing of relevant intermetallic compounds; palladium in grey (radius: 1.37 Å), lithium in green (radius: 1.57 Å).

The capillaries containing the post-mortem samples were left in an argon glovebox for two weeks in order to investigate the phase stability in a supposedly highly inert atmosphere. The patterns were very similar, but after aging an additional phase was observed in the 50%Pd/cb (Figure 5-9). This was indexed as $Pm\bar{3}m$ PdLi (or by Bravais lattice: *cP* PdLi). The difference in oxidative stability between 50%Pd/cb and 50%Pd/gr is unclear. After being formed under highly reducing conditions and then electrochemically quenched, *hP* $PdLi_2$ is clearly unstable and prone to oxidation. This intermediately lithiated *cP* PdLi yields very distinct reflections from $Fm\bar{3}m$ Pd. It was easily identified by new low-angle peaks. This is despite the shortening of the cubic lattice parameter *a*(PdLi) = 2.987 Å because

for $Fm\bar{3}m$, the (001) is unobserved as it does not fulfil the reflection condition for the 0*kl* set: [k, $l = 2n$], and the lowest-angle observed reflection is (111) (d_{111} = 2.30 Å), which fulfils the *hhl* set condition [$h + l = 2n$].

Similar to *hP* PdLi2, the volume expansion of *cF* Pd to *cP* PdLi must be considered. Pristine *cF* palladium has a molar density of 0.068 Pd Å^{-3}, while the *cP* PdLi is much less dense at only 0.038 Pd A^{-3}. This is due to an expansion with respect to the first Pd-Pd shell distance, which increases from 2.762 Å in pristine palladium to 2.987 Å. (+8.1%). For *cF* Pd^{int}Li, the overlap between Pd and Li atoms in the structure is significant, while after the transition to *cP* PdLi, the atoms are well-separated (Figure 5-10b). Hence, it is clear that after a certain lithiation of the *cF* structure, the strain induced by electrostatic repulsion initiates a reorganisation of the framework. The expansion of this transition is much greater than is calculated for the topotactic expansion to the *cF* Pd^{int}Li, Pd-Pd = 2.828 Å (+2.4%). The *cP* PdLi is much more expanded than the topotactic expanded *cF* Pd^{int}Li phase, indicating that our expectation of low volume expansion are not realised. Regardless, unexpected phase behaviour has been overserved, as well as the sensitivity of post-mortem analysis by degradation.

5.3.6 In-operando SXPD

It is paramount to characterise these chemically-sensitive samples as soon as possible, or in an environment that is as close to their operating conditions as possible. At this stage in the investigation, it was also uncertain whether the *cP* PdLi phase participates in the electrochemistry during cycling. An in-operando experiment was designed in order to observe the crystalline phase changes during cycling by SXPD. Coin-cells of 50%Pd/gr and 50%Pd/cb were cycling at 100 mA h g^{-1} and scanned every 5 minutes for 20 hours, totalling

212 patterns each. Three full cycles were completed by both cells. The constant capacity of ~300 mA h g^{-1} shows stable cycling (Figure 5-11), which will be important in reference to the decreasing crystalline mass.

5.3.6.1 Initial quantitative observations

In the initial pattern, palladium metal and graphite are well observed. There is strong diffraction from the copper current-collector and steel cell-casing; these phases are considered spectator phases and will not be discussed further, nor be included in calculations of Bragg composition. The diffraction data are clearly shown to be rich with information on electrochemical phase behaviour, which is clearly very different to that of thermal lithiation (Figure 5-11b).

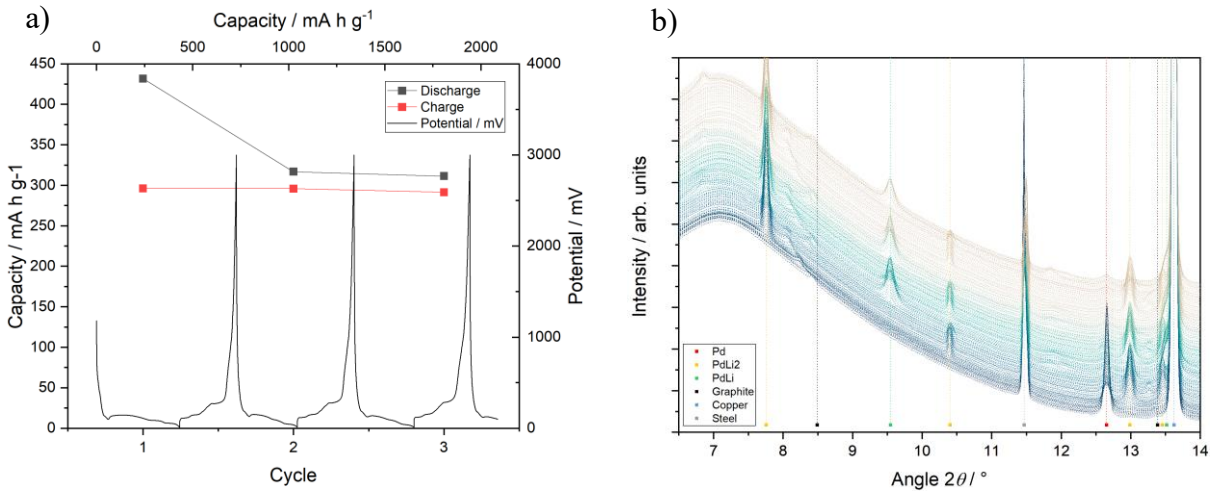


Figure 5-11. Electrochemical cycling of 50%Pd/gr during in-operando SXPD. (b) SXPD patterns of 50%Pd/gr plotted with arbitrary spacing, foregoing time (proportional to capacity) or potential dependence.

Very generally, it is shown that palladium metal is stable for a time, before being almost completely converted into *hP* $PdLi_2$. There is no observation of *cP* PdLi during initial discharge, thus exhibiting a discrete double-lithiation bypass transition. There is no appreciable shifting of *cF* Pd to low-angle to indicate expansion by solid-solution intercalation to *cF* $Pd^{int}Li$ as was seen in the thermal lithiation. The *hP* $PdLi_2$ phase is very strong and sharp in comparison to the initial *cF* Pd phase, which is an unusual demonstration of high crystallinity and particle size after lithiation, i.e. electrochemical sintering. It is thought that the discrete transition allows greater reorganisation and relaxation than topotactic expansion. The *hP* $PdLi_2$ is then stable until charging where it is converted to the discrete *cP* PdLi phase, with no regeneration of *cF* Pd evident. After the first full cycle, the palladium is cycled between *cP* PdLi and *hP* $PdLi_2$ (Figure 5-12).

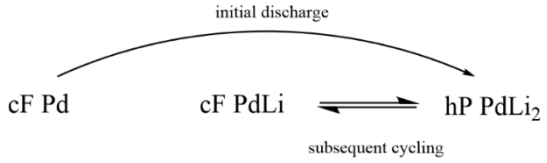


Figure 5-12. Schematic of initial observations of palladium phase-evolution by in-operando SXPD.

Three-dimensional diffraction data

It has been useful to plot the derivative of intensity with respect to angle in order to show weak changes. Using SXPD, even very weak changes can be observed with good signal-to-noise ratio. Additionally, expressing the derivative using colour, the data can also be plotted against Coulombic capacity in order to visualise the structural progression with lithium intercalation (Figure 5-13). Though the potential is the driving force of change rather than capacity, it is impossible to plot the data over potential as the values are non-monotonic.

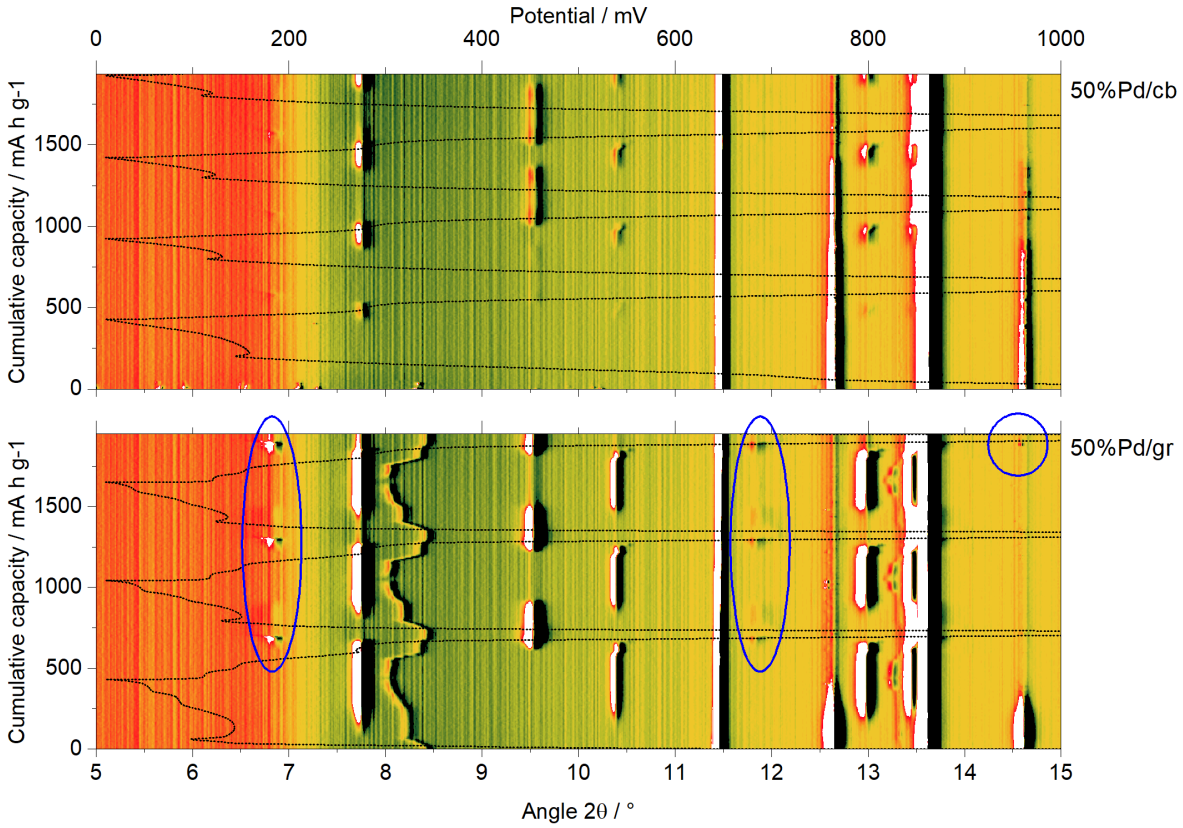


Figure 5-13. Derivative of intensity with respect to angle of 50%Pd/cb, and 50%Pd/gr. Peaks indicated by displaying extreme values of <-2000 in black, and >2000 in white; intermediate negative values shown in green, through to positive in red. Unmodelled short-lived reflections shown by blue circles.

The 50%Pd/gr exhibits much clearer and more significant changes in diffraction than 50%Pd/cb, through much larger magnitude of the derivatives. This is due to much weaker initial palladium signal. In order to investigate the interesting phase behaviour, the 50%Pd/gr data will be focussed on.

Additional observations from this representation of the data are as follows. The *hP* $PdLi_2$ is retained for longer duration (proportional to capacity) than *cP* PdLi. There is very limited overlap between *cP* PdLi and *hP* $PdLi_2$, with only one being present at a time. Some quantitative understanding of the peak shape is available, as *hP* $PdLi_2$ is shown to be

consistently sharper than the *cP* PdLi phase. Regarding shifts in lattice parameter, there is a repeated continuous shift to high angle of *hP* $PdLi_2$ just prior to delithiation. Meanwhile *cP* PdLi remains at a stable lattice parameter. These quantitative observations for the palladium phases will be further analysed using Rietveld refinement.

Additionally, there are two weak and short-lived low-angle peaks at 6.9° and 11.9° (shown by blue circles in Figure 5-13). They are observed strongly under high charging potentials from 300-1100 mV for around three patterns, which is equivalent to around 15 mins of cycling time. The phase quickly disappears, then reappears weakly during the discharge half-cycle from ~180-100 mV, which coincides with a non-monotonic bounce in the potential. Though this bounce is present in the first discharge, the additional peaks are not. There is some evidence that the phase is becoming stronger at every appearance, with the intensity and duration of appearance increasing. Furthermore, there is another peak at 14.6° that is only visible during the third charge. Though relatively weak, the strength and regularity of these observations show they are a real phenomenon with a clear correlation to capacity and potential. The weak scattering and transience of this phase make indexing and phase identification very difficult, and has not been able to be achieved. Frustratingly, this phenomenon remains unmodelled with respect to structure, and unexplained with respect to the cycling behaviour.

5.3.6.2 Refinement, metrics, and data presentation

The refinement was carried out as a batch process, in which refined parameters are used as the starting parameters for the following pattern. The *cF* Pd, *cP* PdLi, and *hP* $PdLi_2$ were treated as Rietveld phases, while the spectator phases, copper ($Fm\bar{3}m$, 3.630 Å) and steel ($Im\bar{3}m$, 3.518 Å), were modelled using the Pawley method in order to improve

parametrisation and reduce computation time. The intensities and lattice parameters of these phases were effectively constant throughout. The weak graphite phase was only evident by two peaks at 8° and 23°, which were modelled as individual peaks with shared peak shape (Figure S5-8). The average residuals of the batch refinement were R_{wp} = 2.78% and GoF = 1.54. It is unwieldy to tabulate the results of 212 patterns. These data are available by request.

Notation

Phase transitions will be referred to by the half-cycle and Li:Pd ratio, e.g. *hP* $PdLi_2$ to *cP* PdLi in the first charge is 1C(2→1). The Bravais lattice is not included in the notation because *cF* $Pd^{int}Li$ is no longer significant. If the transition bypasses *cP* PdLi by a double-lithium process, then two arrows are used, e.g. *cP* Pd to *hP* $PdLi_2$ in the first discharge is 1D(0→→2). If the transition is in the unexpected direction, then the arrow will be underlined, e.g. *cF* Pd to *cP* PdLi in the first charge is 1C(0$\underline{\rightarrow}$1).

Composition parameters

Throughout this thesis, both the relative crystalline-composition as a weight-percentage and the total absolute integrated intensity of individual Bragg phases have been quoted and discussed when appropriate. Each has its own advantages. The relative crystalline-composition is able to show the change as a powder ensemble, and the values are meaningful and simple to understand. However, due to the nature of the normalisation, the values of constituent phases are all negatively correlated. This is a problem when attributing causation within this ternary system, and can lead to misinterpretation. For example, the relative crystalline-composition of *cF* Pd seems to increase during 1C (Figure 5-14a). This is observed because *I*(PdLi) is decreasing faster than *I*(Pd). Both are unstable but this is not

clear in the relative crystalline-composition values. Additionally, crystalline-composition values also fail to show changing total crystallinity. This will become very important when considering phase reversibility and degradation.

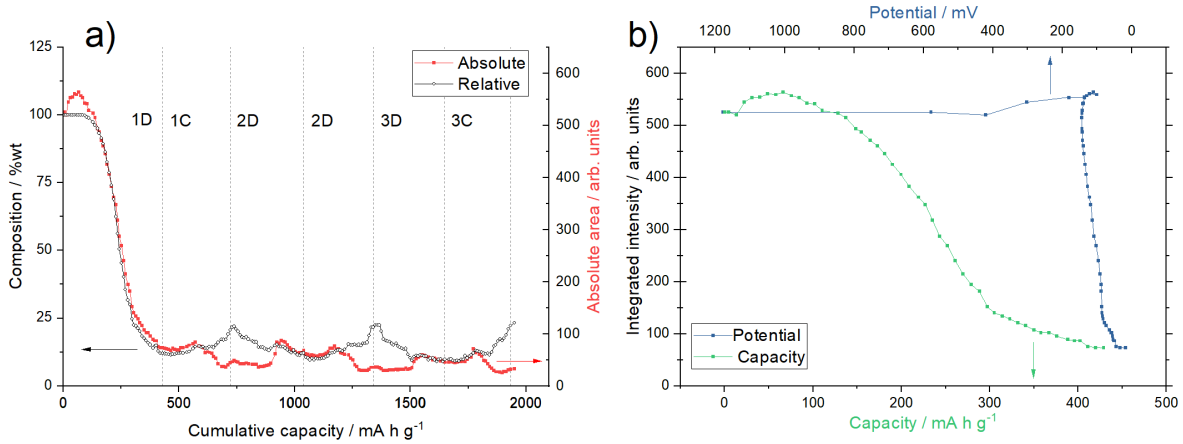


Figure 5-14. Comparison of phase evolution of *cF* Pd by Rietveld refinement: (a) relative crystalline composition and absolute integrated Bragg area over the full cycling; (b) plotting against capacity or potential over the first discharge.

Plotting against capacity or energy

There is also an distinction between plotting the phase-evolution parameters against Coulombic capacity, or against the potential. The three-dimensional data above are plotted against capacity since the potential values are not monotonic. This depiction is more intuitive since this is proportional to the number of lithium ions being de/intercalated, as well as time. Plotting against capacity shows the smooth phase-evolution with increasing lithium concentration (Figure 5-14b). In order to provide continuity, cumulative capacity is used. However, this does not show that most of the change is occurring over a very narrow potential range below 100 mV.

Plotting the entire cycling range against capacity clearly shows the phase evolution. This has been the primary method of identifying the negative correlation of certain phases

in order to define the transitions (Figure 5-15a). The plot against potential is very congested, showing the concentration of phase changes occurring at low potentials near the start and end of charging and discharging, respectively (Figure 5-15b).

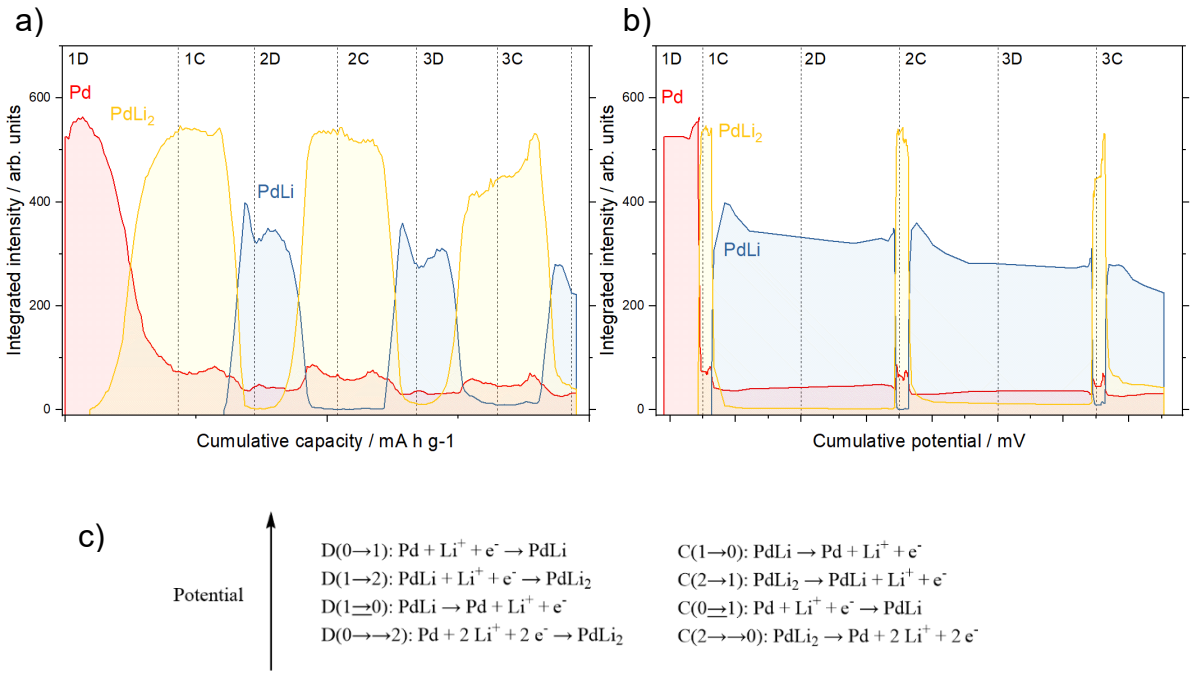


Figure 5-15. Identifying correlation in phase changes. Intensity plotted (a) against cumulative capacity, and (b) against cumulative potential. c) Four discharge and charge transitions.

General observations of refinement

From the Rietveld refinement it is conclusively shown that *cF* Pd does not expand by solid-solution lithiation to the expected *cF* $Pd^{int}Li$ (a = 4.00 Å), but rather a(cF,Pd) exhibits only a small increase during 1D, then varies noisily. There are many additional observations as a result of the retention of *cF* Pd as a minor phase, which were not evident by eye. It is shown that the *cF* Pd phase varies periodically at low intensity as an active participant in de/lithiation.

When charging, the double-lithium transition occurs as a delithiation process C(2→→0) at 200 mV. The magnitude of this change is an order of magnitude lower than the 1D(0→→2). At the oxidising potentials of ~900 mV under charge, the Pd:PdLi:$PdLi_2$ ratio is 2:81:17. Then the dominant *cP* PdLi phase undergoes delithiation C(1→0) at highly oxidising potentials above 2000 mV further regenerating *cF* Pd (Pd:PdLi:$PdLi_2$ = 21:78:1). This transition is shown to be drawn out over a very large potential range at high potential (Figure 5-16). Crucially we have shown using the correlation of in-operando phase identification and the electrochemical data that the first regeneration of *cF* Pd comes directly from the highly unstable doubly-lithiated *hP* $PdLi_2$ under negligibly oxidative potentials, and then from singly-lithiated *cP* PdLi requiring more oxidising conditions.

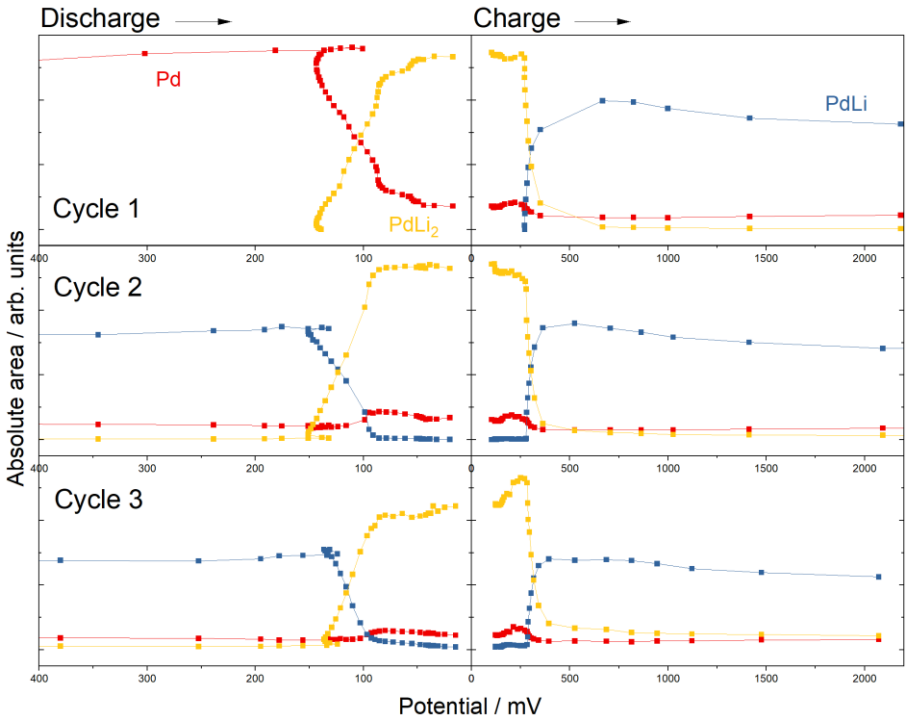


Figure 5-16. Intensity over potential separated by cycle. Reversing the discharge *x*-axis allows the use of non-cumulative potentials, and allows the centring of the plot around low potentials. Note that the *x*-scales are different for discharge and charge.

Overall, four charging transitions and four discharging transitions are identified. Tabulated details can be found in the Appendix: Table S5-2 and Table S5-3. The phase evolution will be discussed sequentially, with lattice parameters presented when relevant. Firstly, the dominant phase behaviour will be presented, followed by the minor transitions, and finally discussion of their reversibility and overpotentials.

5.3.6.3 Initial discharge: anisotropic solid-solution behaviour

cF *Pd expansion and conversion*

The pristine electrode exhibits a strong sharp *cF* Pd phase of lattice parameter 3.9067(2) Å. From out investigations into thermally lithiated palladium, the expected increase in lattice parameter to the topotactic expanded *cF* $Pd^{int}Li$ phase *a*(Pd) = 4.00 Å was not observed. Even if *cF* $Pd^{int}Li$ is not involved, it is sensible to think that *cF* Pd would be lithiated by single electron/lithium processes. However, the observed bypass transition requires two lithium ions and two electrons. The 1:1 molar *cP* PdLi is not observed, the reason for which is unknown but of significant interest.

The first diffraction pattern is collected at 1178 mV. Until 420 mV, the *cF* Pd phase intensity is stable (Figure 5-17). The intensity then increases (to a maximum at 120 mV), and is accompanied by a decrease in lattice parameter from the initial value *a*(Pd) = 3.9067(2) Å to 3.9060(2) Å (Δa = -0.0007 Å); these trends not easily attributed. This lattice parameter is then stable down to 101 mV. This is also the potential at which the potential increases to exhibit a dip of non-monotonic potential with respect to capacity (or time). Coincidentally, patterns are collected at 136 mV on both the downward and upward sides of the potential dip. The capacity accommodated between these potentials is 44 mA h g^{-1}, with 18 mA h g^{-1} being before the peak and 16 mA h g^{-1} after. Up to here, the intensity and lattice parameter has been

stable, and a low electrochemical capacity exhibited. Only 20% of the total initial discharge capacity is accommodated at this potential (Table 5-5).

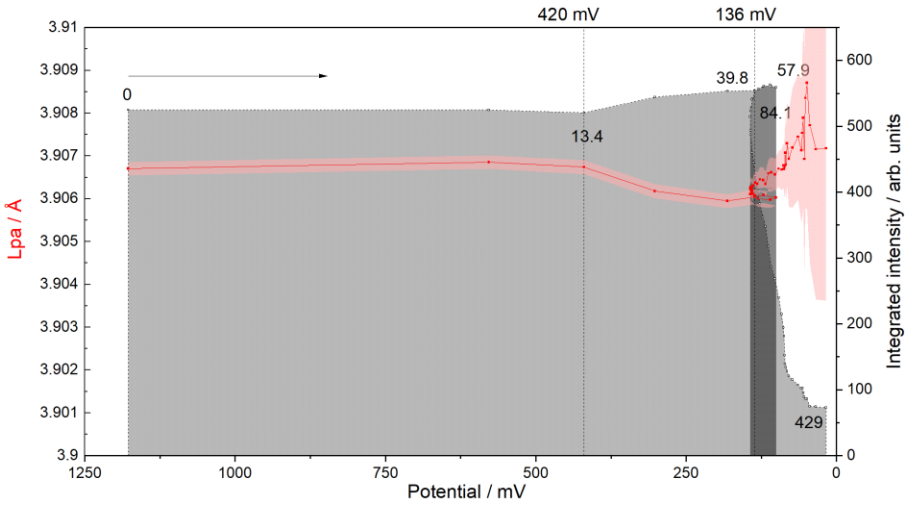


Figure 5-17. Phase evolution of *cF* Pd over 1D over potential; labels show capacity in mA h g^{-1}.

Description	Potential / mV	Capacity / mA h g^{-1}	Relative capacity	(dQ/dV) / mA h g^{-1} mV^{-1}
Stability	1178-420	0-13	0.03	-0.017
Intensity increase	420-136	13-40	0.06	-0.095
Dip: potential decrease	136-101	40-58	0.04	-0.514
Dip: Potential increase	101-136	58-84	0.06	0.743
Remaining discharge	136-17	84-429	0.80	-2.899

Table 5-5. dQ/dV of several potential ranges during 1D, showing the majority of capacity is intercalated from 136-17 mV.

At 136 mV, the *a*(Pd) begins to increase sharply (high errors make analysis unreliable), and the phase intensity decreases rapidly with potential. There is clearly a correlation between the start of the potential bump with the phase instability and unit-cell expansion. These sharp changes with respect to potential show discrete transitions at which *cF* Pd is lithiated to *hP* $PdLi_2$. Here, palladium nanoparticles are shown to be a conversion-type electrode material, rather than an intercalation-type.

This decomposition continues approximately linearly from 136-88 mV. Here, a steeper decomposition is observed from 88-79 mV, then a more gradual decomposition from 79-59 mV. Below 59 mV, the intensity remains stable, ending the half-cycle at 14% of the original value. This shows that the *cF* Pd phase is electrochemically active over a wide range (420-59 mV) involving several discrete processes (136-59 mV). By the end of the discharge, *cF* Pd composes 12%wt of the palladium signal.

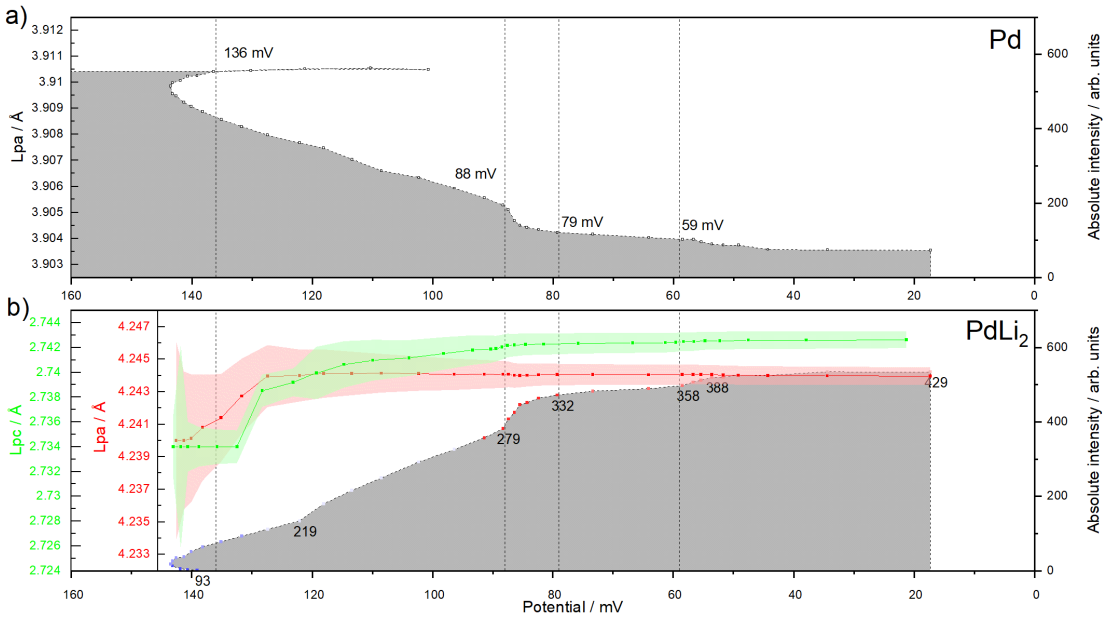


Figure 5-18. Correlation of (a) *cF* Pd and (b) *hP* $PdLi_2$ at low potential over 1D. Potential points coloured by capacity values with key potentials labelled with capacity [mA h g^{-1}]; intensity axes both 700 arb. units, and *x*($PdLi_2$) axes both 0.01 Å.

As the *cF* Pd weakens, the errors for *a*(Pd) become large. This theme of deteriorating accuracy at low intensity is widespread in this refinement. The phases are often being completely removed beneath the background, which is difficult to fit by batch refinement. It is aimed to conduct more supervised refinement, but the large number of patterns is prohibitive. However, by focussing on the emerging strong phase, it has been shown that the inflections have some correlation with *c*($PdLi_2$).

1D: Double lithiation bypass transition to hP *PdLi$_2$*

The decrease in Pd intensity is due to the discrete conversion to *hP* PdLi$_2$ 1D(0→→2), which is interestingly a more favourable transition than formation of *cP* PdLi. The phase appears at 139 mV, which corresponds the Pd phase behaviour. This is equivalent to 19.6% of the total discharge capacity. The weak initial peaks observed during formation are difficult to fit which are often unreliable in the same way the low potential *a*(Pd) is noisy. Here, a constraint has been used which can be seen by the constant initial *a*(PdLi) and *c*(PdLi). These values are not accurate to the material, but are required by the refinement.

From phase formation, both of the PdLi$_2$ lattice parameter increase gradually with decreasing potential. The *a*(PdLi$_2$) becomes stable first at 122 mV, at which the increase in intensity of PdLi$_2$ becomes steeper. Meanwhile *c*(PdLi$_2$) only stabilises below ~80 mV, after which the intensity of PdLi$_2$ remains approximately constant. This staggered stabilisation of lattice parameters and correlation with intensity is highly unexpected. This is an exciting highly phase-specific observation of a discrete *cF* to *hP* change in the palladium framework, as well as solid-solution behaviour that sequentially expands the unit-cell in the *ab*-plane then in the *c*-axis.

Between 136-122 mV, during the formation of *hP* PdLi$_2$, *a*(PdLi$_2$) is increasing. This appearance of the *hP* PdLi2 phase and anisotropic expansion of the lattice is theorised to be a single-lithium lithiation process, which exclusively expands the framework in the *ab*-plane from ~4.240(4) Å to 4.2440(5) Å. This is referred to as *ab*-insertion: [*cF* Pd + $Li^+ + e^-$ → *hP* PdLi]. It is responsible for 38% of the capacity after the appearance of *hP* PdLi$_2$ (Table 5-6). It also occurs in a narrow potential range, which is shown by a large d*Q*/d*V* value of 9.0 mA h g^{-1} mV^{-1}, indicating a discrete transition.

It is possible then that a second one-lithium/electron process takes place between 122-80 mV, which exclusively expands the framework in the *c*-axis from ~2.738(1) Å to 2.7426(7) Å. This is referred to as *c*-insertion: [*hP* PdLi + Li^+ + e^- → *hP* $PdLi_2$]. This is a larger expansion than the *ab*-axes, which is logical considering the compound is effectively a layered material. It is responsible for much less of the post-$PdLi_2$ capacity at 18% and occurs over a much wider potential range, yielding a low d*Q*/d*V* of 1.8 mA h g^{-1} mV^{-1}, indicating a solid-solution process. This solid-solution behaviour of *c*-insertion is supported by the flat plateau in this region on the d(*I*)/d(*V*) plot (Figure 5-19).

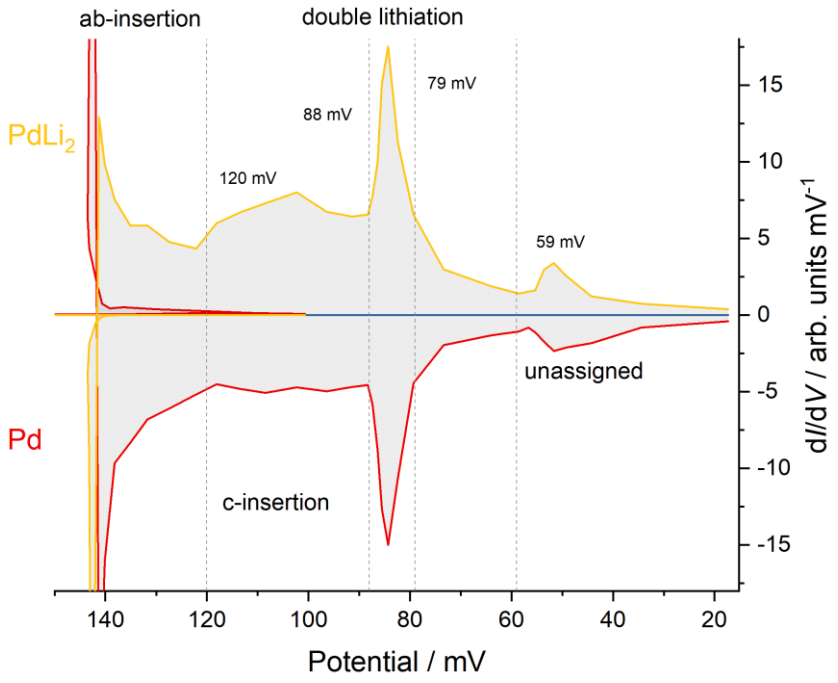


Figure 5-19. Highly negatively-correlated intensities of *cF* Pd and *hP* $PdLi_2$: d*I*/d*V* against potential. Smoothed by calculating change over four data points.

The low potential behaviour of $PdLi_2$ also corresponds to Pd intensity changes: the very steep loss of *cF* Pd at 88-79 mV and gain in *hP* $PdLi_2$ is attributed to a genuine double-

lithium insertion which is allowed by very low potential: [*cF* Pd + 2 Li^+ + 2 e^- → *hP* $PdLi_2$]. This is accompanied by a small but discrete increase in *c*($PdLi_2$).

There are two periods of phase stability between 79-59 mV and 54-17 mV. This is reasonably attributed to graphite intercalation. The beginning of these plateaus correspond well to the redox peaks of graphite when cycled as a control, which were centred 80 mV and 50 mV (Figure 5-8). Between these plateaus, there is a small discrete transition at 60 mV. As with the other discrete transition at 88 mV, the *c*($PdLi_2$) also increases slightly. This transition is unattributed. By the end of discharge the crystalline Pd:$PdLi_2$ mass ratio is 12:88.

Description	Potential / mV	Capacity / mA h g^{-1}	Relative capacity / mA h g^{-1}	Δ relative capacity / frac	d*Q*/d*V* / mA h g^{-1} mV^{-1}
ab-insertion	136-122	93	0-126	0.38	-9.00
c-insertion	122-88	219	126-186	0.18	-1.76
Double lithiation	88-79	279	186-239	0.16	-5.89
Graphite lithiation	79-59	332	239-265	0.08	-1.30
Additional transition	59-54	358	265-295	0.09	-6.00
Graphite lithiation	54-17	388	295-336	0.12	-1.11

Table 5-6. Phase evolution of *cF* Pd and *hP* $PdLi_2$ during 1D.

Closer inspection of 1D(0→→2) has revealed the low *a*(Pd) expansion, no *cF* $Pd^{int}Li$ formation, numerous correlated lattice parameter and intensity changes, and interrogation of the capacity dependence. Using this proposed mechanism, the apparent double-lithium bypass transition from *cF* Pd to *hP* $PdLi_2$ is shown to be highly complex. The transition was thought to bypass any equimolar palladium-lithium intermediate. However, it is only the formation of a *cP* phase that is bypassed, with the many discrete increases in intensity attributed to single-electron processes. The genuine double-lithium transition is thought to be observed as the low capacity transitions at highly reducing potentials.

5.3.6.4 Standard cycling: triphasic reversible transitions

The dominant phase transitions after 1D is (1↔2). This can be clearly seen by plotting the change in intensity with capacity, d*I*/d*Q*, against capacity, which shows approximately symmetric direct conversion between *hP* $PdLi_2$ and *cP* PdLi (Figure 5-20). (The d*I*/d*V* against potential plot is highly congested at low potentials: Figure S5-9). In the standard d*Q*/d*V* plot, potential plateaus of high electrochemical capacity are observed as peaks, with the integrated area being equivalent to capacity. These redox peaks must be assigned to various intercalations and electron transfers. Here, the absolute integrated intensity of Bragg phases as a metric of change allows phase-specific assignment.

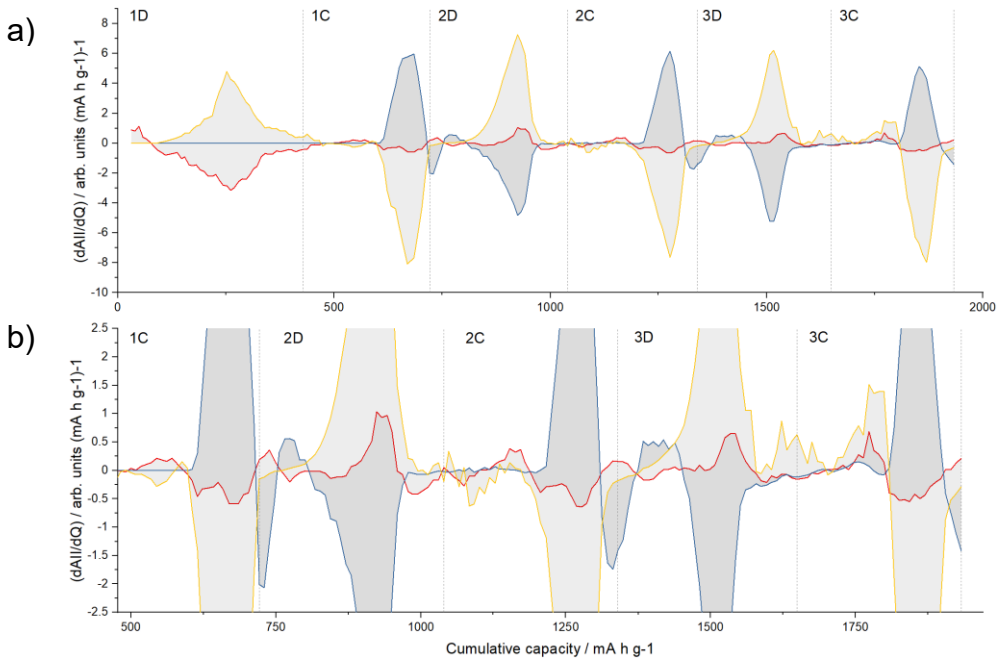


Figure 5-20. Change in intensity with capacity, d*I*/d*Q* against cumulative capacity. Smoothed by calculating change over four data points. (a) The entire cycled range, and (b) omitting 1D in order to show minor changes.

However, additional to this dominant transition, there are several small but negatively-correlated intensity changes indicating additional phase transitions. These

additional weak transitions are very subtle and have required the interrogation of Rietveld parameters to be observed, quantified, and analysed. Fortunately, the correlation is mostly evident. Hence the phase fluctuations are able to be ascribed to only one transition, but this is untrue for 3C, for which all three phases increase during charge.

C(2→1): further anisotropy of hP $PdLi_2$ on delithiation

When charging, there is an immediate increase in the intensity of *cF* Pd, and an associated negatively correlated decrease in the intensity of *hP* $PdLi_2$, which occurs between 0 mV and 220 mV (Figure 5-21a): the expected range observed in discharge. This is ascribed to the double-delithiation C(2→→0) transition, which bypasses *cP* PdLi. Though analogous to 1D(0→→2), this transition is orders of magnitude weaker for all three charge half-cycles, and no subtle correlation to *cF* Pd is observed due to this weakness. The intensity of *cF* Pd increases to a local maximum at ~230 mV, corresponding to a phase ratio of Pd:$PdLi_2$ = 15:85. During this transition, the lattice parameters of *hP* $PdLi_2$ both decrease linearly as a solid-solution delithiation (Figure 5-21c).

At 254 mV, the intensity of *hP* $PdLi_2$ begins to decrease significantly to near-zero intensity at 350 mV. Evidence of *cP* PdLi is first only observed at 276 mV. These two decreases in intensity are ascribed to C(0→1) and C(2→1). These are shown to be negatively correlated by the d(*I*)/d(*Q*) plot (Figure 5-21b).

The $PdLi_2$ is proven to be highly involved. Between the start of charge and 220 mV, the lattice parameters both show slight linear contraction, as is expected from the deintercalation of interstitial lithium. At 220 mV, *c*($PdLi_2$) decreases suddenly by 0.0081 Å to a minimum at 270 mV (2.7426(7) Å to 2.735(6) Å), the *a*($PdLi_2$) increases from 4.2437(5) Å to a maximum of 4.2450(6) Å at 276 mV, which corresponds to the local maximum of

c($PdLi_2$) in the bump. The *a*($PdLi_2$) remains high, then decreases until disappearance of the phase by 350 mV. Strangely, the decreasing *a*($PdLi_2$) exhibits a bump at 270 mV (maximum of 2.7353(9) Å at 276 mV), before the phase is effectively unobserved at 350 mV. However, the large errors due to the weak phase render this observation debatable. Thus, the sequential expansion of the *a*- and *c*- axes of hP $PdLi_2$ during lithiation, is shown to change to a truly anisotropic volume change on delithiation, in which the hexagonal unit-cell becomes flatter before decomposing. Regarding the lattice parameter of *cP* PdLi, it stays remarkably constant throughout the whole cycling process. The parameter was fixed at 2.987 Å in order to stabilise the fitting of other phases.

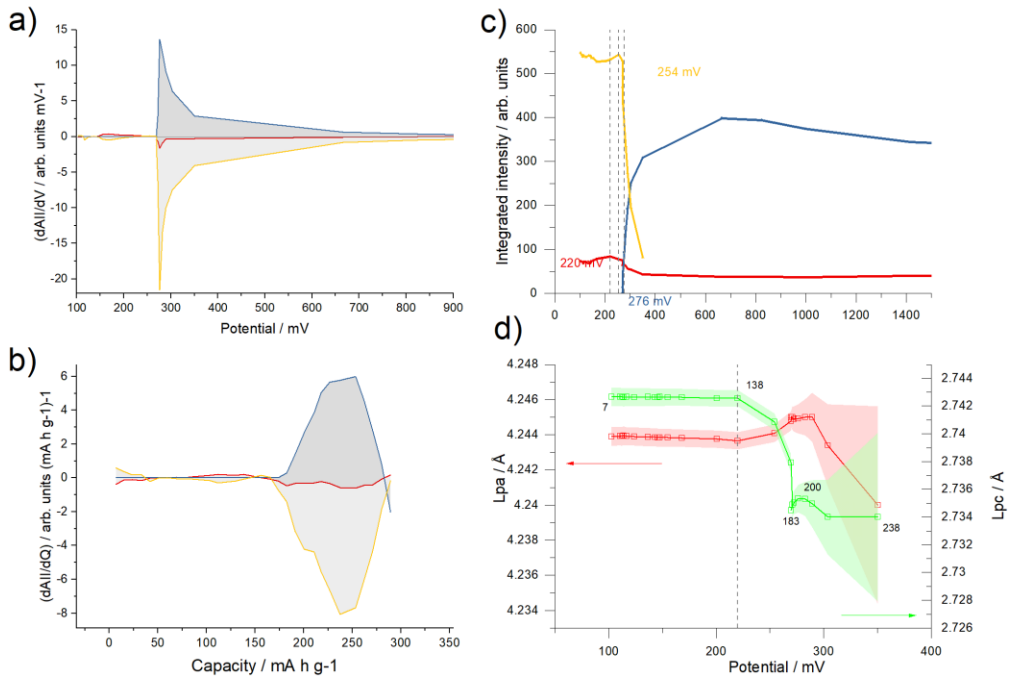


Figure 5-21. Triphasic cycling of 1C. (a) d*I*/d*V* against potential, and (b) d*I*/d*Q* against capacity. Both intensity-derivative plots smoothed by calculating change over four data points. (c) Raw intensity values; labels show local maximum intensity of *cF* Pd (red) and $PdLi_2$ (yellow), and the appearance of *cP* PdLi (blue). (d) $PdLi_2$ lattice parameters against potential; capacity labels in [mA h g^{-1}]

With *cF* Pd and *hP* $PdLi_2$ both decreasing at 220 mV, the intensity of *cP* PdLi then increases significantly with clear negative correlation with *hP* $PdLi_2$. The unexpected

C(0⟶1) is very minor component of the total change in intensity. Regardless, the change in intensity is observed in every charge half-cycle over many patterns, and is deemed valid. However, it does not make electrochemical sense.

C(1→0): cF Pd regeneration

At high charging potentials, 600-3000 mV, the intensity of *cP* PdLi decreases while *cF* Pd is regenerated C(1→0) as very weak and broad peaks, which indicates that the delithiation produces small crystalline domains. At the end of the charge half-cycle, the *I*(PdLi) has only decreased by 18% of the maximum, which indicates a far from complete phase transition. Similarly, the increase in the *I*(Pd) is very small. Clearly the lithium in *cP* PdLi is far too stable to be de-intercalated onto the lithium anode, requiring higher charging potentials. However, potentials above 3000 mV are increasingly irrelevant for anode-material candidates, because against a standard NMC cathode material (~4 V vs Li^+/Li), this transition would not offer much potential difference. Despite the incomplete transition, it is the second most dominant with respect to change in intensity, with only the lower potential (1↔2) exhibiting more involvement in phase evolution.

5.3.6.5 Degradation: irreversibility and overpotentials

For 2D, the behaviour resembles 1C rather than 1D. The discharge is not observed as a biphasic one-transition process, as was the case for 1D. Instead, the inverse transitions of 1C are observed in the reverse order, i.e. D(0→1), D(1→2), D(1⟶0), and D(0→→2).

Decreasing intensity-steps in D(0→→2)

The 2D(0→→2) transition is an order of magnitude less significant than in 1D, exhibiting relatively little of the highly correlated intensities and lattice parameters of *cF* Pd

and *hP* $PdLi_2$ in 1D(0→→2). Instead, for 2D and 3D, the absence of these transitions can be interpreted (Figure 5-22, bottom left panel). For 2D(0→→2), there is no change in gradient of intensity of *hP* $PdLi_2$ between ~150-90 mV, which had been a marker of lithium *c*-insertion. The discrete increase in intensity at 88 mV that had been attributed to the actual double lithiation process is observed, but at higher potential. Despite this, the intensity fully recovers to 1D levels, indicating that the second unattributed transition at 59 mV also occurs at this higher potential. This combined transition is not observed for 3D, exhibiting a plateau in intensity from 88 mV. However, considering the stable cycling capacity of the electrode, it is surprising that an entire transition is seemingly not occurring in 3D. This is an example of the disassociation between the electrochemical capacity and the crystalline Bragg transitions and intensities.

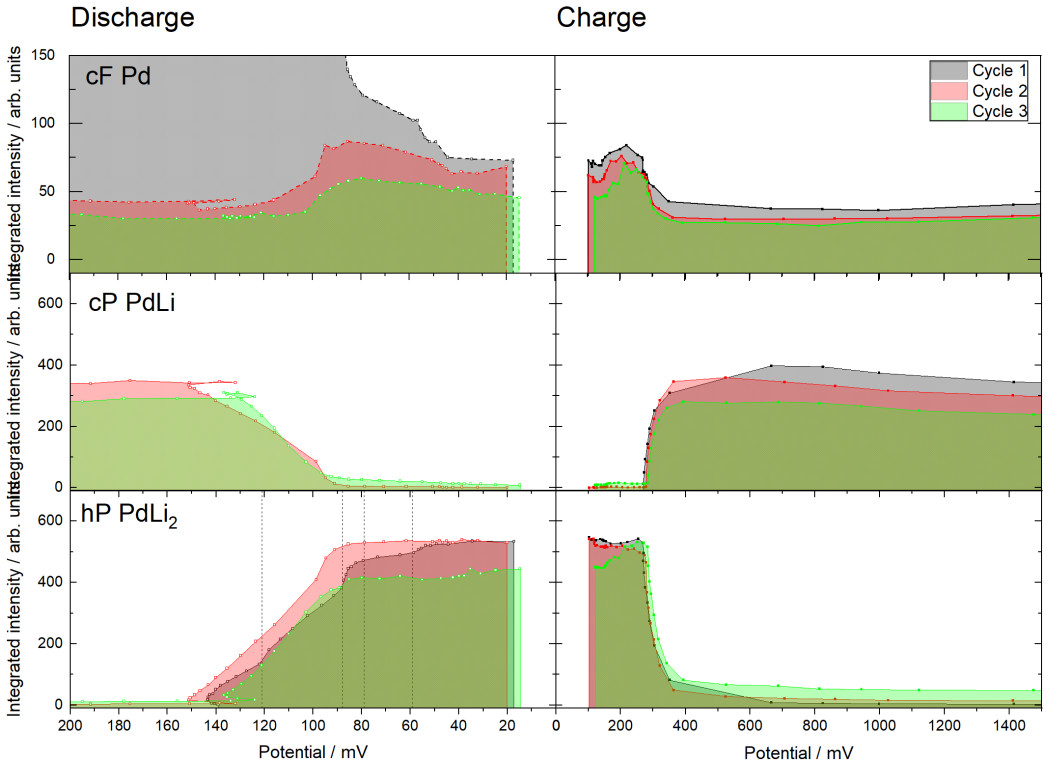


Figure 5-22. Degradation of intensity and potential: comparing the energy and magnitude of transitions over cycling.

With respect to the potential of transitions, discharge transitions tend to occur at increasingly lower potentials, meanwhile the charging potentials remain approximately constant. This indicates that the delithiation process remains reproducible, but the lithiation is increasingly unfavourable, despite the electro-potential gradient. This may occur due to irreversibly intercalated lithium that decreases the available sites for intercalation.

Effect of cycling on $PdLi_2$ lattice parameters

This effect is also observed in the lattice parameter changes for *hP* $PdLi_2$. On discharge the appearance of the phase decreases from 130 mV to 120 mV to 110 mV. Meanwhile, while charging, the *a*($PdLi_2$) increase and *c*($PdLi_2$) decrease occur consistently at 220 mV (though the bump in *c*($PdLi_2$) occurs at increasing potentials: 270 mV, 278 mV, and 286 mV). There will always be a difference in the potentials of discharge and charge, due to the physically guaranteed energy inefficiency. However, the increasing overpotential is cause for concern, even though the Coulombic capacity is stable.

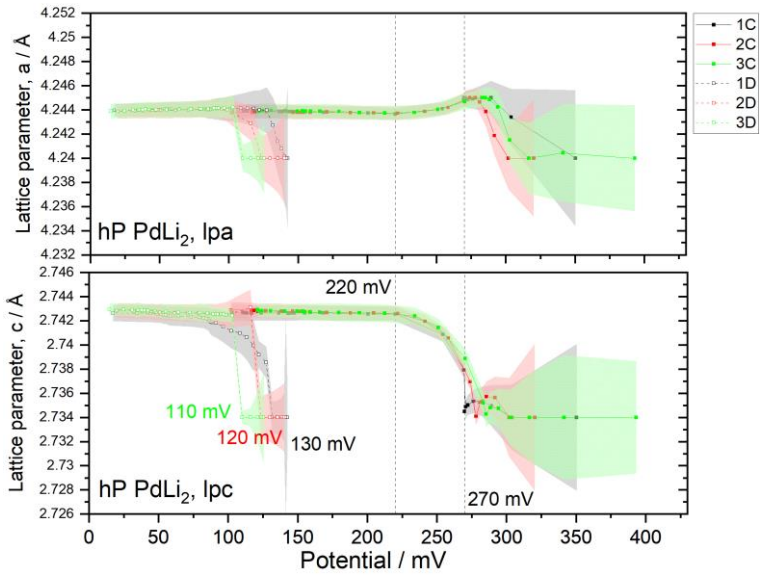


Figure 5-23. Lattice parameter changes for *hP* $PdLi_2$ over three full cycles.

Magnitude of transitions over time

The contribution to Coulombic capacity is difficult to measure. Evidently, not all of the transitions are as important to the electrode's role as a lithium store. Despite all the subtleties of the double-lithium bypass transition (0↔↔2), unexpected direction (0$\underleftrightarrow{}$1) transitions, and the high potential (0↔1), the (1↔2) constitutes the majority of the intensity changes. The length of each transition with respect to capacity cannot yield the associated amount of lithium involved, due to the simultaneous lithium intercalation into graphite at low potentials (Figure 5-8). It is desired to factor graphite intercalation into this investigation in order to plot the phase changes against lithium intercalation into palladium, rather than against the whole electrode. Using an inert carbon support is possible, but the use of carbon black seemed to result in low intensity patterns, as shown above (Figure 5-13).

Instead of using amount of lithium, the importance of the transitions on the electrode as a whole can be presented using the change in intensity as a highly phase-specific metric. This is non-trivial due to the overlap of certain transitions: C(0$\underrightarrow{}$1) and C(2→1) that both result in *I*(PdLi) increasing; D(1→2) and D(1$\underrightarrow{}$0) that both result in *I*(PdLi) decreasing. The magnitude of the transition for charge is defined by the decrease in the intensity of the initial phase, Δ*I*(initial), and for discharge as the increase in the intensity of the final phase, Δ*I*(final) (Figure 5-24). It is quantitatively shown that the expected *cF* Pd ↔ *cP* PdLi (0↔1) transition is by far the most dominant for both discharge and charge (Figure 5-24). The other transitions are an order of magnitude less significant as a proportion of the total intensity change. The double-lithium bypass transition (0↔2) is the least significant, exhibiting 3-5% of the (0↔1)

transitions. It is noted that the magnitudes of the Δ*I* are decreasing with cycling. This shows a loss of crystallinity as the overall intensity decreases.

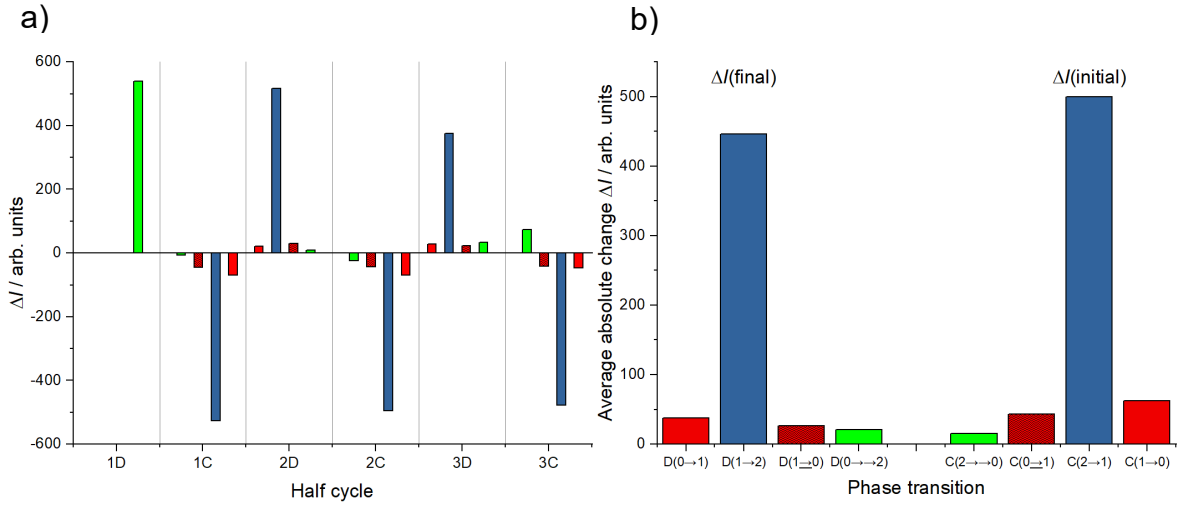


Figure 5-24. Representing the magnitude of the phase transitions by change in intensity. For discharge Δ*I*(final) and for charge Δ*I*(initial) are used. (a) Relative change. (b) Average absolute change; anomalous 1D(0→→2) (large magnitude) and 3C(2→→0) ($PdLi_2$ increases) removed from average.

Decreasing crystallinity

This decrease in recovered intensity is systematic for all phases with cycling, exhibiting lower minima and maxima (Figure 5-22). The *cF* Pd and *cP* PdLi are affected more significantly, with *hP* $PdLi_2$ remaining relatively constant, composing an increasing proportion of the crystalline mass. At a charging potential of 2000 mV (highest common potential sampled), *cP* PdLi exhibits intensity of 330, 285, and 227 arb. units, over the three cycles respectively. If fitted using a polynomial or linear function, this trend indicates a complete loss of the crystalline phase by cycle 6 or 8, respectively. Considering the electrode's stable capacity, the crystallinity does not seem to be linked to stable energy-storage performance.

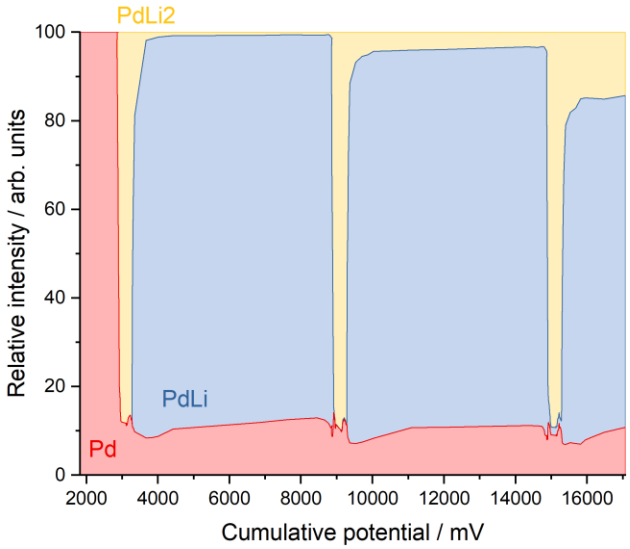


Figure 5-25. Normalised intensity values showing increasing relative composition of *hP* $PdLi_2$ from *cP* PdLi.

5.3.7 Non-crystalline local order by PDF

The loss of intensity in *cF* Pd and *cP* PdLi is not due to conversion to any crystalline phase. In unpublished work, we have used PDF as a complementary scattering technique to allow the interrogation of local ordered structure in palladium nanoparticles.[3] Here, we aimed to use PDF of post-mortem electrode material to determine whether the loss of crystalline volume is due to a complete loss of atomic order, or the retention of local structure. There exist the same limitations of low-scattering lithium as with Bragg experiments, making the elucidation of lithium position and occupancy difficult. The refinement against these data has not been carried out due to time limitations, but some semi-quantitative analysis is presented.

The PDF pattern for the pristine pallidum shows characteristic peaks at 2.74 Å, 3.88 Å, and 4.76 Å, which correspond to values of 2.76 Å, 3.91 Å, and 4.78 Å from the SXPD structure solution. The material is well-ordered, exhibiting clear peaks up to 40 Å. The thermally lithiated sample *cF* $Pd^{int}Li$ exhibited increased distances of 2.82 Å, 4.00 Å, and

4.90 Å, as well as for all other peaks, consistent with the expected topotactic expansion. The material is also well-ordered, exhibiting clear peaks up to 25 Å.

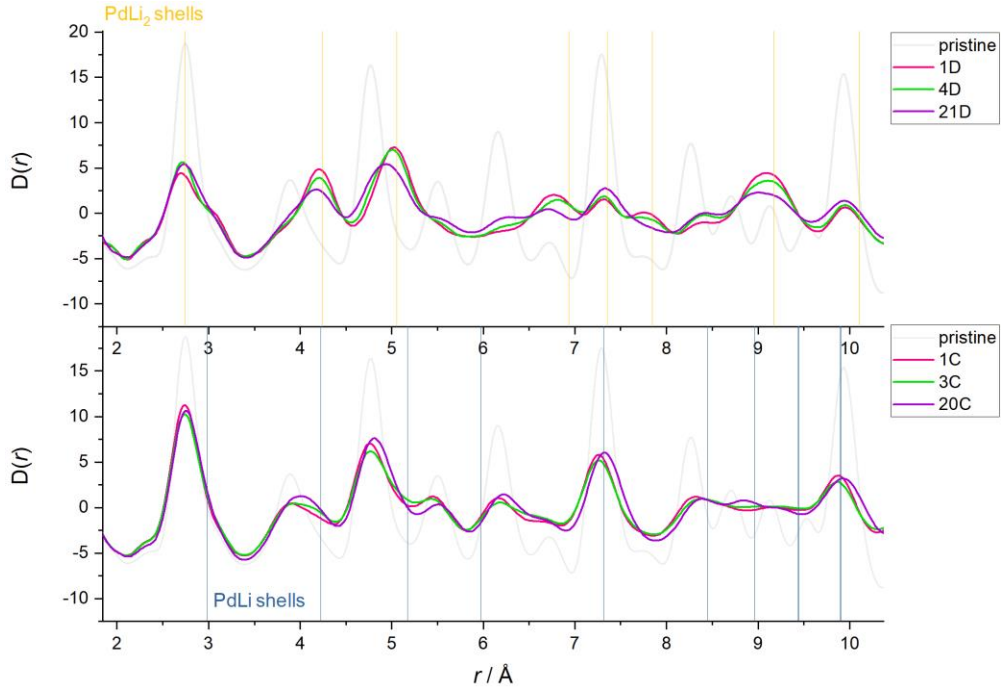


Figure 5-26. PDF of post-mortem 50%Pd/cb Dotted lines show characteristic *hP* $PdLi_2$, solid lines show characteristic *cP* PdLi.

As with the analysis of the bulk, the material becomes more disordered with cycling, in that the peaks become less intense and broader. However, there is a general retention in intensity and width, showing the retention of local order. The charged (delithiated) materials are more ordered than the discharged (lithiated) material, with respect to intensity, width, and ordered distance. The charged materials appear very similar to pristine Pd, with almost no convincing indication of characteristic *cP* PdLi distances. This was unexpected as at the end of charge, the majority of the crystalline phase is *cP* PdLi (Pd:PdLi:$PdLi_2$ = 43:332:3. 36:281:13, 33:225:43, for cycles 1, 2, and 3, respectively). Hence, the desired analysis of the decreasing bulk crystallinity of *cP* PdLi is unable to be conducted. We understand the large

amount of *cF* Pd present to show that there is a large volume of non-crystalline *cF* Pd (either by disorder or crystallite size).

For the discharged material, the variation from pristine *cF* Pd is much greater, showing many of the characteristic distances of *hP* $PdLi_2$. These exhibit much greater changes over cycling by becoming weaker and more contracted. In the bulk analysis, the lattice parameters of *hP* $PdLi_2$ consistently recovered to similar values. However, here it is shown that there is an enduring contraction on the framework.

5.4 Conclusions

5.4.1 Summary

The palladium-lithium system has been investigated, focussing on the phase behaviour of the thermal de/lithiation, and then the electrochemical lithiation as part of the LIB system, in order to establish a relationship between the synthetic conditions, bulk crystalline scattering behaviour, and LIB performance. Palladium nanoparticles were synthesised by an established thermal method, and shown to contain appreciable levels of intercalated carbon, which originates from the organic precursor counterion. An in-situ lithiation method is established, which also forms an expanded interstitially-doped phase, which is shown to impart increased thermal and dissolution stability.

The material was evaluated as an LIB anode material, showing good capacity and stable cycling. Electrochemical lithiation also presents a different method of lithiation that is more controlled and homogeneous than the thermal route. The phase evolution of electrochemical lithiation was carried out by post-mortem and in-operando SXPD, showing complex and well-defined phase behaviour. We predicted that electrochemical lithiation would behave similarly to the thermal chemical lithiation detailed previously.[38] However, this in-operando experiment has revealed that the electrochemical lithiation of palladium metal results in much more significant structural changes, namely discrete phase changes as a conversion-type electrode material. The crystalline intensity decreases over cycling, as well as the local order. However, despite this, the electrochemical capacity is constant, indicating appreciable amorphous lithiation.

Though not explicitly addressed, the advancement of the understanding of this archetypal material will aid a range of similar doped systems that also remain poorly characterised with respect to the solid-state guest-host interaction, solid-solution behaviour, discrete phase transitions, bulk and local order, and electrochemical cyclability

5.4.2 Evaluation and future work

5.4.2.1 $Pd^{int}C$

The identification of inadvertent carbon requires further investigation. The possibility of a ternary compound could have great impact on the application of the material as a catalyst. Electronic characterisation of the $Pd^{int}C$ and $Pd^{int}Li$ materials is desired. It is suggested that a variety of mono-phasic and biphasic samples are analysed by XPS in order to ascertain the varying palladium environment. This would have impact on the application and design of the materials as catalysts.

Their highly lithium-dependent thermal and dissolution stability was attributed using a hypothesis of encapsulation, kinetic barrier, oxidative-atmosphere exclusion, and an internal lithium reservoir. This evidently needs to be addressed further. Full indexing and identification of the lithium side-products CLS1 and CLS2 needs to be carried out, as these additional temperature-dependent phases seem likely to be important. The role of the acetate perhaps as a capping agent and involvement in a passivating layer need to examined. Morphological analysis is required to assess the encapsulation and lithium reservoir, for example by SEM and TEM. Additionally, as the homogeneity of the lithiation process are in doubt, the influence of particle size and metal loading should also be carried out.

5.4.2.2 In-situ lithiation

The development of an in-situ lithiation procedure was shown to be successful, but more direct comparison to post-synthesis lithiation needs to occur. In particular, the lack of VT-SXPD for post-synthesis lithiated samples renders any attribution of the unusual thermal stability and features to the in-situ process to be dubious. Additionally, comparison of the effect of the two procedures on morphology needs to be carried out, for example the effect on particle size and lithium distribution.

5.4.2.3 LIB

LIB evaluation has focused on the structural stability of palladium redox cycling, volume changes, and capacity. Widening the potential range may result in the regeneration of *cF* Pd. However, this has been tested ex-situ and shown not to enhance capacity; in fact, capacity stability was much decreased, as well as large OCV potential losses. It is also realised that for long-duration cycling, in-situ characterisation may be more time-efficient, in which cells are cycled ex-situ in in-situ housings, quenched by halting cycling and analysed by SXPD, before returning to cycling.

Monitoring phase-specific changes in intensity took primary focus, with secondary interrogation of Coulombic capacity and energy efficiency. It is a deficiency in this investigation that quantitative analysis of the energy capacity and efficiency were not conducted. Furthermore, the initial hopes of using the palladium's interstitial sites to store lithium in a low volume expansion framework were not well-founded. It exhibits quite considerable volume expansion at the atomic level. There was no characterisation of macro volume expansion or elucidation of electrode damage, such as by SEM, which now seems

pertinent considering the anisotropic expansion of *hP* $PdLi_2$, and the systematic loss of order with cycling.

Using thermally lithiated $Pd^{int}Li$ and incidental $Pd^{int}C$ as anode materials would be an interesting combination of the thermal and electrochemical work. It is predicted that partially carbon-doped frameworks will exhibit proportionately lower capacities. Meanwhile, pre-lithiation is often used for electrode materials in order to compensate for the irreversible capacity loss associated with initial cycling.[47] Hence, biphasic Pd/ $Pd^{int}Li$ may be advantageous to stable capacity.

Phase aging

It has been shown that there is lasting effect on the emergent phases on intensity, lattice parameter, and phase-transition potential (Figure 5-27). This is despite the proven ex-situ long-term cycling stability. Full analysis and Rietveld refinement of the PDF data collected in this work needs to be conducted. The topic of phase aging and degradation has become a likely long-term research focus.

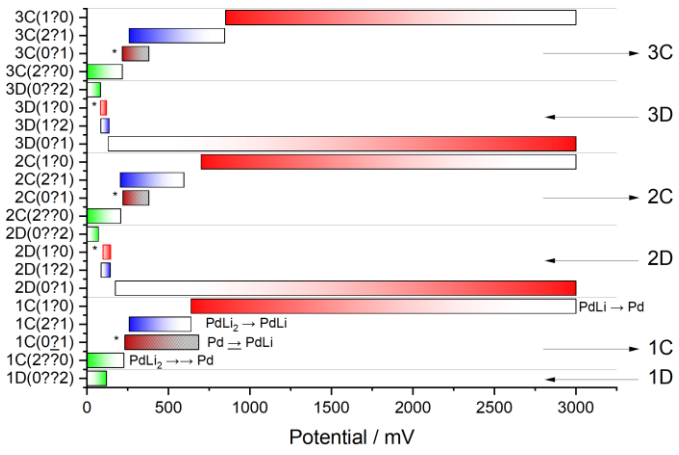


Figure 5-27. Schematic of potential ranges of phase transitions. (Pd↔↔$PdLi_2$) in green, (Pd↔ PdLi) in red, (PdLi↔$PdLi_2$) in blue. Unexpected direction (Pd↔PdLi) transitions marked with * and darkened colour.

5.5 References

(1) Chen, T.; Ellis, I.; Hooper, T. J. N.; Liberti, E.; Ye, L.; Lo, B. T. W.; O'Leary, C.; Sheader, A. A.; Martinez, G. T.; Jones, L.; Ho, P.-L.; Zhao, P.; Cookson, J.; Bishop, P. T.; Chater, P.; Hanna, J. V.; Nellist, P.; Tsang, S. C. E. Interstitial Boron Atoms in the Palladium Lattice of an Industrial Type of Nanocatalyst: Properties and Structural Modifications. J. Am. Chem. Soc. 2019, 141 (50), 19616–19624. https://doi.org/10.1021/jacs.9b06120.

(2) Ellis, I. T.; Wolf, E. H.; Jones, G.; Lo, B.; Li, M. M.-J.; York, A. P. E.; Tsang, S. C. E. Lithium and Boron as Interstitial Palladium Dopants for Catalytic Partial Hydrogenation of Acetylene. Chem. Commun. 2017, 53 (3), 601–604. https://doi.org/10.1039/C6CC08404D.

(3) Chen, T. Local Structural and Electronic Modifications of Palladium by Interstitial Lithium Atoms at the Nanoparticle Scale. Unpublished.

(4) Cervellino, A.; Giannini, C.; Guagliardi, A. Determination of Nanoparticle Structure Type, Size and Strain Distribution from X-Ray Data for Monatomic f.c.c.-Derived Non-Crystallographic Nanoclusters. J. Appl. Crystallogr. 2003, 36 (5), 1148–1158. https://doi.org/10.1107/S0021889803013542.

(5) Rees, G. J.; Orr, S. T.; Barrett, L. O.; Fisher, J. M.; Houghton, J.; Spikes, G. H.; Theobald, B. R. C.; Thompsett, D.; Smith, M. E.; Hanna, J. V. Characterisation of Platinum-Based Fuel Cell Catalyst Materials Using 195Pt Wideline Solid State NMR. Phys. Chem. Chem. Phys. 2013, 15 (40), 17195. https://doi.org/10.1039/c3cp52268g.

(6) Hooper, T. J. N.; Partridge, T. A.; Rees, G. J.; Keeble, D. S.; Powell, N. A.; Smith, M. E.; Mikheenko, I. P.; Macaskie, L. E.; Bishop, P. T.; Hanna, J. V. Direct Solid State NMR Observation of the 105 Pd Nucleus in Inorganic Compounds and Palladium Metal Systems. Phys. Chem. Chem. Phys. 2018, 20 (41), 26734–26743. https://doi.org/10.1039/C8CP02594K.

(7) Pryadchenko, V. V.; Srabionyan, V. V.; Mikheykina, E. B.; Avakyan, L. A.; Murzin, V. Y.; Zubavichus, Y. V.; Zizak, I.; Guterman, V. E.; Bugaev, L. A. Atomic Structure of Bimetallic Nanoparticles in PtAg/C Catalysts: Determination of Components Distribution in the Range from Disordered Alloys to "Core–Shell" Structures. J. Phys. Chem. C 2015, 119 (6), 3217–3227. https://doi.org/10.1021/jp512248y.

(8) Akamaru, S.; Hara, M.; Matsuyama, M. Alloying Effects on the Hydrogen-Storage Capability of Pd–TM–H (TM=Cu, Au, Pt, Ir) Systems. J. Alloys Compd. 2014, 614, 238–243. https://doi.org/10.1016/j.jallcom.2014.06.118.

(9) Flanagan, T. B.; Wang, D.; Luo, S. Thermodynamics of H in Disordered Pd−Ag Alloys from Calorimetric and Equilibrium Pressure−Composition−Temperature Measurements. J. Phys. Chem. B 2007, 111 (36), 10723–10735. https://doi.org/10.1021/jp073484v.

(10) Hwang, S.-M.; Lee, H.-Y.; Jang, S.-W.; Lee, S.-M.; Lee, S.-J.; Baik, H.-K.; Lee, J.-Y. Lithium Insertion in SiAg Powders Produced by Mechanical Alloying. Electrochem. Solid-State Lett. 2001, 4 (7), A97–A100. https://doi.org/10.1149/1.1375176.

(11) Iwasawa, T.; Tokunaga, M.; Obora, Y.; Tsuji, Y. Homogeneous Palladium Catalyst Suppressing Pd Black Formation in Air Oxidation of Alcohols. J. Am. Chem. Soc. 2004, 126 (21), 6554–6555. https://doi.org/10.1021/ja031936l.

(12) Evangelisti, C.; Panziera, N.; Pertici, P.; Vitulli, G.; Salvadori, P.; Battocchio, C.; Polzonetti, G. Palladium Nanoparticles Supported on Polyvinylpyridine: Catalytic Activity in Heck-Type Reactions and XPS Structural Studies. J. Catal. 2009, 262 (2), 287–293. https://doi.org/10.1016/j.jcat.2009.01.005.

(13) Chan, C. W. A.; Mahadi, A. H.; Li, M. M.-J.; Corbos, E. C.; Tang, C.; Jones, G.; Kuo, W. C. H.; Cookson, J.; Brown, C. M.; Bishop, P. T.; Tsang, S. C. E. Interstitial Modification of Palladium Nanoparticles with Boron Atoms as a Green Catalyst for Selective Hydrogenation. Nat. Commun. 2014, 5, 5787. https://doi.org/10.1038/ncomms6787.

(14) Chan, C. W. A.; Tam, K. Y.; Cookson, J.; Bishop, P.; Tsang, S. C. Palladium with Interstitial Carbon Atoms as a Catalyst for Ultraselective Hydrogenation in the Liquid Phase. Catal. Sci. Technol. 2011, 1 (9), 1584–1592. https://doi.org/10.1039/C1CY00257K.

(15) Lin, J.-Y.; Xi, C.; Li, Z.; Feng, Y.; Wu, D.-Y.; Dong, C.-K.; Yao, P.; Liu, H.; Du, X.-W. Lattice-Strained Palladium Nanoparticles as Active Catalysts for the Oxygen Reduction Reaction. Chem. Commun. 2019. https://doi.org/10.1039/C9CC00447E.

(16) Bugaev, A. L.; Guda, A. A.; Pankin, I. A.; Groppo, E.; Pellegrini, R.; Longo, A.; Soldatov, A. V.; Lamberti, C. Operando X-Ray Absorption Spectra and Mass Spectrometry Data during Hydrogenation of Ethylene over Palladium Nanoparticles. Data Brief 2019, 24, 103954. https://doi.org/10.1016/j.dib.2019.103954.

(17) Fortea-Pérez, F. R.; Mon, M.; Ferrando-Soria, J.; Boronat, M.; Leyva-Pérez, A.; Corma, A.; Herrera, J. M.; Osadchii, D.; Gascon, J.; Armentano, D.; Pardo, E. The MOF-Driven Synthesis of Supported Palladium Clusters with Catalytic Activity for Carbene-Mediated Chemistry. Nat. Mater. 2017, 16 (7), 760–766. https://doi.org/10.1038/nmat4910.

(18) Ishikawa, Y.; Kimura, S.; Takase, K.; Yamamoto, K.; Kurashige, Y.; Yanai, T.; Murahashi, T. Modulation of Benzene or Naphthalene Binding to Palladium Cluster Sites by the Backside-Ligand Effect. Angew. Chem. 2015, 127 (8), 2512–2516. https://doi.org/10.1002/ange.201409499.

(19) Ulvestad, A.; Welland, M. J.; Collins, S. S. E.; Harder, R.; Maxey, E.; Wingert, J.; Singer, A.; Hy, S.; Mulvaney, P.; Zapol, P.; Shpyrko, O. G. Avalanching Strain Dynamics during the Hydriding Phase Transformation in Individual Palladium Nanoparticles. Nat. Commun. 2015, 6 (1), 10092. https://doi.org/10.1038/ncomms10092.

(20) Sytwu, K.; Hayee, F.; Narayan, T. C.; Koh, A. L.; Sinclair, R.; Dionne, J. A. Visualizing Facet-Dependent Hydrogenation Dynamics in Individual Palladium Nanoparticles. Nano Lett. 2018, 18 (9), 5357–5363. https://doi.org/10.1021/acs.nanolett.8b00736.

(21) Akiba, H.; Kofu, M.; Kobayashi, H.; Kitagawa, H.; Ikeda, K.; Otomo, T.; Yamamuro, O. Nanometer-Size Effect on Hydrogen Sites in Palladium Lattice. J. Am. Chem. Soc. 2016, 138 (32), 10238–10243. https://doi.org/10.1021/jacs.6b04970.

(22) Srabionyan, V. V.; Bugaev, A. L.; Pryadchenko, V. V.; Avakyan, L. A.; van Bokhoven, J. A.; Bugaev, L. A. EXAFS Study of Size Dependence of Atomic Structure in Palladium Nanoparticles. J. Phys. Chem. Solids 2014, 75 (4), 470–476. https://doi.org/10.1016/j.jpcs.2013.12.012.

(23) Zhao, Z.; Huang, X.; Li, M.; Wang, G.; Lee, C.; Zhu, E.; Duan, X.; Huang, Y. Synthesis of Stable Shape-Controlled Catalytically Active β-Palladium Hydride. J. Am. Chem. Soc. 2015, 137 (50), 15672–15675. https://doi.org/10.1021/jacs.5b11543.

(24) Mortazavi, S. Z.; Parvin, P.; Reyhani, A.; Golikand, A. N.; Mirershadi, S. Effect of Laser Wavelength at IR (1064 Nm) and UV (193 Nm) on the Structural Formation of Palladium Nanoparticles in Deionized Water. J. Phys. Chem. C 2011, 115 (12), 5049–5057. https://doi.org/10.1021/jp1091224.

(25) Koppers, M.; Cagnetta, R.; Shigeoka, T.; Wunderlich, L. C.; Vallejo-Ramirez, P.; Qiaojin Lin, J.; Zhao, S.; Jakobs, M. A.; Dwivedy, A.; Minett, M. S.; Bellon, A.; Kaminski, C. F.; Harris, W. A.; Flanagan, J. G.; Holt, C. E. Receptor-Specific Interactome as a Hub for Rapid Cue-Induced Selective Translation in Axons. eLife 2019, 8, e48718. https://doi.org/10.7554/eLife.48718.

(26) Bugaev, A. L.; Usoltsev, O. A.; Guda, A. A.; Lomachenko, K. A.; Pankin, I. A.; Rusalev, Y. V.; Emerich, H.; Groppo, E.; Pellegrini, R.; Soldatov, A. V.; van Bokhoven, J. A.; Lamberti, C. Palladium Carbide and Hydride Formation in the Bulk and at the Surface of Palladium Nanoparticles. J. Phys. Chem. C 2018, 122 (22), 12029–12037. https://doi.org/10.1021/acs.jpcc.7b11473.

(27) Bugaev, A. L.; Guda, A. A.; Lazzarini, A.; Lomachenko, K. A.; Groppo, E.; Pellegrini, R.; Piovano, A.; Emerich, H.; Soldatov, A. V.; Bugaev, L. A.; Dmitriev, V. P.; van Bokhoven, J. A.; Lamberti, C. In Situ Formation of Hydrides and Carbides in Palladium Catalyst: When XANES Is Better than EXAFS and XRD. Catal. Today 2017, 283, 119–126. https://doi.org/10.1016/j.cattod.2016.02.065.

(28) Vogel, W.; He, W.; Huang, Q.-H.; Zou, Z.; Zhang, X.-G.; Yang, H. Palladium Nanoparticles “Breathe” Hydrogen; a Surgical View with X-Ray Diffraction. Int. J. Hydrog. Energy 2010, 35 (16), 8609–8620. https://doi.org/10.1016/j.ijhydene.2010.05.117.

(29) Hubkowska, K.; Łukaszewski, M.; Czerwiński, A. Influence of Temperature on Hydrogen Electrosorption into Palladium–Noble Metal Alloys. Part 1: Palladium–Gold Alloys. Electrochimica Acta 2010, 56 (1), 235–242. https://doi.org/10.1016/j.electacta.2010.08.093.

(30) Wang, H.; Qian, X.; Liu, S.; Yin, S.; Xu, Y.; Li, X.; Wang, Z.; Wang, L. Boron-Doped PdCuAu Nanospine Assembly as an Efficient Electrocatalyst toward Formic Acid Oxidation. Chem. – Eur. J. 2020, 26 (11), 2493–2498. https://doi.org/10.1002/chem.201905237.

(31) Li, J.; Chen, J.; Wang, Q.; Cai, W.-B.; Chen, S. Controllable Increase of Boron Content in B-Pd Interstitial Nanoalloy To Boost the Oxygen Reduction Activity of Palladium. Chem. Mater. 2017, 29 (23), 10060–10067. https://doi.org/10.1021/acs.chemmater.7b03732.

(32) Tew, M. W.; Nachtegaal, M.; Janousch, M.; Huthwelker, T.; Bokhoven, J. A. van. The Irreversible Formation of Palladium Carbide during Hydrogenation of 1-Pentyne over Silica-Supported Palladium

Nanoparticles: In Situ Pd K and L_3 Edge XAS. Phys. Chem. Chem. Phys. 2012, 14 (16), 5761–5768. https://doi.org/10.1039/C2CP24068H.

(33) Bugaev, A. L.; Guda, A. A.; Pankin, I. A.; Groppo, E.; Pellegrini, R.; Longo, A.; Soldatov, A. V.; Lamberti, C. The Role of Palladium Carbides in the Catalytic Hydrogenation of Ethylene over Supported Palladium Nanoparticles. Catal. Today 2019, 336, 40–44. https://doi.org/10.1016/j.cattod.2019.02.068.

(34) Sakamoto, Y.; Chen, F. L.; Muto, J.; Flanagan, T. B. Phase Transitions in the Palladium-Rich Pd — Li Alloy System and Hydrogen Solubility in the Solid Solution Alloys. Z. Für Phys. Chem. 1991, 173 (2), 235–250. https://doi.org/10.1524/zpch.1991.173.Part_2.235.

(35) Gelatt, C. D.; Williams, A. R.; Moruzzi, V. L. Theory of Bonding of Transition Metals to Nontransition Metals. Phys. Rev. B 1983, 27 (4), 2005–2013. https://doi.org/10.1103/PhysRevB.27.2005.

(36) Ziemecki, S. B.; Jones, G. A.; Swartzfager, D. G.; Harlow, R. L.; Faber, J. Formation of Interstitial Palladium-Carbon Phase by Interaction of Ethylene, Acetylene, and Carbon Monoxide with Palladium. J. Am. Chem. Soc. 1985, 107 (15), 4547–4548. https://doi.org/10.1021/ja00301a031.

(37) Maciejewski, M.; Baiker, A. Incorporation of Carbon into Palladium during Low-Temperature Disproportionation of Carbon Monoxide over Palladium/Zirconia Prepared from Glassy Palladium-Zirconium. J. Phys. Chem. 1994, 98 (1), 285–290. https://doi.org/10.1021/j100052a048.

(38) Ellis, I. T.; Wolf, E. H.; Jones, G.; Lo, B.; Meng-Jung Li, M.; York, A. P. E.; Edman Tsang, S. C. Lithium and Boron as Interstitial Palladium Dopants for Catalytic Partial Hydrogenation of Acetylene. Chem. Commun. 2017, 53 (3), 601–604. https://doi.org/10.1039/C6CC08404D.

(39) Ferro, R. Ricerche Sulle Leghe Dei Metalli Nobili Con Gli Elementi Piu Elettropositivi . 9. Il Composto Li Pd. Atti Della Accad. Naz. Dei Lincei Cl. Sci. Fis. Mat. E Nat. Rendiconti 1966, 41, 348–350.

(40) Kienast, G.; Verma, J.; Klemm, W. Das Verhalten der Alkalimetalle zu Kupfer, Silber und Gold. Z. Für Anorg. Allg. Chem. 1961, 310 (3), 143–169. https://doi.org/10.1002/zaac.19613100304.

(41) Ferro, R. Ricerche Sulle Leghe Dei Metalli Nobili Con Gli Elementi Piu Elettropositivi . 15. Su Alcuni Composti Del Litio Con Palladio e Platino. Atti Della Accad. Naz. Dei Lincei Cl. Sci. Fis. Mat. E Nat. Rendiconti 1968, 45, 564–566.

(42) van Vucht, J. H. N.; Buschow, K. H. J. Note on the Occurrence of Intermetallic Compounds in the Lithium-Palladi-Um System. J. Common Met. 1976, 48 (2), 345–347. https://doi.org/10.1016/0022-5088(76)90014-X.

(43) Loebich, O.; Raub, Ch. J. Das zustandsdiagramm lithium-palladium und die magnetischen eigenschaften der Li-Pd-Legierungen. J. Common Met. 1977, 55 (1), 67–76. https://doi.org/10.1016/0022-5088(77)90261-2.

(44) Loebich, O.; Wopersnow, W. Zur struktur der intermetallischen verbindung LiPd2. J. Common Met. 1979, 63 (2), P83–P88. https://doi.org/10.1016/0022-5088(79)90258-3.

(45) Hull, A. W. X-Ray Crystal Analysis of Thirteen Common Metals. Phys. Rev. 1921, 17 (5), 571–588. https://doi.org/10.1103/PhysRev.17.571.

(46) Jung, R.; Metzger, M.; Maglia, F.; Stinner, C.; Gasteiger, H. A. Oxygen Release and Its Effect on the Cycling Stability of LiNixMnyCozO2 (NMC) Cathode Materials for Li-Ion Batteries. J. Electrochem. Soc. 2017, 164 (7), A1361–A1377. https://doi.org/10.1149/2.0021707jes.

(47) Pender, J. P.; Jha, G.; Youn, D. H.; Ziegler, J. M.; Andoni, I.; Choi, E. J.; Heller, A.; Dunn, B. S.; Weiss, P. S.; Penner, R. M.; Mullins, C. B. Electrode Degradation in Lithium-Ion Batteries. ACS Nano 2020, 14 (2), 1243–1295. https://doi.org/10.1021/acsnano.9b04365.

(48) Choi, M.-J.; Xiao, Y.; Hwang, J.-Y.; Belharouak, I.; Sun, Y.-K. Novel Strategy to Improve the Li-Storage Performance of Micro Silicon Anodes. J. Power Sources 2017, 348, 302–310. https://doi.org/10.1016/j.jpowsour.2017.03.020.

(49) Chen, X.; Li, H.; Yan, Z.; Cheng, F.; Chen, J. Structure Design and Mechanism Analysis of Silicon Anode for Lithium-Ion Batteries. Sci. CHINA Mater. 2019, 62 (11), 1515–1536. https://doi.org/10.1007/s40843-019-9464-0.

(50) Cui, G.; Hu, Y.-S.; Zhi, L.; Wu, D.; Lieberwirth, I.; Maier, J.; Müllen, K. A One-Step Approach Towards Carbon-Encapsulated Hollow Tin Nanoparticles and Their Application in Lithium Batteries. Small 2007, 3 (12), 2066–2069. https://doi.org/10.1002/smll.200700350.

(51) Yu, Y.; Gu, L.; Zhu, C.; van Aken, P. A.; Maier, J. Tin Nanoparticles Encapsulated in Porous Multichannel Carbon Microtubes: Preparation by Single-Nozzle Electrospinning and Application as

Anode Material for High-Performance Li-Based Batteries. J. Am. Chem. Soc. 2009, 131 (44), 15984–15985. https://doi.org/10.1021/ja906261c.

(52) Schmidt, O.; Melchior, S.; Hawkes, A.; Staffell, I. Projecting the Future Levelized Cost of Electricity Storage Technologies. Joule 2019, 3 (1), 81–100. https://doi.org/10.1016/j.joule.2018.12.008.

(53) Peñaranda, A. F.; Romero-Quete, D.; Cortés, C. A. Grid-Scale Battery Energy Storage for Arbitrage Purposes: A Colombian Case. Batteries 2021, 7 (3), 59. https://doi.org/10.3390/batteries7030059.

(54) Nohira, T.; Ito, Y. Thermodynamic Properties of Pd‐Li Alloys. J. Electrochem. Soc. 1998, 145 (3), 785. https://doi.org/10.1149/1.1838346.

(55) Nohira, T.; Ito, Y. Electrochemical Hydrogen Absorbing Behavior of Pd and Pd‐Li Alloys in a Molten LiCl‐KCl‐LiH System. J. Electrochem. Soc. 1997, 144 (7), 2290. https://doi.org/10.1149/1.1837806.

(56) Nohira, T.; Amezawa, K.; Ito, Y. Electrochemical Formation of Pd-Li Alloys in LiCl-KCl Eutectic Melts. J. Appl. Electrochem. 1995, 25 (1), 48–53. https://doi.org/10.1007/BF00251264.

(57) Yamazaki, O.; Yoshitake, H.; Kamiya, N.; Ota, K. Hydrogen Absorption and Li Inclusion in a Pd Cathode in LiOH Solution. J. Electroanal. Chem. 1995, 390 (1), 127–133. https://doi.org/10.1016/0022-0728(95)03944-C.

(58) Chen, T.; Ellis, I.; Hooper, T. J. N.; Liberti, E.; Ye, L.; Lo, B. T. W.; O'Leary, C.; Sheader, A. A.; Martinez, G. T.; Jones, L.; Ho, P.-L.; Zhao, P.; Cookson, J.; Bishop, P. T.; Chater, P.; Hanna, J. V.; Nellist, P.; Tsang, S. C. E. Interstitial Boron Atoms in the Palladium Lattice of an Industrial Type of Nanocatalyst: Properties and Structural Modifications. J. Am. Chem. Soc. 2019, 141 (50), 19616–19624. https://doi.org/10.1021/jacs.9b06120.

(59) Ramgir, N. S.; Hwang, Y. K.; Mulla, I. S.; Chang, J. S. Effect of Particle Size and Strain in Nanocrystalline SnO2 According to Doping Concentration of Ruthenium. Solid State Sci. 2006, 8 (3-4 SPEC. ISS.), 359–362. https://doi.org/10.1016/j.solidstatesciences.2006.02.008.

(60) McCaulley, J. A. Temperature Dependence of the Pd K-Edge Extended x-Ray-Absorption Fine Structure of PdCx. Phys. Rev. B 1993, 47 (9), 4873–4879. https://doi.org/10.1103/PhysRevB.47.4873.

(61) Park, Y.; Kim, W.; Park, H.; Tachikawa, T.; Majima, T.; Choi, W. Carbon-Doped TiO2 Photocatalyst Synthesized without Using an External Carbon Precursor and the Visible Light Activity. Appl. Catal. B Environ. 2009, 91 (1), 355–361. https://doi.org/10.1016/j.apcatb.2009.06.001.

(62) Siri, G. J.; Casella, M. L.; Santori, G. F.; Ferretti, O. A. Tin/Platinum on Alumina as Catalyst for Dehydrogenation of Isobutane. Influence of the Preparation Procedure and of the Addition of Lithium on the Catalytic Properties. Ind. Eng. Chem. Res. 1997, 36 (11), 4821–4826. https://doi.org/10.1021/ie960674b.

(63) Xu, D.; Lv, H.; Liu, B. Encapsulation of Metal Nanoparticle Catalysts Within Mesoporous Zeolites and Their Enhanced Catalytic Performances: A Review. Front. Chem. 2018, 6.

(64) Otor, H. O.; Steiner, J. B.; García-Sancho, C.; Alba-Rubio, A. C. Encapsulation Methods for Control of Catalyst Deactivation: A Review. ACS Catal. 2020, 10 (14), 7630–7656. https://doi.org/10.1021/acscatal.0c01569.

(65) Sangster, J.; Pelton, A. D. The Li-Pd (Lithium-Palladium) System. J. Phase Equilibria 1992, 13 (1), 63–66. https://doi.org/10.1007/BF02645380.

Chapter 6: Locating framework aluminium in ZSM-5 for ammonia synthesis promotion and storage: assessment of indirect and direct characterisation methods

6.1 Abstract

The use of zeolites in the agile ammonia synthesis as a Haber-Bosch catalyst support, rate promoter, or ammonia storage material are all highly dependent on the location, concentration, and strength of Brønsted acid sites (BAS), which are formed by the presence of substitutional Al^{3+} at Si^{4+} sites. The archetypal ZSM-5 structure has been probed by a combination of techniques of varying spatial resolution, site-specificity, and directness to show preferential aluminium occupancy at four of the twelve T-sites.

Imaging of isolated silver atoms (Ag/ZSM-5) by STEM showed preferential adsorption at T6/T12 and T8/T2, and their associated oxygens, but the investigation suffered from restrictive zone axes, poor site-selectivity, and poor spatial resolution. The location of adsorbed trimethyl phosphine oxide by SXPD and NPD yielded T6, T8, and T12 as aluminium sites, further narrowing and reinforcing the results from STEM.

Soft X-ray resonance powder diffraction (SXPD) was applied to zeolite frameworks for the first time in order to directly characterise the aluminium location. Varying the incident XRD energy over the aluminium K-edge results in anomalous scattering and species-specific variations in intensity. Simulated patterns show that this application is valid, with a low concentration of aluminium theoretically affecting the Bragg scattering significantly. This

direct characterisation of the framework aluminium was carried out on I10, DLS, as a novel use of the beamline, requiring procedural optimisation. Simultaneous Rietveld refinement of five patterns yielded aluminium occupancy at T6, T4, and T8.

Thus, we have identified preferential siting of aluminium at the T4, T6, T8, and T12 sites, with multiple characterisation techniques being largely in agreement. Whether with respect to ammonia synthesis promotion, ammonia storage, or other related applications, this aluminium siting in ZSM-5 is crucial in the understanding of adsorption and catalytic behaviour.

6.2 Introduction

6.2.1 Context

Having discussed sustainable hydrogen evolution and electrochemical energy storage, this chapter will be a focal point, both with respect to the agile ammonia synthesis and the analytical problems associated with the characterisation of light-element dopants.

6.2.1.1 Analytical context

Throughout the presentation of this work, the effects of light-element doping and low-scattering-contrast sites have been predominantly observed indirectly by monitoring crystalline changes in the highly-scattering framework by X-ray scattering techniques. The direct characterisation of light elements by SXPD and STEM has been shown to be difficult, in the context of nitrogen-doped TiO_2 and the palladium-lithium system. This emphasises the importance of direct characterisation methods, which will be addressed in this chapter on aluminium siting in zeolites, in which the *Z*-contrast between Si^{4+} and Al^{3+} is one; furthermore, they are isoelectronic. This low contrast will be challenged by a novel

application of resonance soft X-ray powder diffraction (RSXPD), yielding increased resolution of the isoelectronic pair.

6.2.1.2 Agile ammonia synthesis context

Zeolites are frequently used as supports for catalysts in the Haber-Bosch, and capable of ammonia purification and storage.[1–4] However, the location and activity of aluminium sites is not well known, nor is there a single characterisation technique shown to be capable of this. In order to promote the AAS and provide facile ammonia storage by zeolites, the confinement and adsorption of ammonia in zeolite frameworks during the Haber-Bosch must be understood. This is entirely dependent on the aluminium siting.

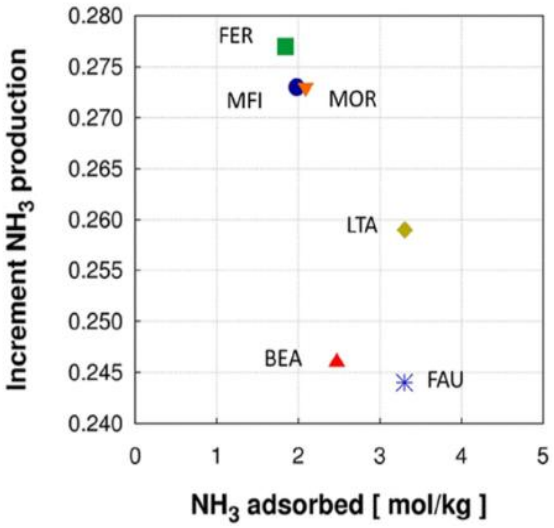


Figure 6-1. The promotion of ammonia yield by various zeolites derived by computational methods. Reproduced from reference [5].

Zeolites have also been assessed for the promotion of thermal ammonia synthesis using computational methods by Martos et al. (Figure 6-1).[5] They concluded that FAU adsorbs most efficiently, while FER promotes synthesis most efficiently. Interestingly, there is an inverse correlation between the two properties. This report is a good example of the

ineffectiveness of computational methods for performance simulations, because the authors do not consider the location of aluminium sites, nor the Brønsted acid site (BAS) strength or accessibility, nor the geometry of the local distortion, nor the effects of BAS-BAS interaction such as hydrogen bonding or ammonia condensation; the model is missing crucial information. In general, the poor understanding of the aluminium siting across zeolite research leads to poor understanding of zeolite synthesis and stability, as well as emergent behaviour regarding adsorption and catalysis.

6.2.2 Zeolites

Zeolites are three-dimensional microporous crystalline materials composed of corner-sharing SiO_4 tetrahedra (T-sites). The use of zeolites in industrial-scale catalysis and adsorption is significant, broad, and well-established, in particular as heterogeneous catalysts in several industrial processes as a safer, greener, and cheaper alternative to harmful and corrosive homogeneous catalysts.[6–8] However, in order to increase our fundamental understanding and allow the rational design of zeolite materials and applications, it is crucial that we remove the current ambiguity surrounding the location of aluminium within zeolite frameworks.

For aluminosilicate zeolites, the doping/inclusion of aliovalent aluminium Al^{3+} is the origin of many of the beneficial physicochemical properties of zeolites, in addition to properties associated with the cavities and pore network. The charge imbalance in the framework is often counterbalanced by labile protons leading to the formation of strongly acidic BAS that are responsible for catalytic activity. The location, concentration, and distribution of aluminium and BAS in zeolites is one of the most significant factors that affect the catalytic behaviours. However, due to the limitation of current characterisation techniques,

direct visualisation and quantitative investigation of the distribution of BAS has long been a challenging task. Thus, direct correlation between the catalytic performance and the siting of BAS and aluminium is rare, often ambiguous, and at worst simply assumed.

6.2.2.1 ZSM-5

This report will focus on the characterisation of ZSM-5,[9,10] the archetypal zeolite used in many catalysis applications such as the alkylation of benzene using methanol,[11] methanol to olefins reaction,[6,8,12] cracking of butane to lower olefins,[13] decarboxylation of GVL to butenes,[14] methanol dehydration to dimethyl ether[15], ethanol dehydration to diethyl ether,[16] and ethylene oxidation to CO_2.[17]

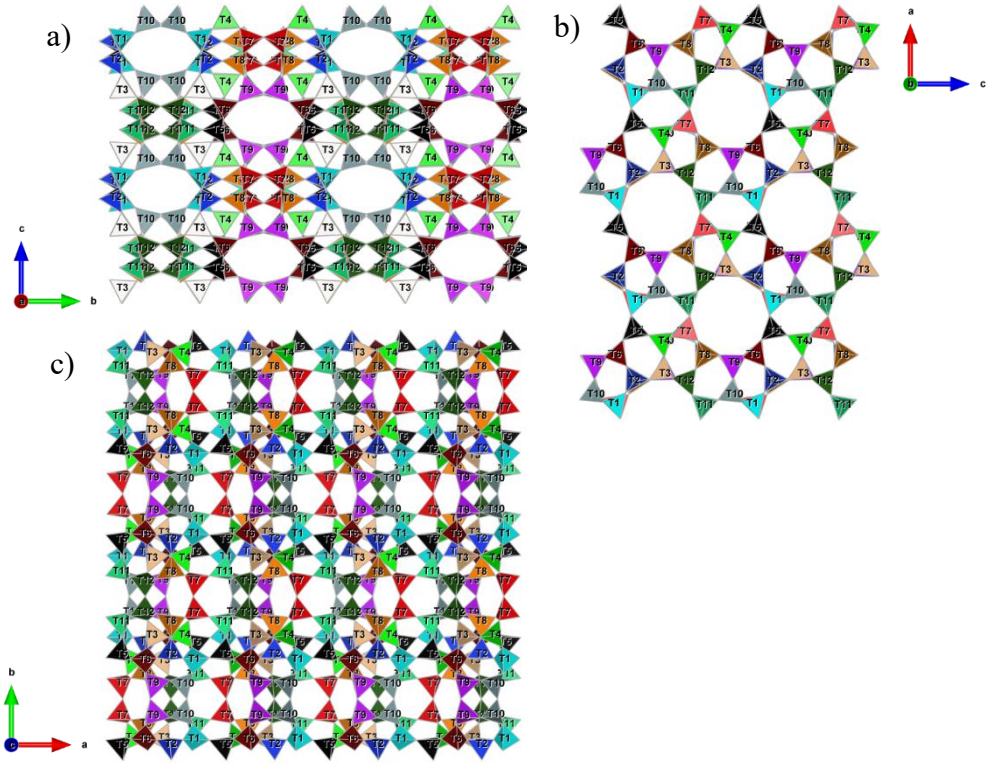


Figure 6-2. Displayed polyhedral structure of ZSM-5 showing the 12 chemically and crystallographically distinct T-sites, viewed along the (a) *a*-axis (sinusoidal channel), (b) *b*-axis (straight channel), and (c) *c*-axis (non-porous).

The structure of the industrially important zeolite ZSM-5 can be produced from an orthorhombic unit-cell containing 12 crystallographically distinct T-sites.[18] An important distinction needs to be noted regarding the location of the 12 inequivalent sites in ZSM-5 (Figure 6-2), which affects the accessibility of the resulting BAS. The majority of sites are exposed to both the straight and sinusoidal channels in the intersection void, but T8 and T11 are exclusively accessible by the straight channel (propagates in *b* axis), and T4 and T10 only by the sinusoidal channel (propagates in *a* axis, oscillates in *c* axis).[19] In this work, O_{BAS} sites will often be identified and the aluminium occupancy assigned to one of the coordinating T-sites. The oxygen site will often be referred to with the adjacent sites, e.g. O18 (T6+T9).

The synthesis of zeolites is known to have direct influence on aluminium siting.[11,20–25] The lowest silicon-to-aluminium ratio for ZSM-5 formation is ~10, which is interestingly similar to the number of inequivalent T-sites.[19] The understanding of underlying phenomena that control the location of aluminium in zeolite catalysts is severely limited.

6.2.3 Types of siting

There exist several types of aluminium-distribution characterisation based on the type of information yielded. These are here separated into three groups, primarily related to the length-scale and spatial specificity: architectural, chemical environment, and crystallographic/spatial site. A fourth type of siting of local Al-Al interaction is also presented, which is a combination of chemical and crystallographic characterisation.

6.2.3.1 Architectural siting

Firstly, at the largest length-scale, aluminium zoning describes the morphological distribution of aluminium at the nanometre-scale within a particle/crystallite or powder. This

information is particularly important for catalytic properties due to effects on diffusion and acidity concentration.[26] Zoning is very important when inducing mesoporosity into ZSM-5 by desilication[27–30] or dealumination.[31–33] This is most often carried out by imaging techniques, such as microscopy[32] and tomography.[34] The wide range of hierarchical zeolite structures is beyond the scope of this thesis.[28,31,35]

6.2.3.2 Chemical-environment siting

Aluminium siting within the literature is most often not site-specific with respect to the crystallographically defined sites, i.e. the characterisation is primarily chemical in nature. The predominant characterisation technique for chemical siting is solid-state nuclear magnetic resonance spectroscopy (SSNMR).[25,36–39] The chemical shift of ^{27}Al and ^{29}Si resonances are correlated with tetrahedral angle in various aluminosilicates,[40–42] as well as the acidity of the associated BAS,[38,39,43,44] as will be shown in this work also. Applied to the ZSM-5 structure, SSNMR spectra can be deconvoluted into groups of T-sites based on environment.[12,45] Han et al. used ^{27}Al 3Q SSNMR to observe two distinct environments in ZSM-5, of which the sites with wider T-O-T angles were shown to be preferentially occupied at low aluminium composition.[46] This partitioning of chemical-environment signals by angle or region of the pore network (sinusoidal, straight, intersection) is non-site-specific.

The chemical environment of an adsorbate can also be measured in order to indirectly infer the environment or location of BAS and aluminium. Trimethylphosphine oxide (TMPO) has been widely used as an SSNMR probe molecule in the study of solid-state acids, due to the high natural abundance of the NMR-active ^{31}P isotope (100%).[38,39,47] Other techniques for chemical siting in ZSM-5 also include Co^{2+} adsorption by UV-vis spectroscopy.[11,48]

6.2.3.3 Crystallographic/spatial siting

Thirdly, crystallographic siting of aluminium characterises the distribution within the asymmetric unit of the unit-cell, directly showing location in relation to the pore network. Reports of site-specific aluminium location is dominated by theoretical calculations. Some have reported that there is no clear preference of Al for any particular T-site, showing a small difference in energy between the most and least stable location of aluminium of <16 kcal mol^{-1},[49,50] or as low as 2 kcal mol^{-1}.[24] In contrast, many now believe the distribution of aluminium is non-random: [T1, T2, T9][51], [T7,T3][52], [T7][53], [T9][8], [T9][54], [T8][55], [T8][56], [T8,T10,T4][57], [T12].[50] Evidently, these sitings are wide ranging and contradictory. However, assumptions in computational studies of application performance is commonplace. Many computational investigations on ZSM-5 simply place aluminium at a recently reported site,[19,58–60], an arbitrary site,[59–62] or even ignore the aluminium completely.[5,63] Computational work on MFI analogues has also shown preferential hetero-siting: Tl-ZSM-5 at [T10, T6],[64] TS-1 (Ti) at [T12],[65] and [T4],[66,67] and FeS-1 at [T8].[68]

Crystallographic siting can be yielded by imaging. A prominent report that influenced this investigation is from Liu et al.,[69] which reports the visualisation of adsorbed molybdenum single atoms in the straight channel of ZSM-5. They identified preference for deposition at T1/T7 (as well as T5/T11 and T2/T8). Evidently, this type of characterisation lacks crystallographic specificity. A similar experiment has been conducted in this work, with the strengths and deficiencies discussed further.

Diffraction techniques can also provide good identification of probe molecules with respect to inequivalent crystallographic sites in order to determine BAS location, and narrow the search for aluminium sites.[3,70–75] The use of neutron scattering has been used in some

cases,[76] but reports are not frequent and generally ineffectual. By X-ray scattering methods, probe molecules must be used to indirectly elucidate the aluminium location. Using Rietveld refinement, the overall crystalline atomic structure and the bulk-averaged bonding interaction between adsorbate and zeolite BAS can be determined. Many reports indicate preferential siting at T6 by adsorption of methanol, pyridine ammonia, DMF, furan, and WO_4^{2-} tungstate.[3,7,70,71,73] Structural analogues of ZSM-5 exhibit much higher scattering contrast which is easily utilised by high-resolution scattering, for example preferential hetero- in TS-1[77] or silicon vacancies silicalite,[77] are both sited at T6 by NPD.

However, crystallographic analyses contain no information on local environment. Evidently, chemical and spatial siting are complementary and necessary for solving this complex characterisation problem, which results from much more than the thermodynamic considerations of electronics, coordination, geometry and steric hindrance, but also kinetic considerations with respect to framework nucleation, aluminium mobility and dynamics, and reversibility.

6.2.3.4 Higher-order crystallographic siting: Löwenstein's Rule

Bragg scattering techniques observe bulk periodicity averaged over a crystal, and then averaged over a powder. This provides excellent evidence for site occupancy as an ensemble, but not with respect to local environment, especially the Al-Al relationship. For example, adjacent T-sites can be identified as preferential aluminium sites by Bragg diffraction without any indication of whether they occupy a single asymmetric unit, or even the same unit-cell (all T-sites are 8d Wyckoff sites). This effectively means Bragg diffraction cannot fully address Löwenstein's rule, a predominant though contested, principle, which states that [Al-O-Al] moieties do not occur.[78] Tang et al.[79] suggest by computational methods that

Löwenstein's rule is upheld in SSZ-13, and that longer Al-Al distances are more energetically favourable. However, other computational reports such as by Fletcher et al.[80] report favourable non-Löwensteinian configurations in CHA, LTA, RHO, ABW, and MOR structures. An extension of Löwenstein's rule is Takaishi's rule, which additionally states that two aluminium atoms cannot occupy a single pentasil ring.[81,82]

Though these analyses contribute important information about local environment, none of them are site-specific about aluminium. It is imperative that the aluminium sites in zeolites are identified at a bulk and local level with site specificity. Though Bragg scattering cannot help with this higher-order siting, the assumption of Löwenstein's rule can be used to test the validity of a particular siting result.[49]

6.2.4 Low scattering contrast

The characteristic Thomson scattering of electromagnetic radiation by different ions is well-defined by their atomic scattering factors.[83] This scattering is elastic and independent of X-ray energy. Distinguishing between elements that have very similar electron densities, i.e. low *Z*-contrast has been historically difficult using inelastic X-ray scattering techniques. The low contrast between the isoelectronic pair of Al^{3+} and Si^{4+} can be seen in their very similar atomic scattering factors (Figure 6-3). Under this far-from-edge regime, diffraction

has been unable to provide enough contrast for aluminium siting in zeolite frameworks. There exist no reports of direct Al/Si distinction in ZSM-5 by XRD.

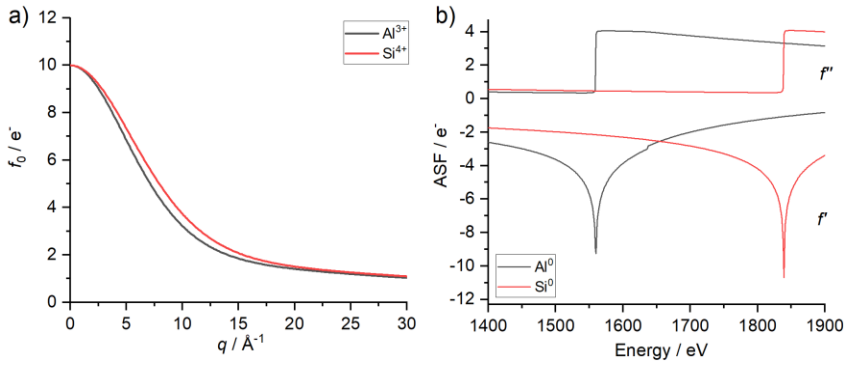


Figure 6-3. (a) Far-from-edge atomic form factors for Al^{3+} and Si^{4+}, which are dependent on scattering angle and independent of energy. (b) ASF for elemental Al^0 and Si^0, which are dependent on energy and independent of scattering angle.

6.2.5 Aims of investigation

Although zeolite science is a well-developed field, which is still vibrant within both academia and industry, the methodology of aluminium siting is still not established. For ZSM-5, the crystallographic siting of aluminium among the 12 T-sites and identification of the corresponding O_{BAS} among the 26 inequivalent bridging oxygens still remains unclear. This fundamental knowledge prevents progression in the understanding of the thermodynamics of synthesis and nucleation, the aluminium location, guest ion/molecule adsorption modes and energy, catalytic mechanisms, and intelligent zeolite design. In order to progress the field, it is imperative to fully understand where the aluminium is, why it is there, how we can influence it, and what effect it has on performance.

Here, it is aimed to probe the aluminium position in ZSM-5 using a wide-range of characterisation techniques. Each technique has its strengths and weaknesses, which will be

compared and evaluated with respect to their limitations and validity. It is aimed to construct a suite of characterisation to provide complementary information in order to inform analyses, show trends in siting, and suggest a well-supported distribution of likely aluminium sites and their occupancy. In particular, resonant diffraction is aimed to directly interrogate the aluminium in the crystalline framework of ZSM-5 for the first time. RSXPD has been applied to the field of zeolites before, but for crystallographic siting of extra-framework atoms, such as resolving Zn^{2+}/Na^{+} in zeolite Y,[84] or Sr^{2+}/Rb^{+} in zeolite X.[85]

ZSM-5 was chosen as the focus of this work due to its commercial and industrial prevalence within the catalysis sector, as well as its status within academia as an archetypal and much researched zeolite structure. It is highly crystalline, shown by STEM (Figure 6-4), which is necessary for scattering and imaging experiments. It has a large unit-cell, which results in numerous high *d*-spacing peaks, which is necessary for the RSXPD investigation. Also, the numerous peaks from the low-symmetry space group provide many variables to fit in order to ensure validity of the structure solution.

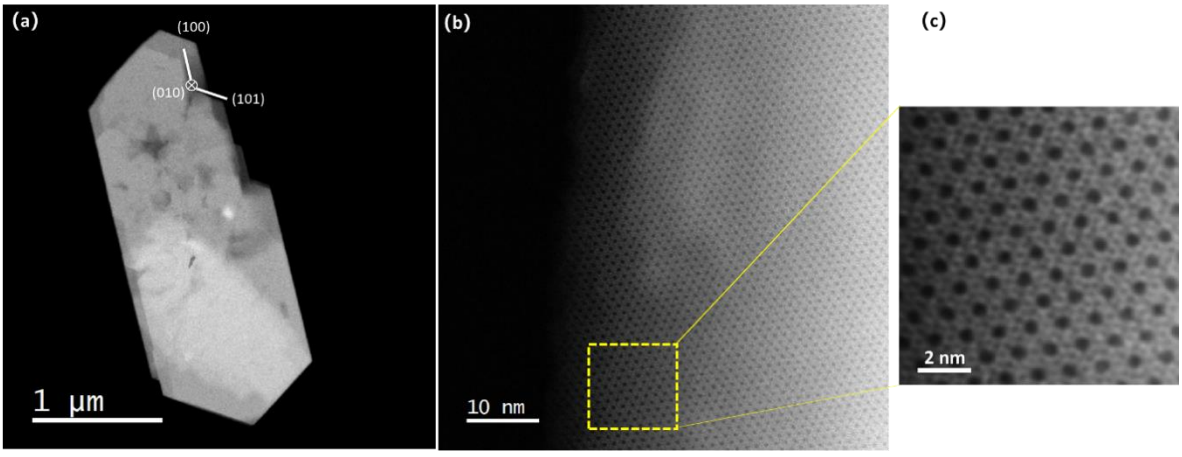


Figure 6-4. STEM imaging of H-ZSM-5 orientated along the <010> zone axis.

The proton form H-ZSM-5 was used as the pristine material and as a starting material for adsorption experiments, because it provides minimum additional electron density to the framework, as well as minimum steric presence. It is also the best approximation of catalytic operating conditions.

6.2.5.1 Outline

Characterisation will be presented in order of increasing spatial specificity: imaging of silver adsorption by STEM, chemical siting of TMPO adsorption by SSNMR, crystallographic siting of TMPO adsorption by SXPD, and finally direct crystallographic siting by RSXPD. Finally, the information will be presented comparatively.

6.3 Results and Discussion

6.3.1 Indirect siting by STEM imaging of Ag adsorption

ZSM-5 was doped with silver atoms to visualise the adsorption at BAS by HAADF-STEM imaging, much like Liu et al.[69] who used molybdenum atoms. Silver impregnation was chosen due to historic work on Ag-ZSM-5 in the Tsang group, as well as current interest in the Ag-doped material for catalysis. The atomically dispersed high-contrast sites can identify the location of O_{BAS} in relation to the pore network. This spatial characterisation does not rely on the crystallinity of the framework, aluminium siting, or adsorption, which can be an advantage over Bragg diffraction methods. All observations are of local structure rather than a bulk averaged structure. Thus, low concentration adsorption can be observed.

6.3.1.1 Site specificity

The technique suffers from a lack of site-specificity because the three-dimensional framework is being viewed solely in the *ac* plane. Along the projected <010> direction, the atomic columns of the 10M-ring each consist of two inequivalent T-sites: [AABB]. The lack of *b*-character leads to observed equivalence of certain crystallographically distinct sites. These pairs appear diametrically opposite one another in the ring. Thus, observations are binned into half as many sites as perhaps expected, with the site specificity also halved. This is true of both oxygen and T-sites. The pairs of equivalently observed T-sites are as follows: T1/T7, T5/T11, T6/T12. T9/3, and T8/2. This is very similar for most oxygen columns. However, two <010>-equivalent oxygen columns (bridging T6+T9/T3+T12) contain eight atoms rather than four per unit cell, as a result of bonding down the zone axis, consisting of two of each O18, O19, and O20, and one of each O25 and O24. This will be referred to as

O18/O19/O20. This further loses site specificity if adsorption is assigned to this oxygen column.

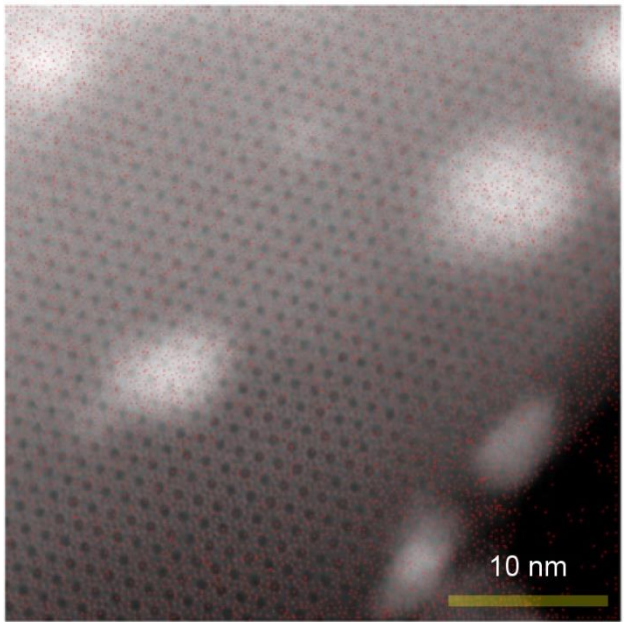


Figure 6-5. Output of intensity-contrast software used to locate high contrast within channels that are attributed to adsorbed Ag atoms.

6.3.1.2 Observations of adsorption

Microscopy was carried out by Ping-Luen Ho, who subsequently developed a program to identify high-contrast areas in the images. These sites were interrogated manually in order to determine their validity, yielding a total of 342 observations. The position of the Ag atom was assigned to the nearest T- or O-sites around the 10M-ring (Table S6-1). The most common observation was to find the channel empty (79 channels, 23.1%). Statistics herein will be relative to the 263 occupied channels. The most frequent Ag position was at T6/T12 (29.7%), followed by T8/T2 (22.1%). Adsorption of Ag at the remaining T-site pairs T9/T3, T5/T11, and T1/T7 are all observed at less than 5% (3.8%, 3.4%, and 2.7%, respectively). The third and fourth most frequent position is the bridging oxygen O8/O2

(T8+T9/T2+T3) and O21/22 (T1+T5/T7+T11) at 10.3% and 9.5% respectively. Observations of adsorption at the remaining three bridging oxygen site pairs O5/O11, O7/O1, and O18/O19/O20 are comparable but lower at 7.6%, 5.7% and 5.3%, respectively. The proportion of occurrences over oxygen sites is 38.4%, and 61.6% over T-sites.

6.3.1.3 Aluminium assignment

The adsorption site has been taken as the framework site closest to the observed Ag discussed. Attributing this adsorption to aluminium occupancy is the aim of this investigation in order to yield a siting distribution, and not to determine the binding geometry. Thus, a degree of processing must be carried out in order to yield an aluminium siting result. Adsorption over T-sites will be attributed to aluminium occupancy at the T-site. Meanwhile, for adsorption at O-sites, the occupancy is split equally to both neighbouring T-sites, purely as a statistical device (blue in Figure 6-6). The general trend remains much the same as the raw observations of adsorption, with T6/T12 still being the most likely aluminium site, and T8/T2 the second. Again, the three other pairs are much less likely, but are much more increased from the raw observations. In fact, after this reassignment, the vast majority of aluminium assignment for these three pairs is from the observation of adsorption at adjacent oxygens. Admittedly this may be mis-assigned.

This aluminium siting is in full agreement with the TMPO/ZSM-5 investigation that will be presented shortly. Based on that supporting characterisation, T6, T8, and T12 are considered preferentially occupied. Hence, adsorption at T8/T2 is thought to be more likely due to aluminium occupancy at T8 than T2. In order to indicate this the pair will now be referred to as <u>T8</u>/T2, with the underlining representing likely aluminium-occupied T-site supported by other methods.

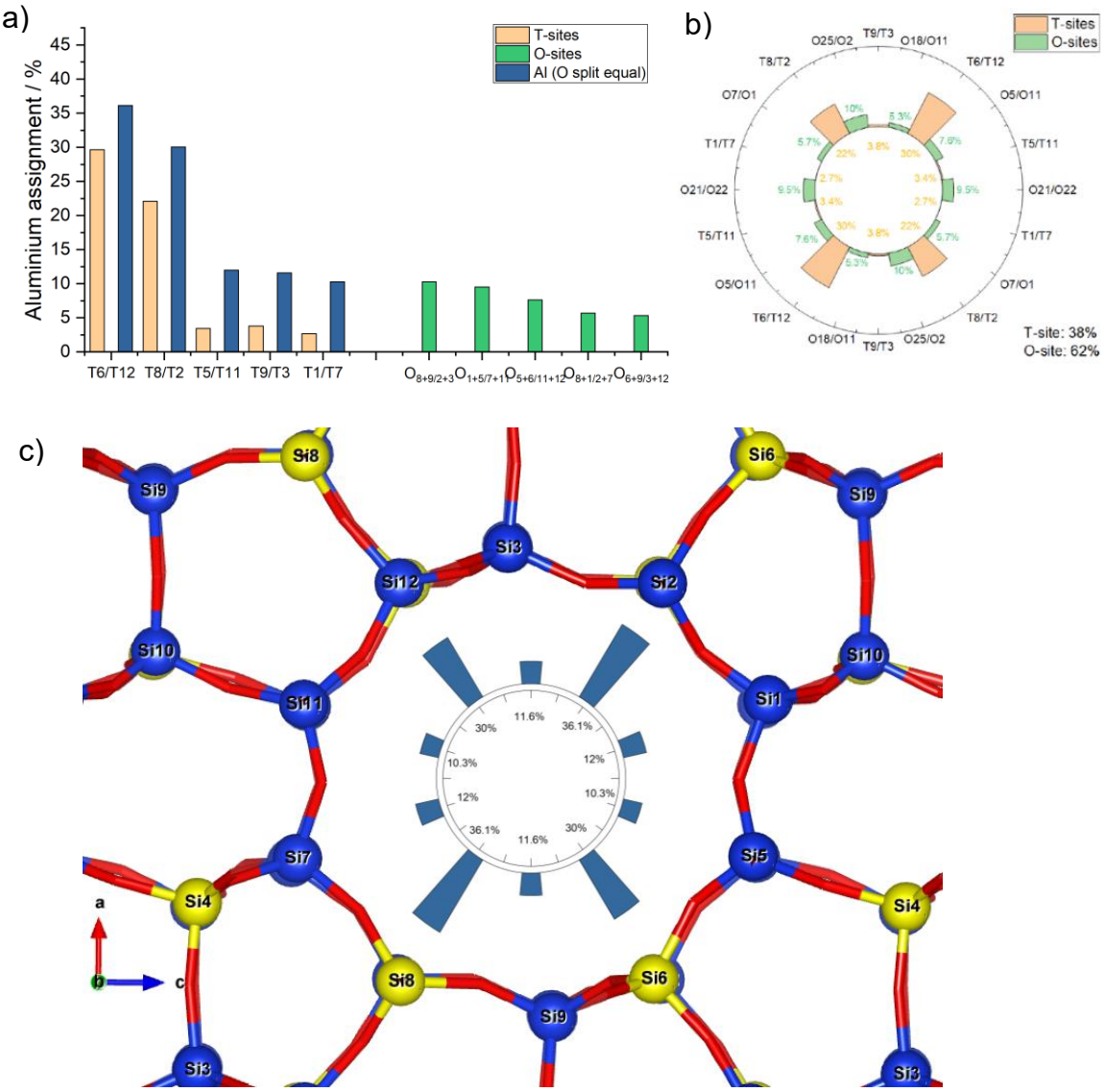


Figure 6-6. (a) Distribution of Ag adsorption and aluminium assignment in the straight channel of ZSM-5 as observed by TEM. (b) Radial representation of raw adsorption observations, and (c) Radial representation of aluminium assignment with the structural representation overlaid. Aluminium sites as derived by RXSPD show in yellow.

6.3.1.4 Evaluation of technique and siting

The aluminium siting from STEM imaging of Ag/ZSM-5 is T6/T12 (36.1%) and T8/T2 (30.0%). Concerning the assignment of adsorption at oxygen sites to a T-site, this is a necessity; though an equal 50:50 split is deemed unlikely. It is more likely that the BAS

originates from aluminium occupancy at one T-site; this is especially true if Löwenstein's rule is assumed to be inviolate.

However, there are significant deficiencies in the site-specificity of this technique. It is unable to view the T4 and T10, which are solely located in the sinusoidal channel. Additionally, none of the ten O-sites in the 10M-ring are coordinated to T4 or T10, and hence no 10M-ring adsorption can be attributed to T4 or T10. This is never acknowledged by Liu et al. Additionally, though the majority of T-sites themselves are observed as part of the 10M-ring, only adsorption directed towards/within the straight pore will be observed. Many T-sites are accessible from different angles resulting in various orientations of adsorption, not just towards the straight channel. In previous work by the Tsang group,[75] SXPD determined three Ag/ZSM-5 adsorption sites, all directed towards the sinusoidal channel (Figure S6-1). Restricted viewing of the sinusoidal channel is clearly a significant deficiency of this type of experiment.

Direct characterisation of aluminium by microscopy techniques is difficult. Initial investigation on atomic-atomic-resolution electron spectroscopy was also carried out, with brief discussion found in the Additional Investigations section of the Conclusion.

6.3.2 Indirect siting using TMPO as a probe molecule

Having identified some aluminium sites by STEM imaging, it was aimed to further narrow the range of possible aluminium occupied sites. Focus turned to greater averaging over the sample in order to yield stronger signals, and thus greater contrast. The electronic and structural properties of adsorption of trimethyl phosphine oxide (TMPO) at BAS was investigated by SSNMR, SXPD, and NPD.

6.3.2.1 Electronic environment by SSNMR

Firstly, the TMPO adsorption in H-ZSM-5 was investigated by SSNMR (Figure 6-7). This work was carried out by Dr. Guangchao Li as part of an as yet unpublished manuscript on RSXPD. All results from ^{1}H, ^{27}Al and ^{29}Si SSNMR of pristine H-ZSM-5 suggest that the structure of the framework is highly crystalline without any significant extra-framework species. After TMPO adsorption, ^{31}P cross-polarisation SSNMR exhibits five deconvoluted peaks at 86 ppm, 76 ppm, 69 ppm, 65 ppm, and 51 ppm. Then a 2D ^{1}H-^{31}P heteronuclear-correlation (HETOR) SSNMR experiment was carried out in order to determine the correlation between TMPO adsorption environments and BAS (Figure 6-7). In general, the interaction of the adsorbed TMPO molecules with BAS will result in a downfield shift of the ^{1}H resonance from the acidic proton, which is observed at 12.8 ppm. This coordination also downfield-shifts the ^{31}P signal caused by the decrease in electron density surrounding the ^{31}P nucleus; this effect is proportionate with BAS acidity. Therefore, the signal at 86 ppm is assigned to TMPO adsorbed at highly acidic BAS.[47] The three less-shifted peaks at 76 ppm, 69 ppm, and 65 ppm have also been shown to be at highly acidic BAS in previous publications.[39,47] Meanwhile, the least shifted peak at 51 ppm is assigned to TMPO adsorbed at silanol groups, or on the very weakly acidic protons that have already adsorbed TMPO.[43,86,87] Indeed, there is no correlation between this adsorption signal and the ^{1}H BAS

signal in the 2D ^{1}H-^{31}P spectrum, as is in agreement with previous reports of very weak adsorption.[86]

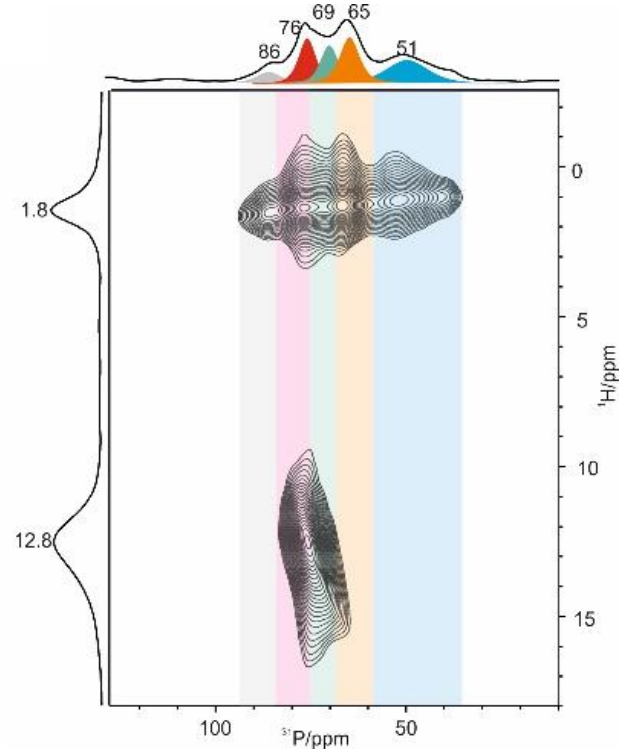


Figure 6-7. ^{1}H-^{31}P heteronuclear-correlation (HECTOR) spectra of TMPO/ZSM-5.

The 2D ^{1}H-^{31}P experiment shows the peaks at 76 ppm, 69 ppm, and 65 ppm are all correlated with the BAS proton with the ^{1}H resonance centred at 12.8 ppm. No BAS correlation to the highly shifted 86 ppm adsorption is attributed to the low concentration of TMPO adsorbed (2.7% of BAS adsorption) (Table 6-1). These phosphorus adsorption environments were shown to be spatially distant from each other by several Ångströms by no correlated signals in the 2D ^{31}P-^{31}P proton-driven spin diffusion (PDSD) SSNMR (Figure S6-2). This indicates that the adsorption of TMPO within an asymmetric unit or unit-cell precludes further proximal adsorption. This local spatial information is also extremely

valuable since it is not available by scattering methods. However, this analysis lacks channel- or site-specificity.

Chemical shift / ppm	Integrated intensity	Relative intensity / %
86	0.05	2.7
76	1.00	54.6
69	0.25	13.7
65	0.53	29.0

Table 6-1. Ratio of integrated area of peaks based on the 1D ^{31}P SSNMR spectrum.

The SSNMR investigation has shown that TMPO is successfully adsorbed by both BAS and weaker physisorption. The observation of numerous BAS adsorptions and strengths will be used to identify sites by NPD.

6.3.2.2 Crystalline adsorption sites by SXPD and NPD

This work was highly collaborative with Dr. Guangchao Li. The spatial location of adsorbed TMPO was investigated by refinement against SXPD and NPD data (Figure 6-8), in order to infer preferential aluminium distribution. Using two techniques with different scattering dependencies results in highly reliable analyses. The SXPD yielded an R_{wp} = 7.93% and GoF = 6.58, and the NPD an R_{wp} = 1.66% and GoF = 1.41 (Table S6-2 and

Table S6-3). The structure solution shows three TMPO adsorption sites in three regions of the pore network: the sinusoidal channel at T6-O18-T9 (TMPO-sin), the straight channel at T7-O17-T8 (TMPO-str), and the intersection at T3-O8-T12 (TMPO-int) (Figure 6-8). Each TMPO molecule was refined to ~1.0 Å of an acidic BAS proton. As a result of the adsorption, the framework O_{BAS}-H_{BAS} lengthened from ~1.09 Å to 1.87 Å, 1.20 Å, and 1.25 Å for the three sites, respectively (Table 6-2). This coordination to the BAS, dynamic distortion to the framework, and consequent formation of $TMPOH^+$ is in good agreement with previous literature.[47] This is analogous to many chemisorption events that underpin the catalytic performance of ZSM-5 materials.

Adsorption site	O_{TMPO}-H_{BAS} / Å	O_{BAS}-H_{BAS} / Å	SXPD occ. / %	NPD occ. / %	Al assignment
TMPO-sin	1.02(5)	1.87(1)	18.7	10.8	T6
TMPO-str	1.08(9)	1.20(2)	41.3	49.7	T8
TMPO-int	1.01(6)	1.25(4)	15.7	39.6	T12

Table 6-2.TMPO adsorption sites in ZSM-5 by SXPD and NPD.

The NPD occupancies of the three sites TMPO-str, TMPO-int, and TMPO-sin, are 49.7%, 39.5%, and 10.8%, respectively. These are in reasonable agreement with the relative composition of adsorption environments as shown by SSNMR: 54.6% for 76 ppm, 29.0% for 65 ppm, and 13.7% for 69 ppm. Thus, based on the characterisation presented thus far, it is hypothesised that T7-O17-T8 in the straight channel is the preferential BAS for TMPO adsorption (76 ppm). Likewise, adsorption in the intersection T3-O8-T12 site is assigned to the 65 ppm signal, and adsorption in the sinusoidal channel T6-O18-T9 at 69 ppm. This assignment is in agreement with increaed chemical shift for adsorption at confined sites due to stronger adsorption by van der Waals interactions.[44,47] Assigning the lower chemical shift

of 65 ppm to adsorption in the large intersection void is reasonable (diameter ~10 Å). The more shifted signals are assigned to adsorption within the more confined channels.

With the location of TMPO identified, the aluminium assignment is investigated by interrogation of T-O bond lengths as derived from NPD. It is noted that the distance of Si-O bond is shorter than that of Al-O bond in zeolites due to the difference in ionic radius of Si^{4+} and Al^{3+}.[80] For the straight channel BAS [T8-O17(H)-T7] moiety, the T8-O17 bond 1.70(7) Å is longer than T7-O17 1.60(7) Å. Hence, it can be concluded that the aluminium is most likely located at T8 rather than T7. This will be demonstrated in notation by underlining: [T8-O17(H)-T7]. Similarly, for the intersection BAS [T3-O8-T12] moiety, the T12-O8 bond 1.68(1) Å is longer than T3-O8 1.61(4) Å, and for the sinusoidal channel BAS [T6-O18(H)-T9] moiety, the T6-O18 bond 1.81(4) Å is much longer than the T9-O18 1.68(3) Å. Using these aluminium assignments, DFT calculations of the optimised adsorption showed similar bond lengths (Table S6-4).

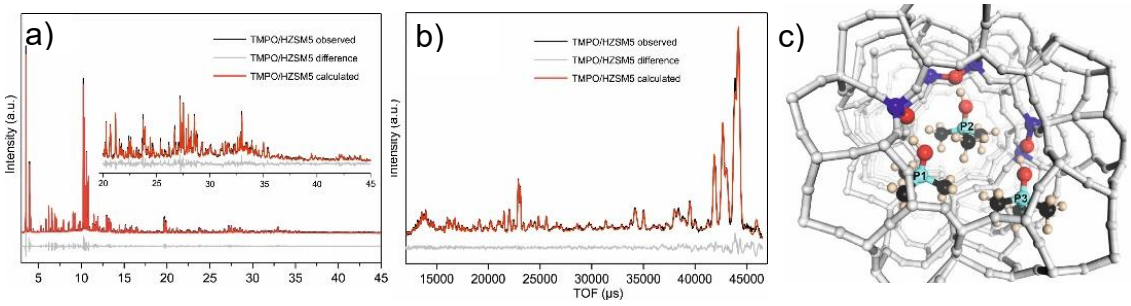


Figure 6-8. (a) SXPD pattern and Rietveld refinement fitting of TMPO/H-ZSM-5. (b) NPD diffraction pattern and Rietveld refinement data of TMPO/H-ZSM-5. (c) Crystallographic model of the three distinct asymmetric TMPO locations as derived by Rietveld refinement of NPD as viewed down the *b*-axis.

The aluminium siting from SSNMR, SXPD, NPD, and DFT of TMPO/ZSM-5 is T8, T12, and T6. This siting is consistent with STEM, and shows that Ag adsorption at the T8/T2

pairing is likely due to aluminium occupancy at T8. However, with respect to aluminium siting this remains an indirect method. The major shortcoming is if aluminium is placed within sheltered environment of the sinusoidal channel such as T4 and T10, which STEM is unable to observe and the bulky TMPO may not be able to access.

6.3.3 Direct crystallographic siting by RSXPD

6.3.3.1 High resolution far-from-edge structure solution on I11

The aim of this experiment was to refine the aluminium occupancy within ZSM-5 by using scattering contrast provided by anomalous scattering factors (ASF). Since the experiment relies on fitting intensity, the positions of the framework were sought to be defined and fixed prior to the RSXPD by collecting a high-resolution pattern on I11, DLS. The higher energy, higher angular-resolution, greater angle-rejection, and enhanced ω-spinning are all advantageous over I10 for the refinement of atomic positions. The incident X-ray energy was far above any aluminium or silicon absorption edges, ensuring that the contribution from ASF was negligible. Low pressure conditions were replicated by evacuating the capillary to 10^{-5} bar.

The structural model was refined against data from 3°-55°, which yielded an R_{wp} = 7.80% and GoF = 1.67. The three orthorhombic lattice parameters (a = 20.10488(7) Å, b = 19.92961(7) Å, c = 13.41721(5) Å) were used to calibrate the resonance patterns with respect to angle, in particular the c lattice parameter. Two solvent dummy atoms were used in order to improve the fitting; using more solvent atoms resulted in trivially improved fitting (Figure S6-3, Table S6-5 and Table S6-6).

6.3.3.2 Instrumentational requirements for RSXPD

The instrumental requirements for this RSXPD experiment are primarily associated with the softness of the X-rays around the Al K-edge: 1500-1600 eV. Within this region, the beam attenuation through air and solids is drastically increased relative to hard X-rays, for which attenuation is often negligible. The attenuation length, λ, is defined as the distance at

which the beam intensity drops to 1/*e* (~37%) of the incident beam intensity, and have been calculated using Hephaestus for various media (Table S6-7). Under atmospheric pressure, the extinction distance of a 1540 eV beam is three orders of magnitude shorter than at 15,000 eV. This results in insufficient flux at the sample for good counting statistic. Hence, the pressure of the atmosphere must be reduced.

The high-vacuum diffractometer on Beamline for Advanced Dichroism Experiments (BLADE) (I10, DLS) was used for this SXRPD investigation. The beamline is is optimised for beam energies of 400-2000 eV; hence high-vacuum environments are standard. The Reflectivity and Advanced Scattering from Ordered Regimes (RASOR) end-station consists of a diffractometer housed within a high-vacuum chamber, which can achieve pressures of 1×10^{-7} bar. Reducing the pressure to high vacuum allows the soft X-rays to travel relatively unhindered, preserving flux and collimation at the sample. At this pressure the attenuation from air by Compton scattering is reduced by a factor of 10^7 because the attenuation-length is inversely proportionate with concentration/density, as dictated by the Beer-Lambert law.

Importantly, soft X-rays have an even shorter extinction depth through solids. The conventional method for containing samples in Debye-Sherrer geometry is borosilicate capillaries, the standard on I11 being 0.1 mm wall-thickness with 0.7 mm internal diameter. Approximating this material as silica, the attenuation depth is found to be only 4.5 μm at 1540 eV. Hence, due to the exceptionally soft X-rays required by this experiment, confinement of the sample within any solid is not feasible. Instead, a carbon-fibre rod was covered with a thin layer of sample using an adhesive.

I10 is primarily used for investigating ordered magnetic structure, and has exclusively carried out single-crystal diffraction. Powder diffraction had never been carried out on I10

before this work. The instrumentation and configuration are optimised for single-crystal experiments. Their requirements to identify magnetic peaks are met by a relatively small flat image detector. Hence, though the end-station is not optimised for powder diffraction, it was thought feasible and worthwhile to establish a procedure for powder data collection, given the other desirable characteristics of the beamline. In many ways, the collection of single-crystal data are far more specialised than for powder data. Thus, this adaptation is not very involved, requiring a new sample mount, data-collection procedure, extended exposure time, and flat-detector corrections.

6.3.3.3 Fluorescence for energy calibration and ASF derivation

Energy calibration

The beamline readout for energy was found to be +0.5 eV of the actual energy, as calibrated by gadolinium foil (Chapter 3: Experimental procedures). All further references to beam energy on I10 have been linearly shifted by -0.5 eV. For example, the Al K-edge for the sample material was shown to be at 1563.5 eV (measured as 1564.0 eV: Figure S6-4). This is in near agreement with other zeolites (1567 eV).[88] The energy calibration affects the ASF derivation, *d*-space conversion, and starting point of energy refinement. When referencing energy, the energy will usually be quoted as an integer, hence will remain unchanged, but the calibrated energy will be used in calculations and refinements. Unfortunately, this calibration was not known during the synthesis of simulated patterns (presented shortly), for which the input energies were used.

Experimental ASF derivation from fluorescence

The ASF of the ZSM-5 aluminium were experimentally derived from the fluorescence spectrum (see Chapter 3: Experimental procedures). The primary difference between the theoretical and the experimentally-derived ASF values is the gradual slopes into the absorption region, the higher maximum of the white-line, and the post-edge fluctuations. This will have an impact on the refinement of aluminium occupancy for edge- and post-edge energies. There are also fine-structure oscillations originating from secondary scattering events and photoelectron recombination. This is important for the high energy-resolution DANES/DAFS experiment discussed in Further Work.

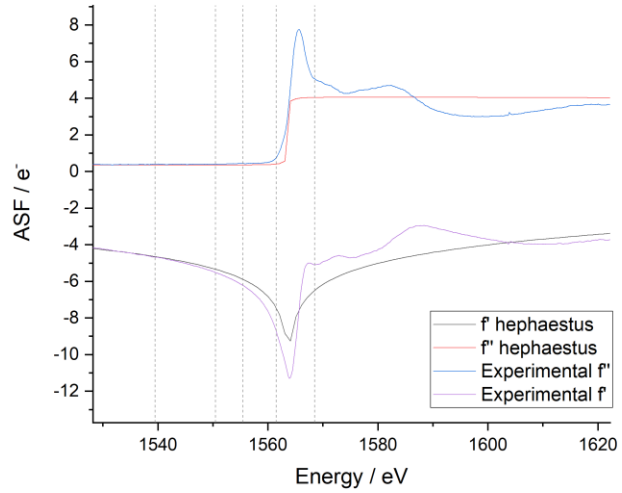


Figure 6-9. Theoretical (shifted from Al^0 edge) and experimentally-derived ASF over the Al^{3+} K-edge of ZSM-5. Experimental real-part of the ASF *f'* yielded by KK transform. Experimentally sampled energies shown by drop-lines.

6.3.3.4 Simulated RSXPD patterns

Simulated patterns were generated for various structures and energies using TOPAS from experimentally-derived Al ASF in order to show that the concentration of substitutional aluminium is resolvable. The aluminium composition (ICP-MS silicon-to-aluminium ratio:

16.75) is assumed to occupy only one tetrahedral site (5.63% of total T-site occupancy) and with the remaining occupancy being silicon, resulting in single site occupied as Si: 0.68 and Al: 0.32. Patterns were simulated for preferential aluminium occupancy at each tetrahedral site (T1-T12), as well as for a non-doped wholly silicon structure (T0). A simulated pattern was generated for each structure at each of the five energies collected experimentally (1540 eV, 1551 eV, 1562 eV, 1556 eV, and 1569 eV), yielding 65 patterns, each containing 45 reflections. The changing intensities are shown to be a direct result of ASF by repeating the simulations using just the standard atomic scattering factors, yielding none of the variation in intensities presented.

Firstly, it was investigated whether the aluminium structures exhibit appreciable change in intensity from the T0 structure, and the feasibility of observing these changes experimentally. The intensities of the T0 structure are shown to decrease approximately linearly with energy to an insignificant degree over all observed reflections (Figure S6-6). Expressed as a fraction of the integrated intensity of the previous energy, it is seen that the intensities typically vary by less than approximately 0.5% from the previous pattern. This is attributed to very small change in the dispersive ASF of silicon and oxygen in this energy range.

In contrast, the simulated intensities of the aluminium structures vary with greater magnitude, and with non-proportionate dependence with energy (Figure S6-7). Furthermore, some reflections increase in intensity over the edge, while others decrease. The intensities of the T6 structure are shown (Figure 6-10), which can vary by as much as 90% from the previous energy, in the case of (201). It is emphasised that some reflections such as (201) and (401) exhibit significant fractional change for all structures and energies.

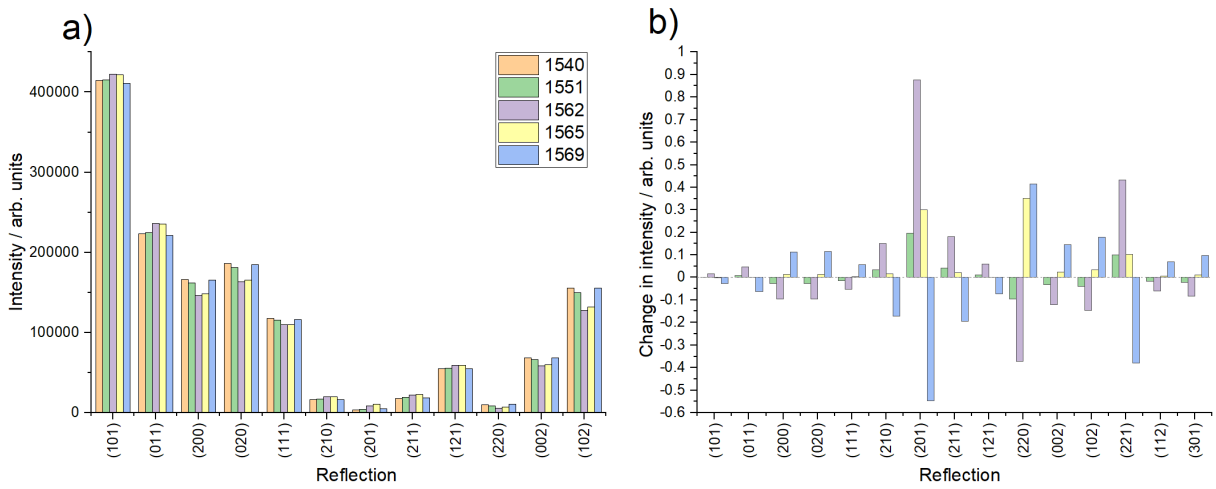


Figure 6-10. Simulated integrated intensities of the first 15 observed reflections at various energies for the T6 structure: (a) raw intensity, and (b) change in intensity from the previous energy pattern.

An example of this is the considerable fractional change due to very low intensity reflections for T0 that become appreciable in the aluminium-structures. For example, (201), is essentially unobserved for the T0 structure ($I \sim 1$). When raw intensity is plotted against a logarithmic scale, the (201) reflection for T0 can easily be seen as the only unobserved reflection in the entire matrix (Figure S6-12b). The reflection is very weakly observed in the experimental far-from-edge high-resolution pattern, the integrated intensity of which is unreliable due to poor signal-to-noise ratio (Figure S6-5). Meanwhile, all aluminium structures exhibit an appreciable (201) reflection ($I > 1\times10^5$). The most concerning aspect of

experimental RSXPD is the low concentration of aluminium, but here it is shown to have significant effect on the diffraction behaviour.

Within each aluminium-structure, the patterns vary appreciably with energy. Comparing each reflection to the T0 at the corresponding energy, the magnitude of the effect of the aluminium siting is derived. Not averaging over the reflections results in a large amount of data to present (45 reflections × 12 T-site structures × 5 energies). Averaged over all reflections and structures, the magnitude of the change from T0 is shown to increase and then decrease in variation in intensity over the Al^{3+} absorption edge (Figure 6-11a). This is in-line with the physical understanding of resonant scattering.

Averaged over all reflections and energy, it is shown that all structures vary similarly as ensemble of reflections (Figure 6-11a). The T6 structure exhibits the highest average magnitude of change in intensity from T0 across all energies. Here, it is shown that this is appreciably different to T0, and that this is most significant at 1562 eV and 1565 eV.

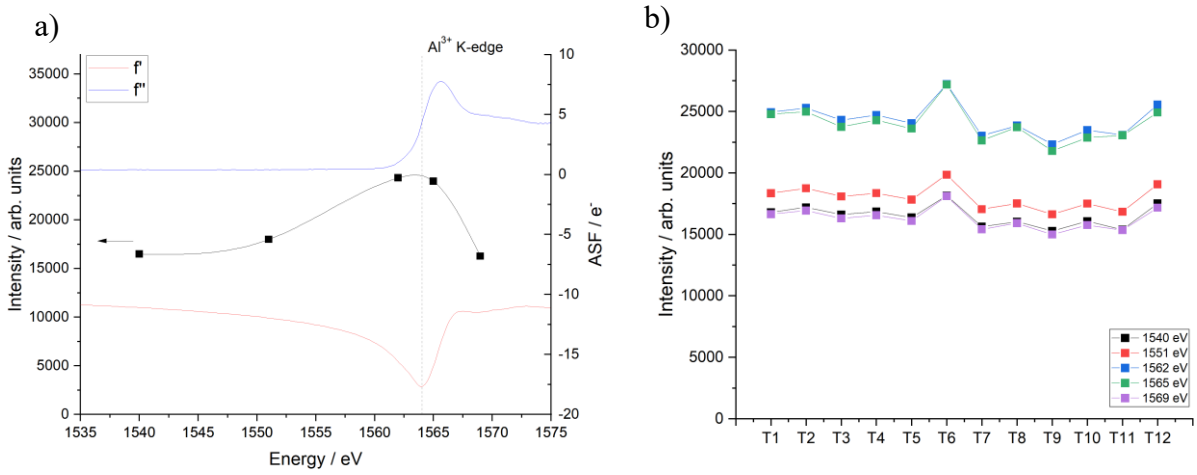


Figure 6-11. Average of the magnitude of change from the T0 structure (a) with respect to energy (markers show the experimentally sampled energies), and (b) with respect to T-site.

However, the aim of this investigation is the differentiating between the aluminium-structures. The simulated intensities are here averaged over energy as this dependence is shown above to be relatively systematic. Even from just the first five reflections, it is clearly shown that the location of the aluminium impacts each reflection very differently (Figure 6-12). This is despite the average change over the reflections being similar.

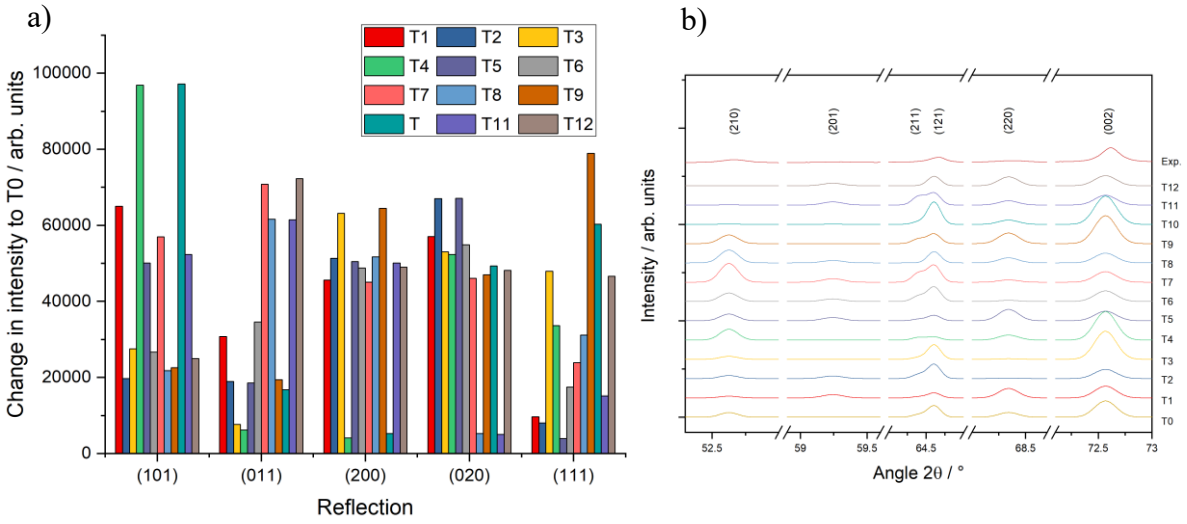


Figure 6-12. (a) The magnitude of the change in intensity from T0 of the first five reflections, averaged over the energy. (b) Simulated patterns at 1562 eV for all structures, and the experimental pattern, showing six consecutive reflections.

These are the non-systematic variations in intensity that will be used to refine the location of the aluminium. The utilisation of 45 non-systematically varying reflections is thought to be enough to yield a low number of possible solutions to the linear phase combination fitting of the experimental data. Furthermore, the experiment will yield five energies, which incurs further T-structure specific dependencies to fit to. These simulated patterns are a satisfactory proof-of-concept from fundamental principles of scattering. It is

also thought to be quite elegant that these are the exact changes in intensity that TOPAS will use to fit the experimental data.

6.3.3.5 Experimental RSXPD patterns

Five RSXPD patterns of ZSM-5 were collected using energies from around the Al^{3+} K-edge: 1540, 1551, 1562, 1565, and 1569 eV. This range aimed to include sampling of the low-energy region (low ASF impact), post-edge, and a few intermediate patterns approaching the *f*' minimum for which the *f*'' will be relatively constant. Patterns around the silicon K-edge were also collected, but suffered from significant absorption due to the high silicon composition (Figure S6-34c). Additionally, the contrast of silicon's ASF will be relatively constant as a function of aluminium siting due to the high background of silicon occupancy. Patterns from around the silicon edge are not considered further.

The raw 2D patterns showed the sample texture and extent of sampling of the Debye-Scherrer cone, which are satisfactory (Figure S6-8a). Geometric corrections were applied (most notably corrections for the flat detector), then integrated azimuthally to yield 1D powder patterns. The resulting patterns are noted for their resemblance to data collected by more conventional processes, exhibiting good data quality considering the rudimentary non-automatic data collection (Figure S6-8b). The background is low, flat, highly predictable, and thus easily fitted. The low angular resolution of 0.006° is far from limiting due to the broad peaks; though the peak-shapes are fairly typical. It is exciting to observe high intensity peaks at high angle. Due to the diminishing standard atomic scattering factors with angle, this region is usually very weak, with high *d*-spacing reflections being increasingly unobservable. Here, the standard scattering factors are combined with the non-angular dependent ASFs of aluminium.

Qualitatively, it can be seen that the peak intensity of the overlapped reflections (101) and (011) increases between 1540 eV to 1565 eV then increases for 1569 eV, which was expected from theory and simulation. Above the K-edge of Al^{3+} the real component of the ASF becomes less negative and the imaginary component becomes less positive, leading to the increased magnitude of the structure factor, $|F|$.

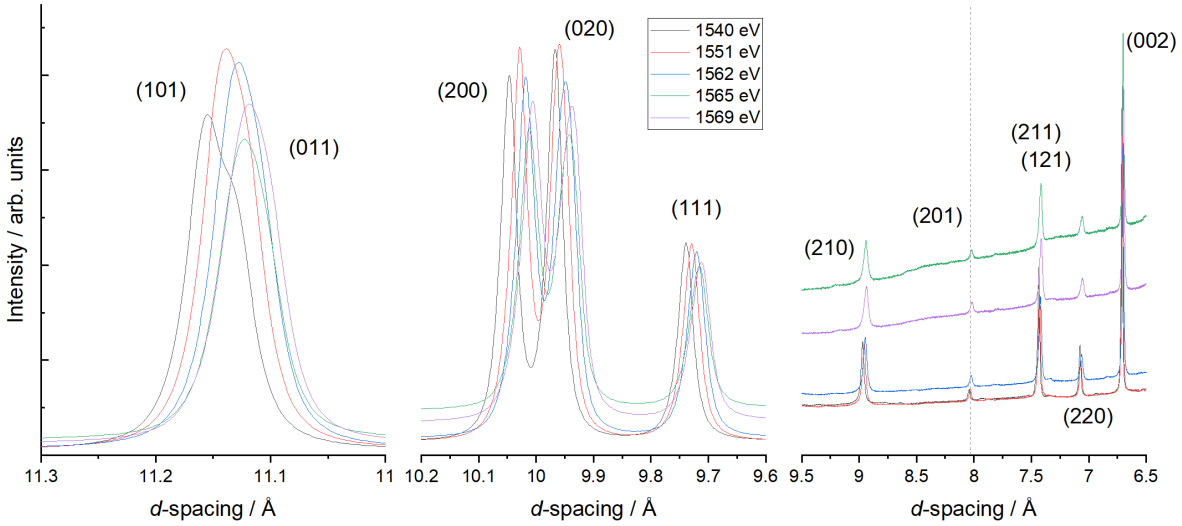


Figure 6-13. Magnified regions of RSXPD patterns against *d*-spacing that demonstrate the non-systematic changes in integrated intensity.

The intensity-dependence on angle 2θ has been expressed against *d*-spacing by conversion using the calibrated beam-energy. It is noted that the *d*-spacing of maximum intensity is not coincident over the five energies, and this is true of any given reflection. Hence, there is some variation from the calibrated energy (beam), zero-error between patterns (sample mounting/environment), or lattice parameters between patterns (sample/chemical). In order to extract accurate integrated intensities by Pawley refinement, it is evident that some parameter/s need to be modified. Since angle, and hence *d*-spacing, varies differently with lattice parameter, zero-error, and energy, all three sets of parameters can be refined

simultaneously. During all refinements, the *c* lattice parameter was fixed to the known value of 13.41721 Å from the refinement of the high-resolution data from beamline I11, in order to calibrate and stabilise the refinement. The *c* lattice parameter was chosen because the two narrowest low-angle principle reflections contain *c*-axis character: (101) and (011). In this investigation of aluminium occupancy, it is not important to fully identify the origin of this angular discrepancy.

Intensities by Pawley refinement

Before attempting to refine the aluminium occupancy, a Pawley refinement was carried out against the five RSXPD patterns in order to establish good fitting with respect to angle. Individual lattice parameters, energies and zero-errors were refined from the expected starting values in order to yield accurate intensities regardless of chemistry. Refined energies were within ±1.3 eV of the input value (Table S6-8). The *a* lattice parameter refines to an average of Δa = -0.043 Å of the known value, and the *b*-parameter to Δb = -0.007 Å. This discrepancy is not explained, but not relevant for the priority of accurately fitting intensity. It may be due to the higher vacuum conditions on I10 (1×10^{-6} bar), which can reach an order of magnitude lower pressure than I11 (1×10^{-5} bar). Reasonably large zero-error values show that this is a major cause of angular discrepancy. It is regretful that the zero-error of the new sample-holder was not calibrated with respect to angle by measuring a standard. This refinement yielded an overall R_{wp} = 3.15%, GoF = 0.98.

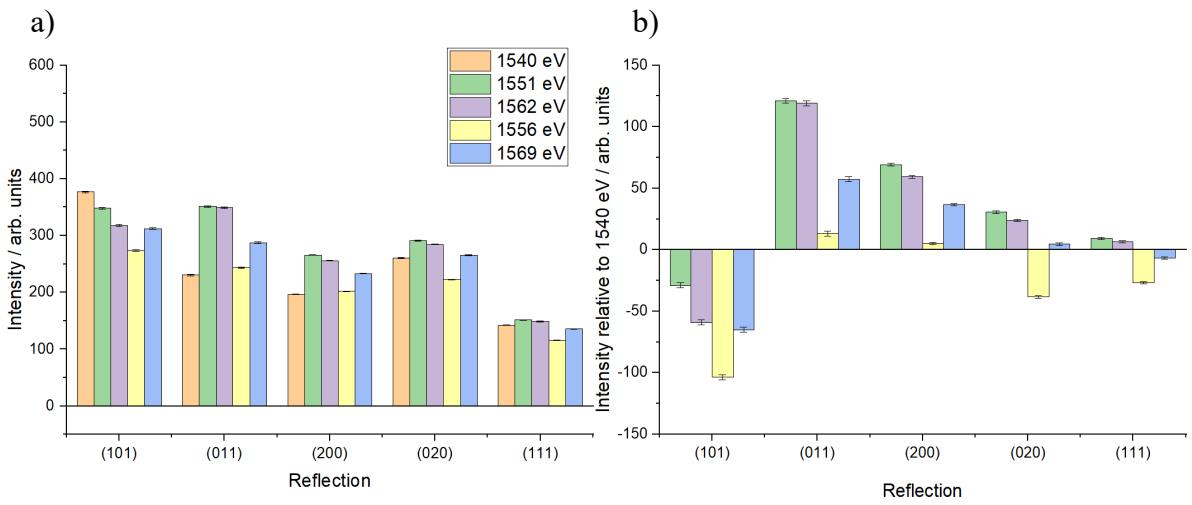


Figure 6-14. Integrated intensities of experimentally observed of ZSM-5 by RSXPD on I10 (whole range plotted in Figure S6-9): (a) absolute intensity, and (b) change in intensity relative to lowest energy 1540 eV.

The extracted Pawley intensities clearly show that the intensity is varying non-systematically with energy (Figure 6-14). Note, that in the extracted Pawley intensities data, there exist artefacts of the non-correlated intensity of reflections within a phase. Due to the similar *a*- and *b*-axes ($\Delta x = 0.175$ Å), reflections (*hkl*) and (*khl*) appear at very similar angles, resulting in peak overlap. Since the intensities are negatively corelated, there are several pairs of reflections in which one reflection is assigned zero intensity.

Rietveld refinement and aluminium siting

A Rietveld refinement was constructed using the fixed atomic coordinates derived from high-resolution data from I11 of the framework and two solvent dummy atoms. It is most important to model the changes in intensity across energy, and not as important to model the absolute intensity. Hence, it is thought reasonable to use solvent/dummy atoms in order to be able to accurately model the change in intensities. It is crucial to use a global scale factor for all patterns in order to model this change using aluminium occupancy. The angular

range of the patterns used was limited to a *d*-spacing of 4.15 Å due to incomplete peaks at higher angle. The backgrounds, peak shapes, energies, zero-errors, and lattice parameters were fixed to those derived by Pawley refinement. These were then all refined (Table S6-8), except the *c* lattice parameter which remained fixed.

The aluminium occupancy of each tetrahedral site was refined. Initially, the total occupancy of aluminium was not constrained, yielding a very good fit (R_{wp} = 3.47%, GoF = 1.08). The aluminium occupancy was widely distributed over ten of the sites, yielding zero occupancy at only T7 and T11 (Figure S6-10). However, the total aluminium occupancy of 3.81 greatly exceeded the known aluminium occupancy. The three sites of highest aluminium occupancy were T6, T4, and T8. The identification of T6 and T8 is thought to agree with other characterisation in this work and in the literature. The identification of T4 is less expected, but is yielded by varied and numerous parameterisation and refinement start-states. However, due to the high occupancy values, this fitting was deemed to be a poor model for the sample. The GoF value was very close to unity also, which indicates the approaching regime of over-parametrisation.

In order to be consistent with our chemical knowledge of the sample, the refinement was repeated but the known silicon-to-aluminium ratio was used to constrain the inequivalent occupancy to 0.676 aluminium and 11.324 silicon per unit unit-cell. The fit was still very good (R_{wp} = 4.33%, GoF = 1.33) (Figure 6-15). The energy (±1.2 eV) and lattice parameters (Δa = -0.041 Å, Δb = -0.006 Å) were again on average refined very close to their expected values (Table S6-8).

The aluminium occupancy was only distributed between three T-sites: again, T8 0.32(1), T4 0.244(2), and T6 0.116(2). All other sites refined to a zero-value, albeit with some error. When given complete freedom, the best fit uses a combination of all T-sites. However, when the refinement is constrained, a combination of the T4, T6, and T8 yields a sufficient fitting. This number of sites is in agreement with Sklenak et al. who showed by calculations that aluminium occupies only 3 to 5 sites.[89]

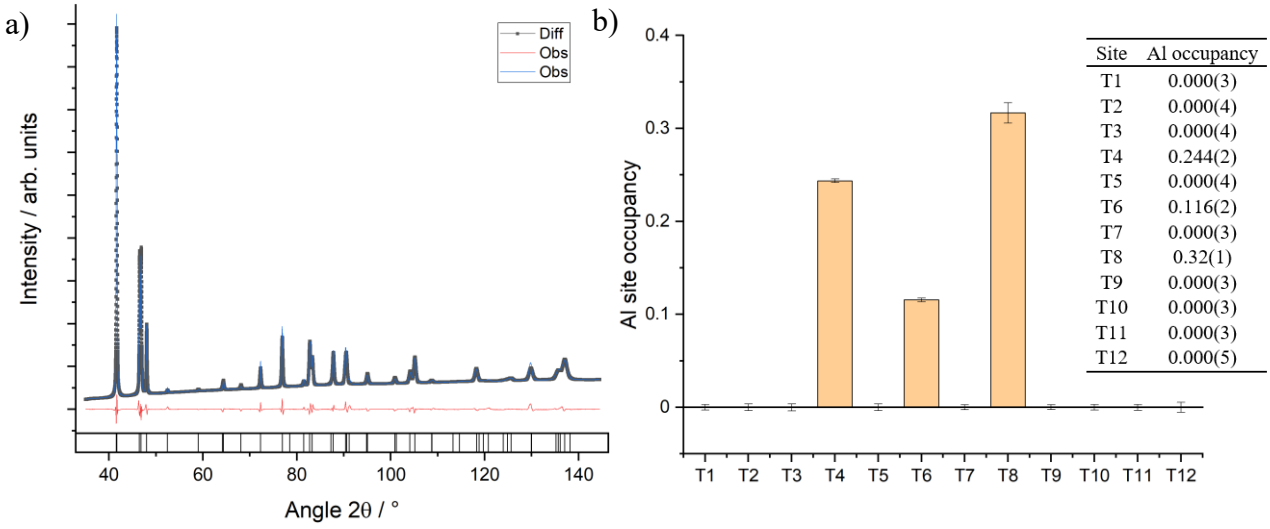


Figure 6-15. Rietveld refinement against experimental RSXPD. (a) Example fitting at 1569 eV. (b) Refined aluminium occupancy.

6.3.4 Comparative discussion of characterisation results

The aluminium siting results of the various characterisation techniques presented herein will be presented comparatively (Figure 6-16). The SSNMR analysis was not crystallographically site-specific so will not be explicitly discussed; primarily, the extent of agreement of RSXPD [T8>T4>T6] with the other methods.

The STEM of Ag/ZSM-5 yielded a siting of [T6/T12>T8/T2], but suffered from loss of site-specificity and restricted range of observation (channel, T-site, geometry of

adsorption). If the aluminium assignment of the <010>-equivalent pair T6/T12 is split between them (and the T8 retains occupancy since T2 is a low likelihood siting), it is shown that T8 is the most occupied site [T8>T6=T12], which is also shown by SXPD, NPD, and RSXPD. The absence of T4 by STEM is inherent to the technique. Despite the T4 site itself being unobservable along <010>, the low adsorption at the T9/T3, T5/T11, and T1/T7 pairs perhaps indicates aluminium occupancy at T4/T10. Of the adjacent tetrahedra to T4 (T1, T3, T5, T7) and T10 (T1, T9, T10, T11), none are observed as high adsorption sites by STEM. This indicates that Löwenstein's rule may be inviolate. In fact, the T1/T7 pair, both of which are adjacent tetrahedra to T4, is the least frequent adsorption site around the 10M-ring (2.7%). Hence, although Ag adsorption at T4 is not observable, we stipulate that the low adsorption at the T5/T11, T9/T3, and T1/T7 pairs indicate a strong aluminium occupancy at T4.

The scattering experiments by SXPD [T8>T6>T12] and NPD [T8>T12>T6] of TMPO/ZSM-5 yielded the same sites as STEM, but in different ratios. The discrepancy between the two scattering techniques is not considered to be a stark indication of invalidity. Both yield T8 as the most populated, which is considered a high preference site. The absence of T4 by SXPD/NPD is thought to be due to the inaccessibility of the sinusoidal channel. For this reason, direct characterisation is shown to be very powerful. Further investigation of the restricted access of the sinusoidal T4 site will be carried out by NPD of NH_3/ZSM-5, but analysis is ongoing.

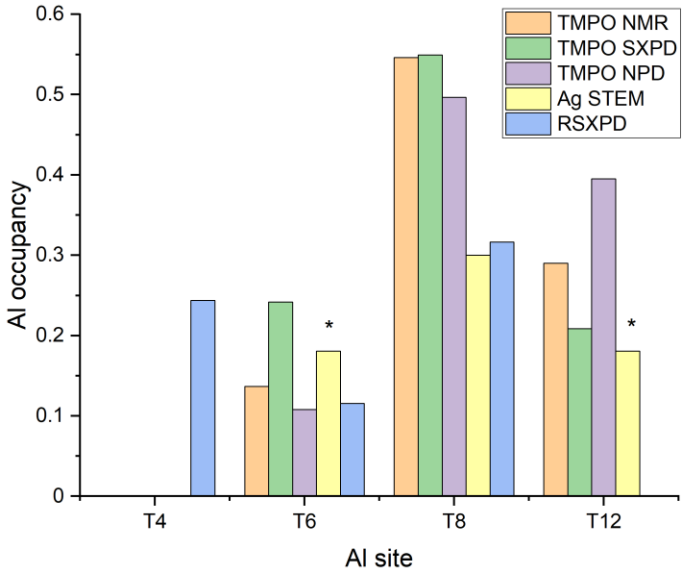


Figure 6-16. Summary of aluminium siting across several characterisation techniques. For STEM, occupancy at the T6/T12 site attributed to both, denoted by *.

Singularly, any of these techniques may be deemed unselective, but as a whole are reported as a suite of mutually supporting characterisation. Aluminium has been found to occupy four of the twelve T-sites, primarily at T6 and T8, with results by TMPO SXPD and NPD also suggesting T12, and RSXPD suggesting T4. The broad agreement with the siting by Ag/ZSM-5 and TMPO/ZSM-5 supports the validity of this new application of RSXPD to zeolite frameworks.

The T8 is a frequent site in literature for preferential aluminium occupancy.[8,55,56] The siting at T6 agrees with several previous reports of indirect probe-molecule identification in ZSM-5,[3,20,70,72,73,75] and shown to be a likely site of hetero-atomic boron[50] and silicalite vacancies.[77] Meanwhile T12 is also reported as likely by many computation studies.[45,49,50,60,90] Siting at T4 is much less common, but has been shown by XAFS and DFT to be a likely site for heteroatomic Ti^{4+} (similar radius to Al^{3+}) in TS-1.[66,67] The full siting here of T4, T6, T8, and T12 is the exact result of computational investigation into silicon

vacancies in the MFI structure.[91] Although these are for different systems, the analytical validity is considered to be much higher than for the indirect or computational Al^{3+}/Si^{4+} studies.

6.3.5 Chemical origins and implications

Considering this final aluminium siting result, some discussion of the chemical reasonability and implications will be presented.

6.3.5.1 Framework formation

Situated in the straight channel, the bond lengths and angles of T8 are more regular (typical of tetrahedral coordination), and especially relative to intersection and sinusoidal sites.[46] It has been previous postulated that more sterically strained T-sites are more active for adsorption and catalysis because the energy barrier to reorganisation, re-coordination, and even the breaking of Al-O bonds is reduced. Hence, thermodynamic stability and high occupancy may in fact be inversely correlated to activity. Regarding thermodynamic stability, it has been common to observe vacancies or heteroatoms at the T8 site in similar and analogous zeolitic structures to ZSM-5. The siting of the titanium heteroatom in TS-1 was long-thought to be statistical/random by both experimental[66,68,92,93] and computational methods[65,94,95]. Currently, it is generally agreed that T8 is a likely heteroatomic site. The same siting has been reported for the iron analogue FeS-1 also.[68] We assert that the T8 is the most thermodynamically stable site.

T6 and T12 are located in the intersection which is known to be the first substructure to nucleate in the formation of ZSM-5 in solution.[96] Hence, it can be inferred that the occupation of aluminium at the intersection is the result of kinetically-controlled irreversible incorporation early in the nucleation process, leading to a kinetically stable occupancy, i.e. T6 and T12 are the lowest energy sites available in the intersection sub-unit, before a lower energy site becomes available as the channels are formed during particle growth. This hypothesis is reliant on negligible reorganisation to thermodynamic-minimum siting after nucleation. The close symmetry-equivalence of T6 and T12 is even more pronounced when the intersectional sub-unit is isolated. Hence, it follows that aluminium occupancy at T6/T12 and T8 as a result of kinetic and thermodynamic control respectively.

6.3.5.2 Local Al-Al interaction

Occupancy at the T4 site in the sinusoidal channel is more challenging to attribute. It is interesting to note that if occupancy at T6 (T2, T3, T5, T9) and T8 (T7, T9, T11, T12) within an asymmetric unit is assumed, the only further siting that upholds Löwenstein's rule are T1 and the sinusoidal sites T4 and T10. It is hypothesised that the strained T4 can be an energetically favourable site when lower energy sites are precluded by surrounding occupancy. We propose that this the siting of T4, T6, and T8 by RSXPD is an observation of the inviolate Löwenstein's rule.

However, though the sites identified by RSXPD do not violate Löwenstein's rule, the result of TMPO/SXPD and NPD includes T12 (T8, T11, T3). The adjacent siting of T8 and T12 that are connected by the O16 bridging oxygen is not direct evidence of both sites being occupied by aluminium in a single asymmetric unit, or even the same unit-cell (remembering that all tetrahedral sites are 8d Wyckoff sites). It can only indicate that across many unit-cells

there are instances of both being occupied with enough periodicity to appreciably effect to Bragg diffraction. The siting is only true as an average across the entirety of the sampled crystalline volume. We aim to contribute to the ongoing debate of Löwenstein pairs by suggesting that if the rule is violable, the [Al_{T8}-O16-Al_{T12}] moiety is the most likely candidate based on this suite of characterisation.

6.3.5.3 Chemical activity

Regardless of why aluminium may be at T4, the observation of a sinusoidal site is important with respect to activity. It is well-known that the geometry of T-sites within the sinusoidal channel are more strained, making them more susceptible to adsorbate interaction. This was seen as a confinement effect on the chemical shift of ^{31}P resonances in SSNMR. It has also been reported that sinusoidal aluminium offers more size-selective catalysis.[11] We propose that the aluminium occupying T4 is responsible for much of the emergent activity.

6.4 Conclusion

6.4.1 Summary

Several structural and electronic characterisation have attempted to further elucidate the location of aluminium within the framework of ZSM-5: indirect siting by the observation of probe molecules/atoms by STEM and Bragg scattering techniques, and direct siting by a novel use of RSXPD on I10, DLS. These have complemented each other, providing different information regarding the region of the pore network, the specific crystallographic site, and indication of the local Al-Al interaction. The collation of the siting results have yielded conclusions greater than the sum of their parts, which we believe has elucidated strong evidence for preferential aluminium occupancy at certain T-sites.

Non-bulk spatial characterisation was carried out by STEM imaging of Ag/ZSM-5. The technique suffered from poor spatial resolution, the viewing of only the straight channel, restricted range of observable T-sites, and inherent loss of site selectivity. The results indicate that T6/T12 and T8/T2 are the most frequent to form Ag-BAS, and thus be occupied by aluminium.

The identification of three TMPO adsorption environments and thus three BAS adsorption sites utilises the widely-reported electronic and local characterisation of zeolite guest-host interactions. The spatial distribution of the adsorption was investigated by SXPD and NPD, which were then correlated to the electronic environments by their relative occupancy ratios. The most populated adsorption is found in the straight channel at T8, then in the intersection at T12, then in the sinusoidal channel through T6, which agrees with arguments of pore accessibility.

Aluminium siting using RSXPD was carried out on I10, DLS, as a novel use of the beamline, requiring procedural optimisation. The technique was shown to be valid by simulated patterns of low concentration ZSM-5. Simultaneous Rietveld refinement of five patterns yielded a siting of T8, T4, and T6.

The location of aluminium must be elucidated for deeper understanding of zeolite systems. We have primarily shown by indirect characterisation that aluminium is preferentially located at sites T8 and T6, and possibly T12. However, we impart greater weighting on aluminium siting by RSXPD due to the direct characterisation of the aluminium, and so also consider T4 to be a likely source of Brønsted acidity. We have provided evidence of preferential siting that underpins so many physicochemical properties regarding ZSM-5 synthesis, local structure, stability, acidity, and chemical activity.

6.4.2 Evaluation and future work

At the time of much of this research, RSXPD had never been applied to zeolites; however, there has been a recent published on aluminium siting by RSPXD of FER zeolites.[97] Despite this, the technique remains relatively unproven in zeolite characterisation. It is not claimed that this technique and work compressively solves the characterisation challenges of aluminium siting, which are decades old, but it offers an additional tool in understanding a system that is relatively poorly characterised considering its industrial importance.

It is expected that this use of RSXPD can be progressed much further, by application to other zeolite samples, structures, and environments, aiding the better understanding of the origin, mechanisms, and eventual design of the chemical activity of a broad range of zeolite materials and the general solid-state catalytic process. In particular, it is desired to further optimise and assess validity by using ZSM-5 materials of varying aluminium composition.

This is most usually carried out by varying reaction stoichiometry, but also could be achieved by dealumination, which could yield an elegant and continuous dataset. Of all of the aluminium-siting work presented here, RSXPD has the highest potential impact. This crystallographic information is thought to be a more important consideration for understanding chemical activity than the non-site-specific chemical analyses that dominate the literature. We consider our work to be a good proof-of-concept and starting point for future RSXPD investigation, especially on I10, which has shown its suitability for powder diffraction, and increased its range of expertise, with positive impact in the synchrotron community.

6.4.3 **Additional investigations**

6.4.3.1 Direct observation of aluminium site by electron spectroscopy

Typically, ZSM-5 is too unstable to withstand the electron flux required for atomic-resolution EDX/EELS. However, as a supporting technique, we could perhaps add singularly inconclusive data to our ensemble of characterisation. We planned to carry out cryogenic STEM in order to decrease beam-damage and yield sufficient counting statistics through summation over long exposure at low flux. Preliminary tests have been carried out, aided by Dr. Tom Slater on E01 JEOL ARM-200F at the electron Physical Science Imaging Centre (ePSIC), UK. Cryogenic cooling was used to allow the flux to be increased by an order of magnitude yielding a beam current of 6 pA, equivalent to 3000 e^{-} $Å^{-2}$. However, this was still approximately five-times too low for good spectroscopic counting statistics.

Additionally, the cryo-holder was only capable of very limited tilting. Hence, the particles were not able to be orientated down the *b*-axis/<010> zone axis in order to achieve good site identification and column summation (Figure S6-11). Future work will involve

using the newly commissioned double-tilt cryo-holder at ePSIC, and on-going collaboration with Dr. Tom Slater who is investigating the effect of cryogenic cooling on the beam tolerance of ZSM-5. In future, the sample should be optimised further, primarily by reducing the sample thickness. The coffin-shaped particles are 50-100 nm deep, which is thick for this analysis. It is suggested that the experiment be carried out using ZSM-5 membrane or thin-film, for which the syntheses has been reported in the literature.[98] This would also reduce charging and beam damage, as well aiding orientation if the crystal can be grown in the *b*-axis/<010> zone axis; though the coffin-shaped particles already naturally lie flat, exposing the <010> face (Figure 6-4).

6.4.3.2 Direct characterisation of aluminium by DAFS

Increasing the number of energies scanned over the edge effectively turns the investigation into a spectroscopic experiment, yielding a diffraction anomalous fine structure (DAFS) dataset. Importantly, the local structure as yielded by DAFS must be crystalline. This is an important distinction which yields clearer and more deconvoluted direct structural observations than individual XRD or XAS. In XRD, the T-O bond length of a given mixed-occupancy tetrahedral site will contain contributions from both T_{Si}-O and T_{Al}-O. In XANES/EXAFS/XAS, the Al-O bond length will contain contributions from all T_{Al}-O across the sample, whether crystalline or not (relevant to zeolites, this will include amorphous non-framework aluminium[36]). On the other hand, DAFS can yield the Al-O bond length and coordination information for a given crystallographic site without contribution from the silicon also occupying that site, as its ASF do not change appreciably over the aluminium edge. In theory, this technique provides direct characterisation of aluminium, that is phase-

specific and site-specific, which can include oxidation state and local coordination. An initial experiment is detailed in the Appendix: Figure S6-13.

Overall, these investigations represent brief attempts to provide further information on the structure of ZSM-5 using synchrotron radiation. Their limitations, errors, and implications have not yet been assessed. More extensive evaluations of the techniques should be carried out in future.

6.5 References

(1) Dietrich, M.; Rauch, D.; Simon, U.; Porch, A.; Moos, R. Ammonia Storage Studies on H-ZSM-5 Zeolites by Microwave Cavity Perturbation: Correlation of Dielectric Properties with Ammonia Storage. J. Sens. Sens. Syst. 2015, 4 (2), 263–269. https://doi.org/10.5194/jsss-4-263-2015.

(2) Kyrlidis, A.; Cook, S. J.; Chakraborty, A. K.; Bell, A. T.; Theodorou, D. N. Electronic Structure Calculations of Ammonia Adsorption in H-ZSM-5 Zeolites. J. Phys. Chem. 1995, 99 (5), 1505–1515. https://doi.org/10.1021/j100005a022.

(3) Ye, L.; Lo, B. T. W.; Qu, J.; Wilkinson, I.; Hughes, T.; Murray, C. A.; Tang, C. C.; Tsang, S. C. E. Probing Atomic Positions of Adsorbed Ammonia Molecules in Zeolite. Chem. Commun. 2016, 52 (16), 3422–3425. https://doi.org/10.1039/C5CC10476A.

(4) Mihaylov, M.; Ivanova, E.; Zdravkova, V.; Andonova, S.; Drenchev, N.; Chakarova, K.; Kefirov, R.; Kukeva, R.; Stoyanova, R.; Hadjiivanov, K. Purification of Hydrogen from CO with Cu/ZSM-5 Adsorbents. Molecules 2022, 27 (1), 96. https://doi.org/10.3390/molecules27010096.

(5) Matito-Martos, I.; García-Reyes, J.; Martin-Calvo, A.; Dubbeldam, D.; Calero, S. Improving Ammonia Production Using Zeolites. J. Phys. Chem. C 2019, 123 (30), 18475–18481. https://doi.org/10.1021/acs.jpcc.9b05366.

(6) Losch, P.; Pinar, A. B.; Willinger, M. G.; Soukup, K.; Chavan, S.; Vincent, B.; Pale, P.; Louis, B. H-ZSM-5 Zeolite Model Crystals: Structure-Diffusion-Activity Relationship in Methanol-to-Olefins Catalysis. J. Catal. 2017, 345, 11–23. https://doi.org/10.1016/j.jcat.2016.11.005.

(7) Lo, B. T. W.; Ye, L.; Tsang, S. C. E. The Contribution of Synchrotron X-Ray Powder Diffraction to Modern Zeolite Applications: A Mini-Review and Prospects. Chem 2018, 4 (8), 1778–1808. https://doi.org/10.1016/j.chempr.2018.04.018.

(8) Wang, S.; Wang, P.; Qin, Z.; Chen, Y.; Dong, M.; Li, J.; Zhang, K.; Liu, P.; Wang, J.; Fan, W. Relation of Catalytic Performance to the Aluminum Siting of Acidic Zeolites in the Conversion of Methanol to Olefins, Viewed via a Comparison between ZSM-5 and ZSM-11. ACS Catal. 2018, 8 (6), 5485–5505. https://doi.org/10.1021/acscatal.8b01054.

(9) Argauer, R. J.; Landolt, G. R. Crystalline Zeolite Zsm-5 and Method of Preparing the Same. US3702886A, November 14, 1972.

(10) Olson, D. H.; Kokotailo, G. T.; Lawton, S. L.; Meier, W. M. Crystal Structure and Structure-Related Properties of ZSM-5. J. Phys. Chem. 1981, 85 (15), 2238–2243. https://doi.org/10.1021/j150615a020.

(11) Wang, Y.; He, X.; Yang, F.; Su, Z.; Zhu, X. Control of Framework Aluminum Distribution in MFI Channels on the Catalytic Performance in Alkylation of Benzene with Methanol. Ind. Eng. Chem. Res. 2020, 59 (30), 13420–13427. https://doi.org/10.1021/acs.iecr.0c00366.

(12) Liang, T.; Chen, J.; Qin, Z.; Li, J.; Wang, P.; Wang, S.; Wang, G.; Dong, M.; Fan, W.; Wang, J. Conversion of Methanol to Olefins over H-ZSM-5 Zeolite: Reaction Pathway Is Related to the Framework Aluminum Siting. ACS Catal. 2016, 6 (11), 7311–7325. https://doi.org/10.1021/acscatal.6b01771.

(13) Sazama, P.; Dědeček, J.; Gábová, V.; Wichterlová, B.; Spoto, G.; Bordiga, S. Effect of Aluminium Distribution in the Framework of ZSM-5 on Hydrocarbon Transformation. Cracking of 1-Butene. J. Catal. 2008, 254 (2), 180–189. https://doi.org/10.1016/j.jcat.2007.12.005.

(14) Lin, L.; Sheveleva, A. M.; da Silva, I.; Parlett, C. M. A.; Tang, Z.; Liu, Y.; Fan, M.; Han, X.; Carter, J. H.; Tuna, F.; McInnes, E. J. L.; Cheng, Y.; Daemen, L. L.; Rudić, S.; Ramirez-Cuesta, A. J.; Tang, C. C.; Yang, S. Quantitative Production of Butenes from Biomass-Derived γ-Valerolactone Catalysed by Hetero-Atomic MFI Zeolite. Nat. Mater. 2020, 19 (1), 86–93. https://doi.org/10.1038/s41563-019-0562-6.

(15) Seiler, M.; Wang, W.; Hunger, M. Local Structure of Framework Aluminum in Zeolite H−ZSM-5 during Conversion of Methanol Investigated by In Situ NMR Spectroscopy. J. Phys. Chem. B 2001, 105 (34), 8143–8148. https://doi.org/10.1021/jp004455m.

(16) Gołąbek, K.; Tabor, E.; Pashkova, V.; Dedecek, J.; Tarach, K.; Góra-Marek, K. The Proximity of Aluminium Atoms Influences the Reaction Pathway of Ethanol Transformation over Zeolite ZSM-5. Commun. Chem. 2020, 3 (1), 1–9. https://doi.org/10.1038/s42004-020-0268-3.

(17) Yang, H.; Ma, C.; Zhang, X.; Li, Y.; Cheng, J.; Hao, Z. Understanding the Active Sites of Ag/Zeolites and Deactivation Mechanism of Ethylene Catalytic Oxidation at Room Temperature. ACS Catal. 2018, 8 (2), 1248–1258. https://doi.org/10.1021/acscatal.7b02410.

(18) Kokotailo, G. T.; Lawton, S. L.; Olson, D. H.; Meier, W. M. Structure of Synthetic Zeolite ZSM-5. Nature 1978, 272 (5652), 437–438. https://doi.org/10.1038/272437a0.
(19) Ghorbanpour, A.; Rimer, J. D.; Grabow, L. C. Periodic, VdW-Corrected Density Functional Theory Investigation of the Effect of Al Siting in H-ZSM-5 on Chemisorption Properties and Site-Specific Acidity. Catal. Commun. 2014, 52, 98–102. https://doi.org/10.1016/j.catcom.2014.04.005.
(20) Pashkova, V.; Sklenak, S.; Klein, P.; Urbanova, M.; Dědeček, J. Location of Framework Al Atoms in the Channels of ZSM-5: Effect of the (Hydrothermal) Synthesis. Chem. Weinh. Bergstr. Ger. 2016, 22 (12), 3937–3941. https://doi.org/10.1002/chem.201503758.
(21) Gábová, V.; Dědeček, J.; Čejka, J. Control of Al Distribution in ZSM-5 by Conditions of Zeolite Synthesis. Chem. Commun. 2003, No. 10, 1196–1197. https://doi.org/10.1039/B301634J.
(22) Dědeček, J.; Kaucký, D.; Wichterlová, B.; Gonsiorová, O. Co^{2+} Ions as Probes of Al Distribution in the Framework of Zeolites. ZSM-5 Study. Phys. Chem. Chem. Phys. 2002, 4 (21), 5406–5413. https://doi.org/10.1039/B203966B.
(23) Dedecek, J.; Balgová, V.; Pashkova, V.; Klein, P.; Wichterlová, B. Synthesis of ZSM-5 Zeolites with Defined Distribution of Al Atoms in the Framework and Multinuclear MAS NMR Analysis of the Control of Al Distribution. Chem. Mater. 2012, 24 (16), 3231–3239. https://doi.org/10.1021/cm301629a.
(24) Schröder, K.-P.; Sauer, J.; Leslie, M.; A.Catlow, C. R. Siting of AI and Bridging Hydroxyl Groups in ZSM-5: A Computer Simulation Study. Zeolites 1992, 12 (1), 20–23. https://doi.org/10.1016/0144-2449(92)90004-9.
(25) Muraoka, K.; Chaikittisilp, W.; Yanaba, Y.; Yoshikawa, T.; Okubo, T. Directing Aluminum Atoms into Energetically Favorable Tetrahedral Sites in a Zeolite Framework by Using Organic Structure-Directing Agents. Angew. Chem. Int. Ed. 2018, 57 (14), 3742–3746. https://doi.org/10.1002/anie.201713308.
(26) Henry, M.; Bulut, M.; Vermandel, W.; Sels, B.; Jacobs, P.; Minoux, D.; Nesterenko, N.; Dath, J. P. Low Temperature Conversion of Linear C4 Olefins Using Acid ZSM-5 Zeolites with Aluminum Concentration Gradient. Appl. Catal. Gen. 2012, 437–438, 96–103. https://doi.org/10.1016/j.apcata.2012.06.019.
(27) Groen, J. C.; Jansen, J. C.; Moulijn, J. A.; Pérez-Ramírez, J. Optimal Aluminum-Assisted Mesoporosity Development in MFI Zeolites by Desilication. J. Phys. Chem. B 2004, 108 (35), 13062–13065. https://doi.org/10.1021/jp047194f.
(28) Groen, J. C.; Peffer, L. A. A.; Moulijn, J. A.; Pérez‐Ramírez, J. Mechanism of Hierarchical Porosity Development in MFI Zeolites by Desilication: The Role of Aluminium as a Pore-Directing Agent. Chem. – Eur. J. 2005, 11 (17), 4983–4994. https://doi.org/10.1002/chem.200500045.
(29) Li, T.; Roy, K.; Krumeich, F.; Artiglia, L.; Huthwelker, T.; Bokhoven, J. A. van. Variation of Aluminium Distribution in Small-Sized ZSM-5 Crystals during Desilication. Chem. – Eur. J. 2019, 25 (69), 15879–15886. https://doi.org/10.1002/chem.201903852.
(30) Jiao, Y.; Forster, L.; Xu, S.; Chen, H.; Han, J.; Liu, X.; Zhou, Y.; Liu, J.; Zhang, J.; Yu, J.; D'Agostino, C.; Fan, X. Creation of Al-Enriched Mesoporous ZSM-5 Nanoboxes with High Catalytic Activity: Converting Tetrahedral Extra-Framework Al into Framework Sites by Post Treatment. Angew. Chem. Int. Ed. 2020, 59 (44), 19478–19486. https://doi.org/10.1002/anie.202002416.
(31) Přech, J.; Bozhilov, K. N.; El Fallah, J.; Barrier, N.; Valtchev, V. Fluoride Etching Opens the Structure and Strengthens the Active Sites of the Layered ZSM-5 Zeolite. Microporous Mesoporous Mater. 2019, 280, 297–305. https://doi.org/10.1016/j.micromeso.2019.02.023.
(32) Danilina, N.; Krumeich, F.; Castelanelli, S. A.; van Bokhoven, J. A. Where Are the Active Sites in Zeolites? Origin of Aluminum Zoning in ZSM-5. J. Phys. Chem. C 2010, 114 (14), 6640–6645. https://doi.org/10.1021/jp1006044.
(33) van Bokhoven, J. A.; Koningsberger, D. C.; Kunkeler, P.; van Bekkum, H.; Kentgens, A. P. M. Stepwise Dealumination of Zeolite Beta at Specific T-Sites Observed with 27Al MAS and 27Al MQ MAS NMR. J. Am. Chem. Soc. 2000, 122 (51), 12842–12847. https://doi.org/10.1021/ja002689d.
(34) Perea, D. E.; Arslan, I.; Liu, J.; Ristanović, Z.; Kovarik, L.; Arey, B. W.; Lercher, J. A.; Bare, S. R.; Weckhuysen, B. M. Determining the Location and Nearest Neighbours of Aluminium in Zeolites with Atom Probe Tomography. Nat. Commun. 2015, 6 (1), 7589. https://doi.org/10.1038/ncomms8589.
(35) Kim, S.; Park, G.; Woo, M. H.; Kwak, G.; Kim, S. K. Control of Hierarchical Structure and Framework-Al Distribution of ZSM-5 via Adjusting Crystallization Temperature and Their Effects on Methanol Conversion. ACS Catal. 2019, 9 (4), 2880–2892. https://doi.org/10.1021/acscatal.8b04493.

(36) Yi, X.; Liu, K.; Chen, W.; Li, J.; Xu, S.; Li, C.; Xiao, Y.; Liu, H.; Guo, X.; Liu, S.-B.; Zheng, A. Origin and Structural Characteristics of Tri-Coordinated Extra-Framework Aluminum Species in Dealuminated Zeolites. J. Am. Chem. Soc. 2018, 140 (34), 10764–10774. https://doi.org/10.1021/jacs.8b04819.

(37) Sklenak, S.; Dědeček, J.; Li, C.; Wichterlová, B.; Gábová, V.; Sierka, M.; Sauer, J. Aluminum Siting in Silicon-Rich Zeolite Frameworks: A Combined High-Resolution 27Al NMR Spectroscopy and Quantum Mechanics / Molecular Mechanics Study of ZSM-5. Angew. Chem. Int. Ed. 2007, 46 (38), 7286–7289. https://doi.org/10.1002/anie.200702628.

(38) Zheng, A.; Liu, S.-B.; Deng, F. 31P NMR Chemical Shifts of Phosphorus Probes as Reliable and Practical Acidity Scales for Solid and Liquid Catalysts. Chem. Rev. 2017, 117 (19), 12475–12531. https://doi.org/10.1021/acs.chemrev.7b00289.

(39) Wiper, P. V.; Amelse, J.; Mafra, L. Multinuclear Solid-State NMR Characterization of the Brønsted/Lewis Acid Properties in the BP HAMS-1B (H-[B]-ZSM-5) Borosilicate Molecular Sieve Using Adsorbed TMPO and TBPO Probe Molecules. J. Catal. 2014, 316, 240–250. https://doi.org/10.1016/j.jcat.2014.05.017.

(40) Thomas, J. M.; Klinowski, J.; Ramdas, S.; Hunter, B. K.; Tennakoon, D. T. B. The Evaluation of Non-Equivalent Tetrahedral Sites from ^{29}Si NMR Chemical Shifts in Zeolites and Related Aluminosilicates. Chem. Phys. Lett. 1983, 102 (2), 158–162. https://doi.org/10.1016/0009-2614(83)87384-9.

(41) Engelhardt, G.; Radeglia, R. A Semi-Empirical Quantum-Chemical Rationalization of the Correlation between SiOSi Angles and 29Si NMR Chemical Shifts of Silica Polymorphs and Framework Aluminosilicates (Zeolites). Chem. Phys. Lett. 1984, 108 (3), 271–274. https://doi.org/10.1016/0009-2614(84)87063-3.

(42) Lippmaa, E.; Samoson, A.; Magi, M. High-Resolution Aluminum-27 NMR of Aluminosilicates. J. Am. Chem. Soc. 1986, 108 (8), 1730–1735. https://doi.org/10.1021/ja00268a002.

(43) Bornes, C.; Sardo, M.; Lin, Z.; Amelse, J.; Fernandes, A.; Ribeiro, M. F.; Geraldes, C.; Rocha, J.; Mafra, L. 1H–31P HETCOR NMR Elucidates the Nature of Acid Sites in Zeolite HZSM-5 Probed with Trimethylphosphine Oxide. Chem. Commun. 2019, 55 (84), 12635–12638. https://doi.org/10.1039/C9CC06763A.

(44) Yi, X.; Li, G.; Huang, L.; Chu, Y.; Liu, Z.; Xia, H.; Zheng, A.; Deng, F. An NMR Scale for Measuring the Base Strength of Solid Catalysts with Pyrrole Probe: A Combined Solid-State NMR Experiment and Theoretical Calculation Study. J. Phys. Chem. C 2017, 121 (7), 3887–3895. https://doi.org/10.1021/acs.jpcc.6b11518.

(45) Derouane, E. G.; Hubert, R. A. Resolution and Assignment of Framework Sites in Zeolite ZSM-5 by Correlation of X-Ray and NMR Measurements. Chem. Phys. Lett. 1986, 132 (3), 315–318. https://doi.org/10.1016/0009-2614(86)80131-2.

(46) Han, O. H.; Kim, C.-S.; Hong, S. B. Direct Evidence for the Nonrandom Nature of Al Substitution in Zeolite ZSM-5: An Investigation by ^{27}Al MAS and MQ MAS NMR. Angew. Chem. Int. Ed. 2002, 41 (3), 469–472. https://doi.org/10.1002/1521-3773(20020201)41:3<469::AID-ANIE469>3.0.CO;2-K.

(47) Zheng, A.; Zhang, H.; Lu, X.; Liu, S.-B.; Deng, F. Theoretical Predictions of 31P NMR Chemical Shift Threshold of Trimethylphosphine Oxide Absorbed on Solid Acid Catalysts. J. Phys. Chem. B 2008, 112 (15), 4496–4505. https://doi.org/10.1021/jp709739v.

(48) Bellmann, A.; Rautenberg, C.; Bentrup, U.; Brückner, A. Determining the Location of Co^{2+} in Zeolites by UV-Vis Diffuse Reflection Spectroscopy: A Critical View. Catalysts 2020, 10 (1), 123. https://doi.org/10.3390/catal10010123.

(49) Fripiat, J. G.; Berger-André, F.; André, J.-M.; Derouanc, E. G. Non-Empirical Quantum Mechanical Calculations on Pentasil-Type Zeolites. Zeolites 1983, 3 (4), 306–310. https://doi.org/10.1016/0144-2449(83)90174-4.

(50) Li, C.; Vidal-Moya, A.; Miguel, P. J.; Dedecek, J.; Boronat, M.; Corma, A. Selective Introduction of Acid Sites in Different Confined Positions in ZSM-5 and Its Catalytic Implications. ACS Catal. 2018, 8 (8), 7688–7697. https://doi.org/10.1021/acscatal.8b02112.

(51) D, Z.; Y, L.; Hm, Z.; L, Z.; Js, G.; Cm, X.; Bj, S. A first-principles evaluation of the stability, accessibility, and strength of Bronsted acid sites in zeolites. J. Catal. 2017, 352, 627–637.

(52) Xing, B.; Ma, J.; Li, R.; Jiao, H. Location, Distribution and Acidity of Al Substitution in ZSM-5 with Different Si/Al Ratios – a Periodic DFT Computation. Catal. Sci. Technol. 2017, 7 (23), 5694–5708. https://doi.org/10.1039/C7CY01639E.

(53) Kim, C. W.; Heo, N. H.; Seff, K. Framework Sites Preferred by Aluminum in Zeolite ZSM-5. Structure of a Fully Dehydrated, Fully Cs^+-Exchanged ZSM-5 Crystal (MFI, Si/Al = 24). J. Phys. Chem. C 2011, 115 (50), 24823–24838. https://doi.org/10.1021/jp208246q.

(54) Jeffroy, M.; Nieto-Draghi, C.; Boutin, A. New Molecular Simulation Method To Determine Both Aluminum and Cation Location in Cationic Zeolites. Chem. Mater. 2017, 29 (2), 513–523. https://doi.org/10.1021/acs.chemmater.6b03011.

(55) Zhang, N.; Liu, C.; Ma, J.; Li, R.; Jiao, H. Determining the Structures, Acidity and Adsorption Properties of Al Substituted HZSM-5. Phys. Chem. Chem. Phys. 2019, 21 (34), 18758–18768. https://doi.org/10.1039/C9CP04050A.

(56) Teraishi, K.; Ishida, M.; Irisawa, J.; Kume, M.; Takahashi, Y.; Nakano, T.; Nakamura, H.; Miyamoto, A. Active Site Structure of Cu/ZSM-5: Computational Study. J. Phys. Chem. B 1997, 101 (41), 8079–8085. https://doi.org/10.1021/jp970957x.

(57) Chu, Z.-K.; Fu, G.; Guo, W.; Xu, X. Exploring the Sodium Cation Location and Aluminum Distribution in ZSM-5: A Systematic Study by the Extended ONIOM (XO) Method. J. Phys. Chem. C 2011, 115 (30), 14754–14761. https://doi.org/10.1021/jp201454t.

(58) Opalka, S. M.; Zhu, T. Influence of the Si/Al Ratio and Al Distribution on the H-ZSM-5 Lattice and Brønsted Acid Site Characteristics. Microporous Mesoporous Mater. 2016, 222, 256–270. https://doi.org/10.1016/j.micromeso.2015.10.030.

(59) Joshi, Y. V.; Thomson, K. T. Embedded Cluster (QM/MM) Investigation of C6 Diene Cyclization in HZSM-5. J. Catal. 2005, 230 (2), 440–463. https://doi.org/10.1016/j.jcat.2004.12.016.

(60) Tranca, D. C.; Zimmerman, P. M.; Gomes, J.; Lambrecht, D.; Keil, F. J.; Head-Gordon, M.; Bell, A. T. Hexane Cracking on ZSM-5 and Faujasite Zeolites: A QM/MM/QCT Study. J. Phys. Chem. C 2015, 119 (52), 28836–28853. https://doi.org/10.1021/acs.jpcc.5b07457.

(61) Brüggemann, T. C.; Vlachos, D. G.; Keil, F. J. Microkinetic Modeling of the Fast Selective Catalytic Reduction of Nitrogen Oxide with Ammonia on H-ZSM5 Based on First Principles. J. Catal. 2011, 283 (2), 178–191. https://doi.org/10.1016/j.jcat.2011.08.009.

(62) Akacem, Y.; Castellà-Ventura, M.; Kassab, E. Theoretical Study of the Aluminum Distribution Effects on the Double Proton Transfer Mechanisms upon Adsorption of 4,4′-Bipyridine on H-ZSM-5. J. Phys. Chem. A 2012, 116 (4), 1261−1271. https://doi.org/10.1021/jp209445s.

(63) Keyvanloo, Z.; Nakhaei Pour, A.; Moosavi, F.; Kamali Shahri, S. M. Molecular Dynamic Simulation Studies of Adsorption and Diffusion Behaviors of Methanol and Ethanol through ZSM-5 Zeolite. J. Mol. Graph. Model. 2022, 110, 108048. https://doi.org/10.1016/j.jmgm.2021.108048.

(64) Heo, N. H.; Kim, C. W.; Kwon, H. J.; Kim, G. H.; Kim, S. H.; Hong, S. B.; Seff, K. Detailed Determination of the Tl+ Positions in Zeolite Tl−ZSM-5. Single-Crystal Structures of Fully Dehydrated Tl−ZSM-5 and H−ZSM-5 (MFI, Si/Al = 29). Additional Evidence for a Nonrandom Distribution of Framework Aluminum. J. Phys. Chem. C 2009, 113 (46), 19937–19956. https://doi.org/10.1021/jp9061913.

(65) Millini, R.; Perego, G.; Seiti, K. Ti Substitution in MFI Type Zeolites: A Quantum Mechanical Study. In Studies in Surface Science and Catalysis; Weitkamp, J., Karge, H. G., Pfeifer, H., Hölderich, W., Eds.; Zeolites and Related Microporous Materials: State of the Art 1994 - Proceedings of the 10th International Zeolite Conference, Garmisch-Partenkirchen, Germany, 17-22 July 1994; Elsevier, 1994; Vol. 84, pp 2123–2129. https://doi.org/10.1016/S0167-2991(08)63774-X.

(66) Dong, J.; Zhu, H.; Xiang, Y.; Wang, Y.; An, P.; Gong, Y.; Liang, Y.; Qiu, L.; Zheng, A.; Peng, X.; Lin, M.; Xu, G.; Guo, Z.; Chen, D. Toward a Unified Identification of Ti Location in the MFI Framework of High-Ti-Loaded TS-1: Combined EXAFS, XANES, and DFT Study. J. Phys. Chem. C 2016, 120 (36), 20114–20124. https://doi.org/10.1021/acs.jpcc.6b05087.

(67) Pirc, G.; Stare, J. Titanium Site Preference Problem in the TS-1 Zeolite Catalyst: A Periodic Hartree-Fock Study. Acta Chim Slov 2008, 9.

(68) Hijar, C. A.; Jacubinas, R. M.; Eckert, J.; Henson, N. J.; Hay, P. J.; Ott, K. C. The Siting of Ti in TS-1 Is Non-Random. Powder Neutron Diffraction Studies and Theoretical Calculations of TS-1 and FeS-1. J. Phys. Chem. B 2000, 104 (51), 12157–12164. https://doi.org/10.1021/jp002167k.

(69) Liu, L.; Wang, N.; Zhu, C.; Liu, X.; Zhu, Y.; Guo, P.; Alfilfil, L.; Dong, X.; Zhang, D.; Han, Y. Direct Imaging of Atomically Dispersed Molybdenum That Enables Location of Aluminum in the Framework of Zeolite ZSM-5. Angew. Chem. Int. Ed. 2020, 59 (2), 819–825. https://doi.org/10.1002/anie.201909834.

(70) Lo, B. T. W.; Lin, W.; Li, M. M. J.; Day, S.; Tang, C.; Tsang, S. C. E. Evaluation of Brønsted and Lewis Acid Sites in H-ZSM-5 and H-USY with or without Metal Modification Using Probe Molecule-Synchrotron X-Ray Powder Diffraction. Appl. Catal. Gen. 2020, 596, 117528. https://doi.org/10.1016/j.apcata.2020.117528.

(71) Ye, L.; Zhao, P.; Li, M. M.-J.; Lo, B. T. W.; Tang, C.; Tsang, S. C. E. Evaluation of the Molecular Poisoning Phenomenon of W Sites in ZSM-5 via Synchrotron X-Ray Powder Diffraction. Chem. Commun. 2018, 54 (51), 7014–7017. https://doi.org/10.1039/C8CC02904K.

(72) Zhao, P.; Ye, L.; Sun, Z.; Lo, B. T. W.; Woodcock, H.; Huang, C.; Tang, C.; Kirkland, A. I.; Mei, D.; Edman Tsang, S. C. Entrapped Single Tungstate Site in Zeolite for Cooperative Catalysis of Olefin Metathesis with Brønsted Acid Site. J. Am. Chem. Soc. 2018, 140 (21), 6661–6667. https://doi.org/10.1021/jacs.8b03012.

(73) Lo, B. T. W.; Ye, L.; Qu, J.; Sun, J.; Zheng, J.; Kong, D.; Murray, C. A.; Tang, C. C.; Tsang, S. C. E. Elucidation of Adsorbate Structures and Interactions on Brønsted Acid Sites in H-ZSM-5 by Synchrotron X-Ray Powder Diffraction. Angew. Chem. Int. Ed. 2016, 55 (20), 5981–5984. https://doi.org/10.1002/anie.201600487.

(74) Ye, L.; Teixeira, I.; Lo, B. T. W.; Zhao, P.; Tsang, S. C. E. Spatial Differentiation of Brønsted Acid Sites by Probe Molecule in Zeolite USY Using Synchrotron X-Ray Powder Diffraction. Chem. Commun. 2017, 53 (70), 9725–9728. https://doi.org/10.1039/C7CC03524A.

(75) Lin, W.-C.; Wu, S.; Li, G.; Ho, P.-L.; Ye, Y.; Zhao, P.; Day, S.; Tang, C.; Chen, W.; Zheng, A.; W. Lo, B. T.; Tsang, S. C. E. Cooperative Catalytically Active Sites for Methanol Activation by Single Metal Ion-Doped H-ZSM-5. Chem. Sci. 2021, 12 (1), 210–219. https://doi.org/10.1039/D0SC04058D.

(76) Smith, L. J.; Davidson, A.; Cheetham, A. K. A Neutron Diffraction and Infrared Spectroscopy Study of the Acid Form of the Aluminosilicate Zeolite, Chabazite (H- SSZ-13). Catal. Lett. 1997, 49 (3), 143–146. https://doi.org/10.1023/A:1019097019846.

(77) Artioli, G.; Lamberti, C.; Marra, G. L. Neutron Powder Diffraction Study of Orthorhombic and Monoclinic Defective Silicalite. Acta Crystallogr. B 2000, 56 (1), 2–10. https://doi.org/10.1107/S0108768199008927.

(78) Löwenstein, W. The Distribution of Aluminum in the Tetrahedra of Silicates and Aluminates. Am. Mineral. 1954, 39 (1–2), 92–96.

(79) Tang, X.; Liu, Z.; Huang, L.; Chen, W.; Li, C.; Wang, G.; Li, G.; Yi, X.; Zheng, A. Violation or Abidance of Löwenstein's Rule in Zeolites Under Synthesis Conditions? ACS Catal. 2019, 9 (12), 10618–10625. https://doi.org/10.1021/acscatal.9b01844.

(80) Fletcher, R. E.; Ling, S.; Slater, B. Violations of Löwenstein's Rule in Zeolites. Chem. Sci. 2017, 8 (11), 7483–7491. https://doi.org/10.1039/C7SC02531A.

(81) Takaishi, T.; Kato, M. Determination of the Ordered Distribution of Aluminum Atoms in Zeolitic Frameworks. Part I. Zeolites 1995, 15 (8), 689–700. https://doi.org/10.1016/0144-2449(95)00067-G.

(82) Takaishi, T.; Kato, M.; Itabashi, K. Determination of the Ordered Distribution of Aluminum Atoms in a Zeolitic Framework. Part II. Zeolites 1995, 15 (1), 21–32. https://doi.org/10.1016/0144-2449(94)00015-K.

(83) Jablonski, A.; Salvat, F.; Powell, C. J.; Lee, A. Y. NIST Electron Elastic-Scattering Cross-Section Database Version 4.0; NIST Standard Reference Database Number 64; National Institute of Standards and Technology, 2006.

(84) Wilkinson, A. P.; Cheetham, A. K.; Tang, S. C.; Reppart, W. J. Cation Distribution in Zeolite Zinc/Sodium-Y by Resonant X-Ray Diffraction. J. Chem. Soc. Chem. Commun. 1992, No. 20, 1485–1487. https://doi.org/10.1039/C39920001485.

(85) Palancher, H.; Hodeau, J.-L.; Pichon, C.; Bérar, J.-F.; Lynch, J.; Rebours, B.; Rodriguez‐Carvajal, J. Direct Localization of Atoms in Mixed-Occupancy Powders by Resonant Contrast Diffraction. Angew. Chem. Int. Ed. 2005, 44 (11), 1725–1729. https://doi.org/10.1002/anie.200461642.

(86) Xin, S.; Wang, Q.; Xu, J.; Chu, Y.; Wang, P.; Feng, N.; Qi, G.; Trébosc, J.; Lafon, O.; Fan, W.; Deng, F. The Acidic Nature of "NMR-Invisible" Tri-Coordinated Framework Aluminum Species in Zeolites. Chem. Sci. 2019, 10 (43), 10159–10169. https://doi.org/10.1039/C9SC02634G.

(87) Hernandez-Tamargo, C. E.; Roldan, A.; de Leeuw, N. H. DFT Modeling of the Adsorption of Trimethylphosphine Oxide at the Internal and External Surfaces of Zeolite MFI. J. Phys. Chem. C 2016, 120 (34), 19097–19106. https://doi.org/10.1021/acs.jpcc.6b03448.

(88) Drake, I. J.; Zhang, Y.; Gilles, M. K.; Teris Liu, C. N.; Nachimuthu, P.; Perera, R. C. C.; Wakita, H.; Bell, A. T. An In Situ Al K-Edge XAS Investigation of the Local Environment of H+- and Cu+-

Exchanged USY and ZSM-5 Zeolites. J. Phys. Chem. B 2006, 110 (24), 11665–11676. https://doi.org/10.1021/jp058244z.

(89) Sklenak, S.; Dědeček, J.; Li, C.; Wichterlová, B.; Gábová, V.; Sierka, M.; Sauer, J. Aluminium Siting in the ZSM-5 Framework by Combination of High Resolution 27Al NMR and DFT/MM Calculations. Phys. Chem. Chem. Phys. 2009, 11 (8), 1237–1247. https://doi.org/10.1039/B807755J.

(90) Brändle, M.; Sauer, J. Acidity Differences between Inorganic Solids Induced by Their Framework Structure. A Combined Quantum Mechanics/Molecular Mechanics Ab Initio Study on Zeolites. J. Am. Chem. Soc. 1998, 120 (7), 1556–1570. https://doi.org/10.1021/ja9729037.

(91) Yuan, S.; Si, H.; Fu, A.; Chu, T.; Tian, F.; Duan, Y.-B.; Wang, J. Location of Si Vacancies and [Ti(OSi)4] and [Ti(OSi)3OH] Sites in the MFI Framework: A Large Cluster and Full Ab Initio Study. J. Phys. Chem. A 2011, 115 (5), 940–947. https://doi.org/10.1021/jp110977m.

(92) Gleeson, D.; Sankar, G.; Catlow, C. R. A.; Thomas, J. M.; Spanó, G.; Bordiga, S.; Zecchina, A.; Lamberti, C. The Architecture of Catalytically Active Centers in Titanosilicate (TS-1) and Related Selective-Oxidation Catalysts. Phys. Chem. Chem. Phys. 2000, 2 (20), 4812–4817. https://doi.org/10.1039/B005780K.

(93) Henry, P. F.; Weller, M. T.; Wilson, C. C. Structural Investigation of TS-1: Determination of the True Nonrandom Titanium Framework Substitution and Silicon Vacancy Distribution from Powder Neutron Diffraction Studies Using Isotopes. J. Phys. Chem. B 2001, 105 (31), 7452–7458. https://doi.org/10.1021/jp0107715.

(94) Jentys, A.; Catlow, C. R. A. Structural Properties of Titanium Sites in Ti-ZSM5. Catal. Lett. 1993, 22 (3), 251–257. https://doi.org/10.1007/BF00810371.

(95) To, J.; Sokol, A. A.; French, S. A.; Catlow, C. R. A.; Sherwood, P.; Dam, H. J. J. van. Formation of Heteroatom Active Sites in Zeolites by Hydrolysis and Inversion. Angew. Chem. Int. Ed. 2006, 45 (10), 1633–1638. https://doi.org/10.1002/anie.200503006.

(96) Chang, C. D.; Bell, A. T. Studies on the Mechanism of ZSM-5 Formation. Catal. Lett. 1991, 8 (5), 305–316. https://doi.org/10.1007/BF00764192.

(97) Pinar, A. B.; Rzepka, P.; Knorpp, A. J.; McCusker, L. B.; Baerlocher, C.; Huthwelker, T.; van Bokhoven, J. A. Pinpointing and Quantifying the Aluminum Distribution in Zeolite Catalysts Using Anomalous Scattering at the Al Absorption Edge. J. Am. Chem. Soc. 2021, 143 (43), 17926–17930. https://doi.org/10.1021/jacs.1c06925.

(98) Yan, Y.; Davis, M. E.; Gavalas, G. R. Preparation of Zeolite ZSM-5 Membranes by In-Situ Crystallization on Porous .Alpha.-Al2O3. Ind. Eng. Chem. Res. 1995, 34 (5), 1652–1661. https://doi.org/10.1021/ie00044a018.

(99) Huo, H.; Peng, L.; Gan, Z.; Grey, C. P. Solid-State MAS NMR Studies of Brønsted Acid Sites in Zeolite H-Mordenite. J. Am. Chem. Soc. 2012, 134 (23), 9708–9720. https://doi.org/10.1021/ja301963e.

Chapter 7: Ending remarks

7.1 Agile ammonia synthesis and light-element doping

Here, we have presented three studies into the agile ammonia synthesis (AAS) pathway: photocatalytic hydrogen evolution, electrochemical storage for energy arbitrage, and ammonia confinement and storage in zeolites. Though not included here, work on the Haber-Bosch was also carried out during this period of study, and will be included in the following description of the AAS pathway.

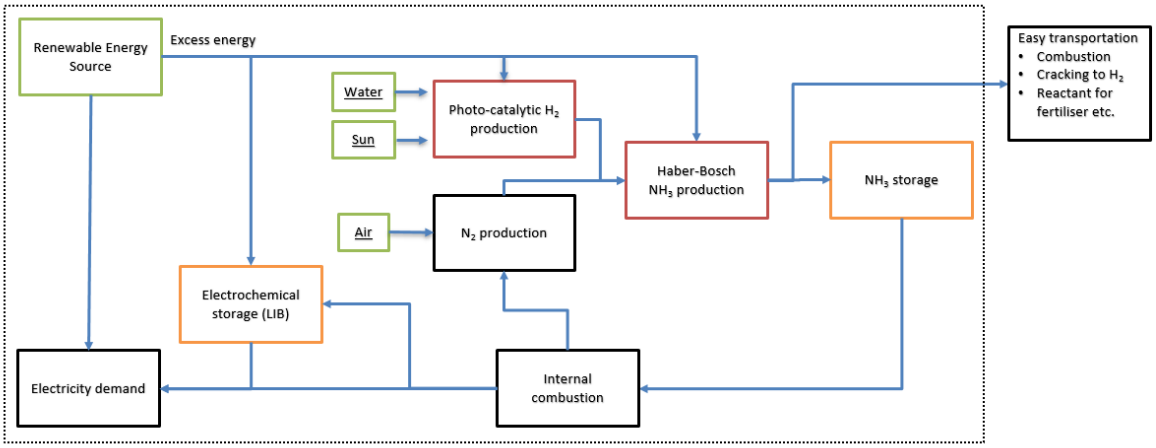


Figure 7-1. Repeated figure from Chapter 1: Introduction. Schematic of self-contained agile ammonia synthesis pathway, featuring many of the systems presented in this document. Renewable inputs shown in green, energy-vector-producing reactions in red, and energy vectors/storage solutions in orange.

It is possible to produce hydrogen gas from only solar irradiance and water by using N-TiO_2 and solar furnaces or powered by electricity from renewable energy sources. The electricity can be stored as electrochemical energy in LIB in order to be released when required, either into the grid for financial gain or locally for high-frequency consumer needs.

Palladium nanoparticles can offer good cycling stability as the energy storage material. Using the hydrogen and excess intermittent electricity from an on-site renewable source, the Haber-Bosch reaction can produce ammonia: a valuable and relatively safe energy vector. The rate-limiting step of the Haber-Bosch is much reduced over ruthenium nanoparticles, particularly when supported on aliovalent perovskites which can facilitate hydrogen spill-over and reduce poisoning. The confinement and removal of ammonia in porous zeolite frameworks can promote the Haber-Bosh by affecting the steady state. Ammonia can be easily stored and combusted on-site when electricity is demanded.

7.2 Archetypal inorganic frameworks and light-element doping

The range of solid-state characterisation techniques and analyses presented in this thesis have ranged from laboratory-based UV-vis spectroscopy to novel RSXPD on I10, DLS, to attempts at boundary-pushing atomic-resolution EELS. This varied work has had a common theme of observing and quantifying the effect of light-elements doped into highly-scattering frameworks, either for enhanced electronic properties, or electrochemical storage. All of these host materials are generally considered simple, archetypal, and effective within their fields. However, here we have shown doping to introduce emergent properties, structural complexity, enhanced performance, and scientific intrigue. Broadly, the cumulative and complementary array of observations have coalesced into meaningful conclusions, presented in the individual research chapters. Several chemical themes are retrospectively evident.

- Beneficial (or at least non-disadvantageous) disorder, in particular by the effect of previously doped or abstracted frameworks: local reorganisation around oxygen vacancies, decreasing crystallinity of repeated electro-lithiation, and importance of the

sequence of aluminium deposition during synthesis in zeolites as a result of local preclusion of Löwenstein pairs.

- Anisotropic volume expansion: TiO_2 materials and *hP* $PdLi_2$ were shown to have strong anisotropic dependences on temperature and potential, respectively.
- In-situ syntheses: $TiNO_x$ formation from anatase during VT-SXPD, and inadvertent carbon intercalation, one-step thermal lithiation and possible encapsulation of palladium

It is clear that the enhancements of light-element doping are not simple, nor currently very well-defined. For all systems, vital contributions are made to further defining the structure-activity relationship, impacting the various high-impact fields of green chemistry and environmental science, photocatalysis, chemical and electrochemical energy storage, adsorption and catalysis, porous frameworks, and synchrotron instrumentation and procedure.

7.3 X-ray scattering techniques and light-element doping

The repeated use of SXPD evidently unifies a lot of this work, with specific expertise demonstrated in variable-temperature and in-operando data collection, multi-dimensional large-scale datasets and batch refinement, and collating complementary analyses. However, another theme of the work has been the consistent inability of elastic SXPD to directly identify light elements: the nitrogen or oxygen vacancies in N-TiO_2, the interstitial lithium in various Pd-Li intermetallic compounds, or substitutional aluminium in zeolites. Only by the use of inelastic scattering has RSXPD yielded direct characterisation. However, it cannot be said that elastic scattering is not effective at characterising these materials, as is evident by the foundational contribution it has made to this thesis.

7.3.1 The future of the analytical problem

7.3.1.1 High quality experiments

Although there are shortcomings with X-ray scattering and light-element doping, the intersection of the fields is far from fully explored, and the academic and industrial interest is far from saturated. The application of established knowledge to new, industrially relevant, and academically interesting systems often yield the simplest and most rewarding investigations. There is still much improvement to be gained from the experimental design of established techniques. In the Conclusions section of each chapter, future work has been suggested, mainly as further experiments using the techniques and analyses already discussed. It is regrettable that key experiments for all three studies are still currently under analysis: thermal expansion of TiO_2 in argon, PDF analysis of post-mortem electrode material, and NPD analysis of sinusoidal accessibility by ammonia.

7.3.1.2 High quality instrumentation

An example of increasing the efficacy of light-element characterisation is in the collection of complementary data simultaneously. Here, most analyses of a material have been carried out separately of each other (exceptions being STEM/EDX/EELS, and in-operando SXPD/LIB), with sample reliability assumed and correlations asserted (as is common throughout the chemical sciences). Several beamlines now offer simultaneous collection of multiple techniques, such as DIAD at DLS (imaging and diffraction), BM23 at ESRF (diffraction and XAS), BL28XU at SPring-8 (XPS, diffraction, XAS), and 11.02 at ALS (imaging, XAS, diffraction).

The limitations of standard SXPD to identify light-elements against a highly-scattering framework are predominantly of contrast and flux. Provided there is some difference in scattering, it is poor counting statistics that result in poor contrast by the low signal-to-noise ratio and inaccurate peak shapes. Other properties such as beam-size and energy may also be relevant. With respect to ever improving instrumentation, we list here several instrumental/configurational improvements that are being made within the solid-state characterisation community at DLS.

The Diamond Light Source is being upgraded to Diamond-II in the next few years, collating requests and expertise from across the chemical sciences in order to keep increasing the bounds of observation, and providing evermore advanced techniques as standard. This upgrade is primarily of the storage ring, offering low emittance, increased capacity, and high energy. The upgrade proposed for the Versatile Soft X-ray beamline (VerSoX-II) is predicted to increase flux by over 100-times, yielding faster and higher quality data. The upgrade to the nano-ARPES beamline will decrease the beam spot size from 700 nm to <100 nm allowing characterisation of even smaller particles. The direct and selective analysis of the multi-phasic highly nitrogenated TiO_2 photocatalyst mixture would be ideal. New beamlines will also be created, with Coherent Soft X-ray Imagine and Diffraction offering imaging, ptychography, tomography, and coherent diffraction at 760-times the flux and 5-times the spatial resolution of the current analogous beamlines, allowing fast, real-time 3D reconstructions. This technique could help correlate electrochemical cycling of palladium nanoparticles with morphological volume and shape changes and electrode degradation with diffraction behaviour.

7.3.1.3 High quality samples

It is emphasised that the sample is often the limiting factor in advanced characterisation. For standard SXPD, if the sample is not crystalline enough (with respect to order or crystallite size), instrumental improvements will not be advantageous. The requirement of crystalline order for Bragg diffraction will never be overcome, nor does it need to be. In fact, in many cases it is an advantage to be phase-selective. Both the limitations and applications of powder diffraction will remain numerous.

It is also common for samples to be unreliably contrasting due to compositional uncertainty. Deficiencies in the scientist's assumptions about the composition or structure of a sample, or understanding of the system as a whole can also be limiting factors. As low-contrast sites yield so little changes to the parent structure, all larger contrast properties must be considered and fitted first, otherwise risking excellent fitting by an incorrect model. For example, if a low-contrast site is being refined against a series of overlapping peaks, the other phase must be well-defined first, which is entirely non-trivial. There is no such thing as a poor sample; it has just been poorly understood and poorly applied.

7.4 Final remarks

‘*It may be that this solution is not the final one.’*

Fritz Haber, accepting the 1918 Nobel Prize in Chemistry

Though, the materials and applications of the systems studied are varied, the theme of structural characterisation unites them. By using various X-ray scattering methods and complementary techniques, certain unknown aspects of their structure and performance have been elucidated. Looking to the future, this work has provided many avenues for further and adjacent research, many of which are in high impact sectors of high social relevance.

Beyond the value of this work from an academic perspective, it has been my aim to contribute to the alleviation of the alarming energy and climate crises through the chemical sciences. Academically, I am very proud of this work, and I also believe that it may offer a small contribution to our wider society. Thus, I am happy to conclude this thesis here.

Christopher Foo, April 2022

Appendices

List of Figures

Figure S3-1. Calibration of input temperature (hot air blower) to sample temperature by using the well-known thermal expansion of platinum metal. Experimental data in black; interpolated values in red. Curve of $x = y$ shown as black line. i

Table S3-1. Interpolated temperatures and error propagation by linear interpolated between two closest experimental values.Figure S3-2. Fluorescence over reference foils: (a) Gd M2-edge, and (b) Al K-edge. i

Figure S3-3. Experimental fluorescence spectrum (blue) and calibrated spectrum (red). Theoretical spectrum shown in black. ii

Figure S4-1. Laboratory-configuration XRD patterns of N-doped TiO_2 materials treated with ammonia at different temperatures; (a) pure phase anatase and, (b) P25. iii

Figure S4-2. Pawley fitting of P0 at room temperature. iii

Figure S4-3. (a) Change in lattice parameter from room temperature of anatase and rutile in P0 and P3. (b) Increase in tetragonality of the unit-cell, and hence coordination up to 450°C. iv

Figure S4-4. EPR spectra of P1 (a) aged in air; deactivated P1 re-calcined at various temperatures in (b) N_2, (c) liquid water, and (d) water vapour; reproduced from reference [43]. (e,f) Calculated energy barriers for photocatalytic water-splitting reaction calculated using activity against temperature, and oxygen-vacancy formation calculated using EPR data against temperature; reproduced from reference [1]. v

Figure S4-5. Pseudo-*I4$_1$/amd* unit cell within the pristine supercell. Planes of the new *I4$_1$/amd* faces: *a*: red, *b*: green, *c*: blue. vi

Figure S4-6. Fourier difference electron density map from using: (a) a standard titanium nitride phase, (b) a titanium oxynitride phase. The grey-scales are the same for both maps. Plane shown is at 0.25 *a* along (001). viii

Figure S5-1. TEM micrographs and STEM EDX micrographs of 50%Pd doped with a large excess of lithium 3.5eq. The low concentration of oxygen shows that the palladium is in the desired reduced metallic form. Lithium is not able to be mapped by EDX ix

Figure S5-2. The retention of expanded $Pd^{int}Li$ phase in in-situ lithiated 50%Pd after washing. ix

Figure S5-3. VT-SXPD heatmaps of in-situ lithiated palladium nanoparticles using various lithium equivalents (L to R: 0.2eq, 0.5eq, 1.5eq). x

Figure S5-4. VT-SXPD patterns of in-situ lithiated 50%Pd showing low-angle impurity peaks: strong CLS1 at 4.3° and other unindexed peaks. Black lines added to show disappearance of peaks or groups of peaks. xi

Figure S5-5. VT-SXPD patterns of in-situ lithiated 50%Pd showing emergent high-temperature, low-angle impurity peaks: CLS2. xi

Figure S5-6. Vegard occupancies of the pristine *cF* Pd for all samples, as well as the expanded $Pd^{int}Li$ for 0.2eq showing the small dip in occupancy at 150-250°C. (b) Total Vegard occupancies for Pd and $Pd^{int}Li$ (not included δ-contracted phases). xvi

Figure S5-7. Rietveld fitting of high-temperature SXPD patterns showing high-angle reflections (331), (420), (422), and (511). xvi

Figure S5-8. Fitting of peaks assigned to graphite at (a) 23° and (b) 8°. xvii

Figure S5-9. Change in intensity against cumulative potential. Smoothed by calculating change over four data points. xix

Figure S6-1. Adsorption geometries of Ag adsorption in ZSM-5, derived by SXPD. Reproduced from report by Lin et al.[75] (a) Space-fill viewed down *b*-axis (<010> zone axis) showing poor expected contrast against the framework. (b) Isolated absorption modes, viewed down the *a*-axis. xx

Figure S6-2. SSNMR characterisation. SSNMR spectra of pristine H-ZSM-5: (a) ^{1}H, (b) ^{27}Al, and (c) ^{29}Si. (b) 2D ^{31}P-^{31}P proton-driven spin diffusion SSNMR spectra of TMPO/H-ZSM-5 xxi

Figure S6-3. (a) Dependence of residual parameter R_{wp} on channel solvent atoms. (b) Rietveld fitting of far-from-edge pattern (15 keV) using two-solvent structure at 10^{-5} bar collected on I11, DLS. (c) Corresponding structure solution viewed down the a-axis; silicon: blue, framework oxygen: red, solvent oxygen: white. xxvi

Figure S6-4. (a) Absolute, and first and second derivative of experimental fluorescence spectra over the Al K-edge of reference aluminium foil and Z38 sample. Energies are uncalibrated. (b) Energy calibration and (c) 1D patterns around silicon K-edge, which suffer from significant absorption. xxviii

Figure S6-5. Observation of very weak (201) reflection which is shown to be dependent on the presence of aluminium and its siting. xxix

Figure S6-6. Simulated integrated intensities of the first 15 observed reflections at various energies for non-aluminium structure T0: (a) raw intensity, and (b) change in intensity from the previous energy pattern. xxix

Figure S6-7. Change in intensity relative to T0 over all structures, energies (five squares within each T-site column), and reflections: (a) linear, and (b) fractional change. xxx

Figure S6-8. Typical diffraction pattern yielded by RSXPD on I10: (a) raw 2D (left to right: 35-~90°), and (b) processed 1D. xxx

Figure S6-9. Integrated intensities of 45 reflections experimentally observed of ZSM-5 by RSXPD on I10. (a) Absolute intensity, no errors shown. (b) Change in intensity relative to lowest energy 1540 eV, errors shown. xxxi

Figure S6-10. Aluminium occupancy by RSXPD without constraint on total occupancy. xxxii

Figure S6-11. Preliminary investigation of atomic-resolution EELS to directly visualise the aluminium site in ZSM-5. xxxii

Figure S6-12. Raw intensity of each reflection for each structure. Intensity plotted against (a) linear, and (b) logarithmic colour scales. The five experimental energies from the main RSXPD experiment are shown as five segments within each column. The reflections within the region analysed for DANES/DAFS is shown within black box. xxxiii

Figure S6-13. (a) RSXPD patterns as contour plots. (b) Integrated intensities as derived by Pawley refinement. xxxiv

List of Tables

Table S3-1. Interpolated temperatures and error propagation by linear interpolated between two closest experimental values.Figure S3-2. Fluorescence over reference foils: (a) Gd M2-edge, and (b) Al K-edge. i

Table S4-1. Absolute lattice parameters and errors from Pawley refinement of VT-SXPD P0 and P3. iv

Table S4-2. Linear thermal expansion coefficients and errors (all $\times 10^{-6}$) from Pawley refinement of VT-SXPD P0 and P3. v

Table S4-3. Change in geometry of four-membered rings after oxygen abstraction. vi

Table S4-4. Bond lengths of under-coordinated titanium sites. vi

Table S4-5. Structural information for Rietveld refinements of A4 using an anatase and titanium nitride phase. vii

Table S4-6. Rietveld refinement of A4 VT-SXPD. vii

Table S5-1. Rietveld refinement of VT-SXPD of in-situ lithiated 50%Pd/C. xii

Table S5-2. Tabulated labelling and schematic representation of in-operando phase transitions with respect to intensity. xviii

Table S5-3. Tabulated potential and intensity ranges of in-operando phase transitions. xviii

Table S6-1. Observations of Ag-absorption in the straight channel of ZSM-5 by viewing down <010>. xx

Table S6-2. Atomic parameters from the Rietveld refinement of TMPO/H-ZSM-5 measured at 25 °C based on SXRD data. xxii

Table S6-3. Atomic parameters from the Rietveld refinement of TMPO/H-ZSM-5 measured at 25 °C based on NPD data. xxiii

Table S6-4**.** DFT-optimised bond lengths of TMPO adsorbed on BAS: Al substitution at T6, T8, and T12 sites. xxiv

Table S6-5. Structural information derived from Rietveld fitting at far-from-edge energy. xxvi

Table S6-6. Atomic coordinates of Rietveld refinement of Z38 at 15 keV (I11) using a two-solvent-atom structure. Errors and occupancies also shown. xxvii

Table S6-7. Distance of total extinction of beam through different media. xxviii

Table S6-8. Angle-dependent parameters as refined by Pawley and Rietveld refinement for the five RSXPD patterns. xxxi

Chapter 3: Experimental procedures

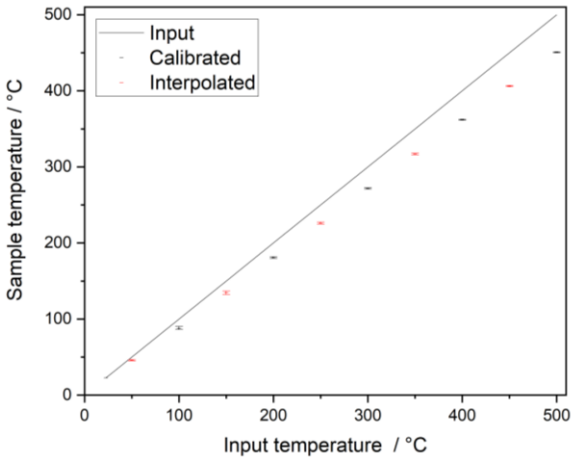


Figure S3-1. Calibration of input temperature (hot air blower) to sample temperature by using the well-known thermal expansion of platinum metal. Experimental data in black; interpolated values in red. Curve of $x = y$ shown as black line.

Table S3-1. Interpolated temperatures and error propagation by linear interpolated between two closest experimental values.

Input temperature / °C	Fraction between calibrated points	Experimental interval / °C	Temp. above lower point / °C	Interpolated temperature / °C
50	0.355	66(2)	23.3(7)	45.8(7)
150	0.500	93(2)	46(1)	134(2)
250	0.500	91(1)	45.5(7)	226(1)
350	0.500	90(1)	45.1(5)	317(1)
450	0.500	89(1)	44.3(5)	406.2(8)

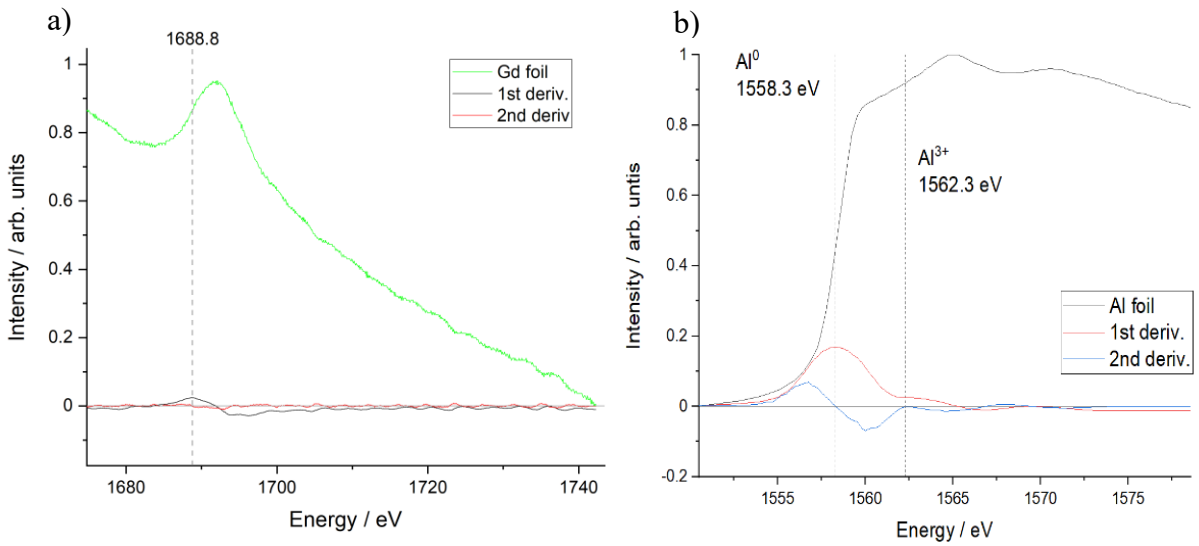


Figure S3-2. Fluorescence over reference foils: (a) Gd M2-edge, and (b) Al K-edge.

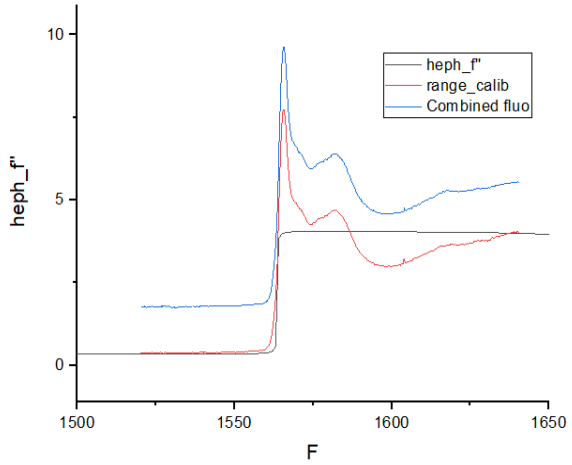


Figure S3-3. Experimental fluorescence spectrum (blue) and calibrated spectrum (red). Theoretical spectrum shown in black.

Chapter 4: TiO_2

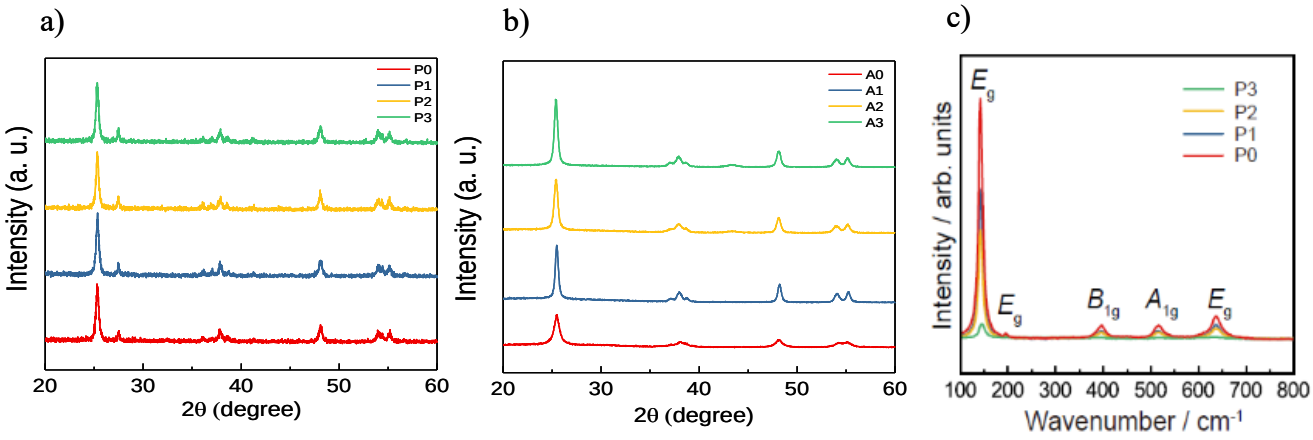


Figure S4-1. Laboratory-configuration XRD patterns of N-doped TiO_2 materials treated with ammonia at different temperatures; (a) pure phase anatase and, (b) P25.

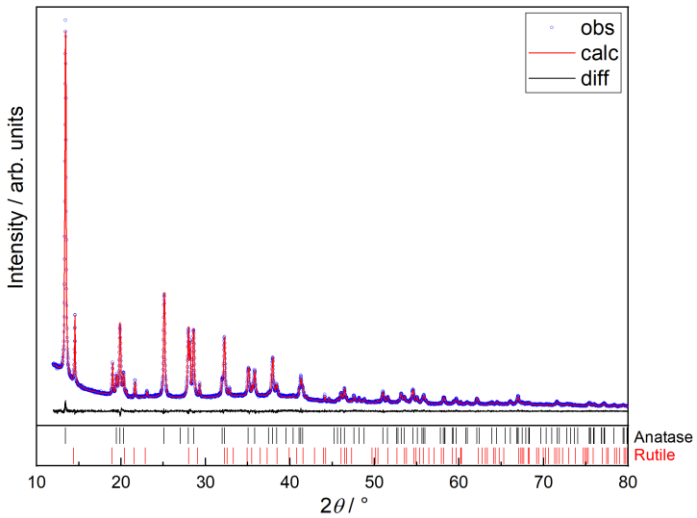


Figure S4-2. Pawley fitting of P0 at room temperature.

Table S4-1. Absolute lattice parameters and errors from Pawley refinement of VT-SXPD P0 and P3.

P0

Temp / °C	R_{wp} / %	GoF	Ana *a* / Å	Ana *c* / Å	Rut *a* / Å	Rut *c* / Å
22.5	3.83	1.19	3.78534(6)	9.5073(2)	4.59395(8)	2.95877(8)
45.8	3.74	1.16	3.78575(6)	9.5088(2)	4.59455(8)	2.95945(8)
88.3	3.81	1.20	3.78647(6)	9.5114(2)	4.59628(8)	2.96075(8)
135.6	3.83	1.19	3.78733(6)	9.5147(2)	4.59780(8)	2.96203(9)
180.7	3.82	1.19	3.78817(6)	9.5186(2)	4.59943(8)	2.96357(9)
225.3	3.78	1.18	3.78889(6)	9.5248(2)	4.60101(9)	2.96505(9)
270.7	3.73	1.17	3.78965(6)	9.5307(2)	4.60284(9)	2.96622(9)
315.1	3.70	1.16	3.79057(6)	9.5360(2)	4.60446(9)	2.96766(9)
360.8	3.73	1.16	3.79152(6)	9.5411(2)	4.60615(9)	2.9689(1)
404.9	3.71	1.15	3.79246(6)	9.5463(2)	4.60778(9)	2.9702(1)
449.2	3.67	1.14	3.79340(6)	9.5515(2)	4.60953(9)	2.9716(1)

P3

Temp / °C	R_{wp} / %	GoF	Ana *a* / Å	Ana *c* / Å	Rut *a* / Å	Rut *c* / Å
22.5	3.97	1.51	3.78536(6)	9.5070(2)	4.59404(9)	2.95864(8)
45.8	3.94	1.47	3.78576(6)	9.5082(2)	4.59485(9)	2.95940(9)
88.3	3.81	1.50	3.78650(6)	9.5105(2)	4.59631(9)	2.96070(9)
135.6	4.04	1.51	3.78737(6)	9.5137(2)	4.59800(9)	2.9621(1)
180.7	3.97	1.48	3.78820(6)	9.5184(2)	4.5996(1)	2.9634(1)
225.3	3.95	1.47	3.78880(6)	9.5251(2)	4.6014(1)	2.9648(1)
270.7	3.96	1.47	3.78957(7)	9.5311(2)	4.6029(1)	2.9662(1)
315.1	3.86	1.47	3.79049(7)	9.5362(2)	4.6045(1)	2.9674(1)
360.8	4.02	1.44	3.79147(7)	9.5415(2)	4.6062(1)	2.9689(1)
404.9	3.97	1.47	3.79244(7)	9.5465(2)	4.6078(1)	2.9701(1)
449.2	3.99	1.48	3.79333(7)	9.5517(2)	4.6093(1)	2.9715(1)

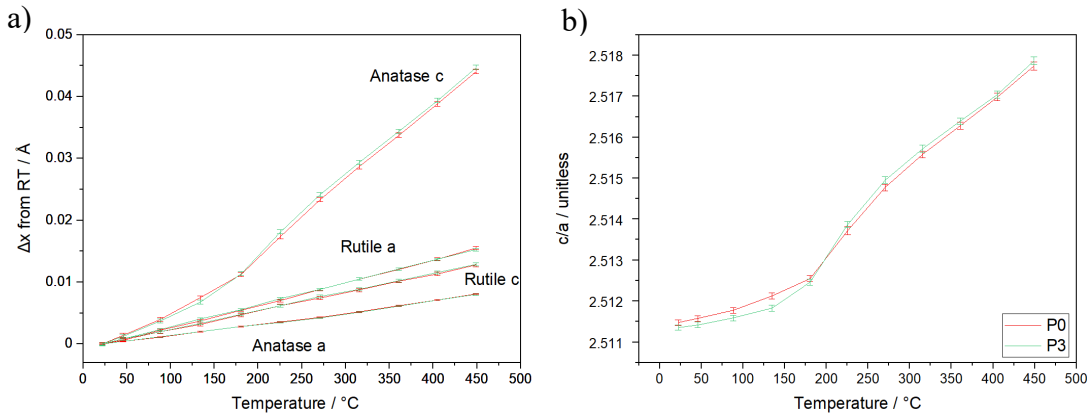


Figure S4-3. (a) Change in lattice parameter from room temperature of anatase and rutile in P0 and P3. (b) Increase in tetragonality of the unit-cell, and hence coordination up to 450°C.

Table S4-2. Linear thermal expansion coefficients and errors (all $\times 10^{-6}$) from Pawley refinement of VT-SXPD P0 and P3.

Temperature / °C	P0 *a* / °C^{-1}	P0 *c* / °C^{-1}	P3 *a* / °C^{-1}	P3 *c* / °C^{-1}
34.1	4.6(9)	6(1)	4(1)	5(1)
66.9	4.5(5)	6.5(7)	4.6(6)	5.8(8)
111.2	4.9(6)	7.6(7)	5.0(6)	7.2(8)
157.5	4.8(5)	8.9(7)	4.7(6)	10.7(9)
203.4	4.1(5)	14.2(8)	3.5(5)	16.1(9)
249.0	4.4(5)	13.8(7)	4.4(6)	13.2(8)
294.2	5.4(5)	12.3(7)	5.4(6)	11.7(8)
339.3	5.5(5)	12.0(7)	5.8(6)	12.3(8)
384.1	5.6(5)	12.3(7)	5.8(6)	11.9(8)
428.4	5.6(5)	12.2(7)	5.3(6)	12.4(8)

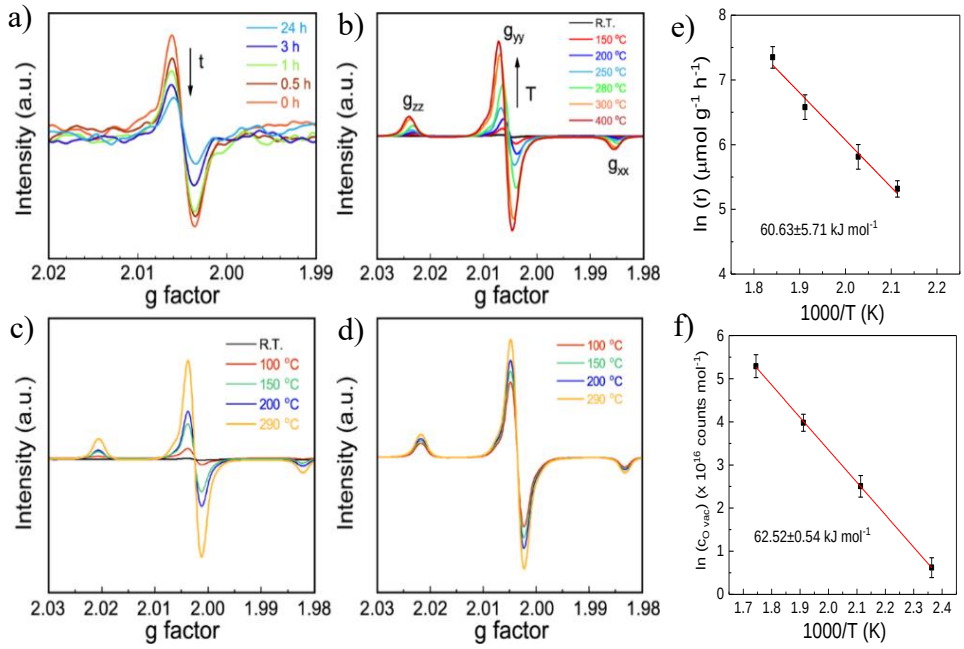


Figure S4-4. EPR spectra of P1 (a) aged in air; deactivated P1 re-calcined at various temperatures in (b) N_2, (c) liquid water, and (d) water vapour; reproduced from reference [43]. (e,f) Calculated energy barriers for photocatalytic water-splitting reaction calculated using activity against temperature, and oxygen-vacancy formation calculated using EPR data against temperature; reproduced from reference [1].

Table S4-3. Change in geometry of four-membered rings after oxygen abstraction.

	P1 plane of 4M-ring	Pristine θ[Ti-O-Ti] / °	Vacancy θ[Ti-O_{int}-Ti] / °	Difference $\Delta\theta$[Ti-O-Ti] / °
V_{Os1}	*ab*	94.2	130.5	36.3
V_{Os2}	*ab*	102.2	138.4	36.2
V_{Os3}	*ac*	103.9	124.3	20.4
V_{Oss3}	*ac*	97.7	169.9	72.2

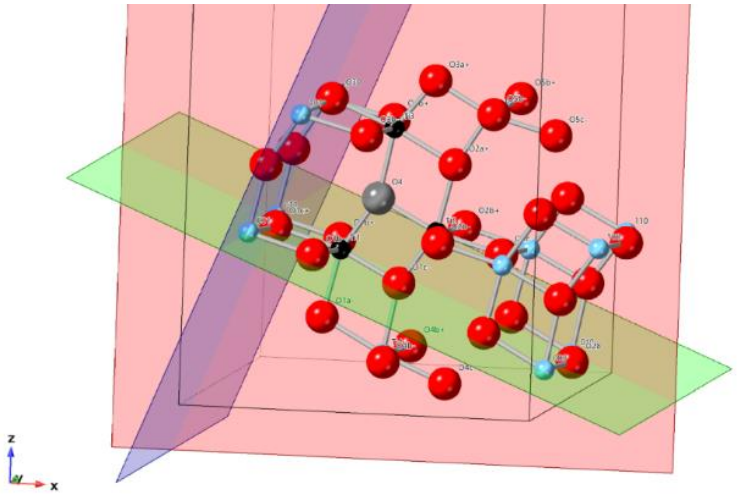


Figure S4-5. Pseudo-*I4₁/amd* unit cell within the pristine supercell. Planes of the new *I4₁/amd* faces: *a*: red, *b*: green, *c*: blue.

Table S4-4. Bond lengths of under-coordinated titanium sites.

Central metal site	Bond direction	Pristine / Å	V_{Oss3} / Å	Δ / Å	strain / unitless
Ti_{ss1}	*a*	2.069	1.900	-0.169	-0.0817
	b	1.935	1.919	-0.016	-0.0083
		1.935	1.919	-0.016	-0.0083
	c	2.023	1.959	-0.064	-0.0316
	a/*c*	1.961	1.809	-0.152	-0.0775
Ti_{ss2}	*a*	2.066	1.917	-0.149	-0.0721
	b	1.935	1.92	-0.015	-0.0078
		1.935	1.919	-0.016	-0.0083
	c	2.022	1.931	-0.091	-0.0450
	a/*c*	1.88	1.828	-0.052	-0.0277
Ti_{s1}	*a*	1.864	1.824	-0.040	-0.0215
	b	1.933	1.913	-0.020	-0.0103
		1.933	1.913	-0.020	-0.0103
	c	2.042	1.972	-0.070	-0.0343
		2.071	2.071	0.000	0
Ti_{b2}	*a*	2.15	3.684	1.534	0.7135
	b	1.932	1.913	-0.019	-0.0098
		1.932	1.911	-0.021	-0.0109
	c	2.071	2.077	0.006	0.0029
		2.026	1.972	-0.054	-0.0267

Table S4-5. Structural information for Rietveld refinements of A4 using an anatase and titanium nitride phase.

	structural model	$Ti^{3+}N$	$Ti^{3+}N^{3-}(O^{2-})$	$Ti^{3+}N^{3-}(O^{2-})O_{int}$
residuals	R_{wp} / %	3.380	3.387	3.348
	R_{exp} / %	1.707	1.707	1.706
	GoF	1.980	1.985	1.962
anatase	space group		$I4_1/amd$	
	lpa / Å	3.78517(1)	3.78517(1)	3.7851(1)
	lpc / Å	9.51065(6)	9.51065(6)	9.5107(3)
	volume / Å^3	136.264(1)	136.264(1)	136.265(1)
	composition / %wt.	67.55(5)	67.00(5)	66.36(6)
	oxygen coordinate, O_z	0.20767(6)	0.20770(6)	0.20746(6)
	Ti beq / Å^2	0.414(6)	0.416(6)	0.420(6)
	O beq / Å^2	0.52(1)	0.50(1)	0.509(1)
TiN/TiNO	space group		$Fm\bar{3}m$	
	lpa / Å	4.184230(3)	4.184230(3)	4.1843(1)
	volume / Å^3	73.260(1)	73.260(1)	73.262(1)
	composition / %wt	32.45(5)	33.90(5)	33.64(6)
	Ti coordinates		(0, 0, 0)	
	Ti occ.	0.9998(8)	0.9021(7)	0.9507(8)
	Ti beq / Å^2	0.76(1)	0.77(1)	0.80(1)
	N coordinates		(0, 0, 0.5)	
	N occ.	1.476(4)	1.010(3)	1.076(3)
	N beq / Å^2	0.87(2)	0.50(2)	0.56(2)
	O coordinates		(0.25, 0.25, 0,25)	
	O occ.			0.030(3)
	O beq / Å^2			0.0(4)

Table S4-6. Rietveld refinement of A4 VT-SXPD.

Temperature / °C	R_{wp} / %	GoF	Anatase *a* / Å	Anatase / %wt	$TiNO_x$ *a* / Å	$TiNO_x$ / %wt	Ti occ.	N occ.	O occ.
22	3.38	1.97	3.7852(1)	66.4 (2)	4.1843(1)	33.61(6)	0.95(3)	1.08(3)	0.03(3)
40	3.33	1.94	3.7855(1)	65.6 (2)	4.1849(1)	34.36 (6)	0.92(3)	1.04(3)	0.03(3)
60	3.37	1.97	3.7858(1)	66.0(2)	4.1855(1)	34.03(6)	0.93(3)	1.05(3)	0.03(3)
80	3.34	1.94	3.7862(1)	65.8(2)	4.1861(1)	34.21(6)	0.92(3)	1.04(3)	0.03(3)
100	3.33	1.94	3.7865(1)	66.0 (2)	4.1866(1)	33.96(6)	0.93(3)	1.06(3)	0.03(3)
120	3.35	1.95	3.7869(1)	65.8 (2)	4.1871(1)	34.20 (6)	0.92(3)	1.05(3)	0.03(3)
140	3.32	1.93	3.7872(1)	65.9 (2)	4.1876(1)	34.06 (6)	0.92(3)	1.05(3)	0.03(3)
160	3.30	1.92	3.7876(1)	66.4(2)	4.1881(1)	33.60 (6)	0.93(3)	1.05(3)	0.03(3)
180	3.25	1.89	3.7880(1)	65.8 (2)	4.1886(1)	34.18 (6)	0.91(3)	1.03(3)	0.03(3)
200	3.17	1.84	3.7884(1)	65.9 (2)	4.1889(3)	34.09 (6)	0.90(3)	1.03(3)	0.03(3)
220	3.16	1.84	3.7887(1)	66.1 (2)	4.1893(1)	33.90 (6)	0.90(3)	1.02(3)	0.03(3)
240	3.12	1.81	3.7890(1)	66.1 (2)	4.1895(1)	33.90(6	0.89(3)	1.02(3)	0.03(3)
260	3.04	1.77	3.7894(1)	66.6(2)	4.1896(1)	33.41(6)	0.90(3)	1.04(3)	0.04(3)
280	2.99	1.74	3.7897(1)	68.0(2)	4.1896(1)	32.03(6)	0.94(3)	1.08(3)	0.04(3)
300	2.96	1.71	3.7901(1)	68.1(2)	4.1895(1)	31.90(6)	0.92(3)	1.08(3)	0.04(3)
320	2.91	1.69	3.7904(1)	68.2(2)	4.1893(1)	31.84 (6)	0.90(3)	1.06(3)	0.04(3)
340	2.88	1.68	3.7907(1)	69.1 (2)	4.1889(1)	30.92(6)	0.90(3)	1.08(3)	0.04(3)
360	2.81	1.63	3.7912(1)	69.6(2)	4.1886(1)	30.43 (6)	0.87(3)	1.06(3)	0.05(3)
380	2.76	1.61	3.7916(1)	71.7(2)	4.1881(1)	28.31 (7)	0.90(3)	1.11(3)	0.05(3)
400	2.79	1.62	3.7921(1)	73.5(2)	4.1876(1)	26.54(7)	0.86(3)	1.08(3)	0.04(3)
420	2.81	1.63	3.7925(1)	76.2(2)	4.1871(1)	23.78(7)	0.84(3)	1.08(3)	0.04(4)
440	2.89	1.68	3.7930(1)	79.8(2)	4.1868(1)	20.22(9)	0.81(3)	1.04(3)	0.03(5)
460	3.02	1.76	3.7934(1)	84.8(2)	4.1864(1)	15.2(1)	0.80(3)	1.04(3)	0.02(7)
480	3.18	1.84	3.7938(1)	86.5(2)	4.1857(2)	13.5(1)	0.69(3)	0.91(3)	0.2(2)
500	3.40	1.94	3.7942(1)	92.4(2)	-	-	-	-	-
520	3.46	2.00	3.7947(1)	89.2 (2)	-	-	-	-	-
540	3.31	1.93	3.7951(1)	83.5(2)	-	-	-	-	-
560	3.24	1.89	3.7955(1)	79.5(2)	-	-	-	-	-
580	3.23	1.88	3.7958(1)	84.2(2)	-	-	-	-	-

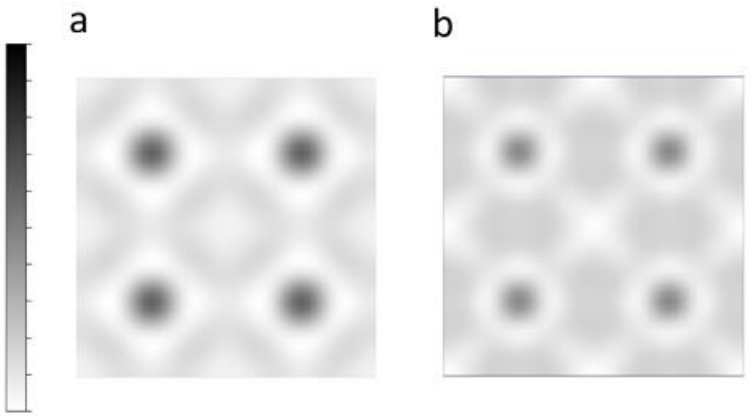


Figure S4-6. Fourier difference electron density map from using: (a) a standard titanium nitride phase, (b) a titanium oxynitride phase. The grey-scales are the same for both maps. Plane shown is at 0.25 *a* along (001).

Chapter 5: Palladium

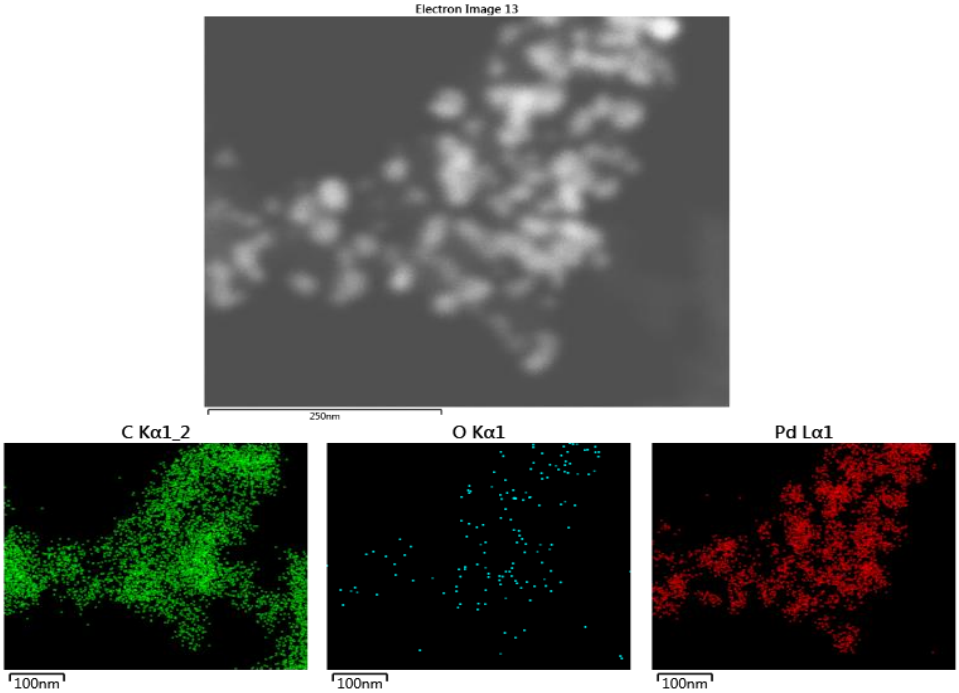


Figure S5-1. TEM micrographs and STEM EDX micrographs of 50%Pd doped with a large excess of lithium 3.5eq. The low concentration of oxygen shows that the palladium is in the desired reduced metallic form. Lithium is not able to be mapped by EDX

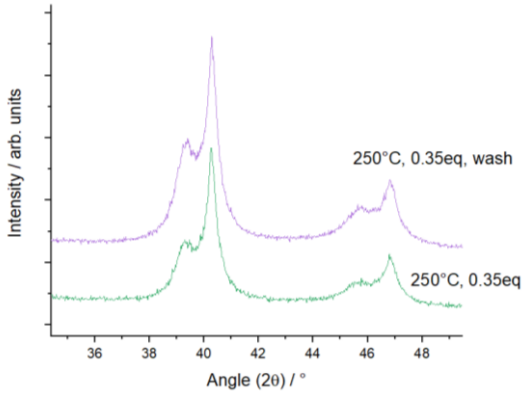


Figure S5-2. The retention of expanded $Pd^{int}Li$ phase in in-situ lithiated 50%Pd after washing.

VT-SXPD of in-situ lithiated palladium nanoparticles

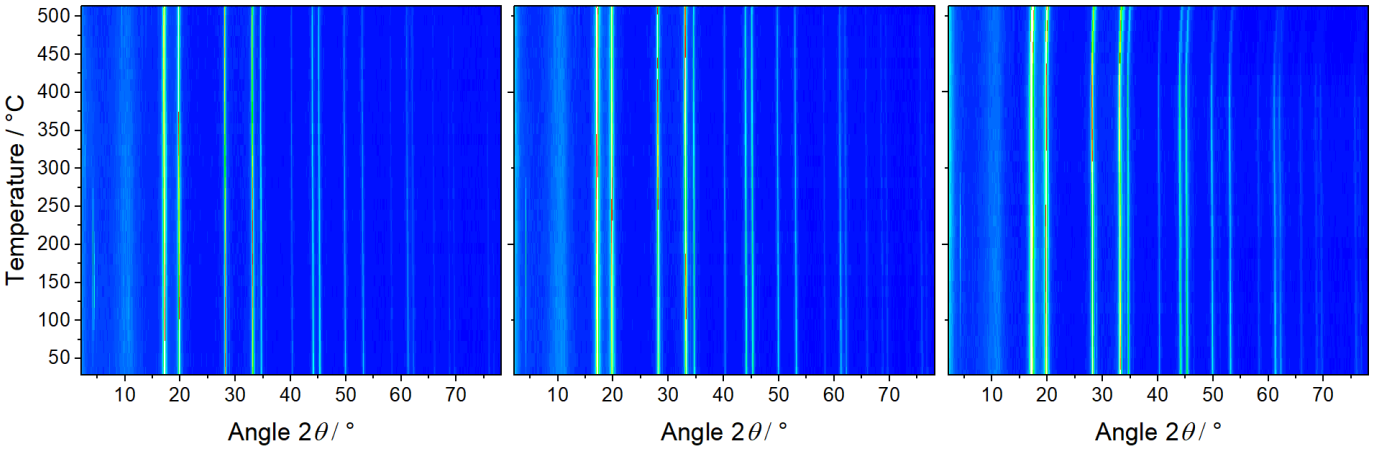


Figure S5-3. VT-SXPD heatmaps of in-situ lithiated palladium nanoparticles using various lithium equivalents (L to R: 0.2eq, 0.5eq, 1.5eq).

Low-angle impurity phase for in-situ lithiated palladium by SXPD

There is a strong low-angle reflection observed in the 0.2eq patterns at 4.27° between room temperature and 302°C. It is completely unobserved at 316°C. The reflection is also observed for the other lithiated materials but not for the pristine sample, indicating that it is some crystalline lithium side-product (CLS1) (Figure S5-4). This peak becomes unobserved at 316°C, 310°C, and 295°C for the samples increasing in lithiation, respectively. For the 0.5eq and 1.5eq materials some other weak reflections are observed at 2.8°, 4.93°, 6.52°, and 11.3°. And for the 1.5eq, many more low-angle peaks are observed. All of these peaks disappear at differing temperatures, and due to the general weakness it is difficult to discern if this is due to destruction of the phase, or the intensity just dropping below the background. No information could be extracted from this by indexing or individual thermal stability.

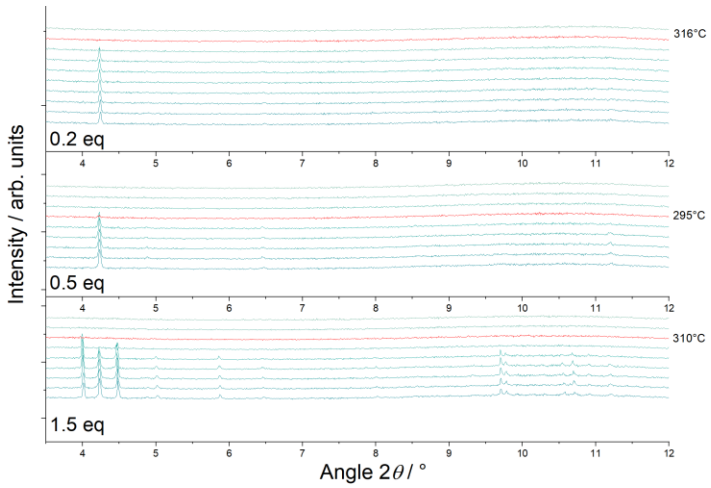


Figure S5-4. VT-SXPD patterns of in-situ lithiated 50%Pd showing low-angle impurity peaks: strong CLS1 at 4.3° and other unindexed peaks. Black lines added to show disappearance of peaks or groups of peaks.

Between 9° and 15°, another unidentified crystalline lithium side-product emerges at high temperature. This is attributed to the presence of another higher lithium content side-product (CLS2). These reflections have also not been indexed, with no coincidence with known palladium-lithium structures (Figure S5-5).

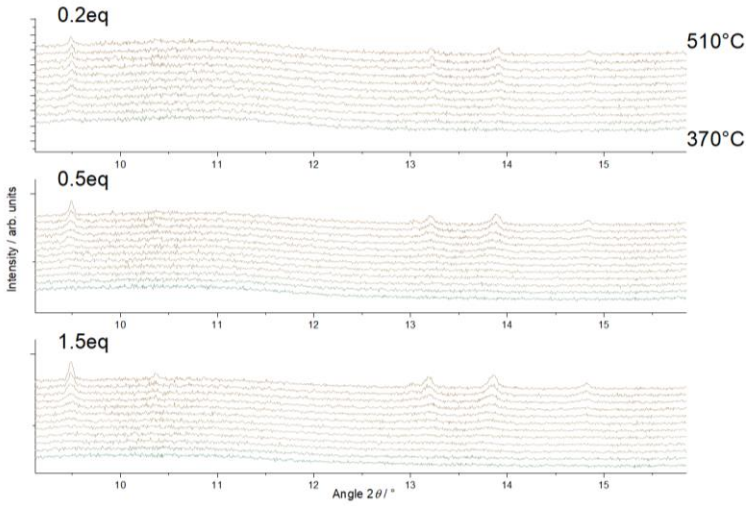


Figure S5-5. VT-SXPD patterns of in-situ lithiated 50%Pd showing emergent high-temperature, low-angle impurity peaks: CLS2.

Table S5-1. Rietveld refinement of VT-SXPD of in-situ lithiated 50%Pd/C.

0.2eq

Temperature / °C	GoF	Pd / Å	Pd / %wt	$Pd^{int}Li$ / Å	$Pd^{int}Li$ / %wt	Emergent $Pd^{int}Li$ / Å	Emergent $Pd^{int}Li$ / %wt
28	1.412	3.8995(3)	3.99739(3)	6.6(1)	93.4(1)	-	-
49	1.391	3.9000(3)	3.99796(3)	6.6(1)	93.4(1)	-	-
65	1.378	3.9007(3)	3.99855(3)	6.6(1)	93.4(1)	-	-
80	1.355	3.9015(3)	3.99913(3)	6.5(1)	93.5(1)	-	-
94	1.355	3.9021(3)	3.99968(3)	6.5(1)	93.5(1)	-	-
109	1.354	3.9027(3)	4.00025(3)	6.5(1)	93.5(1)	-	-
123	1.358	3.9031(3)	4.00074(3)	6.5(1)	93.5(1)	-	-
137	1.337	3.9039(3)	4.00122(3)	6.5(1)	93.5(1)	-	-
152	1.332	3.9046(3)	4.00169(3)	6.7(1)	93.3(1)	-	-
166	1.294	3.9057(3)	4.00198(3)	6.9(1)	93.1(1)	-	-
181	1.369	3.9062(3)	4.00209(3)	7.3(1)	92.7(1)	-	-
194	1.399	3.9082(3)	4.00189(3)	8.5(1)	91.5(1)	-	-
209	1.494	3.9099(2)	4.00182(3)	9.5(1)	90.5(1)	-	-
224	1.513	3.9112(2)	4.00185(3)	9.4(1)	90.6(1)	-	-
238	1.494	3.9121(3)	4.00237(3)	8.7(1)	91.3(1)	-	-
252	1.441	3.9128(3)	4.0031(3)	8.1(1)	91.9(1)	-	-
267	1.426	3.9142(3)	4.00401(3)	7.6(1)	92.4(1)	-	-
281	1.440	3.9154(3)	4.00505(3)	70(1)	93.0(1)	-	-
295	1.460	3.9165(3)	4.00606(3)	6.6(1)	93.4(1)	-	-
309	1.483	3.9178(4)	4.00755(3)	5.8(1)	94.2(1)	-	-
324	1.399	3.9187(4)	4.00876(3)	5.5(1)	94.5(1)	-	-
338	1.398	3.9198(4)	4.00956(3)	4.9(1)	95.1(1)	-	-
352	1.386	3.9210(4)	4.01013(3)	4.7(1)	95.3(1)	-	-
367	1.322	3.9220(4)	4.01065(3)	4.6(1)	95.4(1)	-	-
381	1.318	3.9234(4)	4.01108(3)	4.4(1)	95.6(1)	-	-
395	1.306	3.9255(5)	4.01141(3)	4.4(1)	95.6(1)	-	-
409	1.326	3.9273(5)	4.01162(3)	4.3(1)	95.7(1)	-	-
423	1.414	3.9305(4)	4.0109(3)	5.0(1)	95.0(1)	-	-
438	1.508	3.9367(4)	4.00943(4)	6.6(1)	93.4(1)	-	-
452	1.429	3.9330(4)	4.00901(7)	8.1(2)	79.4(4)	4.00901(7)	12.5(3)
466	1.266	3.9370(3)	4.0091(1)	12.7(2)	48.6(6)	4.0091(1)	38.7(6)
480	1.202	3.9366(2)	4.0103(3)	16.8(3)	22.7(8)	4.0103(3)	60.4(8)
495	1.093	3.9302(3)	3.99091(9)	13.9(3)	67.7(6)	3.99091(9)	18.4(6)
509	1.045	3.9276(2)	3.9854(1)	20.2(4)	45.4(8)	3.9854(1)	34.4(8)
513	1.023	3.9229(2)	3.9786(2)	27.3(5)	37.8(8)	3.9786(2)	35.0(7)

0.5eq

Temperature / °C	GoF	Pd / Å	Pd / %wt	$Pd^{int}Li$ / Å	$Pd^{int}Li$ / %wt	Emergent $Pd^{int}Li$ / Å	Emergent $Pd^{int}Li$ / %wt
28	1.182	3.8990(2)	3.99806(3)	3.57(8)	96.43(8)	-	-
49	1.204	3.8997(2)	3.99885(3)	3.48(8)	96.52(8)	-	-
65	1.180	3.9005(2)	3.99946(3)	3.43(8)	96.57(8)	-	-
80	1.157	3.9012(2)	3.99996(3)	3.55(9)	96.46(9)	-	-
94	1.180	3.9020(2)	4.00051(3)	3.55(8)	96.45(8)	-	-
109	1.179	3.9023(2)	4.00106(3)	3.41(8)	96.59(8)	-	-
123	1.161	3.9033(2)	4.00158(3)	3.57(8)	96.44(8)	-	-
137	1.146	3.9038(2)	4.00213(3)	3.63(9)	96.37(9)	-	-
152	1.174	3.9046(2)	4.00265(3)	3.63(9)	96.37(9)	-	-
166	1.176	3.9053(2)	4.00327(3)	3.53(8)	96.47(8)	-	-
181	1.140	3.9064(2)	4.00404(3)	3.44(9)	96.56(9)	-	-
194	1.187	3.9074(2)	4.00470(3)	3.23(8)	96.77(8)	-	-
209	1.167	3.9081(2)	4.00545(3)	3.10(8)	96.90(8)	-	-
224	1.131	3.9089(3)	4.00614(3)	3.04(9)	96.96(9)	-	-
238	1.161	3.9093(3)	4.00671(3)	2.87(8)	97.13(8)	-	-
252	1.151	3.9103(3)	4.00718(3)	2.90(8)	97.10(8)	-	-
267	1.148	3.9113(3)	4.00775(3)	2.79(9)	97.21(9)	-	-
281	1.190	3.912(3)	4.00841(3)	2.68(8)	97.32(8)	-	-
295	1.161	3.9133(3)	4.00912(3)	2.63(8)	97.37(8)	-	-

Temperature / °C	GoF	Pd / Å	Pd / %wt	$Pd^{int}Li$ / Å	$Pd^{int}Li$ / %wt	Emergent $Pd^{int}Li$ / Å	Emergent $Pd^{int}Li$ / %wt
309	1.163	3.9146(3)	4.00981(3)	2.55(9)	97.46(9)	-	-
324	1.169	3.9156(3)	4.01046(3)	2.47(8)	97.53(8)	-	-
338	1.169	3.9188(3)	4.01114(3)	2.28(8)	97.72(8)	-	-
352	1.182	3.9216(3)	4.0118(3)	2.05(8)	97.95(8)	-	-
367	1.274		4.01238(3)		100	-	-
381	1.250		4.01286(3)		100	-	-
395	1.249		4.01337(3)		100	-	-
409	1.252		4.01387(3)		100	-	-
423	1.265		4.01433(3)		100	-	-
438	1.236		4.01462(3)		100	-	-
452	1.231		4.01479(3)		100	-	-
466	1.239		4.0148(3)		100	-	-
480	1.246		4.01485(3)		100	-	-
495	1.309		4.01465(3)		100	-	-
509	1.450		4.01385(3)		100	-	-
513	1.766		4.01448(3)		41.5(8)	3.9923(4)	58.5(8)

1.5eq

Temperature / °C	GoF	Pd / Å	Pd / %wt	$Pd^{int}Li$ / Å	$Pd^{int}Li$ / %wt	Emergent $Pd^{int}Li$ / Å	Emergent $Pd^{int}Li$ / %wt
28	1.079	3.8985(2)	4.2(1)	3.99800(3)	95.8(1)		
49	1.100	3.8994(2)	4.2(1)	3.99882(3)	95.8(1)		
65	1.065	3.9003(2)	4.0(1)	3.99941(3)	96.0(1)		
80	1.041	3.9008(2)	4.2(1)	3.99993(3)	95.8(1)		
94	1.050	3.9014(2)	4.2(1)	4.00049(3)	95.8(1)		
109	1.074	3.9023(2)	4.4(1)	4.00108(3)	95.6(1)		
123	1.050	3.9030(2)	4.3(1)	4.00169(3)	95.7(1)		
137	1.033	3.9039(2)	4.4(1)	4.00215(3)	95.6(1)		
152	1.054	3.9041(2)	4.5(1)	4.00273(3)	95.5(1)		
166	1.043	3.9054(2)	4.1(1)	4.00348(3)	95.9(1)		
181	1.050	3.9065(2)	4.1(1)	4.00417(3)	95.9(1)		
194	1.038	3.9075(2)	3.8(1)	4.00482(3)	96.2(1)		
209	1.026	3.9085(2)	3.9(1)	4.00543(3)	96.1(1)		
224	1.035	3.9094(2)	3.9(1)	4.00598(3)	96.1(1)		
238	1.046	3.9101(2)	3.7(1)	4.00662(3)	96.3(1)		
252	1.029	3.9108(2)	3.6(1)	4.00725(3)	96.4(1)		
267	1.061	3.9116(2)	3.5(1)	4.00797(3)	96.5(1)		
281	1.063	3.9128(3)	3.2(1)	4.00871(3)	96.8(1)		
295	1.054	3.9142(3)	3.0(1)	4.00949(3)	97.0(1)		
309	1.073	3.9160(3)	2.7(1)	4.01023(3)	97.3(1)		
324	1.089	3.9178(3)	2.5(1)	4.01094(3)	97.5(1)		
338	1.084	3.9207(4)	2.26(9)	4.01156(3)	97.74(9)		
352	1.074	3.9236(4)	1.90(9)	4.01221(3)	98.10(9)		
367	1.140			4.01280(3)	100		
381	1.154			4.01335(3)	100		
395	1.147			4.01389(3)	100		
409	1.127			4.01427(3)	100		
423	1.154			4.01457(3)	100		
438	1.152			4.01478(3)	100		
452	1.167			4.01500(3)	100		
466	1.180			4.01502(3)	100		
480	1.206			4.01515(3)	100		
495	1.337			4.01499(3)	100		
509	1.491			4.01435(3)	100		
513	1.679			4.01521(3)	44.2(7)	3.9937(3)	55.8(7)

Vegard's law

In order to use Vegard's law in this way, thermal expansion of the start- and end-points must be defined: zero-occupancy Pd (taken from the pristine Pd control sample presented with respect to incidental carbon) and the wholly lithiated $Pd^{int}Li$ (show to be stable in 0.5eq and 1.5eq). As stated, in all of the metrics presented herein the expanded $Pd^{int}Li$ phase for both 0.5eq and 1.5eq are almost entirely coincident with each other. The effect of thermal expansion on $Pd^{int}Li$ is taken from the 1.5eq phase. In order to define these, three assumptions are made.

(1) The interstitial lithium occupancy of the maximally lithiated $Pd^{int}Li$, is ~0.15: reasonable.

(2) The pristine Pd control phase is completely unlithiated at high temperature: reasonable.

(3) The $Pd^{int}Li$ phase remains maximally lithiated at 0.15 occupancy at 513°C: known to be inaccurate.

The maximum occupancy of the $Pd^{int}Li$ is unclear, but this estimate is sufficient for relative comparison of lattice parameter changes. Assumption (3) is largely reasonable because the expanded $Pd^{int}Li$ is largely stable at the highest temperature for 0.5eq/1.5eq. However, due to the start of a small decrease in lattice parameter in the final few patterns, which is attributed to delithiation. This assumption is known to be inaccurate. But in order to estimate the chemical effect of temperature, this assumption is deemed valid enough. Evidently, if the occupancy of the expanded phase is assumed to be 0.15 throughout the temperature range, then any increase in lattice parameter of other phases will result in a total

Vegard occupancy of more than 0.15 (also true of 0.5eq which has very similar expanded phase behaviour) (Figure S5-6). This is an artefact of the calculation method and assumptions.

Using Equation 5-1, Vegard occupancies are calculated for the pristine Pd phases for all samples, as well as the expanded $Pd^{int}Li$ for 0.2eq that is observed to undergo appreciable delithiation/high-angle shift above 400C.

$$a(T,Pd^{int}Li_x) = (1-x/0.15)\ a(T,Pd) + x/0.15\ a(T,Pd^{int}Li_{0.15})$$

Equation 5-1. Vegard's law applied to $Pd^{int}Li$ at any given temperature by using experimentally observed thermal expansion of end-phases.

Due to the way these values are calculated, the trends are largely carried over from the relative lattice-parameter changes; instead of being relative to room temperature these values are relative to the pristine Pd control material.

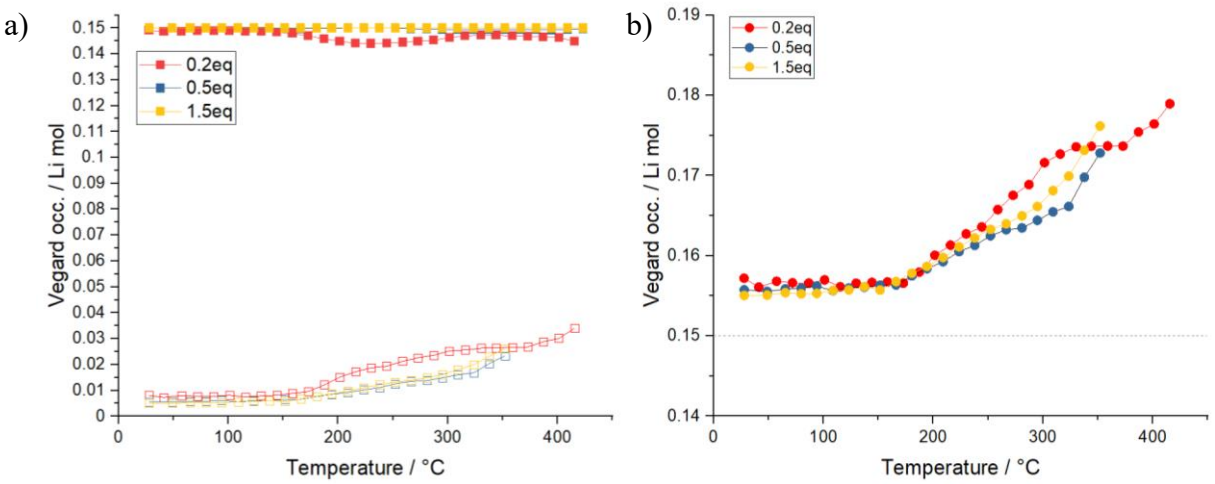


Figure S5-6. Vegard occupancies of the pristine *cF* Pd for all samples, as well as the expanded $Pd^{int}Li$ for 0.2eq showing the small dip in occupancy at 150-250°C. (b) Total Vegard occupancies for Pd and $Pd^{int}Li$ (not included δ-contracted phases).

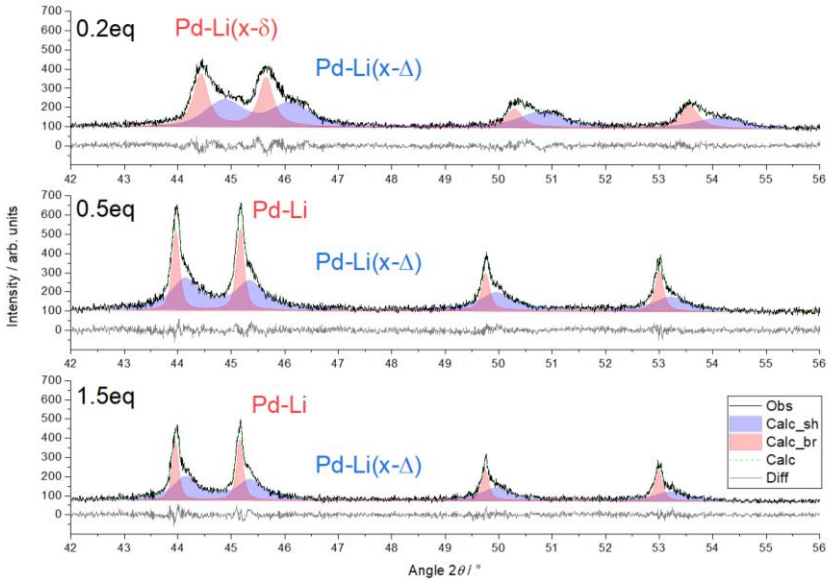


Figure S5-7. Rietveld fitting of high-temperature SXPD patterns showing high-angle reflections (331), (420), (422), and (511).

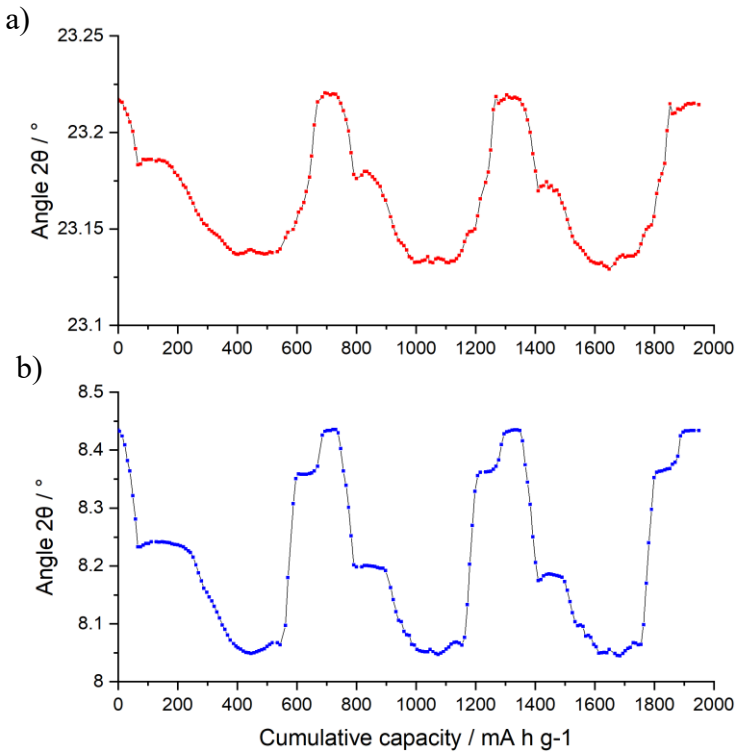


Figure S5-8. Fitting of peaks assigned to graphite at (a) 23° and (b) 8°.

Table S5-2. Tabulated labelling and schematic representation of in-operando phase transitions with respect to intensity.

Half cycle	Transition	Schematic			
1D	1D(0→→2)	Pd		→→	$PdLi_2$
1C	1C(2→→0)	Pd		←←	$PdLi_2$
	1C(0→1)	Pd	→	PdLi	
	1C(2→1)			PdLi	← $PdLi_2$
	1C(1→0)	Pd	←	PdLi	
2D	2D(0→1)	Pd	→	PdLi	
	2D(1→2)			PdLi	→ $PdLi_2$
	2D(1→0)	Pd	←	PdLi	
	2D(0→→2)	Pd		→→	$PdLi_2$
2C	2C(2→→0)	Pd		←←	$PdLi_2$
	2C(0→1)	Pd	→	PdLi	
	2C(2→1)			PdLi	← $PdLi_2$
	2C(1→0)	Pd	←	PdLi	
3D	3D(0→1)	Pd	→	PdLi	
	3D(1→2)			PdLi	→ $PdLi_2$
	3D(1→0)	Pd	←	PdLi	
	3D(0→→2)	Pd		→→	$PdLi_2$
3C	3C(2→→0)	Pd		←←	$PdLi_2$
	3C (0→1)	Pd	→	PdLi	
	3C(2→1)			PdLi	← $PdLi_2$
	3C(1→0)	Pd	←	PdLi	

Table S5-3. Tabulated potential and intensity ranges of in-operando phase transitions.

	Potential / mV			*I*(initial) / arb. units			*I*(final) / arb. units		
Transition	Start	End	Range	Start	End	Range	Start	End	Range
1D(0→→2)	120	0	120	560	70	-490	0	540	540
1*c*(2→→0)	0	226	226	536	530	-6	70	82	12
1*c*(0→1)	232	686	454	82	37	-45	0	397	397
1*c*(2→1)	259	638	379	538	11	-527	0	397	397
1*c*(1→0)	638	3000	2362	397	327	-70	37	44	7
2D(0→1)	3000	173	2827	44	42	-2	327	348	21
2D(1→2)	142	86	56	345	5	-340	8	525	517
2D(1→0)	145	98	47	305	72	-233	37	67	30
2D(0→→2)	70	0	70	83	68	-15	533	542	9
2*c*(2→→0)	0	207	207	542	517	-25	68	74	6
2*c*(0→1)	220	380	160	74	31	-43	1	351	350
2*c*(2→1)	204	594	390	520	25	-495	2	351	349
2*c*(1→0)	700	3000	2300	351	281	-70	31	36	5
3D(0→1)	3000	130	2870	36	31	-5	280	309	29
3D(1→2)	136	85	51	309	28	-281	36	411	375
3D(1→0)	120	82	38	80	26	-54	36	59	23
3D(0→→2)	82	0	82	59	49	-10	411	444	33
3*c*(2→→0)	0	217	217	444	518	74	49	69	20
3*c*(0→1)	217	379	162	69	27	-42	14	279	265
3*c*(2→1)	258	845	587	530	53	-477	13	273	260
3*c*(1→0)	850	3000	2150	273	226	-47	26	32	6

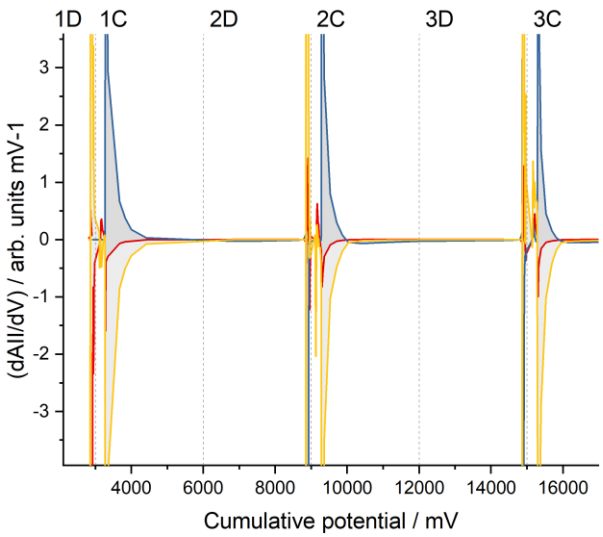


Figure S5-9. Change in intensity against cumulative potential. Smoothed by calculating change over four data points.

Chapter 6: Zeolites

Ag/ZSM-5 by STEM

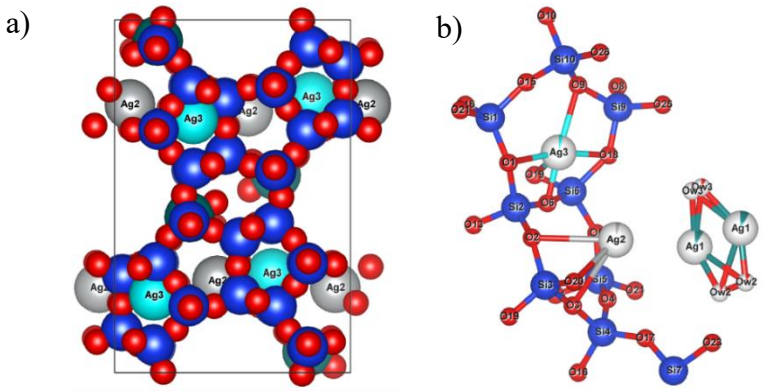


Figure S6-1. Adsorption geometries of Ag adsorption in ZSM-5, derived by SXPD. Reproduced from report by Lin et al.[75] (a) Space-fill viewed down *b*-axis (<010> zone axis) showing poor expected contrast against the framework. (b) Isolated absorption modes, viewed down the *a*-axis.

Table S6-1. Observations of Ag-absorption in the straight channel of ZSM-5 by viewing down <010>.

Site	Observations / %	Reassigning O to T / %
T9/T3	3.80	11.60
O25/O2	10.27	-
T8/T2	22.05	30.04
O7/O1	5.70	-
T1/T7	2.66	10.27
O21/O22	9.51	-
T5/T11	3.42	11.98
O5/O11	7.60	-
T6/T12	29.66	36.12
O18/O11	5.32	-

TMPO/ZSM-5

TMPO/ZSM-5 by SSNMR

By ^{1}H SSNMR, two hydrogen environments are observed at 4.2 ppm and 1.8 ppm, which are assigned to the proton of BAS and of silanol, respectively[99] (Figure S6-2). By ^{27}Al SSNMR, aluminium environments were observed at 55 ppm and a very weak signal at 0 ppm, which are assigned to four-coordinated framework aluminium and extra-framework aluminium, respectively. By ^{29}Si SSNMR, three environments are observed. Two strong signals at -112 ppm and -115 ppm are assigned to Si(0Al, 4Si) sites, while the weak signal peak at -105 ppm is assigned to silicon adjacent to an aluminium, Si(1Al, 3Si). Greater aluminium coordination is prohibited by Löwenstein's rule.[78]

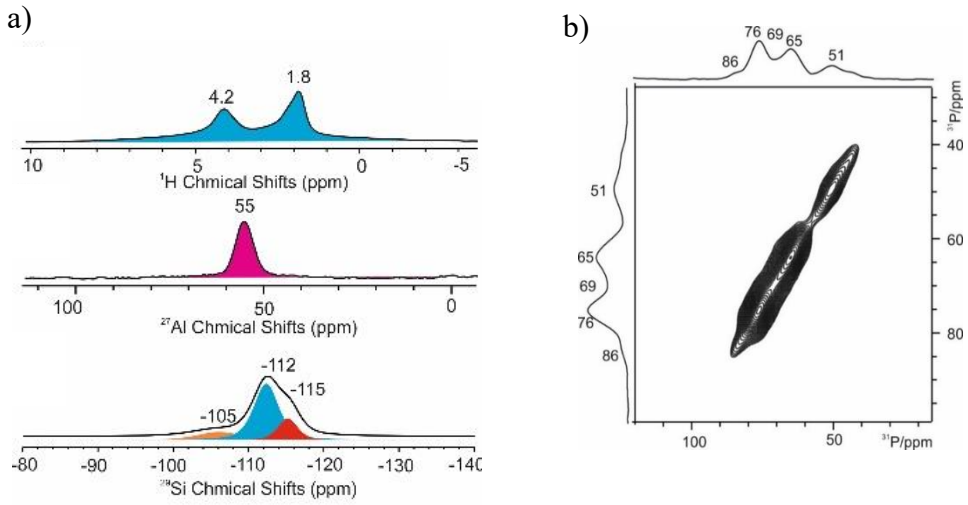


Figure S6-2. SSNMR characterisation. SSNMR spectra of pristine H-ZSM-5: (a) ^{1}H, (b) ^{27}Al, and (c) ^{29}Si. (b) 2D ^{31}P-^{31}P proton-driven spin diffusion SSNMR spectra of TMPO/H-ZSM-5.

TMPO/ZSM-5 by scattering

Table S6-2. Atomic parameters from the Rietveld refinement of TMPO/H-ZSM-5 measured at 25 °C based on SXRD data.

Species	Site	*x*	*y*	*z*	SOF	B_{eq} (Å^2)
Framework	O01	0.3760(4)	0.0396(3)	0.7697(3)	1	2.5(6)
	O02	0.3077(4)	0.0502(3)	0.9255(3)	1	2.5(6)
	O03	0.2004(4)	0.0566(3)	0.0198(3)	1	2.5(6)
	O04	0.0992(3)	0.0557(3)	0.9201(3)	1	2.5(6)
	O05	0.1129(2)	0.0498(3)	0.7237(3)	1	2.5(6)
	O06	0.2446(6)	0.0501(3)	0.7516(3)	1	2.5(6)
	O07	0.37405(4)	0.8360(3)	0.7631(3)	1	2.5(6)
	O08	0.31099(4)	0.8438(3)	0.9273(3)	1	2.5(6)
	O09	0.1969(5)	0.8494(3)	0.0239(3)	1	2.5(6)
	O10	0.0852 (5)	0.8422(3)	0.9002(3)	1	2.5(6)
	O11	0.1215(6)	0.8397(3)	0.7357(3)	1	2.5(6)
	O12	0.2463(5)	0.8418(3)	0.7528(3)	1	2.5(6)
	O13	0.3041(6)	0.9417(3)	0.8224(3)	1	2.5(6)
	O14	0.0777 (7)	0.9468(3)	0.8136(3)	1	2.5(6)
	O15	0.4156(6)	0.1117(3)	0.5909(3)	1	2.5(6)
	O16	0.4091(5)	0.9834(3)	0.5948(3)	1	2.5(6)
	O17	0.4021 (6)	0.8673(3)	0.5814(3)	1	2.5(6)
	O18	0.1844(6)	0.1294(3)	0.6208(3)	1	2.5(6)
	O19	0.2013(5)	0.00380(3)	0.5967(3)	1	2.5(6)
	O20	0.2011 (6)	0.8702(3)	0.5809(3)	1	2.5(6)
	O21	0.9959(6)	0.0439(3)	0.7886(3)	1	2.5(6)
	O22	0.9974(6)	0.8464(3)	0.7905(3)	1	2.5(6)
	O23	0.4189(7)	0.75	0.6477(3)	1	2.5(6)
	O24	0.1887(8)	0.75	0.6547(3)	1	2.5(6)
	O25	0.2908(5)	0.75	0.0529(3)	1	2.5(6)
	O26	0.1100(8)	0.75	0.0690(3)	1	2.5(6)
	Si01	0.4213(3)	0.05047	0.6683(3)	1	1.2(4)
	Si02	0.3072(4)	0.0305(3)	0.8144(3)	1	1.2(4)
	Si03	0.2775(3)	0.0625(3)	0.0415(3)	1	1.2(4)
	Si04	0.1205(3)	0.06055	0.0279(3)	1	1.2(4)
	Si05	0.0724(3)	0.0319(3)	0.8145(3)	1	1.2(4)
	Si06	0.1864(3)	0.05797	0.6743(3)	1	1.2(4)
	Si07	0.4240(3)	0.8243(3)	0.6741(3)	1	1.2(4)
	Si08	0.3100(3)	0.8739(3)	0.8167(3)	1	1.2(4)
	Si09	0.2799(3)	0.8248(3)	0.0260(3)	1	1.2(4)
	Si10	0.1210(3)	0.8240(3)	0.0294(3)	1	1.2(4)
	Si11	0.0704(3)	0.8714(3)	0.8200(3)	1	1.2(4)
	Si12	0.1903(4)	0.8285(3)	0.6843(3)	1	1.2(4)
TMPO-1	P1	0.57173	0.26002	0.69533	0.30(5)	10(5)
	Oa1	0.50060	0.24707	0.71586	0.30(5)	15(8)
	Ca2	0.59142	0.34849	0.72463	0.30(5)	15(8)
	Ca3	0.62348	0.20418	0.77349	0.30(5)	15(8)
	Ca4	0.58933	0.24359	0.56218	0.30(5)	15(8)
TMPO-2	P2	0.49009	0.63660	0.00934	0.7(1)	20.0
	Ob1	0.46474	0.69039	-0.05651	0.7(1)	30.0
	Cb2	0.42684	0.61642	0.10485	0.7(1)	30.0
	Cb3	0.50796	0.56085	-0.06568	0.7(1)	30.0
	Cb4	0.56721	0.66519	0.07128	0.7(1)	30.0
TMPO-3	P3	0.25190	0.74010	0.35583	0.3(2)	16(7)
	Oc1	0.25734	0.66812	0.38154	0.3(2)	20(10)
	Cc2	0.16825	0.75733	0.30460	0.3(2)	20(10)
	Cc3	0.26508	0.79137	0.46907	0.3(2)	20(10)
	Cc4	0.31556	0.76171	0.26164	0.3(2)	20(10)

Table S6-3. Atomic parameters from the Rietveld refinement of TMPO/H-ZSM-5 measured at 25 °C based on NPD data.

Species	Site	*x*	y	*z*	SOF	B_{eq} (Å^2)
Framework	O01	0.3735(5)	0.0544(7)	0.7629(6)	1	2.5(6)
	O02	0.3020(5)	0.0533(5)	0.9212(5)	1	2.5(6)
	O03	0.1953(5)	0.0595(3)	0.0210(5)	1	2.5(6)
	O04	0.0977(5)	0.0651(5)	0.9200(5)	1	2.5(6)
	O05	0.1168(5)	0.0604(5)	0.7278(5)	1	2.5(6)
	O06	0.2441(5)	0.0530(5)	0.7454(8)	1	2.5(6)
	O07	0.3862(5)	0.8539(5)	0.7725(8)	1	2.5(6)
	O08	0.3068(5)	0.8383(4)	0.9201(7)	1	2.5(6)
	O09	0.2095(5)	0.8435(4)	0.0163(8)	1	2.5(6)
	O10	0.0916(5)	0.8451(5)	0.9035(8)	1	2.5(6)
	O11	0.1086(5)	0.8461(5)	0.7327(5)	1	2.5(6)
	O12	0.2445(5)	0.8366(5)	0.7636(5)	1	2.5(6)
	O13	0.3076(5)	0.9466(5)	0.8054(5)	1	2.5(6)
	O14	0.0829(5)	0.9500(5)	0.8182(5)	1	2.5(6)
	O15	0.4108(5)	0.1204(5)	0.5657(5)	1	2.5(6)
	O16	0.4003(5)	1.0022(5)	0.6084(5)	1	2.5(6)
	O17	0.4017(5)	0.8654(5)	0.5834(5)	1	2.5(6)
	O18	0.1826(5)	0.1323(5)	0.6224(5)	1	2.5(6)
	O19	0.1962(5)	-0.0023(6)	0.5933(5)	1	2.5(6)
	O20	0.2028(5)	0.8633(5)	0.5694(5)	1	2.5(6)
	O21	0.9940(5)	0.0467(7)	0.7886(5)	1	2.5(6)
	O22	0.9952(5)	0.8575(7)	0.7961(5)	1	2.5(6)
	O23	0.4298(5)	0.75	0.6334(5)	1	2.5(6)
	O24	0.1906(5)	0.75	0.6465(5)	1	2.5(6)
	O25	0.3067(5)	0.75	0.0479(4)	1	2.5(6)
	O26	0.1073(5)	0.75	0.0708(4)	1	2.5(6)
	Si01	0.4275(3)	0.0650(3)	0.6608(4)	1	1.2 (4)
	Si02	0.3103(5)	0.0278(3)	0.8016(5)	1	1.2 (4)
	Si03	0.2808(2)	0.0678(5)	0.0404(5)	1	1.2 (4)
	Si04	0.1165(5)	0.0600(5)	0.0273(5)	1	1.2 (4)
	Si05	0.0704(5)	0.0400(5)	0.8167(5)	1	1.2 (4)
	Si06	0.1846(5)	0.0484(5)	0.6732(5)	1	1.2 (4)
	Si07	0.4197(3)	0.8290(2)	0.6793(5)	1	1.2 (4)
	Si08	0.3063(3)	0.8692(3)	0.8060(5)	1	1.2 (4)
	Si09	0.2767(5)	0.8221(5)	0.0249(5)	1	1.2 (4)
	Si10	0.1031(5)	0.8223(5)	0.0138(5)	1	1.2 (4)
	Si11	0.0679(3)	0.8443(5)	0.8326(5)	1	1.2 (4)
	Si12	0.1786(5)	0.8189(5)	0.67138(5)	1	1.2 (4)
	H7	0.4245(5)	0.87196(5)	0.8257(5)	1	2.5(6)
	H26	0.0972(5)	0.7498(5)	0.1274(4)	1	2.5(6)
	H20	0.1990(5)	0.8210(5)	0.5029(4)	1	2.5(6)
TMPO-1	P1	0.5309	0.2759	0.6586	0.18(2)	10(4)
	Oa1	0.4654	0.2419	0.6562	0.18(2)	16(6)
	Ca2	0.520(6)	0.362(5)	0.686(1)	0.18(2)	16(6)
	Ca3	0.581(2)	0.239(2)	0.751(5)	0.18(2)	16(6)
	Ca4	0.570(2)	0.2680(4)	0.541(6)	0.18(2)	16(6)
	Ha21	0.487(2)	0.382(5)	0.626(4)	0.18(2)	16(6)
	Ha22	0.494(2)	0.367(5)	0.763(5)	0.18(2)	16(6)
	Ha23	0.570(2)	0.386(5)	0.702(2)	0.18(2)	16(6)
	Ha31	0.556(3)	0.244(3)	0.827(7)	0.18(2)	16(6)
	Ha32	0.587(3)	0.183(3)	0.733(5)	0.18(2)	16(6)
	Ha33	0.635(4)	0.258(2)	0.743(5)	0.18(2)	16(6)
	Ha41	0.577(2)	0.212(3)	0.523(6)	0.18(2)	16(6)
	Ha42	0.537(3)	0.292(1)	0.481(7)	0.18(2)	16(6)
	Ha43	0.616(3)	0.302(2)	0.538(6)	0.18(2)	16(6)
TMPO-2	P2	0.489	0.586	-0.031	0.8(1)	20.0
	Ob1	0.466	0.602	-0.133	0.8(1)	30.0
	Cb2	0.424(4)	0.547(3)	0.036(4)	0.8(1)	30.0
	Cb3	0.558(4)	0.530(4)	-0.0371(4)	0.8(1)	30.0
	Cb4	0.513(2)	0.660(5)	0.030(4)	0.8(1)	30.0
	Hb21	0.379(5)	0.583(4)	0.040(4)	0.8(1)	30.0
	Hb22	0.408(5)	0.498(3)	-0.004(5)	0.8(1)	30.0
	Hb23	0.444(5)	0.526(5)	0.110(7)	0.8(1)	30.0
	Hb31	0.542(5)	0.482(4)	-0.077(3)	0.8(1)	30.0

Species	Site	*x*	y	*z*	SOF	B_{eq} (Å^2)
	Hb32	0.600(4)	0.555(4)	-0.081(3)	0.8(1)	30.0
	Hb33	0.582(5)	0.526(5)	0.040(6)	0.8(1)	30.0
	Hb41	0.556(4)	0.685(6)	-0.014(5)	0.8(1)	30.0
	Hb42	0.469(4)	0.696(6)	0.034(4)	0.8(1)	30.0
	Hb43	0.522(2)	0.649(5)	0.113(8)	0.83880	30.0
TMPO-3	P3	0.229	0.707	0.329	0.67(6)	16(7)
	Oc1	0.207	0.681	0.426	0.67(6)	20(10)
	Cc2	0.168(4)	0.762(4)	0.281(3)	0.67(6)	20(10)
	Cc3	0.304(5)	0.751(3)	0.344(1)	0.67(6)	20(10)
	Cc4	0.2403(8)	0.640(4)	0.245(6)	0.67(6)	20(10)
	Hc21	0.118(5)	0.734(4)	0.271(3)	0.67(6)	20(10)
	Hc22	0.160(4)	0.806(5)	0.336(5)	0.67(6)	20(10)
	Hc23	0.189(4)	0.790(4)	0.213(6)	0.67(6)	20(10)
	Hc31	0.297(5)	0.795(4)	0.399(4)	0.67(6)	20(10)
	Hc32	0.344(5)	0.716(4)	0.375(3)	0.67(6)	20(10)
	Hc33	0.327(5)	0.763(3)	0.267(6)	0.67(6)	20(10)
	Hc41	0.281(3)	0.604(5)	0.275(6)	0.67(6)	20(10)
	Hc42	0.191(4)	0.612(5)	0.235(6)	0.67(6)	20(10)
	Hc43	0.248(1)	0.661(5)	0.165(8)	0.67(6)	20(10)

DFT calculations

Using the results of the indirect aluminium siting through the observation of probe molecules by SXPD, aluminium was fully substituted at T6, T8, and T12. After optimisation, the average lengths of Si-O bond and Al-O are 1.6 Å and 1.8 Å (Table S6-4), respectively, which are consistent with the SXPD and NPD results. Additionally, the other bond lengths are also in good agreement with the crystallographic analyses to within an acceptable error. For example, after optimisation TMPO becomes effectively fully coordinated to the acidic BAS proton to form $TMPOH^+$, observed in the short H_{BAS}-O_{TMPO} bond length: 1.04 Å, 1.02 Å and 1.05 Å for TMPO adsorbed on T6, T8 site, and T12 site, respectively (Figure S18). These structures do not deviate much from the experimentally observed states, i.e. 1.07(2) Å for H1-O1, 1.08(9) Å for H2-O2 and 1.01(6) Å for H3-O3.

Table S6-4. DFT-optimised bond lengths of TMPO adsorbed on BAS: Al substitution at T6, T8, and T12 sites.

BAS site	Al site	Si-O_{zeo} / Å	Al-O_{zeo} / Å	H-O_{zeo} / Å	H-O_{TMPO} / Å
T6-O18(H)-T9	T6	1.62	1.79	1.51	1.04
T7-O7(H)-T8	T8	1.62	1.77	1.57	1.02
T3-O20(H)-T12	T12	1.63	1.80	1.46	1.05

RSXPD

Far-from -edge pattern on I11

The experimentally-observed line-profile is modelled using the fundamental parameters approach, in which the emission profile is convoluted with instrumental aberrations from beam divergence (simple axial model) and diffractometer geometry (R_p = 48 m, R_s = 430 mm, w = 0.015 mm).

The structural model was refined from the well-known ZSM-5 structure. The symmetry of the space group *Pnma* yielded 192 framework oxygen sites and 96 framework tetrahedral sites from 26 and 12 inequivalent sites, respectively, per unit-cell. Additionally, two oxygen atoms were refined within the pore in order to model solvent/unattributed electron density, yielding 16 solvent oxygen atoms in the unit-cell (Wyckoff positions: 8d × 2 sites = 16 atoms per unit-cell). Oxygen atoms were modelled as O^{2-} and tetrahedral sites as Si^{4+}. Three Debye-Waller factors were refined for silicon, framework oxygen, and solvent oxygen respectively. Site occupancy factors (SOF) of framework sites were fixed to a value of 1.

Structures containing different number of solvent sites were carried out (Figure S6-3). The refinements showed decreasing improvement in fitting more than two solvent sites, up to quite insignificant improvement for 5 solvent sites (Figure S6-3). For the two-solvent structure, Os1 is located in the centre of the sinusoidal channel, while Os2 is located in the centre of the straight channel. Chemical sensibility need not strictly apply here because the sites are not necessarily modelling spherical atomistic electron density (indicated by large thermal parameters). Hence, even under high vacuum two solvent sites are justified as a fitting aid.

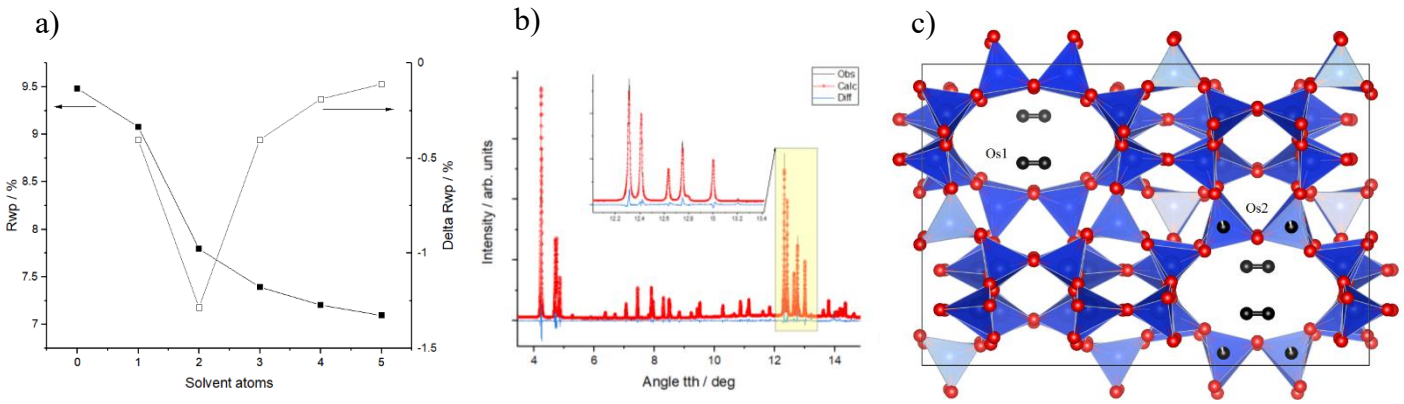


Figure S6-3. (a) Dependence of residual parameter R_{wp} on channel solvent atoms. (b) Rietveld fitting of far-from-edge pattern (15 keV) using two-solvent structure at 10^{-5} bar collected on I11, DLS. (c) Corresponding structure solution viewed down the a-axis; silicon: blue, framework oxygen: red, solvent oxygen: white.

Table S6-5. Structural information derived from Rietveld fitting at far-from-edge energy.

	Z38: 2 solvent
No. bkg parameters	24
R_{exp} / %	4.682
R_{wp} / %	7.795
R_p / %	6.041
GoF	1.665
Space group	*Pnma*
Lattice parameter	
a / Å	20.10488(7)
b / Å	19.92961(7)
c / Å	13.41721(5)
Volume / Å^3	5376.04(3)
Phase density / g cm^{-3}	1.8597(5)
beq (= 8 π^2 × *U*iso) / Å^2	
T-site	2.74(4)
O (framework)	1.37(3)
O (solvent)	20.0(8)

Table S6-6. Atomic coordinates of Rietveld refinement of Z38 at 15 keV (I11) using a two-solvent-atom structure. Errors and occupancies also shown.

Site	*x*	*y*	*z*	SOF
Si1	0.4215(3)	0.0546(4)	0.6652(4)	1
Si2	0.3070(4)	0.0297(4)	0.8102(4)	1
Si3	0.2772(2)	0.0607(3)	0.0280(4)	1
Si4	0.1198(3)	0.0636(3)	0.0287(4)	1
Si5	0.0721(3)	0.0328(3)	0.8132(4)	1
Si6	0.1853(3)	0.0577(3)	0.6705(4)	1
Si7	0.4238(3)	0.8294(3)	0.6729(5)	1
Si8	0.3091(3)	0.8691(3)	0.8215(4)	1
Si9	0.2790(3)	0.8259(3)	0.0322(4)	1
Si10	0.1211(3)	0.8289(3)	0.0257(5)	1
Si11	0.0682(3)	0.8714(3)	0.8118(4)	1
Si12	0.1903(4)	0.8260(3)	0.6795(4)	1
O1	0.3713(5)	0.0529(7)	0.7682(7)	1
O2	0.3070(6)	0.0661(5)	0.9115(6)	1
O3	0.2007(5)	0.0585(5)	0.0251(5)	1
O4	0.0968(4)	0.0619(6)	0.9198(7)	1
O5	0.1139(5)	0.0572(7)	0.7232(7)	1
O6	0.2402(5)	0.0545(7)	0.7391(6)	1
O7	0.3736(6)	0.8485(6)	0.7670(7)	1
O8	0.3088(6)	0.8459(4)	0.9297(6)	1
O9	0.2074(5)	0.8451(4)	0.0202(6)	1
O10	0.0897(5)	0.8396(5)	0.9076(7)	1
O11	0.1208(6)	0.8487(5)	0.7302(7)	1
O12	0.2434(6)	0.8408(5)	0.7498(8)	1
O13	0.3094(5)	0.9490(5)	0.8168(5)	1
O14	0.0768(4)	0.9597(5)	0.8154(6)	1
O15	0.4193(5)	0.1219(5)	0.602(8)	1
O16	0.4070(5)	0.9949(5)	0.5745(8)	1
O17	0.4033(6)	0.8688(5)	0.5761(8)	1
O18	0.1862(6)	0.1320(5)	0.6208(6)	1
O19	0.1927(7)	0.0045(4)	0.5986(6)	1
O20	0.2071(6)	0.8690(5)	0.5645(6)	1
O21	1.0001(5)	0.0489(7)	0.7767(6)	1
O22	0.9920(6)	0.8482(6)	0.8017(7)	1
O23	0.4192(7)	0.75	0.643(1)	1
O24	0.2003(9)	0.75	0.6527(8)	1
O25	0.2958(8)	0.75	0.0785(8)	1
O26	0.1139(8)	0.75	0.0698(9)	1
Os1	0.5928(5)	0.2743(9)	0.6719(7)	1.05591
Os2	0.0118(8)	0.1740(7)	0.5403(1)	0.91947

Table S6-7. Distance of total extinction of beam through different media.

Medium	Chemical formula	Density / g cm^{-3}	Attenuation length at 1540 eV / cm	Attenuation length at 15000eV / cm
Glass	SiO_2	2.2	4.50×10^{-4}	7.8×10^{-2}
ZSM-5	Si_{96} $O1_{92}$	0.72	1.39×10^{-3}	2.4×10^{-1}
Air (1 bar)	N_2:0.78, O_2:0.21, CO_2: 0.03, Ar: 0.01	1.3×10^{-3}	6.9×10^{-1}	4.72×10^{2}
Air (10^{-7} bar)	""	1.3×10^{4}	6.92×10^{6}	4.72×10^{9}

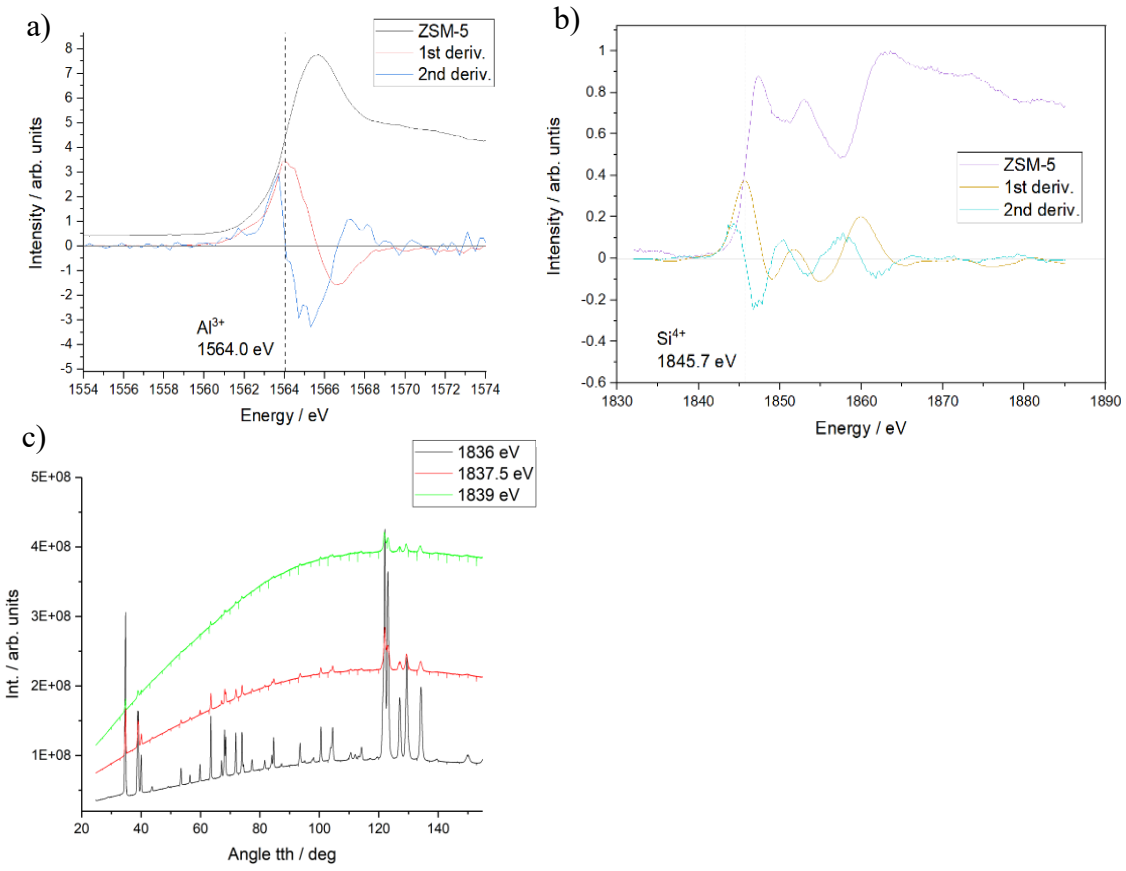


Figure S6-4. (a) Absolute, and first and second derivative of experimental fluorescence spectra over the Al K-edge of reference aluminium foil and Z38 sample. Energies are uncalibrated. (b) Energy calibration and (c) 1D patterns around silicon K-edge, which suffer from significant absorption.

Simulated RSXPD pattern

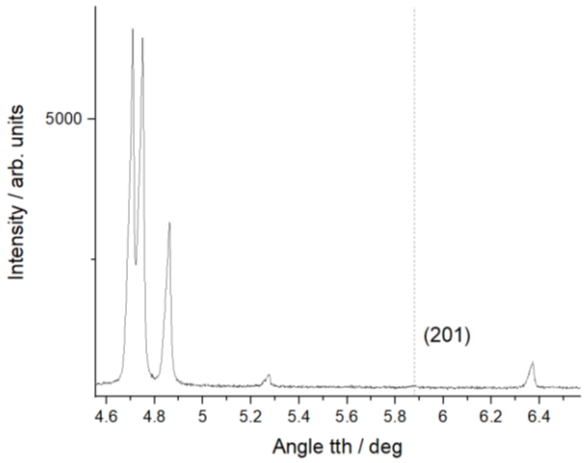


Figure S6-5. Observation of very weak (201) reflection which is shown to be dependent on the presence of aluminium and its siting.

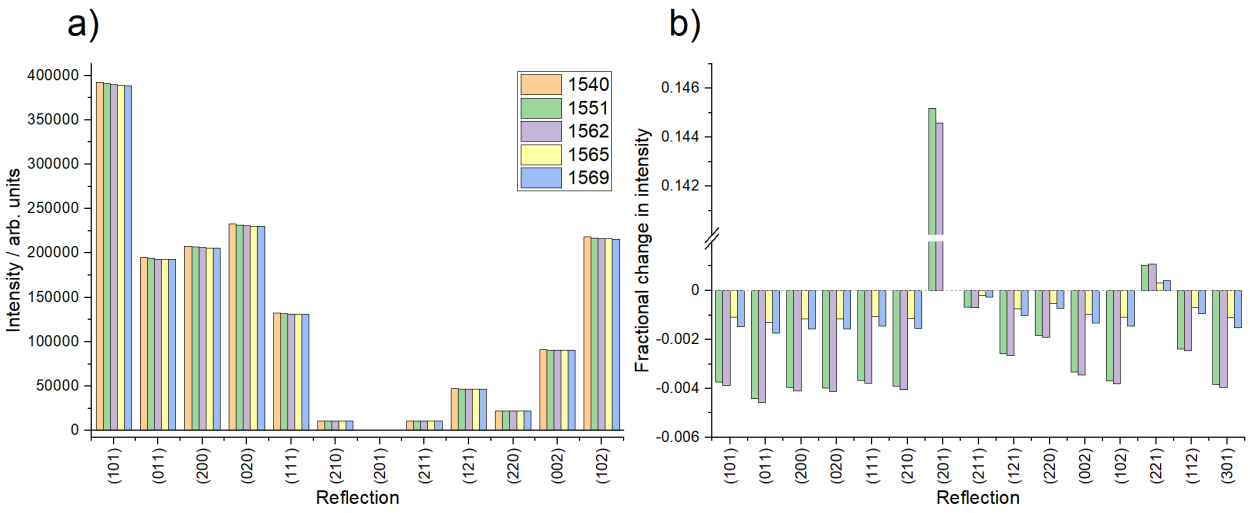


Figure S6-6. Simulated integrated intensities of the first 15 observed reflections at various energies for non-aluminium structure T0: (a) raw intensity, and (b) change in intensity from the previous energy pattern.

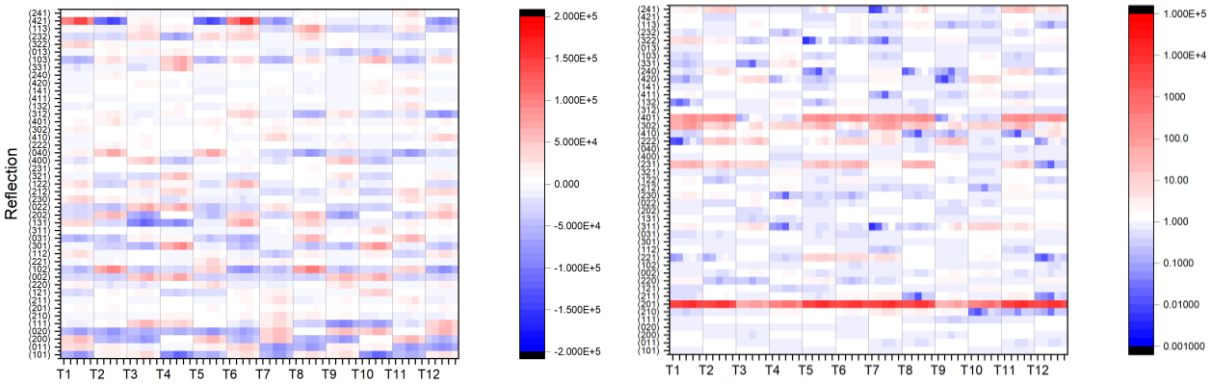


Figure S6-7. Change in intensity relative to T0 over all structures, energies (five squares within each T-site column), and reflections: (a) linear, and (b) fractional change.

Experimental patterns

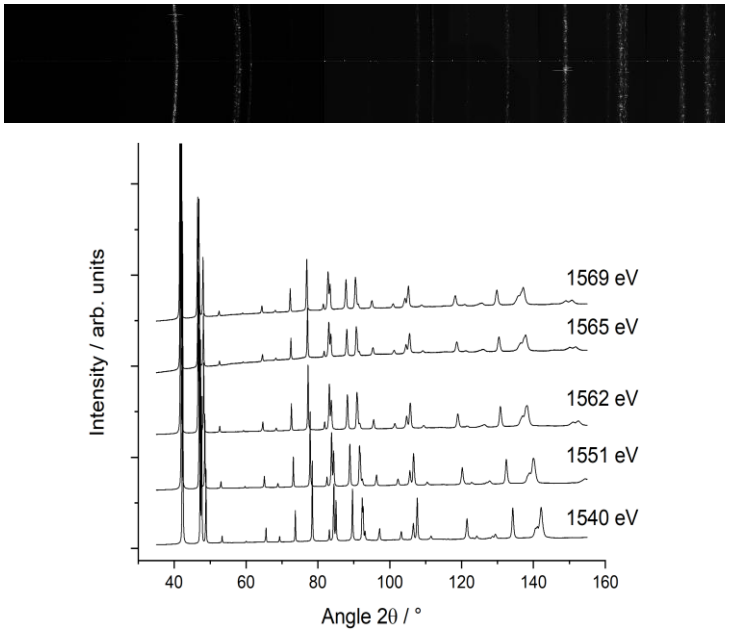


Figure S6-8. Typical diffraction pattern yielded by RSXPD on I10: (a) raw 2D (left to right: 35-~90°), and (b) processed 1D.

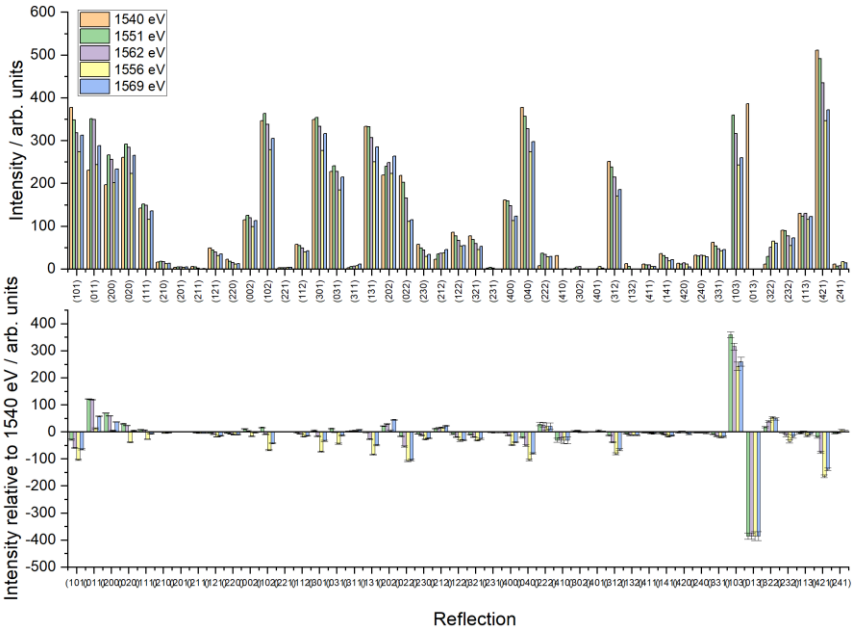


Figure S6-9. Integrated intensities of 45 reflections experimentally observed of ZSM-5 by RSXPD on I10. (a) Absolute intensity, no errors shown. (b) Change in intensity relative to lowest energy 1540 eV, errors shown.

Table S6-8. Angle-dependent parameters as refined by Pawley and Rietveld refinement for the five RSXPD patterns.

	GoF	Energy / eV	*a* / Å	*b* / Å	*c* / Å	Zero-error / °
Pawley	1.24	1541.238(5)	20.08212(8)	19.93092(7)	13.41721	0.0199(2)
	1.06	1551.964(6)	20.06735(9)	19.92862(9)	13.41721	0.0553(2)
	1.00	1562.083(8)	20.0606(1)	19.9237(1)	13.41721	0.0640(3)
	0.70	1564.69(1)	20.0534(2)	19.9178(2)	13.41721	0.0627(4)
	0.79	1568.45(1)	20.0482(2)	19.9136(2)	13.41721	0.0664(4)
Rietveld	1.94	1541.425(5)	20.08304(8)	19.93125(7)	13.41721	0.0319(3)
	1.55	1552.197(6)	20.06808(8)	19.9288(8)	13.41721	0.0689(3)
	1.52	1562.354(9)	20.0623(1)	19.9249(1)	13.41721	0.0814(4)
	1.08	1564.94(1)	20.0551(1)	19.9189(1)	13.41721	0.0791(6)
	1.27	1568.7(1)	20.0520(1)	19.9163(1)	13.41721	0.0875(5)

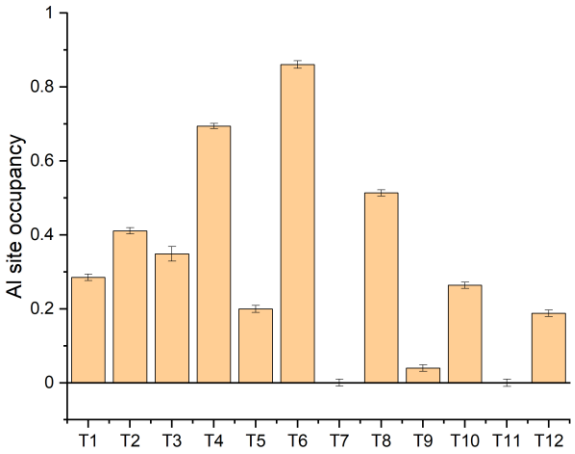


Figure S6-10. Aluminium occupancy by RSXPD without constraint on total occupancy.

Direct aluminium characterisation by EELS

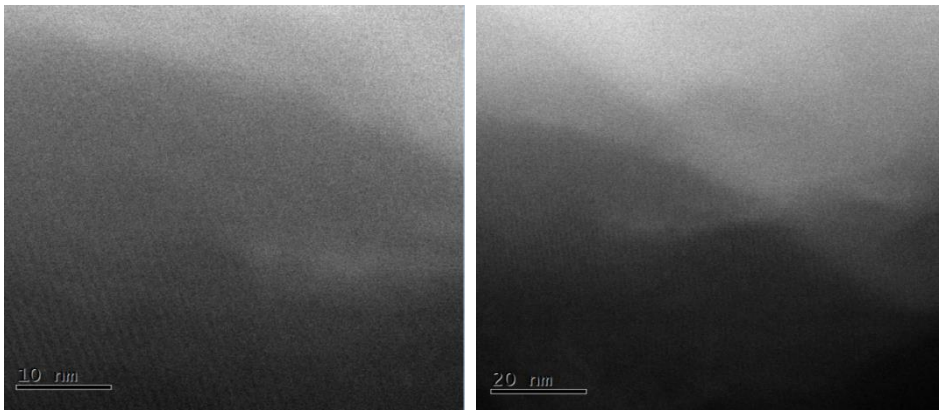


Figure S6-11. Preliminary investigation of atomic-resolution EELS to directly visualise the aluminium site in ZSM-5.

DAFS on I10

While on the RSXPD beamtime it was realised that much of the data-collection time is due to sampling a very wide angular range with a small detector, i.e. 12 sets of 10° patterns. By collecting data from only one 10° range, the number of energies used can be increased by a factor of 12 for a given time-period. The sampling of only one section also foregoes moving the detector, which saves time and eliminates use of the motors, which have been repeatedly failed during these data-collections.

Deciding which 10° range to scan was selected by the following properties: number of reflections, high-angle to maximise ASF contribution (Thompson scattering, f_0, is highly dependent on scattering angle, while ASF are only energy dispersive), symmetry diverse reflections indicated by unrelated Miller indices, narrow peak shape for accurate intensities, low peak overlap. Many of these are fulfilled by the region centred at 79°, which included several non-overlapping reflections and at relatively high angle: (102), (221), (112), (301), and (031).

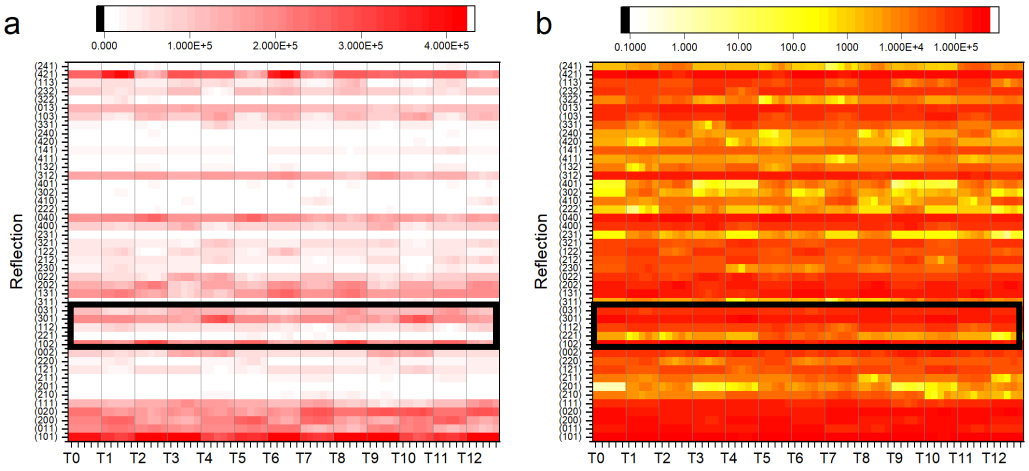


Figure S6-12. Raw intensity of each reflection for each structure. Intensity plotted against (a) linear, and (b) logarithmic colour scales. The five experimental energies from the main RSXPD experiment are shown as five segments within each column. The reflections within the region analysed for DANES/DAFS is shown within black box.

A pattern was collected at ~1 eV intervals. Far more energies were sampled than expected leading to the (102) reflection moving outside of the sampled range. In hindsight, the detector could have been moved at several points in order to keep the *Q*-space region constant. When plotted as a contour plot, the absorption edge is clearly visible at 1569 eV, and the post-edge fine structure is evident by the contour lines (Figure S6-13). These changes are reflection dependent, and as an ensemble should be able to yield phase-specific information. It is even hoped that it is possible to yield site-specific environment characterisation.

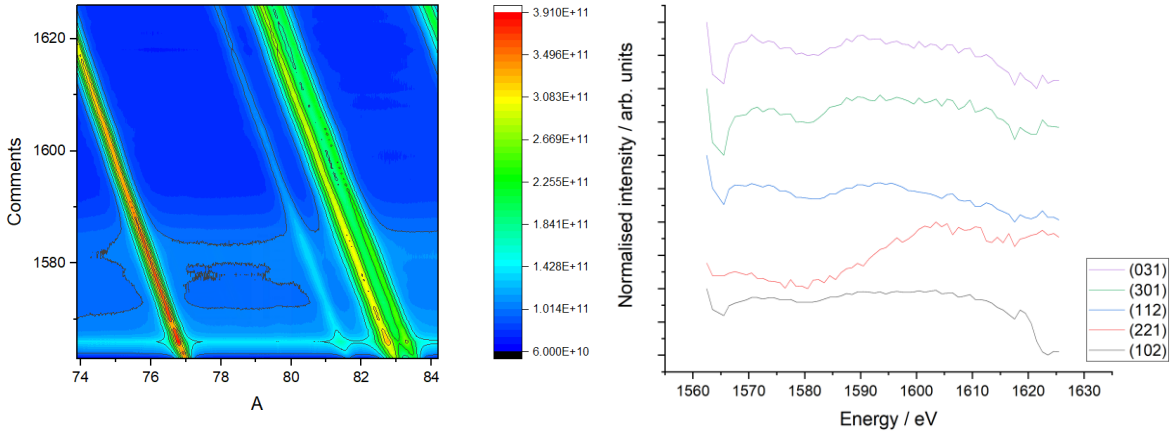


Figure S6-13. (a) RSXPD patterns as contour plots. (b) Integrated intensities as derived by Pawley refinement.

Initial Pawley refinement shows a drop in integrated intensity over the aluminium edge, which is very close to the start of the energy range. It is evident that the data collection was started too close to the edge to observe the pre-edge. However, the fluctuations in intensity remain of interest.

[Intentionally blank]

[End of document]